UNIVERSITY OF SOUTHAMPTON

Faculty of Engineering and Physical Sciences
School of Electronics and Computer Science

# Integrated silicon optomechanical system and its applications

*by*

**Xiangming Xu**
MEng

*A thesis for the degree of*
*Doctor of Philosophy*

December 2021

University of Southampton

Abstract

Faculty of Engineering and Physical Sciences
School of Electronics and Computer Science

Doctor of Philosophy

**Integrated silicon optomechanical system and its applications**

by Xiangming Xu

Optomechanics studies the interaction between the optical force and mechanical objects, and has led to intensive developments in ultra-sensitive measurements, coherent quantum control, optical tweezers, etc. Silicon photonics is a material platform from which Photonics Integrated Circuits can be made, and provide a perfect solution for minimising optical systems. This thesis studies the integration of optomechanics and silicon photonics—integrated silicon optomechanics, and explores its applications in distributed fibre optical sensing (DFOS) and optical trapping. A novel 1.5 $\mu m$ thick Silicon on Insulator (SOI) platform is also demonstrated, which is advantageous to the two applications compared to the widely-used thin SOI platform.

Firstly, this thesis proposes to use the integrated cavity optomechanical system to generate optical probe signals for DFOS. The proposed application is based on optomechanical oscillation (OMO), through which optical pulse trains (OPT) and sweeping-wavelength optical signals (SWOS) for the DFOS application can be generated. Comprehensive analyses on the OMO threshold and oscillation characteristics are conducted, and the extinction ratio (ER), duty cycle (DC) of the OPT and the sweeping range of the SWOS are derived. Examples of utilising OMO-based OPT and SWOS for DFOS applications are then demonstrated. The proposed OMO-based OPT generator and OMO-Based SWOS generator do not rely on external RF sources and optical modulators and can be fully integrated with silicon photonics platform. They thus provide unconventional methods to reshape the optical source generation in DFOS.

Secondly, this thesis presents the design, optimisation and scaling effect of a dual-waveguide optical trap on a SOI platform by comprehensive numerical simulations in Lumerical FDTD Solutions. The simulations demonstrate that the waveguide thickness is a crucial parameter in designing a dual-waveguide optical trap. It was found the optimal waveguide thickness generally increases with the gap distance, accompanied by a periodic feature. The optimal waveguide thickness and gap distance display clear scaling effects over the optical wavelength. This thesis also proposes to use the OMO process to load micro/nano-particles. The OMO process can break the adhesive

connection between the micro/nano-particles and the container's surface. The works above not only pave the way for the design and optimisation of dual-waveguide optical trappings for various applications, but also lays the foundation of a fully on-chip optical trapping system working on vacuum or air.

Lastly, this thesis experimentally demonstrated a novel 1.5 $\mu m$ thick SOI platform for integrated optomechanics, rather than the widely-used thin SOI with a top silicon layer less than 300 $nm$. For both the above two applications, thick SOI shows its advantages. Thick SOI is suitable for fabricating low-frequency mechanical resonators, which are necessary for long-distance DFOS applications. Thick SOI is also essential for dual-waveguide optical trapping with a larger gap distance. In addition, the 1.5 $\mu m$ thick SOI has high power handling capability, low propagation loss, large mode size, and comparatively small bend radius. Individual integrated silicon optomechanical components based on 1.5 $\mu m$ SOI platform are designed, fabricated, and measured, including waveguides, grating couplers, MMIs, Bragg gratings, optical microresonators and mechanical resonators. The measurement results show that all the individual photonics components function well. These works lay a solid foundation for the full integration of a silicon optomechanical system in the future.

# Contents

**List of Figures** ix

**List of Tables** xv

**Declaration of Authorship** xvii

**Acknowledgements** xix

**Definitions and Abbreviations** xxi

**1 Introduction** 1
- 1.1 Research background of optomechanics . . . 1
- 1.2 Motivation and objective . . . 2
- 1.3 Thesis Structure . . . 4

**2 Literature Review** 5
- 2.1 Basics of cavity optomechanics . . . 5
  - 2.1.1 Optical resonator . . . 5
  - 2.1.2 Resonator-waveguide coupling theory . . . 7
  - 2.1.3 Mechanical resonator . . . 10
  - 2.1.4 On-chip silicon cavity optomechanics in practice . . . 12
  - 2.1.5 Cavity optomechanical parameters . . . 13
- 2.2 Silicon photonics . . . 14
- 2.3 Optical trapping . . . 15
  - 2.3.1 The development of optical trapping . . . 15
  - 2.3.2 On-chip optical trapping . . . 16
- 2.4 Distributed fibre optical sensing . . . 19
  - 2.4.1 OTDR using the OPT source . . . 19
  - 2.4.2 OFDR using the SWOS source . . . 21
  - 2.4.3 The need for an integrated optical probe source for DFOS . . . 22
- 2.5 Summary . . . 24

**3 Integrated silicon optomechanics for distributed fibre optical sensing** 25
- 3.1 Cavity optomechanics . . . 26
  - 3.1.1 Cavity optomechanical coupling . . . 26
  - 3.1.2 Dimensionless coupling equations . . . 29
  - 3.1.3 Optomechanical dynamic back-action . . . 30
    - 3.1.3.1 Linearised optomechanical coupling equations . . . 30

3.1.3.2 Optomechanical oscillation threshold . . . 32
3.2 Optomechanical oscillation . . . 35
3.2.1 Oscillation in small amplitude . . . 35
3.2.2 Oscillation in large amplitude regime . . . 39
3.2.2.1 Optomechanical induced chaos . . . 41
3.2.2.2 mushroom-like phase trajectory . . . 41
3.3 Optomechanical OPT generation for OTDR . . . 44
3.3.1 OPT generation in different regimes . . . 44
3.3.2 OMO-Based OPT generation for OTDR . . . 46
3.3.2.1 Time-Frequency (T-F) localisation . . . 46
3.3.2.2 OMO-based OPT generation examples for OTDR . . . 48
3.4 Optomechanical SWOS generation for OFDR . . . 51
3.4.1 SWOS generation theory . . . 52
3.4.2 OMO-based SWOS generation for OFDR . . . 53
3.5 Conclusion and discussion . . . 56

**4 Silicon optomechanics for on-chip optical trapping 59**
4.1 Optical Trapping Force . . . 59
4.2 Dual-waveguide optical trapping . . . 62
4.2.1 Finite-difference time-domain (FDTD) method . . . 63
4.2.2 Dual-waveguide configuration . . . 63
4.2.3 Intensity field profile . . . 65
4.2.4 Optical trapping force and trapping potential . . . 66
4.2.5 Optical trapping capability for different particle size . . . 68
4.3 Dual-waveguide optical trapping optimisation and scaling effect . . . 70
4.3.1 Intensity field distribution over different waveguide thickness . . . 70
4.3.2 Optimal waveguide thickness for optical trapping . . . 72
4.3.3 Scaling effect over the wavelength . . . 74
4.4 Optomechanical oscillation for separating micro/nano-particles . . . 78
4.4.1 Micro/nano-article loading . . . 78
4.4.2 Micro/Nano Particles separation threshold . . . 79
4.4.3 Optomechanical oscillation for separating particles . . . 80
4.5 Conclusion and discussion . . . 81

**5 Integrated optomechanical components based on thick SOI platform 83**
5.1 The advantages of a thick SOI platform . . . 83
5.1.1 Low mechanical frequency . . . 84
5.1.2 High power handling . . . 85
5.1.3 Low waveguide propagation loss . . . 85
5.1.4 Large mode size . . . 86
5.2 Integrated photonic components design . . . 86
5.2.1 1.5 $\mu m$ thick SOI platform . . . 86
5.2.2 Optical waveguide . . . 87
5.2.3 Grating coupler . . . 89
5.2.4 Multimode interferometer (MMI) . . . 93
5.2.5 Waveguide Bragg grating . . . 94
5.3 Device fabrication . . . 98

5.3.1 Fabrication flow . . . 98
5.3.2 Fabrication imperfection analysis . . . 100
5.4 Integrated photonic components measurement . . . 102
5.4.1 Measurement setup . . . 102
5.4.2 Grating coupler . . . 103
5.4.3 MMI . . . 105
5.4.4 Waveguide Bragg grating . . . 106
5.5 Measurement and parameter extraction of optical microresonators . . . 110
5.6 Brownian motion measurement of mechanical resonators . . . 113
5.7 Conclusion and discussion . . . 117

**6 Conclusion** **119**
6.1 Summary . . . 119
6.2 Outlook . . . 121

**References** **123**

**Publication List** **137**

# List of Figures

2.1 Schematic illustration of a Fabry-Perot optical cavity with length $L$. . . . 6
2.2 Schematic illustration of a Fabry-Perot optical cavity coupled to an external field. . . . 7
2.3 (A) An evanescently coupled unidirectional resonator-waveguide system made from a WGM resonator coupled to a bus waveguide. (B) The three coupling regimes of the resonator-waveguide coupling system, shown as the transmission spectrum over the laser detuning. . . . . 9
2.4 Schematic diagram of a mechanical resonator. . . . . 10
2.5 Examples of on-chip silicon cavity optomechanical systems. (a) Microtoroids in which the scattering-radiation pressure drives the rim of the cavity and changes the optical path length [49]. (b) Microdisk optical cavity with integrated wrap-around coupling waveguide, in which the coupling is induced by the scattering-radiation force due to the photon momentum transfer [50]. (c) Racetrack microresonator, in which part of the waveguide is suspended to form the mechanical resonator. The gradient force between the suspended waveguide and substrate leads to optomechanical coupling [51]. (d) Microdisk resonator, the gradient force between the suspended beam and microdisk cavity couples them together [52]. (e) Double-micro-ring cavity, where the gradient force between the two vertically stacked ring cavities realises the optomechanical coupling[53]. (f) 1-D photonic crystal cavity, in which optical mode and mechanical mode can be both confined to the small defect region in the nanobeam and are coupled through the scattering-radiation force [54]. (g) 2-D photonic crystal cavity, in which optical mode and mechanical mode can be both confined to the small defect region in the membrane and are coupled through the scattering-radiation force [55]. (h)"Zipper" photonic crystal cavity, where the two nanobeams are coupled through the gradient optical force [43]. . . . . 14
2.6 Development of optical trapping [66]. (a) Particles are driven along the direction of the light by radiation pressure force. (b) Particles are simultaneously attracted towards the centre of the beam by gradient force, where the light intensity is highest. (c) Particles are levitated by pointing the laser vertically upwards, where radiation pressure force balances the gravity. (d) Particles are trapped by optical tweezers formed by a focused laser beam. . . . . 16
2.7 Various on-chip optical trapping structures (A) Waveguide trapping [70] (B) Ring resonator trapping [71] (C) Photonic crystal cavity trapping [72] 17

2.8 Various dual-waveguide trapping devices. (A) The first design of dual-waveguide trapping based on two multimode strip $Si_3N_4$ waveguides [73]. (B) The first experimental dual-waveguide trapping with $Ta_2O_5$ waveguide [35]. (C) Dual-waveguide trapping based on freeform optics using polymer [37]. . . . . 18
2.9 Schematic diagram of an OTDR. . . . . 20
2.10 Schematic diagram of an OFDR. . . . . 21

3.1 (A) Schematic diagram of an optomechanical system in the WGM form with cavity resonant frequency $\omega_{cav}$ and damping rate $\kappa$. The mechanical resonator with resonant frequency $\Omega_m$, damping rate $\Gamma_m$, and effective mass $m_{eff}$ is coupled with the optical cavity through a coupling coefficient $G$. The optomechanical system is excited with an input light through a coupling rate $\kappa_e/2$, and the transmitted optical field through the drop port is the output. (B) An on-chip WGM optomechanical system composed of a microdisk resonator and two bus waveguides which are coupled through the optical scattering radiation force. (C) An on-chip WGM optomechanical system composed of a micro-racetrack optical cavity and two bus waveguides which are coupled through the optical gradient force. . . . . 27
3.2 (A-D) The normalised optomechanical damping rate $\widetilde{\Gamma_{opt}}$ as a function of $\tilde{P}$ and $\widetilde{\Delta}$ for $\tilde{\kappa} = 0.1$, $\tilde{\kappa} = 0.5$, $\tilde{\kappa} = 2$ and $\tilde{\kappa} = 10$, respectively. The contours in the figure show the OMO threshold for $\widetilde{\Gamma_m} = 0.001, 0.01, 0.1, 1$. 33
3.3 OMO dead-zone shown as a relationship of $\widetilde{\Gamma_m}$ and $\tilde{\kappa}$. In the dead-zone, no oscillation will occur under any $\tilde{\Delta}$ and $\tilde{P}$. . . . . 33
3.4 (A) Threshold power $\tilde{P}_{thres}$ for OMO process as a function of $\tilde{\kappa}$ and $\widetilde{\Delta}$ when $\widetilde{\Gamma_m} = 1/5000$. (B)The minimum threshold power $\tilde{P}^{min}_{thres}$ and the corresponding normalised optimal detuning $\widetilde{\Delta}^{norm}_{opt} = \widetilde{\Delta}_{opt}/(1+\tilde{\kappa})$ as a function of $\tilde{\kappa}$. . . . . 34
3.5 The simulated time trace of $\tilde{x}$ over $\tilde{t}$ in an OMO process. The simulated optomechanical parameters are: $\tilde{\kappa} = 100$, $\widetilde{\Gamma_m} = 1000$, $\widetilde{\Delta} = 30$, $\tilde{P} = 4 \times 10^5$, with the initial displacement set at the equilibrium state $\widetilde{x_{init}} = 147.3$. 36
3.6 (A-D) The amplitude-dependent effective optomechanical damping rate $\widetilde{\Gamma_{opt}}$ as a function of $\widetilde{\Delta}$, $\tilde{A}$ when $\tilde{\kappa} = 0.1$, $\tilde{\kappa} = 0.5$, $\tilde{\kappa} = 2$ and $\tilde{\kappa} = 10$, respectively. $\tilde{P}$ is set to a constant as 1. The contour lines shows the possible steady-state when $\widetilde{\Gamma_m} = 10^{-3}, 10^{-4}$ and $10^{-5}$ respectively. . . . 38
3.7 (A-D) The evolution of the OMO process phase space trajectories with the increase of normalised input power $\tilde{P}$ for $\tilde{\kappa} = 0.1$, $\tilde{\kappa} = 0.5$, $\tilde{\kappa} = 2$ and $\tilde{\kappa} = 10$, respectively. The $\widetilde{\Gamma_m}$ is set to a constant as 0.001, and $\widetilde{\Delta}$ is set to an optimised value for OMO according to Section 3.1.3.2. The initial condition of the numerical simulation is set to $\tilde{a} = \tilde{x} = \dot{\tilde{x}} = 0$. . . . . 40
3.8 (A-C) The calculated Lyapunov exponents variation of the OMO process with the increase of normalised input power $\tilde{P}$ for $\tilde{\kappa} = 0.1$, $\tilde{\kappa} = 0.5$ and $\tilde{\kappa} = 2$ respectively, corresponding to the evolution diagrams shown in Figure 3.7 . . . . . 42
3.9 (A) The phase space trajectory showing the velocity and displacement. (B, C, D) The time-domain change of oscillation displacement, velocity and acceleration. Note the simulation results are for an optomechanical system in deeply USR with $\tilde{\kappa} = 100$, $\widetilde{\Gamma_m} = 0.01$, $\widetilde{\Delta} = 20$, $\tilde{P} = 4e7$. . . . . 43

3.10 (A) Three dimensional phase space trajectory showing the phonon cavity number-displacement-velocity variation. (B) The time-domain variation of acceleration (top) and the cavity photon number (bottom). Note the simulation results are for an deeply unresolved sideband optomechanical system with $\tilde{\kappa} = 100$, $\widetilde{\Gamma_m} = 0.01$, $\widetilde{\Delta} = 20$, $\tilde{P} = 4e7$. . . . . 44
3.11 (a-d) OPT generation with normalised optical cavity decay rates $\tilde{\kappa} = 0.1, 0.5, 2, 10$, respectively. Other parameters are kept as constant: $\widetilde{\Gamma_m} = 1/1000$, $\tilde{\Delta} = 1$, $\tilde{P} = 100$. . . . . 45
3.12 The characteristics of the generated OPT under different parameters. (A, B, C) The ER variation with $\tilde{P}$ and $\widetilde{\Gamma_m}$ when $\tilde{\kappa} = 10$, $\tilde{\kappa} = 40$, $\tilde{\kappa} = 100$, respectively. (D, E, F) The DC variation with $\tilde{P}$ and $\widetilde{\Gamma_m}$ when $\tilde{\kappa} = 10$, $\tilde{\kappa} = 40$, $\tilde{\kappa} = 100$, respectively. The laser detuning $\tilde{\Delta}$ is set to a constant at the optimal value associated with a minimum threshold power. . . . . 47
3.13 Comparison between OMO based optical pulse and the traditional optical pulse (A) in time-domain. (B) in frequency-domain. The pulses all have 50 ns FWHM and 1$\mu$s period. The OMO based optical pulse is generated in an optomechanical system with $\tilde{\kappa} = 100$. . . . . 48
3.14 The upper-left box shows the schematic of an OMO-based OPT generator. It is formed by suspending part of a racetrack-shaped microresonator on an SOI substrate, where the mechanical resonator (suspended beam) is coupled to the optical cavity. The other three boxes show the classical OPT generators utilized in three types of DFOS (BOTDR, Phi-OTDR, and POTDR), which use a function generator and an EOM to generate OPT. These traditional OPT generators can be replaced by the OMO-based OPT generator. EOM: Electro-optic modulator, FC: Fibre coupler, PS: Polarisation scrambler, PD: Photodetector, LC: Local oscillator, BPF: Bandpass filter. . . . . 49
3.15 The schematic diagram of generating SWOS with the OMO process in a cavity optomechanical system. Two laser sources, with one being single-wavelength and another being broadband, are injected into the optomechanical system through the two ends. The single-wavelength laser with proper laser detuning and optical power can drive the mechanical resonator into oscillation. This oscillation, in turn, changes the optical cavity resonance frequency. Another broadband laser passing through the optical cavity is filtered into a single-wavelength laser source, whose frequency is modulated by the OMO process. The linewidth of the broadband laser source is chosen to be smaller than the FSR of the optical microcavity. During the experiment, two optical isolators should be put on the output of the two laser sources (port 1 and port 3) to isolate the laser transmitted back from the multimode interferometer (MMI). . . . . 52
3.16 The schematic diagram of using the OMO-based SWOS in an OFDR application. The proposed OMO-based SWOS can replace the traditional sweeping-frequency sources, and the generated optical pulse trains can be used as a trigger signal to synchronise the sweeping system and signal processing system. Also, two optical isolators should be put on the output of the two laser sources to isolate the laser transmitted back from the multimode interferometer (MMI). . . . . 54

3.17 (A, B, C) The simulated mechanical oscillation amplitude $\widetilde{A}$ variation with $\tilde{P}$ and $\widetilde{\Gamma_m}$ when $\tilde{\kappa} = 10,\ 40,\ 100$, respectively. The laser detuning $\tilde{\Delta}$ is set to a constant at the optimal value associated with a minimum threshold power. The frequency-sweeping range depends on both the mechanical frequency and the mechanical resonant frequency, which can be expressed as $\Delta F = \widetilde{A}\Omega_m$. . . . . 55

4.1 Qualitative analysis of optical force in Ray optics treatment . . . . . 60
4.2 Schematic of the simulation model for the dual-waveguide optical trap. Two identical rib waveguides are separated by a gap distance L, and two in-phase mode sources with the same powers of 50 $mW$ are placed at 0.5 $\mu$m from the end facet of the waveguides with opposite injection directions. To maintain the single-mode condition, the waveguide width is set to be $w = 0.87\ t$, where $t$ is the thickness of the waveguide. . . . . 64
4.3 TE mode profile of the rib waveguide from the two in-phase mode sources. 64
4.4 (A and B) Field intensity profile for a gap distance $L = 1\ \mu m$ in XY plane and XZ plane, respectively. (C and D) Field intensity profile for a gap distance $L = 3\ \mu m$ in XY plane and XZ plane, respectively. . . . . 66
4.5 (A, B and C) The simulated optical force and trapping potential for a silica sphere with 200 $nm$ diameter trapped at the centre of a dual-waveguide optical trap with waveguide thickness $t = 3.5\ \mu m$ and gap distance $L = 4\ \mu m$ in the y-axis, z-axis and x-axis respectively. Note that the applied optical power is 50 $mW$ each. . . . . 67
4.6 The simulated optical force and trapping potential for a silica sphere with radius of 50 $nm$, 100$nm$, 150 $nm$ and 200 $nm$ trapped at the centre of a dual-waveguide optical trap with waveguide thickness $t = 3.5\ \mu m$ and gap distance $L = 4\ \mu m$ in the y-axis, z-axis and x-axis respectively. Note that the applied optical power is 50 $mW$ each. . . . . 69
4.7 Field intensity profile in the x-axis for dual-waveguide trap with waveguide thickness from 0.5 $\mu m$ to 4 $\mu m$ when (A) the gap distance $L$=0.775 $\mu m$. (B) the gap distance $L$=2.325 $\mu m$. (C) the gap distance $L$=3.875 $\mu m$. (D) the gap distance $L$=5.425 $\mu m$. The grey line in the figures show the contour map of the optical intensity. . . . . 71
4.8 (A,B, and C) The field intensity as a function of the gap distance $L$ and the waveguide thickness $t$ at the centre, X1, X2, respectively. The colour represents the optical intensity. The wavelength $\lambda = 1550\ nm$ . . . . . 73
4.9 The extracted maximum optical intensity and optimal waveguide thickness $t_{op}$ as a function of the gap distance L at the centre, X1, X2. The blue curves represent the extracted data for the optical waveguide thickness $t_{op}$, while the red curves indicate the corresponding maximum optical intensity. The curves with triangular, rectangular, and star shape symbols represent the data for the trapping point at the centre, X1, and X2, respectively. . . . . 74
4.10 (A,B, and C) Normalised optimal waveguide thickness $t_{op\_norm} = t_{op}/\lambda$ as a function of the normalised gap distance $L_{norm} = L/\lambda$ at the trapping point at the centre, X1, X2, respectively. . . . . 75

4.11 From top to bottom: Maximum intensity as a function of normalized gap distance $L_{norm} = L/\lambda$ at the trapping point at the centre, X1, X2, respectively. In each figure, the curves for different wavelengths are plotted with different colours and symbols. . . . . 76
4.12 The required minimum acceleration needed to break the adherent force and separate a silica sphere from a flat surface. . . . . 80

5.1 Total internal reflection, describing the working principle of a dielectric waveguide. . . . . 87
5.2 The cross-section and mode profile of rib and strip waveguide (A) Cross-section of a strip waveguide. (B) Cross-section of rib waveguide. (C) TE mode field profile of a strip waveguide. (D) TE mode profile of a rib waveguide. . . . . 88
5.3 Cross-section of a silicon rib waveguide. . . . . 89
5.4 Schematic cross-section of a grating coupler. . . . . 90
5.5 Schematic of a grating coupler. (A) Conventional design (B) Inverse taper design . . . . . 91
5.6 The FDTD simulation model for (A) Conventional grating coupler (B) Grating coupler with reverse taper design . . . . . 92
5.7 The FDTD simulation results for (A) Conventional grating coupler (B) Grating coupler with reverse taper design . . . . . 93
5.8 The schematic diagram of (A) $2 \times 2$ MMI and (B) $1 \times 2$ MMI . . . . . 94
5.9 Simulated field profile of the designed $1 \times 2$ MMI . . . . . 94
5.10 Schematic diagram of a Bragg grating . . . . . 95
5.11 A top view schematic of a Bragg grating . . . . . 96
5.12 Simulated transmission and reflection spectrum of the Bragg grating with the dimension parameters. . . . . 97
5.13 The schematic diagram of the fabrication process. There are two Ebeam lithography steps and two ICP etches. The steps from (A) to (E) are processed for the waveguide, grating coupler and alignment marks; The steps from (F) to (I) is the processing of micro-gap and beam; The last HF vapour etch step suspends the beam and form the mechanical resonator. 99
5.14 Thin wall caused by thin resist . . . . . 101
5.15 The schematic diagram of the waveguide cross-section view after the second resist spin . . . . . 101
5.16 The schematic diagram of the experimental setup used to measure the on-chip photonic devices. . . . . 102
5.17 The fibre coupling platform . . . . . 103
5.18 The SEM images of the fabricated grating coupler. (A) shows the inverse taper connected to uniformly etched gratings. (B) shows the measured dimensional size of the grating period, with grating period $\Lambda = 857\ nm$ and teeth width $w = 427\ nm$, which are close to the designed parameters $860\ nm$ and $430\ nm$ respectively shown in the last section. . . . . 104
5.19 (A) The measurement and simulation result of a single grating coupler with inverse taper design, the coupling angle is set to be $-13.4°$. The data is obtained from the measured coupling efficiency divided by a factor of 2 because there are two grating couplers. (B) The measurement results of the grating coupler with coupling angle varying from $-11°$ to $-15°$. . 105
5.20 The image of the fabricated $1 \times 2$ MMI. . . . . 105

5.21 Schematic of the cascaded MMIs test structure, with the input of an MMI connected to one of the outputs of another MMI. . . . . 106
5.22 The measurement result of the cascaded MMIs. The lines with black dots are the experimental measurement results, and the red line shows the linear fitted data. An average power spitting ratio of 2.96 $dB$ is inferred from the results, which shows the functionality of the fabricated MMI. . 106
5.23 Waveguide Bragg grating . . . . . 106
5.24 Measurement results for the waveguide Bragg gratings without gap, the parameters are (A) $\Lambda = 226\ nm$, $N = 1500$. (B) $\Lambda = 226\ nm$, $N = 3000$. (C) $\Lambda = 228\ nm$, $N = 1500$. (D) $\Lambda = 228\ nm$, $N = 3000$. (E) $\Lambda = 230\ nm$, $N = 1500$. (F) $\Lambda = 230\ nm$, $N = 3000$; . . . . . 107
5.25 The test results of Bragg grating with gaps for different periods. (a) Period $\Lambda = 226\ nm$. (b) Period $\Lambda = 228\ nm$. (c) Period $\Lambda = 230\ nm$ . . . . . 109
5.26 The images of the fabricated racetrack-shape optical microresonator . . . 110
5.27 The measured transmission spectrums of the racetrack-shape microresonator for six different coupling distances, 250 $nm$, 350 $nm$, 450 $nm$, 550 $nm$, 650 $nm$, 750 $nm$ . . . . . 111
5.28 (A) The extracted values of optical damping rate $\kappa_e$, $\kappa_i$, and $\kappa = \kappa_i + \kappa_e$ for different gap distances. (B) The extracted values of optical Q-factor $Q_e$, $Q_i$, and $1/Q = 1/Q_e + 1/Q_i$ for different gap distances. . . . . 112
5.29 The calculated waveguide loss . . . . . 113
5.30 Suspended cantilever mechanical resonator . . . . . 114
5.31 Detection scheme of the cantilever motion [164]. When a focused beam of electrons hits the surface of an oscillating nanostructure, the secondary electron current $I$ is modulated by the mechanical motion of nanostructure. Spectral analysis of the SE current thus provides the motion information of the nanostructure. . . . . 115
5.32 The measured thermal noise spectrum originated from the Brownian motion of the suspended cantilever beam with a length of (A) 12 $\mu m$. (B) 8 $\mu m$. (C) 6 $\mu m$. The insets show the enlarged view of the thermomechanical spectrum (blue) and the Lorentz fitting (red) near the peak. . . . 116

# List of Tables

3.1 The comparison between OMO oscillation amplitude $\tilde{A}$ obtained analytically from harmonic ansatz (Figure 3.6) and numerically from solving the coupling equations (Figure 3.7), when $\tilde{P} = 1$, $\Gamma_m = 0.001$, and $\tilde{\kappa} = 0.1, 0.5, 2, 10$ respectively. $\tilde{\Delta}$ is set to an optimised value associated with a minimum threshold power for OMO. . . . . 41
3.2 Variance in the time-domain and frequency-domain with the product of the two variances for different optical pulse shapes . . . . . 48
3.3 Four sets of optomechanical parameters of the OMO-based OPT generator for an OTDR application . . . . . 50
3.4 The characteristics of the generated OPT and corresponding OTDR measurement specifications for the four sets of optomechanical parameters . 51
3.5 The spatial resolution and laser coherent length of the OFDR measurement using the OMO-based SWOS with the optomechanical parameters in Case 4 in Table 3.3 and other two ideal cases. . . . . 56

4.1 The value of normalised optimal waveguide thickness $t_{op\_norm}$ when the Normalised gap distance $L_{norm}$ matches the standing wave condition for trapping point at Center, X1 and X2. . . . . 77

5.1 The measurement and simulation results of Bragg grating without a gap. 108
5.2 The fundamental in-plane resonant mode frequency of the suspended cantilever obtained from finite element simulation and experiment, respectively. . . . . 115

# Declaration of Authorship

I declare that this thesis and the work presented in it is my own and has been generated by me as the result of my own original research.

I confirm that:

1. This work was done wholly or mainly while in candidature for a research degree at this University;
2. Where any part of this thesis has previously been submitted for a degree or any other qualification at this University or any other institution, this has been clearly stated;
3. Where I have consulted the published work of others, this is always clearly attributed;
4. Where I have quoted from the work of others, the source is always given. With the exception of such quotations, this thesis is entirely my own work;
5. I have acknowledged all main sources of help;
6. Where the thesis is based on work done by myself jointly with others, I have made clear exactly what was done by others and what I have contributed myself;
7. Parts of this work have been published. A list of publications is provided in the end of this thesis.

Signed:..... Date:.....

# Acknowledgements

First of all, I would like to express my sincere gratitude to my supervisor, Dr. Jize Yan, for his continuous supports and guidance throughout my PhD. I was always inspired and motivated by his multitude of ideas and brilliant insights. I could not have asked for a better supervisor to learn how to do research. I also want to thank my second supervisor Prof. David Thomson. He was so kind and never hesitated to offer helps to me. I am so grateful for his supports and guidance in silicon photonics design and fabrication.

This PhD project was funded by Faculty of Engineering and Physical Sciences, for which I am greatly thankful. I also want to express my gratitude to China Scholarship Council for covering my living expenses over my PhD.

Thanks to all members in our group, Yu Feng, Hailong Pi, Wangke Yu, Chuang Sun, Shumeng Wang, Gaoce Han, Adam Li for the stimulating discussions and nice atomosphere. Special thanks to Hailong, Wangke and Chuang for the helps in the lab experiments when I was not able to due to the COVID.

Thanks to Prof.Ulbricht Hendrik, Dr.Muddassar Rashid, Tiberius Georgescu for the collaboration in levitated optomechanics. Thanks to Dr. Bruce Ou, Tongjun Liu for your continuous help, especially for the stunning setup for measuring the Brownian motion. Bruce has helped me a lot, not only in the experiments including fibre coupling stage building and tunable laser configuration, but also in inspiring me in various aspects. Thanks to the cleanroom support in the device fabrication and testing, Ali Khokhar, Kian Kiang, Anushka Gangnaik and Arzubiaga Libe.

I would also want to thank my friends in Southampton, especially those who joined me with Badminton and Parkrun. These moments are my best memories in Southampton, which I will never forget.

Lastly, I would like to express deepest gratitude to my wife, Yucheng, who stands with me and loves me always. Thanks to our lovely boy, Ian, who joined us in my last year of PhD, for bringing me the joy and happiness. You both are the motivation that supports me through this hard year. Thanks to my parents and sisters for their enduring love and supports.

# Definitions and Abbreviations

| | |
|---|---|
| LIGO | Laser Interferometer Gravitational-Wave Observatory |
| Q-factor | Quality-factor |
| OMO | Optomechanical Oscillation |
| DFOS | Distributed Fibre Optical Sensing |
| CMOS | Complementary Metal Oxide Semiconductor |
| MEMS/NEMS | Micro/Nano-Electro-Mechanical-System |
| SOI | Silicon On Insulator |
| FSR | Free Spectral Range |
| PSD | Power Spectral Density |
| FWHM | Full Width at Half Maxima |
| WGM | Whispering Gallery Mode |
| OTDR | Optical Time-Domain Reflectometry |
| OFDR | Optical Frequency-Domain Reflectometry |
| OCDR | Optical Coherence-Domain Reflectometry |
| POTDR | Polarisation Optical Time-Domain Reflectometry |
| BOTDR | Brillouin Optical Time-Domain Reflectometry |
| Phi-OTDR | Phase Optical Time-Domain Reflectometry |
| SNR | Signal-to-Noise Ratio |
| ER | Extinction Ratio |
| DC | Duty Cycle |
| OPT | Optical Pulse Trains |
| SWOS | Sweeping-Wavelength Optical Signals |
| RSR | Resolved-Sideband Regime, $\kappa < \Omega_m (\tilde{\kappa} < 1)$ |
| USR | Unresolved-Sideband Regime, $\kappa > \Omega_m (\tilde{\kappa} > 1)$ |
| FDTD | Finite-Difference Time-Domain |
| TE | Transverse Electric |
| SEM | Scanned Electron Microscope |
| ICP | Inductively Coupled Plasma |
| $\lambda_{cav}$ | The resonant wavelength of the optical cavity |
| $\omega_{cav}$ | The resonant angular frequency of the optical cavity |
| $\omega_L$ | Laser angular frequency |
| $\Delta$ | Laser detuning, $\Delta = \omega_L - \omega_{cav}$ |

| | |
|---|---|
| $n_g$ | Group refractive index |
| $\kappa_i$ | Optical cavity intrinsic energy decay rate |
| $\kappa_e$ | Optical cavity external energy decay rate |
| $\kappa$ | Optical cavity energy decay rate (linewidth), $\kappa = \kappa_e + \kappa_i$ |
| $a$ | Optical field amplitude |
| $n_c$ | Optical cavity photon number, $n_c = \lvert a \rvert^2$ |
| $s$ | Input laser amplitude field |
| $m_{eff}$ | Effective mass of a mechanical resonator |
| $\Omega_m$ | Mechanical resonance angular frequency |
| $\Gamma_m$ | Mechanical damping rate |
| $Q_m$ | Mechanical Q-factor |
| $x$ | Mechanical displacement |
| $\chi_m(\Omega)$ | Mechanical susceptibility |
| $S_{xx}(\Omega)$ | Displacement power spectral density |
| $G$ | Optomechanical coupling coefficient, $G = -\partial\omega_{cav}(x)/\partial x$ |
| $P_{in}$ | The real input laser power, $P_{in} = \hbar\omega_L \lvert s \rvert^2$ |
| $\tilde{a}$ | Dimensionless normalised optical field amplitude, $\tilde{a} = a\Omega_m/(2\sqrt{\frac{\kappa_e}{2}}s)$ |
| $\tilde{x}$ | Dimensionless normalised mechanical displacement, $\tilde{x} = Gx/\Omega_m$ |
| $\widetilde{\Delta}$ | Dimensionless normalised laser detuning, $\widetilde{\Delta} = \Delta/\Omega_m$ |
| $\tilde{\kappa}$ | Dimensionless normalised optical cavity decay rate, $\tilde{\kappa} = \kappa/\Omega_m$ |
| $\widetilde{\Gamma_m}$ | Dimensionless normalised mechanical damping rate, $\widetilde{\Gamma_m} = \Gamma_m/\Omega_m$ |
| $\tilde{P}$ | Dimensionless normalised input laser power, $\tilde{P} = \frac{2P_{in}G^2}{m_{eff}\Omega_m^4\omega_L}$ |
| $\widetilde{\Gamma_{opt}}$ | Dimensionless normalised optomechanical damping rate |
| $\widetilde{\Gamma_{eff}}$ | Dimensionless normalised effective mechanical damping rate |

# Chapter 1

# Introduction

## 1.1 Research background of optomechanics

Optomechanics studies the interaction between optical radiation pressure and mechanical objects. The concept of optical radiation pressure was first introduced by Kepler in 1619 to explain the phenomenon that comet tails always point away from the Sun, claiming that this is due to the radiation pressure of the sunlight [1]. This claim remained unsubstantiated for more than two centuries before Maxwell's theory of electromagnetism showed that light is an electromagnetic wave and carries momentum and can therefore exert a force [2]. The experimental observations of the radiation pressure force were realized by Lebedew and Nichols and Hull in the 1900s using thermal light sources and a torsion balance [3, 4]. In 1909, Einstein theoretically derived the statistic of radiation pressure force [5], which also led to the discovery of the wave-particle nature of light and quantum mechanics.

However, the magnitude of these effects was too weak to have any significant practical use. For a 1 $W$ of incident beam perpendicular to a totally reflecting mirror, the generated radiation pressure force due to the reflection is around 7 $nN$ [6]. This force is too tiny to be observed and has no prominent effects on macroscopic objects before the invention of the laser in 1960 [7]. A laser can provide a high-intensity, monochromatic, collimated light field which is necessary for studying the optical radiation pressure forces. Since then, the studies on optomechanics have developed mainly into two different research directions.

The first is the cavity optomechanics, where light is confined in an optical cavity and interacts with a mechanical resonator during its circulations [8, 9]. It was first investigated by Braginsky in the context of an interferometer by considering a harmonically

suspended end mirror of an optical cavity. He theoretically studied the coupling process and experimentally demonstrated that the retarded nature of the radiation pressure force in the optical cavity could be used to cool or amplify the motion of the mechanical resonator, which is called dynamic back-action [10, 11]. On the other hand, the mechanical motion of the movable mirror also led to the modulation of the enhanced optical cavity field dramatically, which makes it possible to measure the mechanical motion with extremely high sensitivity and accuracy. The most prominent example is the Laser Interferometer Gravitational-Wave Observatory (LIGO) project for gravitational wave detection [12], which won the 2017 Nobel Prize in Physics for its observation of gravitational waves from a black hole merge. Braginsky also studied the impact of radiation pressure force on the accuracy of this measurement [13, 14], in which he derived the standard quantum limit for the LIGO.

The second is the optical trapping. In the 1970s, Ashkin and his colleagues showed that the radiation pressure force from a focused laser beam could trap and manipulate small micrometre-size dielectric particles [15, 16]. This technique soon led to the application of optical tweezers for trapping and manipulating viruses, cells, bacteria, etc. It now becomes an off-the-shelf tool in bio- and medical-researches [6]. Besides, optical trappings are also essential building blocks for levitated optomechanics [17, 18], where micro/nano dielectric particles are trapped and levitated by the optical radiation pressure force in air or vacuum and decoupled from the environment. This decoupling reduces the environmental dissipation and results in an ultra-high quality factor (Q-factor) of the levitated particles, making it one of the most promising platforms for applications in high-sensitivity sensing [19, 20, 21] and test of quantum physics [22, 23]. The methods of trapping and manipulating with optical radiation pressure were also extended to molecules and atoms. Atoms were trapped and cooled to their motional ground state and the ultracold atoms have enabled many applications including optical atom clocks and precision quantum measurements [24, 25].

## 1.2 Motivation and objective

With the advancements of micro/nano fabrication, the field of optomechanics in both the two research lines has seen a substantial development of miniaturization into micro/nano scale during the last two decades.

A variety of on-chip cavity optomechanical devices has been realised [26], in which many interesting cavity optomechanical effects have been observed, including optical spring [27], bistability [28], normal-mode splitting [29], optomechanical induced transparency [30], optomechanical cooling [31] and optomechanical oscillation (OMO) [32]. Among these effects, OMO is unique and of great importance. It is induced by one of the dynamic back-action — optomechanical amplification, whereby the mechanical

resonator can be driven into self-oscillation by the optical cavity field. Such an on-chip mechanical oscillation can also imprint itself into the optical cavity field, resulting in the modulation on the optical cavity field and therefore acts as an on-chip modulator without external RF sources.

In distributed fibre optical sensing (DFOS) that has been widely used in structure heath monitoring [33], the physical parameters along the fibre can be measured distributedly by injecting intensity-modulated optical pulse trains (OPT) or frequency-modulated sweeping-wavelength optical signal (SWOS) into the fibre and detecting the backscattered light signal. The OMO process thus provides a perfect solution for optical probe signal generation in DFOS due to its on-chip modulation capability. Traditionally, the optical probe signals are generated by discrete components, which are bulky and costly and hinder the large-scale applications of DFOS. There is thus a clear and reasonable incentive to explore the potential of using the on-chip OMO modulation method for the optical probe signal generation (OPT and SWOS) in DFOS.

Along another research line, different on-chip optical trapping platforms have been proposed and experimentally demonstrated. The near-field on-chip optical trapping exploits the exponentially decaying evanescent field from the surface where light is confined [34]. Such near-field trapping can only attract the particles to the surface, which is not desired when one wants to levitate the particles or hold the particles in a specific position. Compared to the near-field trapping, the dual-waveguide trapping, which is the on-chip version of Ashkin's dual-beam trapping, can stably levitate the particles without contact with the chip surface and move the position of the trapped particles by controlling the two beams. Several dual-waveguide optical trapping platforms based on the unusually-used materials $Ti_2O_5$ [35], TripleX [36], polymer [37] have been proposed, however, no systematic analyses and optimisations regarding the waveguide dimension and gap distance have been conducted. Therefore, there is clear motivation to further study and optimise the dual-waveguide optical trapping scheme in a readily available platform such as silicon.

On the other hand, silicon photonics is the photonic system that uses silicon as an optical medium, similar to how electronics is concerned with the transmission and manipulation of electrons [38]. It has experienced an enormous development because of the well-established processing technology of silicon and the capability with complementary-metal-oxide-semiconductor (CMOS) technologies. It provides the path to miniaturise the optical system. In addition, silicon is also the perfect material platform for making micro/nano mechanical structures, which has boosted the development of the Micro/Nano-Electro-Mechanical-System (MEMS/NEMS) [39]. Silicon is thus the most promising platform for integrated optomechanics. However, the widely used silicon photonics material platform is the silicon on insulator (SOI) with top silicon layer at several hundred nanometres, which usually has high propagation loss, loss power handling, small

mode size and thus limits its application range. Therefore, there is a strong incentive to explore a thicker SOI platform for integrated silicon optomechanical systems.

This project first aims to explore the applications of integrated silicon optomechanics, both in cavity optomechanics and optical trapping. For the integrated silicon cavity optomechanics, the OMO process was exploited to generate optical probe signals for DFOS applications. For the optical trapping, comprehensive analyses and optimisation of a dual-waveguide trapping system based on SOI platform were conducted. Lastly, the fabrication and measurement of optomechanical components based on a novel 1.5 $\mu m$ thick SOI platform are discussed.

## 1.3 Thesis Structure

• Chapter 1: Introduction. This chapter outlines the research background and objectives of this project.

• Chapter 2: Literature Review. The second chapter first reviews the underlying physics and properties of the cavity optomechanical system, followed by the typical implementation examples. I then introduce relevant knowledge and related literature about this project, including silicon photonics, optical trapping and DFOS.

• Chapter 3: Integrated silicon optomechanics for distributed fibre optical sensing. In this chapter, I studied the OMO process in an integrated cavity optomechanical system and explored its applications for DFOS. The optomechanical dynamic back-action effect was first introduced, followed by an analysis of the OMO in different regimes. Lastly, the application of this OMO process for optical probe signals generation in DFOS was shown explicitly.

• Chapter 4: Silicon optomechanics for on-chip optical trapping. In this chapter, the optical trapping capability of the SOI-based dual-waveguide structure was demonstrated. Also, the dual-waveguide optical trapping scheme is optimised and scaling effects are shown. In addition, it is shown that the OMO process can be utilised to load micro/-nano particles, which is an essential step for on-chip particle loading.

• Chapter 5: Integrated optomechanical components based on thick SOI platform. This chapter will present the on-chip integrated optomechanical components design, fabrication, and measurement based on a 1.5 $\mu m$ thick SOI platform. The experimental results indicate that the components all function well and these components pave the way for the full integration of on-chip silicon optomechanics.

• Chapter 6: Conclusions and perspectives. In this chapter, I conclude this thesis by giving the conclusions and outlooks towards the integrated silicon optomechanical systems in the future.

# Chapter 2

# Literature Review

In this chapter, I will first review the underlying physics and properties of the cavity optomechanical system, followed by the typical implementation examples. I then introduce relevant knowledge and related literature reviews about this project, including silicon photonics, optical trapping and DFOS.

## 2.1 Basics of cavity optomechanics

Cavity optomechanics describes the interactive coupling between an optical resonance mode and a mechanical resonance mode. In this section, the properties and relevant physics of the basic components of a cavity optomechanical system, namely the optical resonators and the mechanical resonators, will be introduced. After that, I also discussed the various geometric forms of chip-scale cavity optomechanical systems that have been demonstrated.

### 2.1.1 Optical resonator

The optical cavity, also known as the optical resonator, is the basic component of a cavity optomechanical system. It confines light by resonantly recirculating the optical field when the standing wave condition is met, i.e. the single optical path length during a round-trip corresponds to an integer multiple of the laser wavelength. The optical cavity has played a crucial role in modern optical devices such as lasers, filters, accurate measurement tools and nonlinear optics experiments[40].

Optical cavities have been realized experimentally in various forms, such as the microtoriod [41], microdisk [42], photonic crystal cavity [43], etc. The Fabry-Perot cavity

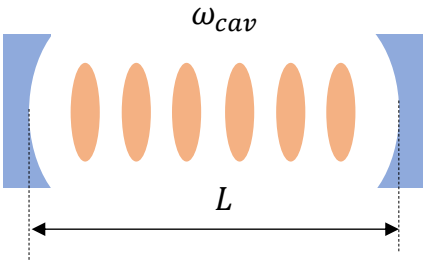


FIGURE 2.1: Schematic illustration of a Fabry-Perot optical cavity with length $L$.

model is the most straightforward example to mathematically describe an optical cavity. It should be noted that the analysis presented here is not limited to this particular system.

The Fabry-Perot cavity consists of two highly reflective mirrors separated by a distance $L$ as shown in Figure 2.1. This cavity contains a series of optical modes whose resonance wavelengths satisfy the standing wave condition,

$$\lambda_{cav,m} = \frac{2nL}{m}, \tag{2.1}$$

where $m$ is the integer mode number, $n$ is the refractive index of the medium inside the cavity. The corresponding angular optical resonance frequencies are thus given by,

$$\omega_{cav,m} = 2\pi \cdot \frac{c}{\lambda_{cav,m}} = m \cdot \pi \frac{c}{nL}, \tag{2.2}$$

where $c$ is the light of speed. The free spectral range (FSR) of the optical cavity is defined as the separation of two adjacent resonant modes. When considering the dispersion effect in the optical cavity, i.e. light with different wavelengths travel at different speeds, the FSR (in wavelength) is given as,

$$FSR = \frac{\lambda^2}{2Ln_g}. \tag{2.3}$$

Here, $n_g = n - \lambda \frac{dn}{d\lambda}$ is the group refractive index which describes the overall propagation of the light. Since the input laser wavelength can be tuned to select a single optical mode, a single optical mode whose angular frequency is $\omega_{cav}$ and wavelength is $\lambda_{cav}$ will be focused hereafter.

Light can not be stored in an optical cavity forever due to unavoidable optical losses from various sources. The optical loss is characterised by the cavity photon energy decay rate $\kappa = 1/\tau$ (unit: rad/s), where $\tau$ is the cavity photon lifetime. The optical loss sources can be decomposed into two parts: the intrinsic optical loss $\kappa_i$ describing the internal losses such as absorption or scattering loss, and the external loss $\kappa_e$ representing losses due to external coupling such as waveguide coupling or tapered fibre coupling. The total cavity loss equals the sum of individual loss sources, i.e. $\kappa = \kappa_i + \kappa_e$.

Another important figure of merit to characterise the optical cavity is the optical Q-factor, which is defined as the ratio of cavity photon lifetime to the optical period,

$$Q = \omega_{cav}\tau = \frac{\omega_{cav}}{\kappa}, \tag{2.4}$$

$$\frac{1}{Q} = \frac{\kappa_i}{\omega_{cav}} + \frac{\kappa_e}{\omega_{cav}} = \frac{1}{Q_i} + \frac{1}{Q_e}, \tag{2.5}$$

where $Q_i$ is the intrinsic optical Q-factor and the $Q$ is called the loaded optical Q-factor.

### 2.1.2 Resonator-waveguide coupling theory

In cavity optomechanics, an optical cavity is coupled to the external coupling channel, for instance, a waveguide or a tapered fibre. The coupled waveguide-resonator system has been analysed and derived in [44], which provides a useful tool for the study of the dynamical characteristics of the cavity optomechanical system.

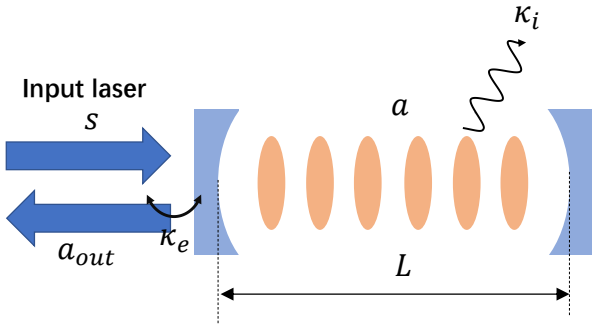


FIGURE 2.2: Schematic illustration of a Fabry-Perot optical cavity coupled to an external field.

Here, the example of the Fabry-Perot cavity coupled to an external field through one end of the mirrors as shown in Figure 2.2 is used to describe the resonator-waveguide coupling principle. It should be noted that Figure 2.2 shows a single-sided coupling case, where one of the mirror is completely reflective and the light inside the cavity can only couple out in one direction down the external field. For the double-sided coupling scheme, photons inside the optical cavity are likely to couple out and propagate in either direction along the optical cavity. This double-sided coupling case will be used for the optical probe signal generation in Chapter 3.

The equation describing the dynamics of the above single-sided coupling optical cavity field can be written as [44]:

$$\frac{da(t)}{dt} = -i\omega_{cav}a(t) - \frac{\kappa}{2}a(t) + \sqrt{\kappa_e}s(t), \tag{2.6}$$

where $\omega_{cav}$ is the cavity resonance angular frequency. The complex mode amplitude inside the cavity is defined as $a(t)$ and $n_c = |a(t)|^2$ is normalised to equal the photon

number in the cavity, such that the optical cavity mode energy is given by $\hbar\omega_L|a|^2$, where $\hbar$ is the reduced Planck constant. $s(t)$ describes the input field amplitude and $|s(t)|^2$ is normalised to be the input photon flux, such the input optical laser power is $P_{in} = \hbar\omega_L|s(t)|^2$. The optical cavity is driven by an input laser with angular frequency $\omega_L$, therefore $s(t)$ is set to be $s(t) = \hat{s}(t)e^{-i\omega_L t}$. For the convenience of further analysis, the equation is transformed into a rotating framework with the laser frequency $\omega_L$ by using $a(t) = \hat{a}(t)e^{-i\omega_L t}$. The modified equation of the time evolution of field amplitude is thus given by,

$$\dot{\hat{a}}\left(t\right)e^{-i\omega_L t} - i\omega_L\hat{a}\left(t\right)e^{-i\omega_L t} = -i\omega_{cav}\hat{a}\left(t\right)e^{-i\omega_L t} - \frac{\kappa}{2}\hat{a}\left(t\right)e^{-i\omega_L t} + \sqrt{\kappa_e}\hat{s}\left(t\right)e^{-i\omega_L t}. \quad (2.7)$$

Multiplying each side with $e^{i\omega_L t}$, the above equation can be transformed to:

$$\dot{\hat{a}}\left(t\right) = i\Delta\hat{a}\left(t\right) - \frac{\kappa}{2}\hat{a}\left(t\right) + \sqrt{\kappa_e}\hat{s}\left(t\right), \quad (2.8)$$

where the laser detuning $\Delta = \omega_L - \omega_{cav}$ has been introduced, which is the frequency difference between the laser and the optical cavity. A positive value of detuning means blue detuning, while a negative detuning means red detuning. By setting the input driven amplitude as a constant $\hat{s}(t) = \bar{s}$, the above first-order ordinary differential Equation 2.8 can be solved as,

$$\hat{a}\left(t\right) = Ce^{-\frac{1}{2}t(\kappa-2i\Delta)} + \frac{\sqrt{\kappa_e}\bar{s}}{\frac{\kappa}{2} - i\Delta}. \quad (2.9)$$

where $C$ is a complex amplitude decided by the initial conditions of the differential equation. The first term is the transient damping part, and the second term is the steady-state part. For time scale much longer than $\tau$, the first term quickly decays and only the second term is of relevance, such that the steady-state field amplitude is given by,

$$\bar{a} = \frac{\sqrt{\kappa_e}\bar{s}}{\frac{\kappa}{2} - i\Delta}. \quad (2.10)$$

The mean photon number inside the cavity is,

$$n_c = |\bar{a}|^2 = \frac{\kappa_e|\bar{s}|^2}{\Delta^2 + \kappa^2/4} = \frac{\kappa_e}{\Delta^2 + \kappa^2/4}\frac{P_{in}}{\hbar\omega_L}. \quad (2.11)$$

When the detuning $\Delta$ is zero, the cavity photon number reaches the maximum value as

$$n_{c,max} = \frac{4\kappa_e|\bar{s}|^2}{\kappa^2} = \frac{4P_{in}\kappa_e}{\kappa^2\hbar\omega_L}. \quad (2.12)$$

According to the theory derived in [44], the reflected field amplitude $a_{out}$ in the steady-state is given by,

$$a_{out} = \bar{s} - \sqrt{\kappa_e}\bar{a}. \quad (2.13)$$

Thus the reflection coefficient in steady-state can be found as,

$$R = \frac{|a_{out}|^2}{|\bar{s}|^2} = \left(1 - \frac{\kappa_e}{\kappa/2 - i\Delta}\right)^2 = 1 - \frac{\kappa_e \kappa_i}{\Delta^2 + \kappa^2/4}. \tag{2.14}$$

This coefficient corresponds to a Lorentzian spectrum over the laser detuning, with $\kappa$ being the FWHM linewidth of the Lorentzian spectrum. It should be noted that Equation 2.13 and Equation 2.14 only describe the single-sided coupling case where there is only one output from the optical cavity. Apart from the reflected field from the input mirror of the Fabry-Perot cavity model shown in Figure 2.1.2, the relations shown in Equation 2.13 and Equation 2.14 also describe the transmitted field of an evanescently coupled unidirectional resonator-waveguide system, such as the whispering gallery mode (WGM) resonator coupled to a bus waveguide as shown in Figure 2.3 (A). In a WGM resonator, the optical mode is confined and propogated along the rim of a circular resonator.

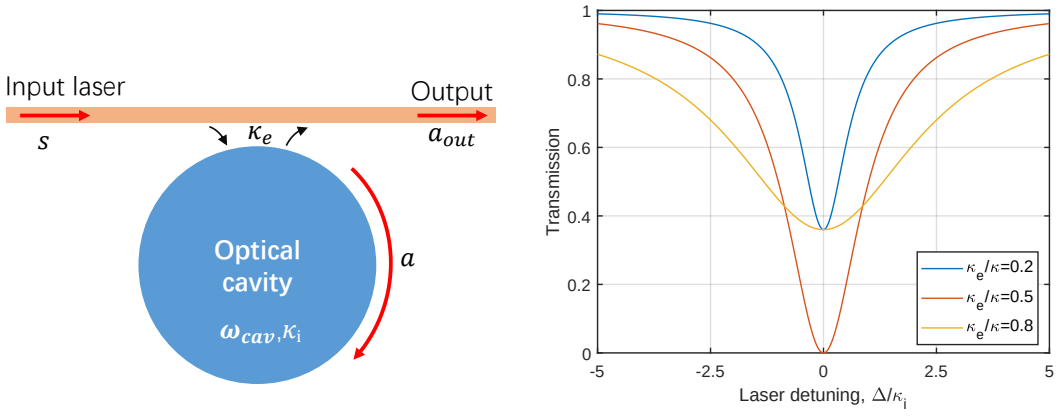


(A) (B)

FIGURE 2.3: (A) An evanescently coupled unidirectional resonator-waveguide system made from a WGM resonator coupled to a bus waveguide. (B) The three coupling regimes of the resonator-waveguide coupling system, shown as the transmission spectrum over the laser detuning.

In Figure 2.3 (B), the transmission spectrums over laser detuning according to Equation 2.14 were plotted for three different values of $\kappa_e$ and the same value of $\kappa_i$. $\kappa_e$ can be continuously tuned by varying the external coupling strength, for example, by changing the reflectivity of the mirror of a Fabry-Perot cavity, or by changing the gap between a bus waveguide and a WGM resonator. Three coupling regimes can be defined from Equation 2.14: undercoupled regime ($\kappa_e < \kappa_i$), critical coupled ($\kappa_e = \kappa_i$), and overcoupled ($\kappa_e > \kappa_i$). In the undercoupled regime, the optical losses are dominated by the intrinsic loss rate, and the cavity has a higher optical Q-factor. This regime is useful for measuring the intrinsic optical Q-factor of the optical cavity. The critical coupled regime is the case where the intrinsic loss rate equals the external loss rate. It can be found that the transmission on cavity resonance ($\Delta = 0$) becomes zero in this regime,

and the intracavity photon number on resonance reaches maximum. This regime is usually preferred for optical filters application which requires a high extinction ratio.

### 2.1.3 Mechanical resonator

A mechanical resonator is a prominent and basic example of a classical mechanical system, for instance, a spring or pendulum. It has been used as an impressive tool for addressing fundamental theoretical questions and results in a plethora of applications [45]. Their intrinsic elasticity and clamping condition result in a restoring force towards a given equilibrium position and a dissipative vibrational motion in the mechanical resonators. In this part, I will briefly review the relevant features and equations of the motion of a mechanical resonator, followed by noise analysis when measuring a mechanical resonator.

A canonical mechanical resonator is shown in Figure 2.4, in which a mechanical object with effective mass $m_{eff}$ experiences an external force $F_{ex}$, an elastic force $F_k = kx$ and a damping force $F_c = c\dot{x}$. Here, $k$ is the spring constant of the system, and $c$ is the damping coefficient. Note $m_{eff}$ is the effective mass of the mechanical resonator. For the simple case of a centre-of-mass oscillator of a point-like mass, for instance, the trapped particle, $m_{eff}$ is the mass of the object. A comprehensive treatment of effective mass in optomechanical experiments is given by Pinard [46]. It should also be noted that $F_{ex}(t)$ is given by the thermal Brownian force in the absence of any other external forces.

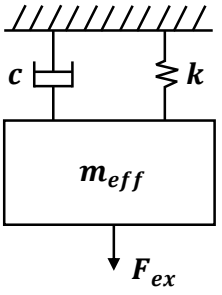


FIGURE 2.4: Schematic diagram of a mechanical resonator.

Therefore, the generic equation describing the motion of a mechanical resonator is given by:

$$m_{eff}\frac{d^2x(t)}{dt^2} + c\frac{dx(t)}{dt} + kx(t) = F_{ex}(t), \tag{2.15}$$

where $x(t)$ is the mechanical displacement. By introducing the mechanical resonance frequency $\Omega_m = \sqrt{k/m_{eff}}$ and the damping rate $\Gamma_m = c/m_{eff}$, a more general form of

the equation can be obtained by rearranging the original Equation 2.15 to,

$$\frac{d^2x(t)}{dt^2} + \Gamma_m \frac{dx(t)}{dt} + \Omega_m^2 x(t) = \frac{F_{ex}(t)}{m_{eff}}. \tag{2.16}$$

The damping rate $\Gamma_m$ describes the loss of the mechanical energy, and can be related to the mechanical Q-factor by $Q_m = \Omega_m/\Gamma_m$. The dimensionless Q-factor characterises the ratio between the stored energy in the resonator and the energy lost in one period of oscillation. Higher Q-factor indicates a lower energy loss. Various loss mechanisms contribute to the total mechanical energy loss [45], which can be divided into intrinsic and extrinsic sources. The intrinsic source mainly includes materials-induced loss and fundamental anharmonic effects such as thermoelastic damping and phonon-photon interactions. The extrinsic source includes viscous damping due to the interaction with the surrounding gas molecules and clamping loss caused by the radiation of elastic wave energy to the substrate through the clamping support. Therefore, the resulting mechanical Q-factor is given by

$$\frac{1}{Q_{total}} = \sum \frac{1}{Q_i}, \tag{2.17}$$

where $i$ represents the different loss sources.

The Equation 2.16 can be solved in the frequency domain by performing a Fourier transform via $x(\Omega) = \int_{-\infty}^{\infty} x(t)e^{i\Omega t}dt$ to yield the following,

$$x(\Omega) = \chi_m(\Omega_m)F_{ex}(\Omega), \tag{2.18}$$

$$\chi_m(\Omega) = \frac{1}{m_{eff}(\Omega_m^2 - \Omega^2) - im_{eff}\Gamma_m\Omega}. \tag{2.19}$$

Equation 2.19 corresponds to a linear response description of the mechanical resonator, $\chi_m(\Omega)$ is called the mechanical susceptibility and physically it represents the mechanical displacement response to unit acceleration at frequency $\Omega$. The zero-frequency response is given by $\chi_m(0) = [m_{eff}\Omega_m^2]^{-1} = k^{-1}$, where $k$ is the spring constant.

In the practical optomechanical applications, the displacement $x(t)$ can not be measured directly. The power spectral density (PSD) is mostly utilised as a useful tool for analysing the dynamics of the mechanical resonator. For a given quantity $r(t)$, the PSD is obtained by taking the Fourier transform of its autocorrelation function according to the Wiener Khinchin theorem,

$$S_{rr}(\Omega) = \int_{-\infty}^{\infty} \langle r(t)r(t+\tau)\rangle e^{i\Omega\tau}d\tau, \tag{2.20}$$

If the Fourier transform of the quantity $r(\Omega)$ is already known, then the PSD can be approximated by,

$$S_{rr}(\Omega) = \langle r(\Omega)r(-\Omega)\rangle. \tag{2.21}$$

Thus, for a mechanical resonator experiencing a sum of external force with the PSD as $S_{FF}(\Omega)$, the displacement PSD can be expressed as,

$$S_{xx}(\Omega) = S_{FF}(\Omega)|\chi_m(\Omega)|^2 = \frac{1}{m_{eff}^2} \frac{S_{FF}(\Omega)}{(\Omega_m^2 - \Omega^2)^2 + (\Gamma_m \Omega)^2}. \tag{2.22}$$

The fundamental force acting on the mechanical resonator is the thermal force which causes thermal or Brownian motion and can be described by the fluctuation-dissipation theorem [47], which shows that the double-sided PSD of the thermal force $S_{FF}^{th}$ can be obtained as [48]:

$$S_{FF}^{th}(\Omega) = \frac{2k_B T}{\Omega} Im(\chi_m(\Omega)^{-1}) = 2m_{eff}\Gamma_m k_B T. \tag{2.23}$$

where $k_B$ is the Boltzmann constant and $T$ is the ambient temperature. It is obvious that the PSD of the thermal force is frequency independent and white. It depends on the ambient temperature $T$, mechanical damping rate $\Gamma_m$, and effective mass of the resonator $m_{eff}$. The associated double-sided thermal motion displacement PSD $S_{xx}^{th}$ can thus be expressed as,

$$S_{xx}^{th}(\Omega) = \frac{1}{m_{eff}^2} \frac{2m_{eff}\Gamma_m k_B T}{(\Omega_m^2 - \Omega^2)^2 + (\Gamma_m \Omega)^2}. \tag{2.24}$$

This expression gives rise to Lorentzian peaks located at $\Omega = \pm\Omega_m$ and with full width at half maxima (FWHM) of $\Gamma_m$. Integration of the displacement PSD $S_{xx}^{th}(\Omega)$ leads to the root-mean-square of the thermal motion $\langle x_{th}^2 \rangle$ as,

$$\langle x_{th}^2 \rangle = \frac{1}{2\pi} \int_{-\infty}^{\infty} S_{xx}^{th}(\Omega) d\Omega = \frac{k_B T}{m_{eff}\Omega_m^2}. \tag{2.25}$$

The above Equation 2.25 indeed confirms the equipartition theorem, which relates the temperature of a system to its average energies, specially $\frac{1}{2} m_{eff}\Omega_m^2 \langle x_{th}^2 \rangle = \frac{1}{2} k_B T$.

### 2.1.4 On-chip silicon cavity optomechanics in practice

The research on micro/nano cavity optomechanics has been prosperous in the last two decades due to the advent of high-quality optical microcavities and advanced nanofabrication techniques. Various on-chip cavity optomechanical systems based on silicon material platform have been proposed and demonstrated, in which the mechanical displacement alters the optical cavity resonance and thereby the photon number inside it.

Optical microcavities are the key components for the on-chip cavity optomechanics and the localised light in small volume leads to stronger optomechanics coupling effects. Classified by the geometric features of the optical cavities, there are mainly two

typical types of on-chip silicon cavity optomechanical system, either based on the whispering gallery mode (WGM) cavities [49, 50, 51, 52, 53] shown in Figure 2.5 (a-e) or the photonics crystal cavities [43, 54, 55] shown in Figure 2.5 (f-h). For the WGM cavities, light is confined in the rim of a circular cavity. Examples are microtoroidal cavity (Figure 2.5 (a)), microdisk cavity (Figure 2.5 (b, d)), racetrack microresonator (Figure 2.5 (c)) and double-micro-ring cavity (Figure 2.5 (e)). Photonic crystal cavity confines light in a very small mode volume by creating a photonic bandgap around the optical cavity. It can be a one-dimensional nanobeam (Figure 2.5 (f)), a two-dimensional defect cavity (Figure 2.5 (g)), or a "zipper" photonic crystal cavity (Figure 2.5 (h)).

From the point of the coupling mechanism, they generally utilise two types of radiation pressure force coupling: either the scattering-type coupling in which the optical cavity field interacts with the mechanical resonator through momentum transfer [49, 50, 54, 55] shown in Figure 2.5 (a-b, f-g), or the gradient force coupling in which optomechanical coupling is induced by optical gradient force due to the near-field effect [51, 52, 53, 43] as shown in Figure 2.5 (c-e, h). For either case of the coupling mechanism, the optomechanical coupling is realized by varying the optical cavity resonance frequency through mechanical motion.

### 2.1.5 Cavity optomechanical parameters

In terms of the real system parameters, a large number of previously demonstrated devices can work as roadmaps when designing an application-oriented cavity optomechanical system. Mechanical frequency $\Omega_m$ with values varying from $\sim MHz$ (suspended nanobeam, microtoroid) to $\sim GHz$ (photonic crystal cavity) have been demonstrated. Optomechanical devices with effective mass $m_{eff}$ ranging from $g$ to $zg$ have been realised [26]. In terms of the optomechanical coupling, remarkably large optomechanical coupling coefficient $G$ of around 100 GHz nm$^{-1}$ has been obtained in the photonic crystal structure [43], where $G$ denotes the optical cavity resonance frequency shift per mechanical displacement.

In addition, the Q-factor of the on-chip optical cavity can be very high in the order of millions, such as the chemically etched wedge resonator [56], the reflow processed silica microtoroid structure [41] and the $Si_3N_4$ microresonator fabricated using the Damascene process [57]. The Q-factor of micro-nano mechanical resonator also saw breakthrough these years by sophisticated elastic phononic engineering [58], and an exceptionally low mechanical dissipation and Q-factor as high as 800 million was realised [59]. Therefore, there is a flexible design space for the on-chip cavity optomechanical system.

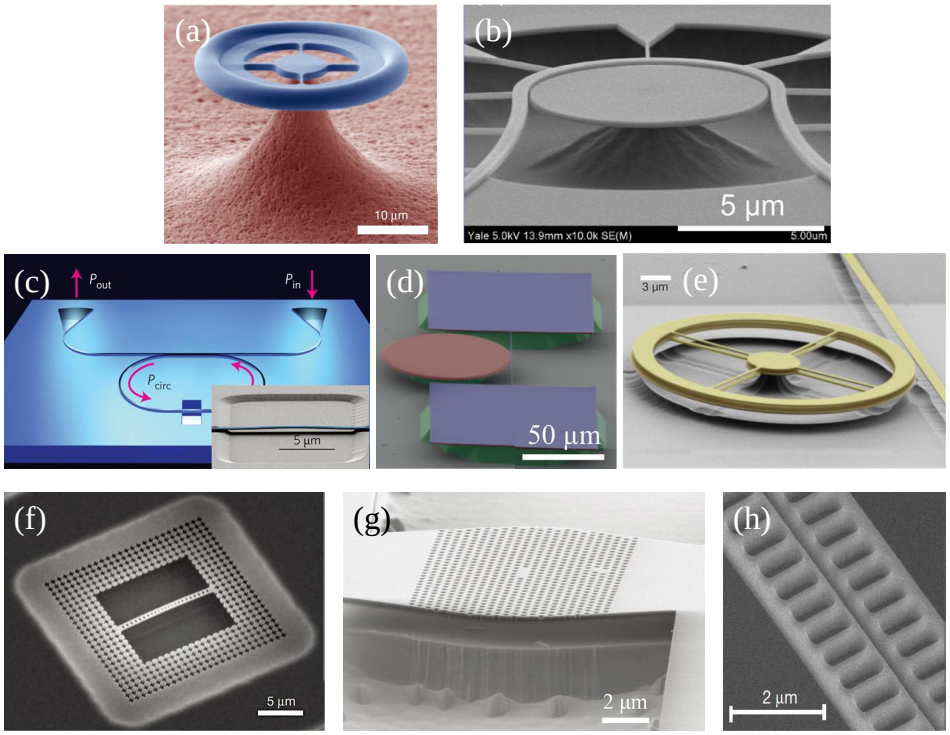


FIGURE 2.5: Examples of on-chip silicon cavity optomechanical systems. (a) Microtoroids in which the scattering-radiation pressure drives the rim of the cavity and changes the optical path length [49]. (b) Microdisk optical cavity with integrated wrap-around coupling waveguide, in which the coupling is induced by the scattering-radiation force due to the photon momentum transfer [50]. (c) Racetrack microresonator, in which part of the waveguide is suspended to form the mechanical resonator. The gradient force between the suspended waveguide and substrate leads to optomechanical coupling [51]. (d) Microdisk resonator, the gradient force between the suspended beam and microdisk cavity couples them together [52]. (e) Double-micro-ring cavity, where the gradient force between the two vertically stacked ring cavities realises the optomechanical coupling[53]. (f) 1-D photonic crystal cavity, in which optical mode and mechanical mode can be both confined to the small defect region in the nanobeam and are coupled through the scattering-radiation force [54]. (g) 2-D photonic crystal cavity, in which optical mode and mechanical mode can be both confined to the small defect region in the membrane and are coupled through the scattering-radiation force [55]. (h)"Zipper" photonic crystal cavity, where the two nanobeams are coupled through the gradient optical force [43].

## 2.2 Silicon photonics

Silicon Photonics is a branch of Photonic Integrated Circuits and uses silicon as the platform to integrate complex optical functions into an on-chip photonic circuit. The use of silicon for integrated photonics was proposed as early as 1985 by Soref [60]. It was firstly designed and driven for communication systems and has seen its wide applications in telecom and datacom area [61, 62].

There are actually a wide variety of material platforms to build Photonic Integrated Circuits, such as lithium niobate, polymers, tantalum oxide, silicon, etc. However, silicon is the most promising platform mainly because of its compatibility with CMOS,

where the process of silicon has been developed by industry to a sufficient level. Therefore, the mature silicon-based fabrication process can be directly utilized, which is very beneficial when pursuing high volume manufacturing at a low cost. In addition, the SOI substrate that has been widely used for CMOS technologies is an ideal platform for making photonics components. The top silicon layer is transparent to infrared light with a wavelength range above 1.1$\mu m$ and has a large refractive index (3.48 for 1550 $nm$) compared to the buried $SiO_2$ (1.44 for 1550 $nm$), which results in a tightly confined optical waveguide mode and a compact footprint.

A typical fully integrated silicon photonics system consists of the following components [38]: light sources (laser); Passive photonic components such as waveguides, grating couplers, directional couplers, filters, splitters and (de) multiplexers; Modulators that modulate the optical field through the change of applied electronic signals; Photodetectors that convert optical signals to electronic signals.

## 2.3 Optical trapping

Since the pioneering works by Arthur Ashkin [15, 63, 64], optical trapping utilising the optical radiation force has developed extensively and led to applications in various aspects. This part will briefly introduce the history and development of optical trapping and the emerging on-chip optical trapping field.

### 2.3.1 The development of optical trapping

The first demonstration of optical trapping was reported in 1970 by Arthur Ashkin [15]. He found that micron-sized particles in liquid solution can be accelerated in the direction of light and driven into the beam axis by a continuous laser. The particles will wander by Brownian motion after the laser beam is blocked. When two opposing equal laser beams are used, particles will be trapped stably at the equilibrium point. Soon after that, Ashkin demonstrated the first levitation of particles of 15-25 $\mu m$ in diameter in air and vacuum by pointing the laser of 100-500 $mW$ vertically to the particle. Hence the radiation pressure force can offset the gravity [65, 63]. In 1986, another breakthrough was achieved by Ashkin [64]. He reported the first gradient force optical trap, where a single focused laser beam was used to trap a particle in all three degrees of freedom in liquid. This technique soon led to the application of optical tweezers for trapping and manipulating viruses, cells, and bacteria, and it now becomes a standard tool in biophysics [6]. In 2018, half of the Nobel Prize in Physics was awarded to Arthur Ashkin for his contributions to optical tweezers. The development of optical trapping is shown in Figure 2.6 [66].

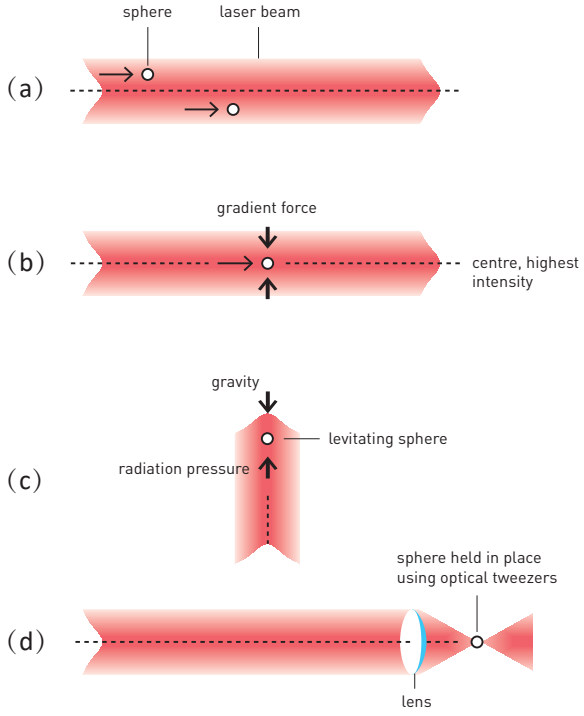


FIGURE 2.6: Development of optical trapping [66]. (a) Particles are driven along the direction of the light by radiation pressure force. (b) Particles are simultaneously attracted towards the centre of the beam by gradient force, where the light intensity is highest. (c) Particles are levitated by pointing the laser vertically upwards, where radiation pressure force balances the gravity. (d) Particles are trapped by optical tweezers formed by a focused laser beam.

Among the various optical trapping schemes that have been proposed, single-beam trapping and dual-beam trapping have been most widely used. In the single-beam optical trapping, a laser beam is tightly focused to form an optical trap with the dominating optical gradient force than the scattering force. This can be realised by lenses [64] or parabolic mirrors [67]. However, single-beam optical trapping shows a limitation in the application for trapping large particles where the dominating radiation scattering force will overpower the gradient force and thus push the particle out of the trap. On the contrary, in dual-beam optical trapping which can be achieved using fibre [68] or free space laser beam [69], the optical gradient force is used to trap particles, while the axial radiation scattering forces from the two counter-propagating laser beams are balanced and thus make the optical trapping more stable. In the meantime, the particle trapping position can also be controlled by changing the relative power, frequency, or phase of the laser beams.

### 2.3.2 On-chip optical trapping

The conventional optical trappings rely on bulky, costly benchtop setup and usually involves fibre or free space components, which limits its batch production and further

applications. With the advance of silicon photonic, there is a strong desire to realise the optical trapping on the chip.

Various on-chip optical trapping schemes have been proposed and demonstrated. Optical waveguide trapping shown in Figure 2.7 (A) has been reported in [70]. The particle is actually pulled down to the waveguide surface by optical gradient force and driven by the radiation scattering-pressure force of the evanescent field of the waveguide, and this has been used for particle transportation. Ring resonators shown in Figure 2.7 (B) [71] were also used for optical trapping. In a ring resonator, the intensity field is magnified with an intensity building factor. Therefore, the evanescent field is stronger than that in a single waveguide with the same input power. In a ring resonator optical trapping, particles are localized near the waveguide surface and propelled around the ring in a periodic basis. The photonic crystal shown in Figure 2.7 (C) [72] is a cavity-based on-chip optical trapping scheme. The photonic crystal cavity is formed by fabricating some defects on a photonic crystal, within which only light with a specific wavelength can exist. Thus an optical cavity is introduced, and the field intensity can be greatly enhanced when working at the resonance of the cavity. The strong evanescent field of the cavity can be used to trap particles.

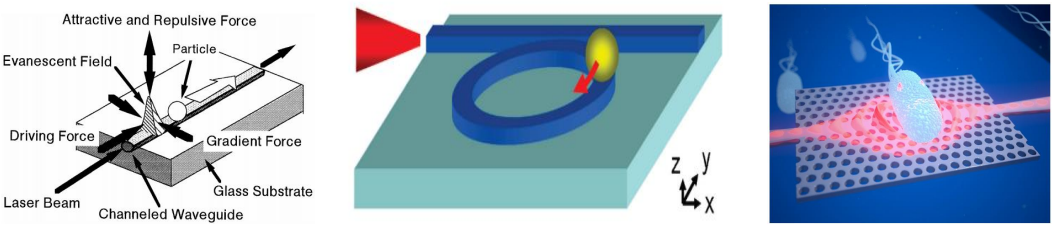


(A) (B) (C)

FIGURE 2.7: Various on-chip optical trapping structures (A) Waveguide trapping [70] (B) Ring resonator trapping [71] (C) Photonic crystal cavity trapping [72]

The above introduced on-chip trapping schemes rely on the evanescent field of the confined optical mode to produce the optical force, which only allows 2D particle manipulation when the particles are in close proximity to the chip surface. However, this kind of optical trapping generated from the exponentially decaying evanescent field always attracts the particles to the chip surface and cannot stably trap the particle at a specific position. This is where dual-waveguide optical trapping can play a role. Dual-waveguide trapping, which combines state of the art micro/nano fabrication technology and the dual-beam optical trapping scheme, enables mass production and at the same time avoids any delicate mounting and alignment of optical fibres as in the conventional dual-beam trapping. Besides, in the dual-waveguide trapping, the particles can be held stably in a specific position away from the chip surface.

A variety of dual-waveguide optical trapping schemes have been proposed and experimentally demonstrated, with some of them shown in Figure 2.8. In 2011, Jacob

Caro and co-workers first proposed and numerically verified the dual-waveguide optical trapping scheme with two multimode strip $Si_3N_4$ waveguides launching counter-propagating beams into a fluidic channel [73]. Later on, they experimentally demonstrated dual-waveguide optical traps based on a structure called the TripleX platform [36, 74, 75, 76], on which they successfully trapped polystyrene beads and realised on-chip single-beam Raman spectroscopy. Olav Gaute Hellesø demonstrated similar dual-waveguide optical traps using waveguide loops made of 150-180 *nm* tantalum pentoxide ($Ta_2O_5$) on oxidised silicon substrates, where polystyrene microspheres and red blood cells were propelled along the waveguides and stably trapped in the gap area [35, 77]. In the following years, they carried out on-chip optical trappings for Raman spectroscopy [78], lifting of particles [79], and they also used rib waveguides for on-chip optical trapping [80]. Quite recently, the dual-polymer-waveguide trapping based on freeform optics was proposed and experimentally demonstrated [37]. They used the two-photon polymerization process to control the shape of the waveguide ends to get strong intensity gradients and larger trapping potential.

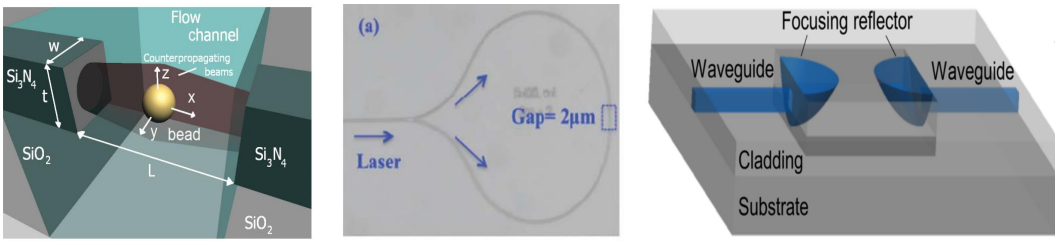


(A) (B) (C)

FIGURE 2.8: Various dual-waveguide trapping devices. (A) The first design of dual-waveguide trapping based on two multimode strip $Si_3N_4$ waveguides [73]. (B) The first experimental dual-waveguide trapping with $Ta_2O_5$ waveguide [35]. (C) Dual-waveguide trapping based on freeform optics using polymer [37].

Among the works on dual-waveguide trapping mentioned above, intensive numerical simulations and experiments have been performed to study the field intensity profile, optical trapping force, and trapping potential acting on particles with different radii and under different gap distances. It was found that both the particle size and gap distance have significant effects on the trapping force and potential. The waveguide cross-section is manifestly another crucial geometric parameter, as it determines how the mode profile is distributed and how the guided waveguide mode is converted into the radiation mode outside the waveguide facet boundaries. However, no research has been conducted to systematically investigate the effect of waveguide geometric size on trapping capability until now, particularly the waveguide thickness under the single-mode condition. This is critical for maximising the optical trapping capability. There is thus a gap which requires further studies.

## 2.4 Distributed fibre optical sensing

The distributed fibre optical sensing (DFOS) system injects an input light signal into the fibre and measures the physical parameters along the fibre distributedly by detecting the scattered light signal at the end of the fibre. Unlike the traditional sensing system, which measures the physical parameters at a specific location, the DFOS can perform the measurements continuously along the entire length of the sensing optical fibre [33]. If the physical parameter along the fibre changes, the scattered signal in the fibre will be modulated. By measuring the modulated signal changes, one can get the physical parameters along the fibre. This working concept resembles the sonar or radar in the sense that they both send electromagnetic waves into the medium and measure the reflected signal from the target. However, the sonar and radar systems do not provide continuous information of the medium between the source and target, while DFOS can measure the spatial distribution of the measurands along the sensing fibre. This feature makes it an ideal sensing scheme for multi-point measurements, such as structural health monitoring in civil infrastructures (buildings, bridges, dams, tunnels, highways, oil and gas pipelines, etc.).

The criteria for DFOS include sensing range, measurement time, measurand resolution and spatial resolution [33]. The sensing distance is the length of the sensing fibre under test. The measurement time is the data reading and analysis time of DFOS to achieve the required measurand resolution. The measurand resolution and spatial resolution are the ability of the sensor to distinguish small measurand value changes and the measurand values at closely spaced locations, respectively.

The reflection signal is from the light-matte scattering process in the optical fibre. There are three types of scattering in the fibre: Rayleigh scattering, Brillouin scattering and Raman scattering, of which the Rayleigh scattering is an elastic scattering and the scattered light has the same frequency as the incident light, while the Brillouin scattering and Raman scattering are inelastic scatterings resulting in a shifted frequency. The scattering signal containing a spatial distribution of the measurands can be interrogated in three domains: the time domain, the frequency domain and the correlation domain. Depending on the different domains, DOFS systems can be divided into three categories: optical time-domain reflectometry (OTDR), optical frequency-domain reflectometry (OFDR) and optical coherence-domain reflectometry (OCDR). Here, I will briefly introduce the operating principles of the former two types of DOFS systems that have been widely used.

### 2.4.1 OTDR using the OPT source

The first OTDR was demonstrated in 1976 [81]. The schematic diagram of a typical Rayleigh scattering based OTDR is shown in Figure 2.9. In an OTDR system, OPT is

launched into the fibre. The optical scattering process in the fibre changes the propagation direction to all directions. The fraction of light that falls into the acceptance angle of the fibre will be directed into the reverse direction and reflected into the launching end. By using the optical circulator, this back-scattered light is separated and sent to the photodetector and then for signal processing. It should be noted that this schematic diagram is just a simple illustration of the Rayleigh scattering based OTDR, which measured the intensity of Rayleigh scattering light or the Polarisation optical time-domain reflectometry (POTDR) measuring the polarisation change. For the Brillouin optical time-domain reflectometry (BOTDR) or Phase optical time-domain reflectometry (Phi-OTDR), another reference light beam from the laser source is needed.

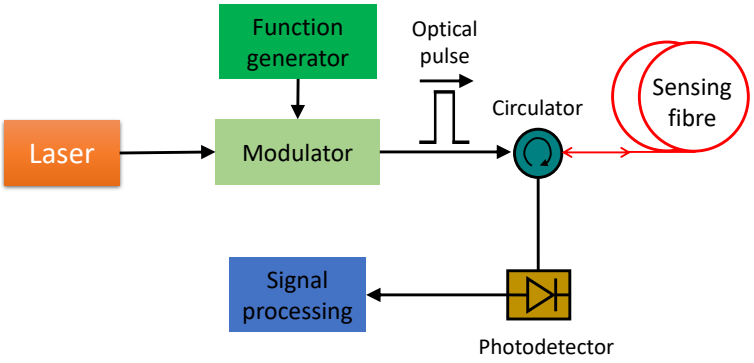


FIGURE 2.9: Schematic diagram of an OTDR.

In an OTDR, the position of a measurand can be precisely estimated by evaluating the time between sending and receiving an optical pulse. The spatial resolution of an OTDR system is thus given by,

$$\delta z = \frac{cW}{2n_g}, \tag{2.26}$$

Where $c$ is the speed of light, $W$ is the pulse width and $n_g$ is the group index in the fibre.

For OTDR, the sensing distance is limited by the repetition rate of the OPT, which should be low enough to avoid overlapping the backscatter signals with the sending pulses from the fibre. The maximum sensing distance is given by,

$$z = \frac{c}{2fn_g}, \tag{2.27}$$

where $f$ is the repetition rate of the OPT. The measurement time is determined by the signal-to-noise ratio (SNR) and the required measurement resolution. Therefore, the measurement usually needs to cover many cycles of averaging to improve the SNR. The SNR can be increased by enhancing the extinction ratio (ER) or the probe energy of the pulses [82, 83]. From Equation 2.26, it can be found a finer spatial resolution requires a narrower optical pulse width. For a fixed probe power, this means lower probe energy and thus lower SNR, resulting in a lower measurement resolution during

the same measurement time. In addition, a finer spatial resolution requires a wider detection bandwidth [33], which increases the noise level and degrades the measurement resolution. Therefore, the measurand resolution and spatial resolution are correlated to each other, and there is a trade-off between them [33]. A single optical pulse must be evaluated cooperatively in both the time(T)–domain and frequency(F)–domain. In [84], the author proposed to use the Time-Frequency (T-F) localisation to evaluate the optical pulse quality for DFOS. T-F localisation describes the extent to that a pulse is restricted in both the T–domain and F–domain. The mean square deviation of the time and frequency distribution of a signal is defined as,

$$\Delta T^2 = \int_{-\infty}^{+\infty} t^2 |f(t)^2|, \tag{2.28}$$

$$\Delta F^2 = \int_{-\infty}^{+\infty} f^2 |F(f)^2|, \tag{2.29}$$

Where $\Delta T$ and $\Delta F$ are the variance of the signal $f$ in T–domain and F–domain, respectively. Smaller $\Delta T$ and $\Delta F$ means the pulse performs better in time and frequency localisation. The product $\Delta T \times \Delta F$ can be used as an evaluation factor for the pulse performance evaluation.

### 2.4.2 OFDR using the SWOS source

OFDR is a technique that retrieves the measurands information along the fibre in the frequency domain. Figure 2.10 shows the schematic diagram of a typical OFDR. It usually uses a SWOS source and a heterodyne detection method. The probe laser is frequency-swept and sent to the sensing fibre through a coupler. The scattered light from the sensing fibre then beats with the reference light reflected from a Faraday rotator mirror. The beat signal is detected by a photodetector and then for signal processing.

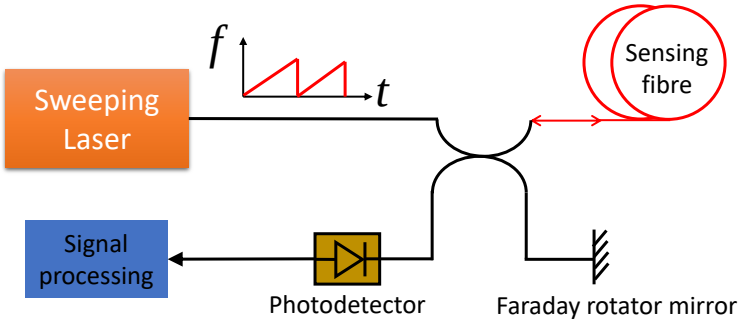


FIGURE 2.10: Schematic diagram of an OFDR.

The measurement can be understood as follow: the laser frequency is swept with a predefined shape (usually a linear shape), a particular beat frequency, which is the frequency difference between the reference and the scattered light, is thus related to the position where the scattering takes place. The spatial resolution of an OFDR is determined by [33],

$$\delta z = \frac{c}{2n_g \cdot \Delta F} \tag{2.30}$$

Where $\Delta F$ is the frequency-sweeping range, $n_g$ is the group index in the fibre, $c$ is the speed of light. Therefore, the spatial resolution of OFDR is decided by the sweeping range of SWOS source, that a larger sweeping range leads to a finer spatial resolution. A few tens of $GHz$ would result in a spatial resolution in $cm$ scale, which makes the OFDR more advantageous compared to OTDR in applications requiring high spatial resolution.

Similar to that in the OTDR, the sensing distance is partially determined by the period of the frequency-sweeping. The period of the frequency-sweeping needs to be longer than the round-trip time for the probe light to be launched and scattered back to avoid light overlapping. The sensing distance also depends on the laser linewidth, with a narrower and more coherent laser source leading to a longer sensing distance. However, unlike the OTDR, the trade-off between spatial resolution and measurand resolution in OTDR does not exist in OFDR. The spatial resolution is determined by the frequency-sweeping range, which is not related to the continuous or long-duration probe signal in OFDR. Thus a high SNR and measurement resolution can be obtained without sacrificing the spatial resolution. This is another factor that makes OFDR attractive in high spatial-resolution sensing applications.

OFDR has a high requirement for the SWOS source. The laser must be highly coherent and is able to sweep over a table and wide range. This has limited the application of OFDR to short sensing distance in the past few years. It has been used to characterise the optical components or even photonic integrated circuits [85, 86]. With the development of high-quality frequency-sweeping laser sources, the sensing distance has been extended to around 100 $km$ [87]. With the aid of an auxiliary interferometer, a five $cm$ spatial resolution over a fibre distance of 40 $km$ can be even obtained using OFDR, which is well beyond what has been achieved in OTDR [88].

### 2.4.3 The need for an integrated optical probe source for DFOS

The main obstacles preventing the current DFOS system from large-scale applications are their high cost (£60k-£100k per unit) and large size (usually the size of a computer workstation), of which a big portion of cost and size come from the optical probe signal generation system.

For the OTDR systems, as shown in Figure 2.9, the OPT is currently generated by single-wavelength continuous-wave lasers, discrete optical modulators, functional generators or arbitrary wave generators, which are all bulky and expensive. Recently, integrated OPT generation is achieved by a few approaches, including mode-locked semiconductor lasers [89, 90], microresonator-based Kerr soliton frequency comb [91, 92] and on-chip optical modulator [93, 94]. The approach of semiconductor mode-locked laser does not need an extra laser, but requires phase-lock design and heterogeneous integration, which needs a complicated process flow and is usually not CMOS compatible. In addition, an external DC or RF source is also needed to activate the pump and tune the laser. The approach of microresonator-based Kerr soliton frequency comb injects a narrow-band laser source into an optical microresonator with a high Q-factor. It uses the cascaded four-wave-mixing process to generate OPT. The soliton threshold power increases with decreasing repetition rate [92] — this power scaling usually leads to high power consumption for a repetition rate below 10 $GHz$ that is highly desired for OTDR applications due to the sensing distance requirement [33]. In addition, repetition rate reduction needs a larger cavity length, a higher Q-factor and precise dispersion control, resulting in a more challenging fabrication process. The approach of the on-chip optical modulator generates OPT by modulating the input laser source with the electrical-optical or thermal-optical effects. In addition to the complex fabrication process involving metallisation and doping, an external bulky radio frequency (RF) source is also needed, which are the bottleneck for the system-on-chip applications.

For the OFDR systems, as shown in Figure 2.10, a SWOS is required. Various methods to generate SWOS have been used. In [95], the frequency of a commercial distributed feedback laser diode is swept by modulating the current through the electrode with a function generator. In [87], the authors use a small piezoelectric transducer (PZT) actuator to expand or contract the laser resonator to modulate the frequency of a narrow linewidth fibre laser. In [96], a fibre laser is fed to an acoustic optical modulator (AOM) which is driven by a function generator with a sweeping frequency. All of these methods include discrete modulators and function generators, which are complex and costly. Recently, [97] uses a Santec TSL-550 tunable laser and build-in continuous frequency-sweeping function to get the sweeping-frequency optical probe signal. However, these sweeping lasers are very expensive. For example, the sweeping lasers from Luna [98], Santec [99], Keysight [100] all cost more than £30$K$ per unit, and they are also quite bulky.

To solve the issues mentioned above about the traditional methods of generating optical probe signals in DFOS, the key scientific challenge is to minimise and reduce the cost the optical signal generators in DFOS. Therefore, the best way should be to realise a fully integrated optical probe signal generation on chip, which requires further researches.

## 2.5 Summary

This chapter first describes the related theories and principles behind cavity optomechanics, including optical resonators and mechanical resonators. A zoo of recently demonstrated on-chip silicon cavity optomechanical devices were also reviewed. Silicon photonics technologies are reviewed, in which the benefits and advantages of using silicon platforms for integrated optomechanics were discussed. Lastly, optical trapping and DFOS are introduced, which work as the motivations of this thesis.

# Chapter 3

# Integrated silicon optomechanics for distributed fibre optical sensing

As been reviews in Chapter 2, the current DFOS systems are bulky and costly, mainly comes from the optical probe signal generator used to interrogate the system, and there is a clear incentive to solve this issue through the use of an integrated on-chip optical source due to its reduced size and cost. Even though different types of integrated laser sources have been realised [101], of which many use III-V heterogeneous integration with silicon photonics, these integrated laser sources are not readily applicable for DFOS due to the fact that the optical probe signal for DFOS requires a modulation mechanism on the laser source, to generate either intensity-modulated optical pulse trains (OPT) or frequency-modulated sweeping-wavelength optical signal (SWOS).

Here, the issues in traditional DFOS are addressed by investigating an innovative on-chip optical probe signal generation solution based on the optomechanical oscillation (OMO) process in a cavity optomechanical system. OMO is caused by the optomechanical dynamic back-action [102, 103]. The back-action reduces the overall effective damping rate of the mechanical resonator. It then starts the mechanical oscillation when the overall effective damping rate becomes negative. Recently, [104, 105] proposed to use the OMO effects to generate optical frequency sidebands. This method involves a parametric process and potentially can be utilised to generate time-domain OPT based on Fourier transformation. In addition, the mechanical oscillation will periodically change the resonance frequency of the optical cavity, which could also be used to generate a SWOS if a broadband laser is injected into the cavity. Therefore, I here explore the potentials of using integrated optomechanics for the generating of the optical probe signals for OTDR and OFDR, which will provide an important milestone on the path towards high-performance, affordable, and fully integrated dynamic DFOS.

This chapter will first discuss the need for an integrated optical source for DFOS applications. I then introduce the formalism used to describe the cavity optomechanical

system and the resulting optomechanical dynamic back-action effect, followed by a systematic analysis of the optomechanical self-sustained oscillation in different regimes. Lastly, I show that this optomechanical oscillation (OMO) can be utilised for OPT generators that can be used for OTDR applications and the SWOS generators that can be used for OFDR applications.

## 3.1 Cavity optomechanics

This section gives an introduction to the dynamic description of the cavity optomechanical coupling process and the resulting dynamic back-action effect. A theoretical model based on four independent dimensionless parameters which was first introduced by Florian et al. [106] was utilised and adjusted in this work to analytically investigate the cavity optomechanical coupling. A dead-zone was found that forbids the onset of optomechanical oscillation (OMO) and the optimal detuning value and the associated minimum threshold power were derived.

### 3.1.1 Cavity optomechanical coupling

A theoretical model of the cavity optomechanical coupling in the WGM form as shown in Figure 3.1 (A) is considered, in which the displacement of the mechanical resonator modulates the resonance frequency of the optical cavity. It should be noted that the coupling can be realised in different ways as long as the mechanical mode vibration changes the optical resonant frequency. Even for the coupling model based on WGM shown here, the mechanical resonator can be in different forms. As shown in Figure 3.1 (B), the mechanical breathing vibration mode can coexist with the optical mode in the cavity, where the radially-symmetric mechanical volume deformation changes the optical cavity length and the corresponding cavity resonant frequency. This mechanical deformation is caused by the optical scattering radiation force generated from the momentum transfer of the photons circulating inside the optical cavity. Figure 3.1 (C) shows the cavity optomechanical coupling via the optical gradient force coupling, in which the optical gradient force induced by the near-field between the suspended mechanical beam and the substrate causes out-of-plane mechanical deformation of the beam. This mechanical motion can modify the effective refractive index of the optical waveguide, and can therefore modulate the effective path length of the optical cavity and realise cavity optomechanical coupling.

For a small mechanical displacement $x(t)$, the resonance frequency of the optical cavity $\omega_{cav}(x)$ depends linearly on the displacement of the mechanical resonator $x$ and is given by,

$$\omega_{cav}(x) = \omega_{cav} - Gx, \tag{3.1}$$

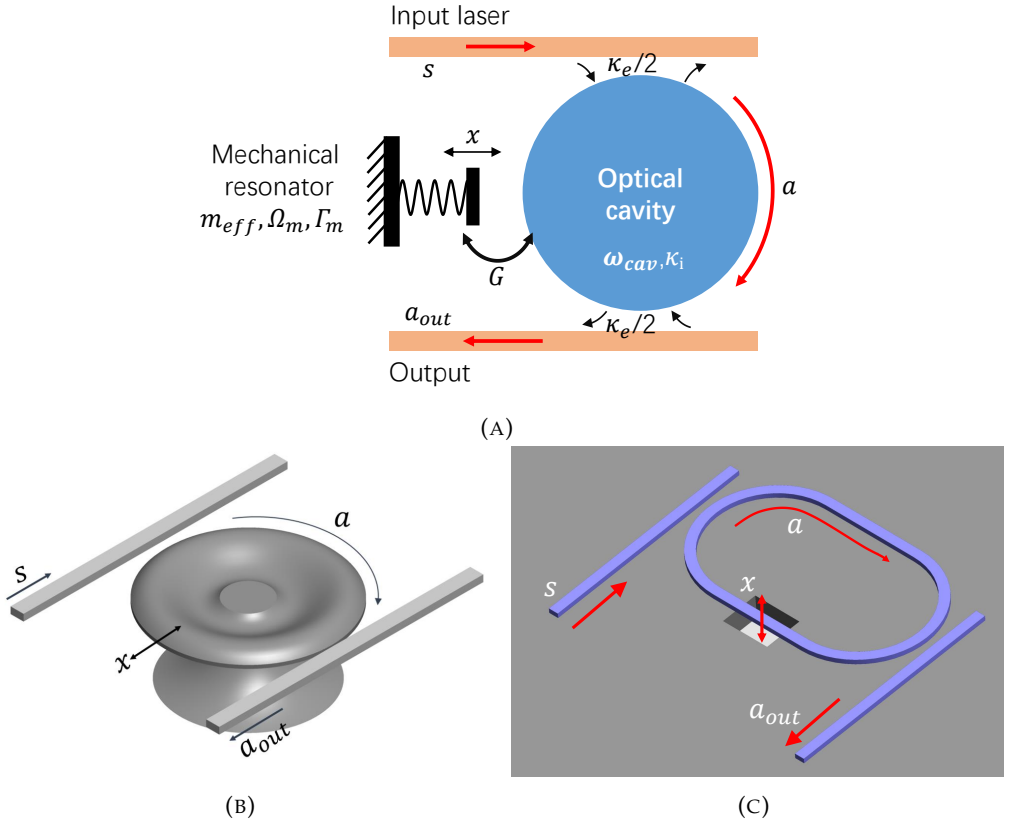


FIGURE 3.1: (A) Schematic diagram of an optomechanical system in the WGM form with cavity resonant frequency $\omega_{cav}$ and damping rate $\kappa$. The mechanical resonator with resonant frequency $\Omega_m$, damping rate $\Gamma_m$, and effective mass $m_{eff}$ is coupled with the optical cavity through a coupling coefficient $G$. The optomechanical system is excited with an input light through a coupling rate $\kappa_e/2$, and the transmitted optical field through the drop port is the output. (B) An on-chip WGM optomechanical system composed of a microdisk resonator and two bus waveguides which are coupled through the optical scattering radiation force. (C) An on-chip WGM optomechanical system composed of a micro-racetrack optical cavity and two bus waveguides which are coupled through the optical gradient force.

where $\omega_{cav}$ is the cavity optical resonance frequency for $x = 0$, and $G = -\partial\omega_{cav}(x)/\partial x$ is the optomechanical coupling coefficient which denotes the cavity resonance frequency shift per displacement. For the cavity optomechanical system where the WGM mode couples with the mechanical breathing mode as shown in Figure 3.1 (B), the optomechanical coupling coefficient is given by $G = \omega_{cav}/R$ [102], where $R$ is the radius of the WGM resonator.

Therefore, when considering the resonance frequency shift caused by the mechanical displacement, the original Equation 2.8 describing the optical cavity field amplitude coupled to an external field can be rearranged to,

$$\frac{da(t)}{dt} = i(\Delta + Gx(t))a(t) - \frac{\kappa}{2}a(t) + \sqrt{\frac{\kappa_e}{2}}s. \tag{3.2}$$

Note here that I have introduced a rotating frame at the laser frequency $\omega_L$, i.e., $a^{real} =$

$a^{here}e^{-i\omega_L t}$ and replaced the $\hat{a}$ with $a$. Here, $a^{here}$ represents the optical cavity field in this Equation 3.2, and $a^{real}$ is the real optical cavity field. This rotating frame method can help to drop the term containing $e^{-i\omega_L t}$, which reduces the complexity in analysing the dynamics of the optical cavity. Laser detuning is introduced as $\Delta = \omega_L - \omega_{cav}$. It should also be note that the last term representing the external field input in above Equation 3.2 has been modified when compared to the original Equation 2.6 as a double-sided coupling case is considered here. The output field is thus given by,

$$a_{out} = \sqrt{\frac{\kappa_e}{2}}a. \tag{3.3}$$

The effect of light on the mechanical resonator which arises due to the radiation pressure force should also be considered. In the context of the WGM coupling to a mechanical breathing mode, the radiation pressure force is generated by the momentum transfer of photons due to the reflection at the mirror surface. The momentum carried by a single photon can be written as:

$$p = \hbar k, \tag{3.4}$$

where $k$ is the wave vector given by $k = 2\pi/\lambda = \omega_{cav}/c$. Therefore, the generated radiation pressure scattering-force due to the reflection of photons in the cavity is [102]:

$$F_{rp}(t) = \frac{2\pi p n_c}{T_{rt}} = \frac{2\pi\hbar\omega_{cav}}{c}\frac{|a(t)|^2}{2\pi R/c} = \hbar G|a(t)|^2, \tag{3.5}$$

with $T_{rt} = 2\pi R/c$ represents the cavity round-trip time of the photon, $n_c = |a(t)|^2$ is the cavity photon number, $G = \omega_{cav}/R$ is the optomechanical coupling coefficient for the WGM cavity. Another mechanism to realize cavity optomechanical coupling is via the gradient radiation force due to the near-field effects with the mechanical resonator in the evanescent field of the optical cavity, for instance in [51, 52]. However, by introducing the optomechanical coupling coefficient $G$ defined as the cavity resonance frequency shift per displacement, Equation 3.5 for the radiation pressure force $F_{rp}$ is a general expression for both the scattering-force coupling and gradient-force coupling, which makes it valid for different types of cavity optomechanical systems.

When neglecting all the thermal fluctuations(including the photon shot noise and the intrinsic thermal noise), the following coupling equations can thus describe the time evolution of the optical mode amplitude $a(t)$ and mechanical displacement $x(t)$[26],

$$\frac{da(t)}{dt} = i(\Delta + Gx(t))a(t) - \frac{\kappa}{2}a(t) + \sqrt{\frac{\kappa_e}{2}}s, \tag{3.6}$$

$$\frac{dx^2(t)}{dt^2} + \Gamma_m\frac{dx(t)}{dt} + \Omega_m^2 x(t) = \frac{\hbar G|a(t)|^2}{m_{eff}}. \tag{3.7}$$

Equation 3.6 describes the dynamics of the optical field, in which $\kappa$ is the photon cavity decay rate and $\kappa_e$ represents the part associated with the external coupling. The effective drive amplitude of the pump laser is $s$ and can be normalised as $s = \sqrt{P_{in}/(\hbar\omega_L)}$ ($P_{in}$ is the input laser power, $\omega_L$ is the laser frequency, $\hbar$ is the reduced Planck Constant). $Gx(t)$ represents the optical resonance frequency shift induced by the mechanical motion. Equation 3.7 describes the temporal motion of mechanical resonator with effective mass $m_{eff}$, resonant frequency $\Omega_m$ and energy damping rate $\Gamma_m$. The term on the right side of Equation 3.7 is the radiation pressure force acting on the mechanical resonator. Equation 3.6 and Equation 3.7 can theoretically describe the physical process of optomechanical coupling and have proved many optomechanical experiments with high precision, both in the linearised regime and nonlinear regime[107, 108].

### 3.1.2 Dimensionless coupling equations

The full coupling equations (Equation 3.6 and Equation 3.7) contain eight parameters, which hinders the analysis of the system. For generality and simplicity, it is desirable to non-dimensionalise the above coupled equations [108, 109]. Here, the variables $t$, $a$, $x$ could be rescaled as $\tilde{t} = \Omega_m t$, $\tilde{a} = a\Omega_m/(2\sqrt{\frac{\kappa_e}{2}}s)$, $\tilde{x} = Gx/\Omega_m$, and the following expressions can be obtained.

$$\frac{da}{dt} = 2\sqrt{\frac{\kappa_e}{2}}s\frac{d\tilde{a}}{d\tilde{t}}, \tag{3.8}$$

$$\frac{dx}{dt} = \frac{\Omega_m^2}{G}\frac{d\tilde{x}}{d\tilde{t}}, \tag{3.9}$$

$$\frac{d^2x}{dt^2} = \frac{\Omega_m^3}{G}\frac{d^2\tilde{x}}{d\tilde{t}^2}. \tag{3.10}$$

The above equations (Equation 3.8, Equation 3.9, Equation 3.10) are substituted to the original cavity optomechanical coupling equations Equation 3.6 and Equation 3.7, and a new set of dimensionless parameters normalised to the mechanical resonant frequency $\Omega_m$ are introduced: $\widetilde{\Delta} = \Delta/\Omega_m$, $\tilde{\kappa} = \kappa/\Omega_m$, $\widetilde{\Gamma_m} = \Gamma_m/\Omega_m$, $\widetilde{\kappa_e} = \kappa_e/\Omega_m$. The original coupled equations can thus be reduced to Equation 3.11 and Equation 3.12 as shown below:

$$\frac{d\tilde{a}}{d\tilde{t}} = i(\widetilde{\Delta} + \tilde{x})\tilde{a} - \frac{\tilde{\kappa}}{2}\tilde{a} + \frac{1}{2}, \tag{3.11}$$

$$\frac{d^2\tilde{x}}{d\tilde{t}^2} + \widetilde{\Gamma_m}\frac{d\tilde{x}}{d\tilde{t}} + \tilde{x} = \widetilde{\kappa_e}\tilde{P}|\tilde{a}|^2, \tag{3.12}$$

where $\tilde{P}$ is the normalised dimensionless input laser power and is given by,

$$\tilde{P} = \frac{2\hbar G^2|s|^2}{m_{eff}\Omega_m^4} = \frac{2P_{in}G^2}{m_{eff}\Omega_m^4\omega_L}. \tag{3.13}$$

For simplicity, in the following analysis, $\widetilde{\kappa_e}/\tilde{\kappa} = 0.5$ would be assumed, and in the experiment this ratio can be varied by changing the coupling rate of the optical resonator

to input/output waveguide. It deserves noting that $\widetilde{\Gamma_m} = \Gamma_m/\Omega_m$ is a direct inverse of the mechanical quality factor $Q_m$.

In the above equations, the real input power $P_{in}$, optomechanical coupling coefficient $G$, mechanical effective mass $m_{eff}$, mechanical resonant frequency $\Omega_m$ and input laser frequency $\omega_L$ have been included into the dimensionless input power $\tilde{P}$. The effects of these parameters can thus all be taken into account in the variation of $\tilde{P}$. By this means, the quantitative dynamics of this system will only depend on four dimensionless parameters: normalised input power $\tilde{P}$, normalised optical cavity decay rate $\tilde{\kappa}$, normalised laser detuning $\widetilde{\Delta}$ and normalised mechanical damping rate $\widetilde{\Gamma_m}$, which greatly ease the complexity of the following analysis.

### 3.1.3 Optomechanical dynamic back-action

In this section, the dynamic back-action of a cavity optomechanical system around its equilibrium state is studied. As will be shown below, this dynamical back-action can reduce the effective damping rate of the mechanical resonator, and eventually leads to the onset of OMO.

#### 3.1.3.1 Linearised optomechanical coupling equations

The above inherently nonlinear coupling equations Equation 3.11 and Equation 3.12 describing the optomechanical system can be solved together by using a perturbative method. Small fluctuations $\epsilon\widetilde{a_1}(\tilde{t})$ and $\epsilon\widetilde{x_1}(\tilde{t})$ around the equilibrium states $\tilde{\bar{a}}$ and $\tilde{\bar{x}}$ are considered,

$$\tilde{a}(\tilde{t}) = \tilde{\bar{a}} + \epsilon\widetilde{a_1}(\tilde{t}), \tag{3.14}$$

$$\tilde{x}(\tilde{t}) = \tilde{\bar{x}} + \epsilon\widetilde{x_1}(\tilde{t}). \tag{3.15}$$

In the above equations, $\epsilon$ is an order parameter much less than 1. Plugging above Equation 3.14 and Equation 3.15 into Equation 3.11 and Equation 3.12 yields the following,

$$\epsilon\dot{\widetilde{a_1}} = \left(i(\widetilde{\Delta} + \tilde{\bar{x}} + \epsilon\widetilde{x_1}) - \frac{\tilde{\kappa}}{2}\right)(\tilde{\bar{a}} + \epsilon\widetilde{a_1}) + \frac{1}{2}, \tag{3.16}$$

$$\epsilon\ddot{\widetilde{x_1}} + \epsilon\widetilde{\Gamma_m}\dot{\widetilde{x_1}} + \tilde{\bar{x}} + \epsilon\widetilde{x_1}(\tilde{t}) = \frac{\tilde{\kappa}\tilde{P}}{2}\left(|\tilde{\bar{a}}|^2 + \epsilon^2|\widetilde{a_1}|^2 + \epsilon(\tilde{\bar{a}}^*\widetilde{a_1} + \tilde{\bar{a}}\widetilde{a_1}^*)\right). \tag{3.17}$$

By neglecting the second-order terms $\propto \epsilon^2$ and keeping only terms up to first order of $\epsilon$, the following four equations could be obtained,

$$0 = \left(i(\widetilde{\Delta} + \tilde{\bar{x}}) - \frac{\tilde{\kappa}}{2}\right)\tilde{\bar{a}} + \frac{1}{2}, \tag{3.18}$$

$$\dot{\tilde{a}_1} = \left(i(\tilde{\Delta} + \tilde{\bar{x}}) - \frac{\tilde{\kappa}}{2}\right)\tilde{a_1} + i\tilde{\bar{a}}\tilde{x_1}, \tag{3.19}$$

$$\tilde{\bar{x}} = \frac{\tilde{\kappa}\tilde{P}}{2}|\tilde{\bar{a}}|^2, \tag{3.20}$$

$$\ddot{\tilde{x_1}} + \widetilde{\Gamma_m}\dot{\tilde{x_1}} + \tilde{x_1} = \frac{\tilde{\kappa}\tilde{P}}{2}(\tilde{\bar{a}}^*\tilde{a_1} + \tilde{\bar{a}}\tilde{a_1}^*). \tag{3.21}$$

Equation 3.18 and Equation 3.20 describe the equilibrium state of the system. Equation 3.19 and Equation 3.21 can be solved in the frequency domain analytically [26] by performing a Fourier transformation. The results are given by,

$$i\tilde{\omega}\tilde{a_1}(\tilde{\omega}) = (i\widetilde{\bar{\Delta}} - \frac{\tilde{\kappa}}{2})\tilde{a_1}(\tilde{\omega}) + i\tilde{\bar{a}}\tilde{x_1}(\tilde{\omega}), \tag{3.22}$$

$$i\tilde{\omega}\tilde{a_1}^*(\tilde{\omega}) = (-i\widetilde{\bar{\Delta}} - \frac{\tilde{\kappa}}{2})\tilde{a_1}^*(\tilde{\omega}) - i\tilde{\bar{a}}\tilde{x_1}(\tilde{\omega}), \tag{3.23}$$

$$(-\tilde{\omega}^2 + i\tilde{\omega}\widetilde{\Gamma_m} + 1)\tilde{x_1}(\tilde{\omega}) = \frac{\tilde{\kappa}\tilde{P}}{2}\left(\tilde{\bar{a}}^*\tilde{a_1}(\tilde{\omega}) + \tilde{\bar{a}}\tilde{a_1}^*(\tilde{\omega})\right). \tag{3.24}$$

Here, $\widetilde{\bar{\Delta}} = \tilde{\Delta} + \tilde{\bar{x}}$ is the modified laser detuning caused by the averaged mechanical displacement offset $\tilde{\bar{x}}$ due to the constant optical radiation pressure force on the mechanical resonator. The express of $\tilde{a_1}(\tilde{\omega})$ and $\tilde{a_1}^*(\tilde{\omega})$ derived from Equation 3.22 and Equation 3.23 can then be plugged into the Equation 3.24 shown above. The results are given by,

$$(-\tilde{\omega}^2 + i\tilde{\omega}\widetilde{\Gamma_m} + 1)\tilde{x_1}(\tilde{\omega}) = \frac{\tilde{\kappa}\tilde{P}}{2}\left(\tilde{\bar{a}}^* \cdot \frac{i\tilde{\bar{a}}\tilde{x_1}(\tilde{\omega})}{i\tilde{\omega} - i\widetilde{\bar{\Delta}} + \frac{\kappa}{2}} - \tilde{\bar{a}} \cdot \frac{i\tilde{\bar{a}}\tilde{x_1}(\tilde{\omega})}{i\tilde{\omega} + i\widetilde{\bar{\Delta}} + \frac{\kappa}{2}}\right). \tag{3.25}$$

The imaginary part and real part of the right side of the above equations can be separated as,

$$\begin{aligned}(-\tilde{\omega}^2 + i\tilde{\omega}\widetilde{\Gamma_m} + 1)\tilde{x_1}(\tilde{\omega}) = {} & i\frac{\tilde{\kappa}\tilde{P}|\tilde{\bar{a}}|^2\tilde{x_1}(\tilde{\omega})}{2}\left(\frac{\frac{\tilde{\kappa}}{2}}{\frac{\tilde{\kappa}^2}{4} + (\tilde{\omega} - \widetilde{\bar{\Delta}})^2} - \frac{\frac{\tilde{\kappa}}{2}}{\frac{\tilde{\kappa}^2}{4} + (\tilde{\omega} + \widetilde{\bar{\Delta}})^2}\right) \\ & + \frac{\tilde{\kappa}\tilde{P}|\tilde{\bar{a}}|^2\tilde{x_1}(\tilde{\omega})}{2}\left(\frac{\tilde{\omega} - \widetilde{\bar{\Delta}}}{\frac{\tilde{\kappa}^2}{4} + (\tilde{\omega} - \widetilde{\bar{\Delta}})^2} - \frac{\tilde{\omega} + \widetilde{\bar{\Delta}}}{\frac{\tilde{\kappa}^2}{4} + (\tilde{\omega} + \widetilde{\bar{\Delta}})^2}\right).\end{aligned} \tag{3.26}$$

The real and imaginary part of the above equation represents the effect of the radiation pressure on the resonance frequency and damping rate of the mechanical resonator. The resulting substantial change of mechanical resonator's dynamics is referred to as the dynamic back-action.

When comparing the two sides of Equation 3.26, it can be found that the optomechanical induced normalised damping rate at the resonant frequency $\omega = \Omega_m$ is given by,

$$\widetilde{\Gamma_{opt}} = \frac{\tilde{\kappa}\tilde{P}|\tilde{\bar{a}}|^2}{4}\left\{\frac{\tilde{\kappa}}{\frac{\tilde{\kappa}^2}{4} + (1 + \widetilde{\bar{\Delta}})^2} - \frac{\tilde{\kappa}}{\frac{\tilde{\kappa}^2}{4} + (1 - \widetilde{\bar{\Delta}})^2}\right\}. \tag{3.27}$$

This yields the normalised effective mechanical damping rate,

$$\widetilde{\Gamma_{eff}} = \widetilde{\Gamma_{opt}} + \widetilde{\Gamma_m}. \tag{3.28}$$

It can be found an effectively blue detuning ($\widetilde{\tilde{\Delta}} > 0$) leads to negative optomechanical damping (anti-damping), while an effectively red detuning ($\widetilde{\tilde{\Delta}} < 0$) leads to a positive optomechanical damping rate (extra damping). The extra damping on the mechanical resonator results in optomechanical cooling [103, 31] where the mechanical vibration is suppressed. In this research, only the case of blue-detuning was studied, where the anti-damping leads to optomechanical heating, and the initial mechanical vibration is amplified. Eventually, the OMO emerges when the overall damping rate $\widetilde{\Gamma_{eff}}$ is reduced to be negative.

#### 3.1.3.2 Optomechanical oscillation threshold

In this section, the OMO threshold is then studied by analysing Equation 3.27 representing the optomechanical damping $\widetilde{\Gamma_{opt}}$. The above Equation 3.18 and Equation 3.20 are used to eliminate the parameter $\tilde{x}$ in Equation 3.27, thus the dimensionless optomechanical damping rate $\widetilde{\Gamma_{opt}}$ can be obtained as a function of only three parameters: $\tilde{P}$, $\tilde{\kappa}$ and $\widetilde{\Delta}$.

In order to find the OMO threshold, as shown in Figure 3.2, the dimensionless optomechanical damping rate $\widetilde{\Gamma_{opt}}$ as a function of $\tilde{P}$ and $\widetilde{\Delta}$ are plotted under four different values of $\tilde{\kappa}$, namely $\tilde{\kappa} = 0.1$, $\tilde{\kappa} = 0.5$, $\tilde{\kappa} = 2$ and $\tilde{\kappa} = 10$. In each of the figures, the colour represents the level of the value of $\widetilde{\Gamma_{opt}}$, and contours for $\widetilde{\Gamma_{opt}} = -0.001, -0.01, -0.1, -1$ are shown, which depict the threshold for OMO when $\widetilde{\Gamma_m} = 0.001, 0.01, 0.1, 1$.

It is clear from the colour bars of the figures that $\widetilde{\Gamma_{opt}}$ has its maximum and minimum value for each $\tilde{\kappa}$. Therefore, there exists a maximum cooling or heating rate for a given value of $\tilde{\kappa}$, even though the input power $\tilde{P}$ varies monotonically. This can be explained by looking at Equation 3.27 and Equation 3.20. Input power $\tilde{P}$ and effective laser detuning $\widetilde{\tilde{\Delta}}$ both contribute to the optomechanical damping rate $\widetilde{\Gamma_{opt}}$ through the dynamic back-action (Equation 3.27). In the meantime, $\tilde{P}$ also changes the static displacement $\tilde{\tilde{x}}$ of the mechanical resonator, i.e. the effective laser detuning $\widetilde{\tilde{\Delta}}$, through the optical radiation-pressure force (Equation 3.20). Therefore, the value of $\widetilde{\Gamma_{opt}}$ would not be monotonically modified when monotonically varying $\tilde{P}$.

The existence of a minimum value of $\widetilde{\Gamma_{opt}}$ could lead to a situation where the overall damping rate $\widetilde{\Gamma_{opt}} + \widetilde{\Gamma_m}$ is always positive when $\widetilde{\Gamma_m}$ is large enough. This situation is called "dead-zone effect", where no OMO can be excited under any detuning $\widetilde{\Delta}$ and $\tilde{P}$ for certain given values of $\tilde{\kappa}$ and $\widetilde{\Gamma_m}$. In the "dead zone", the mechanical resonator still can be heated, and the thermal Brownian motion is amplified. However, due to the large intrinsic mechanical damping, the optomechanical heating simply is not large

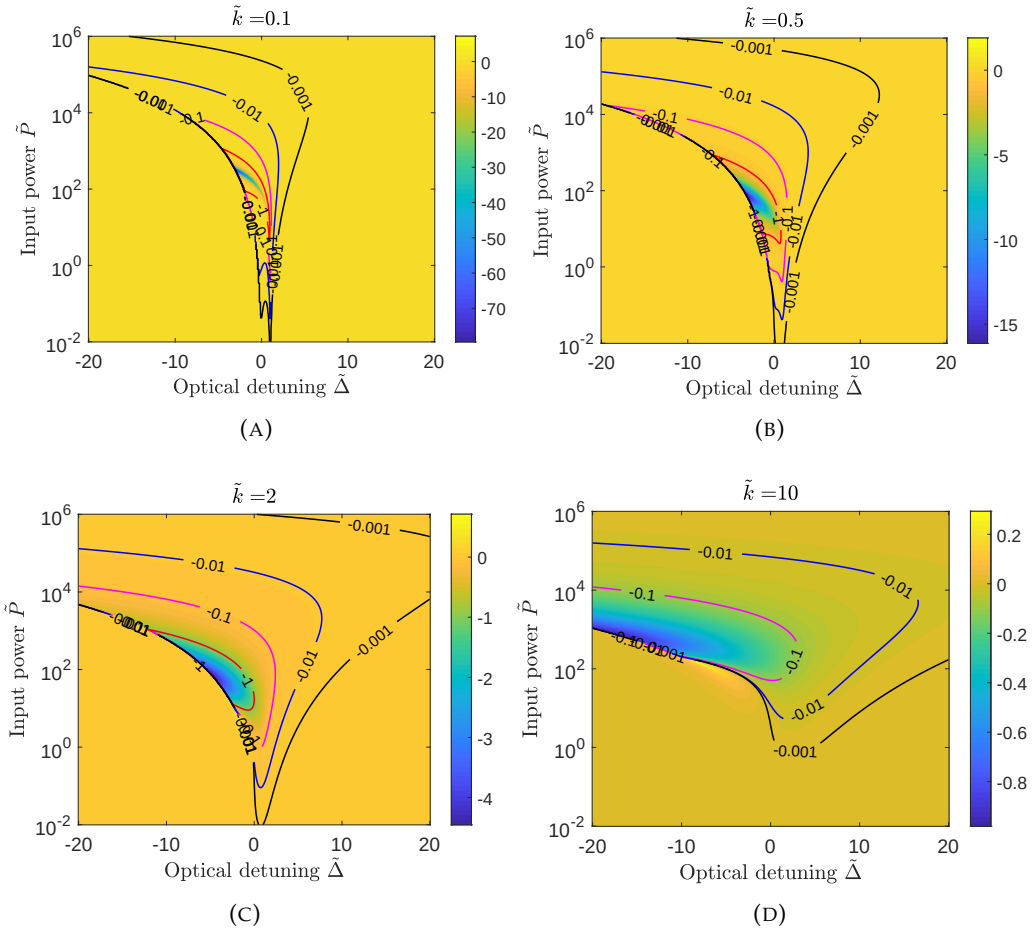


FIGURE 3.2: (A-D) The normalised optomechanical damping rate $\widetilde{\Gamma_{opt}}$ as a function of $\tilde{P}$ and $\widetilde{\Delta}$ for $\tilde{\kappa} = 0.1$, $\tilde{\kappa} = 0.5$, $\tilde{\kappa} = 2$ and $\tilde{\kappa} = 10$, respectively. The contours in the figure show the OMO threshold for $\widetilde{\Gamma_m} = 0.001, 0.01, 0.1, 1$.

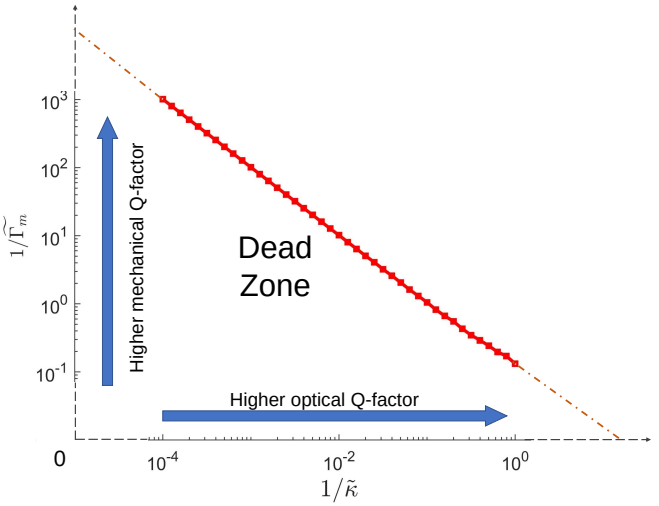


FIGURE 3.3: OMO dead-zone shown as a relationship of $\widetilde{\Gamma_m}$ and $\tilde{\kappa}$. In the dead-zone, no oscillation will occur under any $\tilde{\Delta}$ and $\tilde{P}$.

enough to reduce the effective damping rate to zero. Thus the optomechanical oscillation can not happen. This can be observed from Figure 3.2, in which it is found the

threshold contours for all the four different $\widetilde{\Gamma_m}$ when $\tilde{\kappa} = 0.1$, $\tilde{\kappa} = 0.5$ and $\tilde{\kappa} = 2$. However, there is no oscillation at all for $\tilde{\kappa} = 10$ and $\widetilde{\Gamma_m} = 1$. The absence of the threshold contour for $\tilde{\kappa} = 10$ and $\widetilde{\Gamma_m} = 1$ suggests that this set of parameters lies in the dead-zone for OMO. A wide range of $\tilde{\kappa}$ and $\widetilde{\Gamma_m}$ are analysed and the resulting dead zone is plotted in Figure 3.3. As shown in the figure, the dead zone appears at a combination region with low optical Q-factor and low mechanical Q-factor. When designing an OMO device, the dead zone should be avoided.

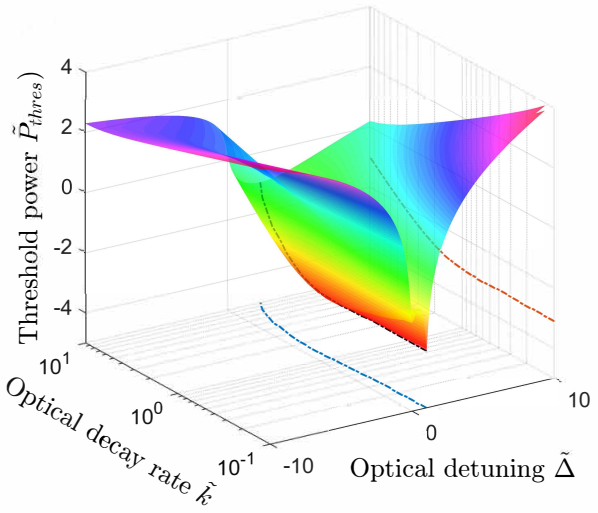


(A)

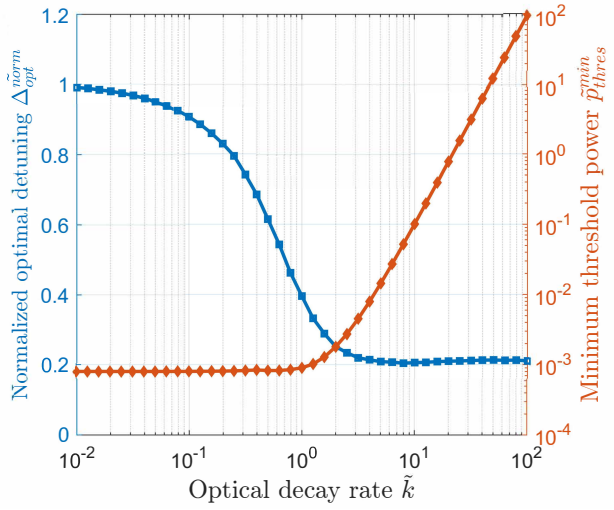


(B)

FIGURE 3.4: (A) Threshold power $\tilde{P}_{thres}$ for OMO process as a function of $\tilde{\kappa}$ and $\widetilde{\Delta}$ when $\widetilde{\Gamma_m} = 1/5000$. (B)The minimum threshold power $\tilde{P}_{thres}^{min}$ and the corresponding normalised optimal detuning $\widetilde{\Delta}_{opt}^{norm} = \widetilde{\Delta}_{opt}/(1+\tilde{\kappa})$ as a function of $\tilde{\kappa}$.

Apart from the dead-zone effect, it can also be found from Figure 3.2 that there exists a minimum threshold power $\tilde{P}_{thres}^{min}$ and an associated optimal laser detuning $\widetilde{\Delta}_{opt}$ for each $\tilde{\kappa}$ and $\widetilde{\Gamma_m}$, corresponding to the Y-coordinate and X-coordinate of the data point

at the contour line with the lowest input power. Here, only the situation far away from the dead-zone is considered, which is usually the preferred case in the experiment. As shown in Figure 3.4 (a), the OMO threshold power $\tilde{P}_{thres}$ as a function of $\tilde{\Delta}$ and $\tilde{\kappa}$ when $\widetilde{\Gamma_m} = 1/5000$ is plotted as a surface. In the valley of the surface, the minimum threshold power is marked as a black line. The projection of this line to the side and bottom can be viewed as the minimum threshold power $\tilde{P}_{thres}^{min}$ and corresponding optimal laser detuning $\widetilde{\Delta}_{opt}$. In Figure 3.4 (b), a normalised optimal detuning factor defined as $\widetilde{\Delta}_{opt}^{norm} = \widetilde{\Delta}_{opt}/(1+\tilde{\kappa})$ has been introduced, which is plotted as a function of $\tilde{\kappa}$ with a blue line. It can be found that in the deeply resolved-sideband regime (RSR) ($\tilde{\kappa} \ll 1$), the laser detuning associated with the minimum threshold power is approaching $\tilde{\Delta} = 1$, while in the deeply unresolved-sideband regime (USR) ($\tilde{\kappa} \gg 1$), the optical laser detuning is around $0.2\tilde{\kappa}$. This suggests an optimal detuning $\Delta_{opt} = \Omega_m$ in the deeply RSR, and $\Delta_{opt} = 0.2\kappa$ in the deeply USR. The associated minimum power $\tilde{P}_{thres}^{min}$ is also plotted along with $\tilde{\kappa}$. The minimum threshold power increases with $\tilde{\kappa}$ in USR, while keeping as a constant in the RSR. It shows that an optomechanical system in the RSR requires less optical input power to start OMO. This is because smaller $\tilde{\kappa}$ means higher optical Q-factor, which enhances the cavity field and leads to a larger field amplitude. A larger field amplitude would then lead to a larger optomechanical heating rate as derived in Equation 3.27 and make the OMO easier to start.

As a summary, here, I have linearised the optomechanical coupling equations for the small fluctuations near the equilibrium state and analysed the optomechanical dynamic back-action effect and the OMO threshold. A dead-zone is found with a combination of low optical Q-factor and mechanical Q-factor. Minimum optical threshold power and the corresponding optimal laser detuning are derived.

## 3.2 Optomechanical oscillation

When the overall effective damping rate $\widetilde{\Gamma_{eff}} = \widetilde{\Gamma_{opt}} + \widetilde{\Gamma_m}$ is decreased to be negative, the mechanical resonator starts to oscillate when small initial fluctuations occur, for instance, the random thermal vibrations originated from the Brownian thermal noise. As shown in Figure 3.5, the simulated time trace of the normalized displacement $\tilde{x}$ over time $\tilde{t}$ in an OMO process is plotted. The mechanical oscillation amplitude grows exponentially until the oscillation reaches a steady-state regime due to the nonlinear saturation effect, which balances the gain and loss of the mechanical resonator.

### 3.2.1 Oscillation in small amplitude

When the optomechanical oscillation amplitude is not too large, the motion is approximately harmonic. An ansatz can be made that the mechanical resonator is oscillating

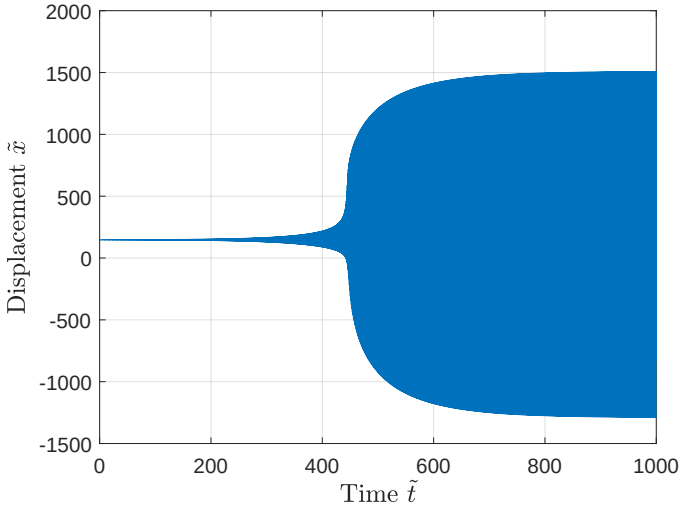


FIGURE 3.5: The simulated time trace of $\tilde{x}$ over $\tilde{t}$ in an OMO process. The simulated optomechanical parameters are: $\tilde{\kappa} = 100$, $\widetilde{\Gamma_m} = 1000$, $\widetilde{\Delta} = 30$, $\tilde{P} = 4 \times 10^5$, with the initial displacement set at the equilibrium state $\widetilde{x_{init}} = 147.3$.

with a sinusoidal pattern as $\tilde{x}(\tilde{t}) = \bar{\tilde{x}} + \tilde{A}cos(\tilde{t})$, where $\bar{\tilde{x}}$ is the dimensionless averaged displacement and $\tilde{A}$ is the dimensionless oscillation amplitude. Here, the oscillation amplitude $\tilde{A}$ in the steady-state under different system parameters will be derived.

By substituting the expression $\tilde{x}(\tilde{t}) = \bar{\tilde{x}} + \tilde{A}cos(\tilde{t})$ into Equation 3.11 and solving the differential equation, the intracavity field can be analytically derived. The analytical solutions can be written as [106],

$$\tilde{a}(\tilde{t}) = e^{i\tilde{A}sin(\tilde{t})} \sum_{n=-\infty}^{\infty} \widetilde{\alpha_n} e^{in\tilde{t}}, \tag{3.29}$$

where

$$\widetilde{\alpha_n} = \frac{J_n(-\tilde{A})}{\tilde{\kappa} - 2i(\tilde{\Delta} + \bar{\tilde{x}} - n)}. \tag{3.30}$$

Here, $J_n$ is the Bessel function of the first kind, so that the photon number inside the cavity is given by,

$$|\tilde{a}(\tilde{t})|^2 = \tilde{a}(\tilde{t}) \cdot \tilde{a}^*(\tilde{t}) = \sum_{n,m=-\infty}^{\infty} \widetilde{\alpha_n} \cdot \widetilde{\alpha_m}^* e^{i(n-m)\tilde{t}}. \tag{3.31}$$

The resulting cavity field consists of a range of frequency sidebands at mechanical harmonics $\pm n\Omega_m$, where $n$ is an integer. At the steady-state, the oscillation amplitude $\tilde{A}$ and averaged displacement $\bar{\tilde{x}}$ are determined by two balance conditions: firstly, the time-averaged input power acting on the mechanical resonator by the radiation pressure force equals the power lost into the environment due to the mechanical damping. Secondly, the time-averaged radiation pressure force causes the averaged mechanical displacement. When looking at Equation 3.11, the following equations describing the

balance conditions could be obtained:

$$\bar{\tilde{x}} = \widetilde{\kappa_e}\tilde{P}\langle|\tilde{a}(\tilde{t})|^2\rangle, \tag{3.32}$$

$$\widetilde{\Gamma_m}\langle\dot{\tilde{x}}^2\rangle = \widetilde{\kappa_e}\tilde{P}\langle|\tilde{a}(\tilde{t})|^2\dot{\tilde{x}}\rangle, \tag{3.33}$$

where the $\langle ...\rangle$ represents the time-averaged operation. The following expressions could be derived,

$$\langle|\tilde{a}(\tilde{t})|^2\rangle = \sum_{n=-\infty}^{\infty}|\widetilde{\alpha_n}|^2, \tag{3.34}$$

$$\langle\dot{\tilde{x}}^2\rangle = \langle\tilde{A}^2\cdot\frac{1-cos(\tilde{t})}{2}\rangle = \frac{\tilde{A}^2}{2}, \tag{3.35}$$

$$\begin{aligned}\langle|\tilde{a}(\tilde{t})|^2\dot{\tilde{x}}\rangle &= \langle\sum_{n,m=-\infty}^{\infty}\widetilde{\alpha_n}\cdot\widetilde{\alpha_m}^* e^{i(n-m)\tilde{t}}\cdot-\tilde{A}sin(\tilde{t})\rangle \\ &= \tilde{A}\langle\sum_{n,m=-\infty}^{\infty}\widetilde{\alpha_n}\cdot\widetilde{\alpha_m}^*\cdot\frac{e^{i(n-m-1)\tilde{t}}-e^{i(n-m+1)\tilde{t}}}{2i}\rangle \\ &= \tilde{A}\left(\sum_{n=-\infty}^{\infty}\widetilde{\alpha_n}\cdot\widetilde{\alpha_{n-1}}^*\cdot\frac{1}{2i}-\sum_{n=-\infty}^{\infty}\widetilde{\alpha_n}^*\cdot\widetilde{\alpha_{n-1}}\cdot\frac{1}{2i}\right) \\ &= \tilde{A}\cdot Im(\sum_{n=-\infty}^{\infty}\widetilde{\alpha_n}^*\cdot\widetilde{\alpha_{n+1}}).\end{aligned} \tag{3.36}$$

The above three expressions are then substituted to the balance conditions Equation 3.32 and Equation 3.33 and the following equations can be obtained,

$$\bar{\tilde{x}} = \widetilde{\kappa_e}\tilde{P}\sum_{n=-\infty}^{\infty}|\widetilde{\alpha_n}|^2, \tag{3.37}$$

$$\frac{\widetilde{\Gamma_m}\tilde{A}}{2} = \widetilde{\kappa_e}\tilde{P}\cdot Im(\sum_{n=-\infty}^{\infty}\widetilde{\alpha_n}^*\cdot\widetilde{\alpha_{n+1}}). \tag{3.38}$$

Analogous to the optomechanical damping rate derived for the equilibrium state in linearised regime (Equation 3.27), the amplitude-dependent effective optomechanical damping rate $\widetilde{\Gamma_{opt}}(\tilde{A})$ could be derived, which was first introduced in [109] and is defined as:

$$\widetilde{\Gamma_{opt}}(\tilde{A}) = -\frac{2\widetilde{\kappa_e}\tilde{P}\cdot Im(\sum_{n=-\infty}^{\infty}\widetilde{\alpha_n}^*\cdot\widetilde{\alpha_{n+1}})}{\tilde{A}}. \tag{3.39}$$

For low amplitude with $\tilde{A}\to 0$, Equation 3.39 can be simplified to Equation 3.27. The balance condition can thus be recast into,

$$\widetilde{\Gamma_{opt}}(\tilde{A}) + \widetilde{\Gamma_m} = 0. \tag{3.40}$$

After eliminating $\bar{\tilde{x}}$ using Equation 3.37, the value of $\widetilde{\Gamma_{opt}}$ could be numerically calculated. Figure 3.6 plotted the simulated value of $\widetilde{\Gamma_{opt}}$ as a function of $\widetilde{\Delta}$ and $\tilde{A}$ when $\tilde{\kappa}=0.1$, $\tilde{\kappa}=0.5$, $\tilde{\kappa}=2$ and $\tilde{\kappa}=10$, respectively. $\tilde{P}$ is set to a constant as 1. The

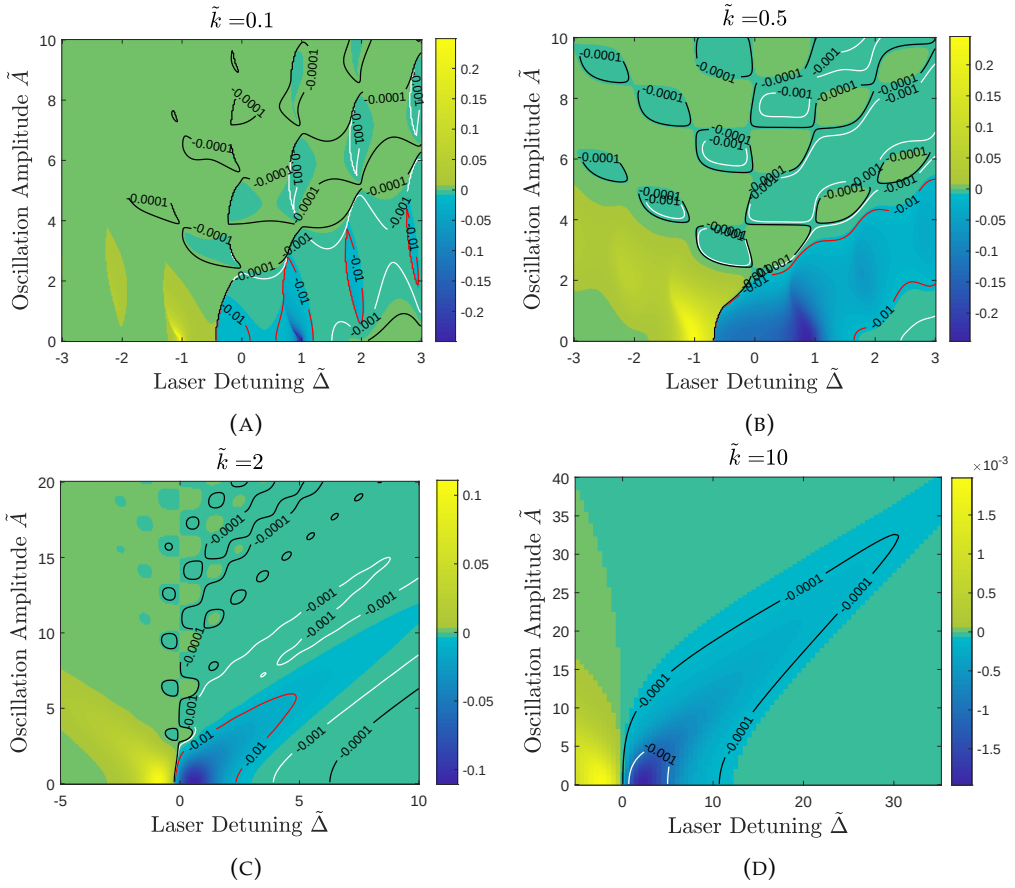


FIGURE 3.6: (A-D) The amplitude-dependent effective optomechanical damping rate $\widetilde{\Gamma_{opt}}$ as a function of $\widetilde{\Delta}$, $\tilde{A}$ when $\tilde{\kappa} = 0.1$, $\tilde{\kappa} = 0.5$, $\tilde{\kappa} = 2$ and $\tilde{\kappa} = 10$, respectively. $\tilde{P}$ is set to a constant as 1. The contour lines shows the possible steady-state when $\widetilde{\Gamma_m} = 10^{-3}$, $10^{-4}$ and $10^{-5}$ respectively.

contour lines $\widetilde{\Gamma_{opt}} = -10^{-3}, -10^{-4}$ and $-10^{-5}$ indicates the possible steady-state when $\widetilde{\Gamma_m} = 10^{-3}$, $10^{-4}$ and $10^{-5}$ respectively. It should be noted that stable solutions are given by the upper part of each contour line where $\widetilde{\Gamma_{opt}}$ increases with increasing $\tilde{A}$. This is because decreasing $\widetilde{\Gamma_{opt}}$ would lead to an increase of the oscillation amplitude $\tilde{A}$, which make the state lies in the lower part of the contour lines critical and unstable.

The maximum heating rate when $\tilde{A} \to 0$ appears at around $\widetilde{\Delta} = 0.2\tilde{\kappa}$ in USR ($\tilde{\kappa} > 1$) (Figure 3.6 (D)) and $\widetilde{\Delta} = 1$ in RSR ($\tilde{\kappa} < 1$) (Figure 3.6 (A)), which agree with the threshold analysis results in Section 3.1.3.2. The onset of OMO from $\tilde{A} = 0$ is a Hopf bifurcation into a limit cycle. Comparing the contour lines with different colours representing the oscillation amplitude for different $\widetilde{\Gamma_m}$, it can be found that a larger value of $\widetilde{\Gamma_m}$ leads to a smaller oscillation amplitude. In Figure 3.6 (D), there is no contour line for $\widetilde{\Gamma_m} = 0.01$. This can be explained by looking at Figure 3.2 (D), where it can be found that the threshold of OMO is not reached for this set of parameters.

In the RSR ($\tilde{\kappa} < 1$) (Figure 3.6 (A,B)), it can be found found that oscillation amplitude $\tilde{A}$ can take multiple stable values under the same system parameters. This corresponds to several stable attractors in this optomechanical system, which has been termed "dynamic multistability" in previous research [106] and experimentally observed in [110, 111]. The figures also show that larger $\widetilde{\Delta}$ generally results in larger $\tilde{A}$. When adiabatically adjusting the laser detuning $\widetilde{\Delta}$, the oscillation amplitude $\tilde{A}$ can be tuned gradually along the contour line, during which the oscillation amplitude can be increased to the extent that can not be acquired from zero initial condition. On the other hand, sweeping back nonadiabatically the laser detuning $\widetilde{\Delta}$ to smaller value allows us to reach attractors with higher amplitude $\tilde{A}$, where the OMO process can not start spontaneously from the state of rest ($\tilde{A} = 0$). In the deeply USR ($\tilde{\kappa} \gg 1$) (Figure 3.6 (D)), the dynamic multistability vanishes, and there is only one steady state for a set of system parameters.

### 3.2.2 Oscillation in large amplitude regime

For large oscillation amplitude, it will be shown here that the harmonic oscillation assumption is no longer valid and the dynamics of the coupled optomechanical system will have to be calculated by numerical simulations. The coupled differential equations Equation 3.11 and Equation 3.12 that can accurately describe the dynamics of the optomechanical system can be numerically solved using the explicit Runge-Kutta method based on Dormand-Prince pair [112] to characterise the OMO characteristics with system parameters variations.

As shown in Figure 3.7, the simulated OMO phase space trajectories are plotted for a period of $\tilde{t} = 500$ after a sufficiently long integration time. A phase space plot is a parametric graph of the velocity $d\tilde{x}/d\tilde{t}$ plotted as a function of the displacement $\tilde{x}$, with the changing variable being the time. Phase-space plots are very useful for analyzing complicated oscillations, with each oscillation way corresponds to a specific phase space pattern. For instance, a limit cycle in the circular or ellipse shape in the phase space represents a harmonic oscillation. In these plots, the $\widetilde{\Gamma_m}$ is set to a constant as 0.001, and $\widetilde{\Delta}$ is set to an optimised value associated with a minimum threshold power for OMO according to Section 3.1.3.2. The initial condition of the numerical simulation is set to $\tilde{a} = \tilde{x} = \dot{\tilde{x}} = 0$.

From the figures, in both the RSR and USR, a stable ellipse limit cycle in phase space can be formed with low input power $\tilde{P}$ ($\tilde{P} = 1e0, 1e2$), which corresponds to a stable OMO process in the long time limit. In Table 3.1, the numerically solved oscillation amplitudes in limit cycles for $\tilde{P} = 1e0$ as shown in Figure 3.7 are compared to the theoretical results predicted from the harmonic oscillation ansatz as shown in Figure 3.6. The results turn out to match well with each other, which verifies the ansatz of the harmonic nature of the OMO in a small oscillation amplitude regime.

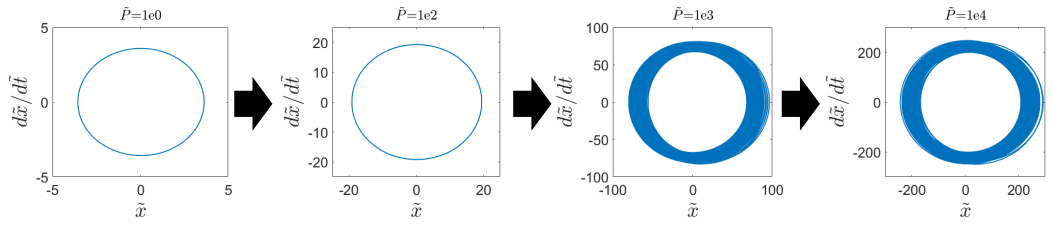


(A) $\tilde{\kappa} = 0.1$

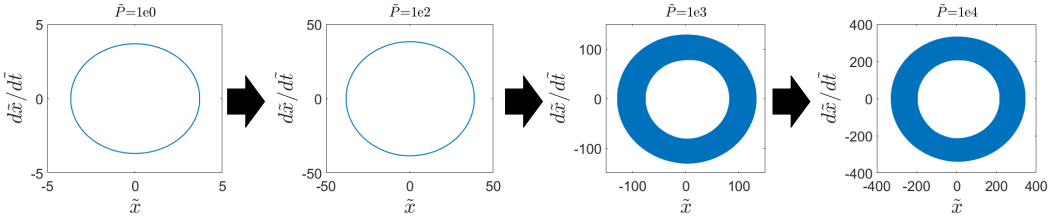


(B) $\tilde{\kappa} = 0.5$

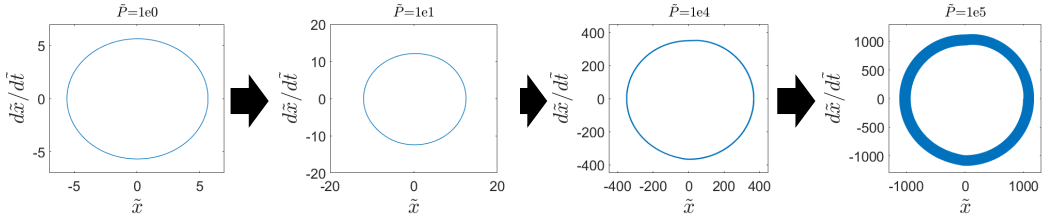


(C) $\tilde{\kappa} = 2$

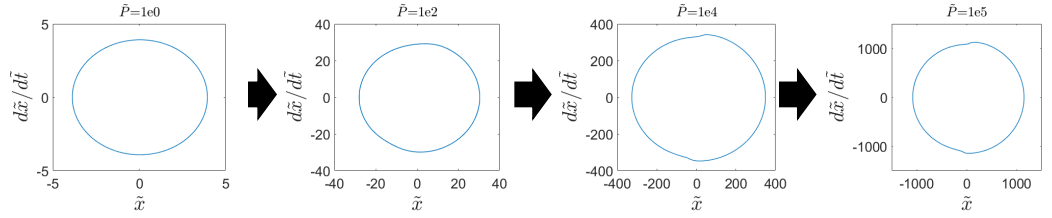


(D) $\tilde{\kappa} = 10$

FIGURE 3.7: (A-D) The evolution of the OMO process phase space trajectories with the increase of normalised input power $\tilde{P}$ for $\tilde{\kappa} = 0.1$, $\tilde{\kappa} = 0.5$, $\tilde{\kappa} = 2$ and $\tilde{\kappa} = 10$, respectively. The $\widetilde{\Gamma_m}$ is set to a constant as 0.001, and $\widetilde{\Delta}$ is set to an optimised value for OMO according to Section 3.1.3.2. The initial condition of the numerical simulation is set to $\tilde{a} = \tilde{x} = \dot{\tilde{x}} = 0$.

With the increase of the input power $\tilde{P}$ and the oscillation amplitude $\tilde{A}$, the simple harmonic oscillation ansatz breaks down, and the OMO process gradually evolves towards different dynamic behaviours for the cavity optomechanical system in USR and outside USR. Outside the USR (Figure 3.7 (A,B,C)), the limit cycle representing a stable OMO process evolves into phase trajectories in a random fashion, indicating the system is in chaos. In the USR (Figure 3.7 (D)), the ellipsoidal-shaped phase trajectory evolves into a mushroom-like shape phase trajectory, which means the simple harmonic motion develops into a periodic motion with two different amplitudes. During the process, there

| | $\tilde{\kappa} = 0.1$ | $\tilde{\kappa} = 0.5$ | $\tilde{\kappa} = 2$ | $\tilde{\kappa} = 10$ |
|---|---|---|---|---|
| $\tilde{A}$ derived from harmonic oscillation ansatz | 3.56 | 3.66 | 5.6 | 3.9 |
| $\tilde{A}$ derived from numerical simulation | 3.59 | 3.68 | 5.65 | 3.91 |

TABLE 3.1: The comparison between OMO oscillation amplitude $\tilde{A}$ obtained analytically from harmonic ansatz (Figure 3.6) and numerically from solving the coupling equations (Figure 3.7), when $\tilde{P} = 1$, $\Gamma_m = 0.001$, and $\tilde{\kappa} = 0.1, 0.5, 2, 10$ respectively. $\widetilde{\Delta}$ is set to an optimised value associated with a minimum threshold power for OMO.

is a sudden change in the velocity of the motion. Here, the two dynamic behaviours will be discussed in detail.

#### 3.2.2.1 Optomechanical induced chaos

The chaos is characterised by positive Lyapunov exponents of the dynamic system, where any small deviation from the initial trajectory grows exponentially with time. The optomechanical chaos has been studied and observed in several works [113, 114]. Here, the Lyapunov exponents of the OMO process with the parameters shown in Figure 3.7 are calculated using the standard method presented in [115, 116], the results are shown in Figure 3.8. The Lyapunov exponents separate regular motion with a negative value from chaotic motion with a positive value.

Four lines are drawn because the optomechanical system is a four-dimensional system, with four variables in the coupling equations. If any of the four values is positive, then the system is in the chaotic regime. It can be found that the Lyapunov exponents diagrams precisely predict the evolvement into chaos in Figure 3.7. For the OMO process with $\tilde{\kappa} = 0.1$ and $\tilde{\kappa} = 0.2$, the system evolves to chaos when $\tilde{P} = 1e3$. While for the system with $\tilde{\kappa} = 2$, a larger power with $\tilde{P} = 1e5$ is required to reach the chaos.

In this chaos regime, the mechanical motion is random and quite sensitive to the initial condition. This poses challenges for using this oscillation to modulate the optical field. Therefore, chaos should be avoided.

#### 3.2.2.2 mushroom-like phase trajectory

It is already shown that the cavity optomechanical system in the deeply USR can display a mushroom-like OMO phase trajectory when the input power $\tilde{P}$ and oscillation amplitude $\tilde{A}$ are sufficiently large. To show this phenomenon more explicitly, an optomechanical system in a deeply USR with $\tilde{\kappa} = 100$, $\widetilde{\Gamma_m} = 0.01$, $\widetilde{\Delta} = 20$, $\tilde{P} = 4e7$ is here simulated. The simulated phase space trajectory is shown in Figure 3.9 (A), as well as the corresponding displacement (Figure 3.9 (B)), velocity (Figure 3.9 (C)) and acceleration (Figure 3.9 (D)) variation with time.

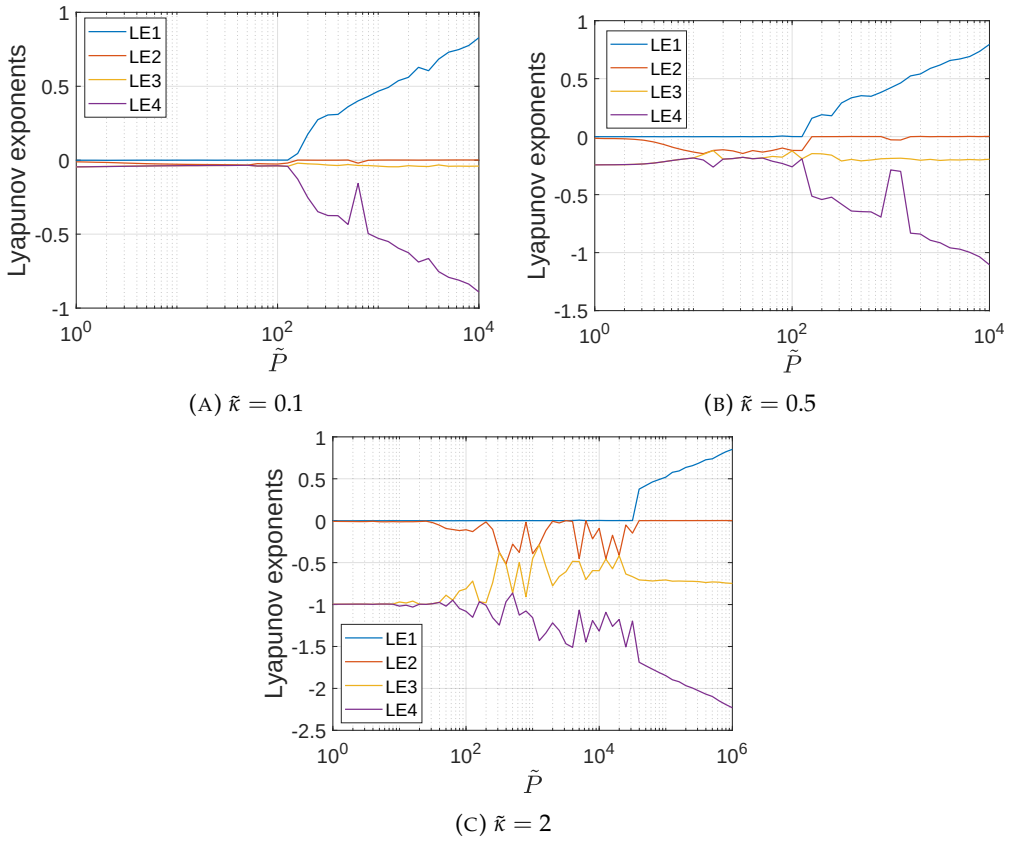


(A) $\tilde{\kappa} = 0.1$ (B) $\tilde{\kappa} = 0.5$

(C) $\tilde{\kappa} = 2$

FIGURE 3.8: (A-C) The calculated Lyapunov exponents variation of the OMO process with the increase of normalised input power $\tilde{P}$ for $\tilde{\kappa} = 0.1$, $\tilde{\kappa} = 0.5$ and $\tilde{\kappa} = 2$ respectively, corresponding to the evolution diagrams shown in Figure 3.7

From the phase space trajectory plot (Figure 3.9 (A)), the OMO display an obvious mushroom-like shape, with two different amplitudes $\tilde{A}_1$ and $\tilde{A}_2$ during one oscillation period. This effect has been observed experimentally in an optomechanical system with a Bose-Einstein condensate [117] and numerically studied in [107, 118]. Although the time-domain displacement diagram shows a harmonic pattern (Figure 3.9 (B)), there is actually an abrupt change in the oscillation velocity during the transit between the oscillation with amplitude $\tilde{A}_1$ and $\tilde{A}_2$ (Figure 3.9 (C)). This abrupt change in velocity would result in an abrupt increase of oscillation acceleration, which is shown in Figure 3.9 (D).

To illustrate the principles behind this mushroom-like phase trajectory, the normalised cavity photon number $|\tilde{a}|^2$ variations along with the phase space trajectory and the acceleration diagram are plotted in Figure 3.10. A clear and perfect coincidence can be found between the abrupt change of the oscillation velocity $d\tilde{x}/d\tilde{t}$ and the peak in cavity photon number $|\tilde{a}|^2$. This coincidence is due to the large-amplitude induced optomechanical interaction in the USR. In this USR, the optical cavity damping rate is much larger than the mechanical resonance frequency. Therefore, the optical cavity can respond quickly enough to the mechanical oscillation, and there is almost no delay between them. For the large amplitude mechanical oscillation, the cavity resonance can

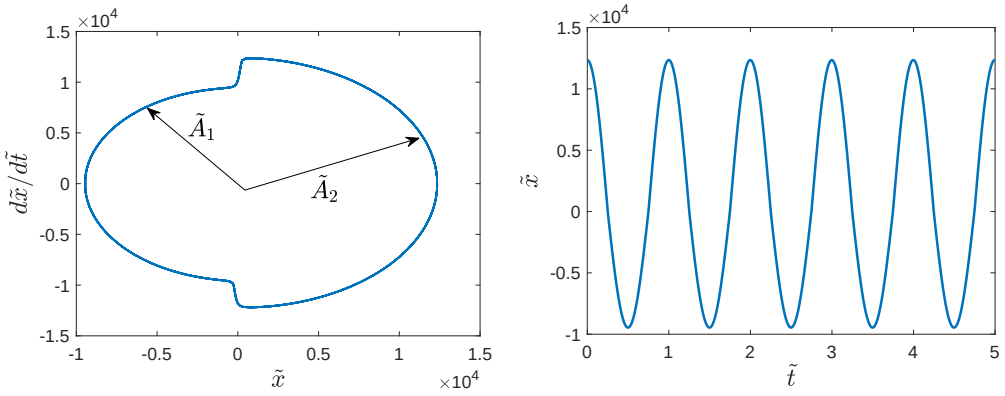


(A) Phase space trajectory




(B) Oscillation displacement

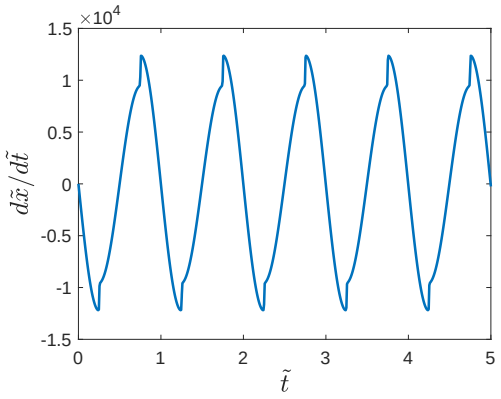


(C) Oscillation velocity

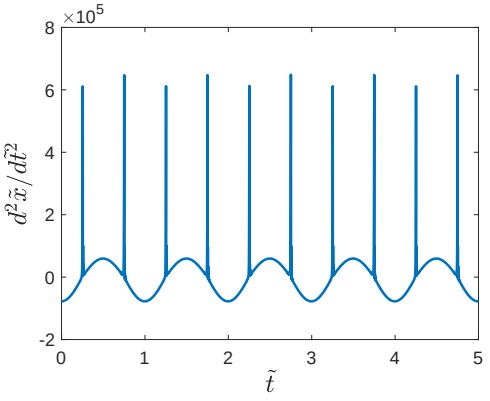


(D) Oscillation acceleration

FIGURE 3.9: (A) The phase space trajectory showing the velocity and displacement. (B, C, D) The time-domain change of oscillation displacement, velocity and acceleration. Note the simulation results are for an optomechanical system in deeply USR with $\tilde{\kappa} = 100$, $\widetilde{\Gamma_m} = 0.01$, $\widetilde{\Delta} = 20$, $\tilde{P} = 4e7$.

be actually shifted significantly away from the input laser frequency, which makes the cavity out of resonance and thus the cavity photon number is nearly zero for most of the time during an oscillation period. When the cavity is empty, the mechanical resonator undergoes a damped harmonic motion represented by two single parts in the phase trajectory with amplitude $\tilde{A}_1$ and $\tilde{A}_2$. However, when the mechanical motion makes the optical cavity resonant with the input pump laser, the cavity would quickly build up, and the cavity photon number increases abruptly, which was shown as the peaks in Figure 3.10. This abrupt change in cavity photon number results in a large optical radiation force on the mechanical resonator, and therefore the mechanical oscillation experiences a large acceleration and thus, the velocity changes abruptly.

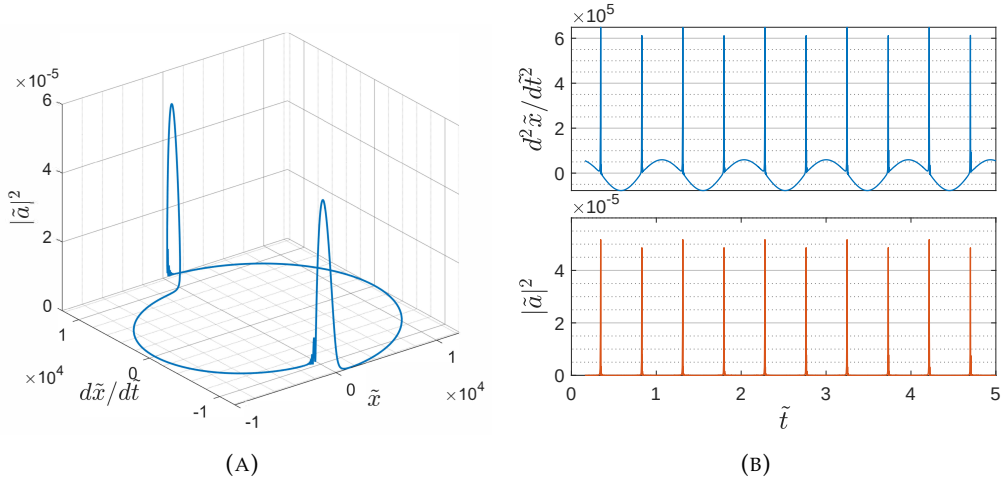


FIGURE 3.10: (A) Three dimensional phase space trajectory showing the phonon cavity number-displacement-velocity variation. (B) The time-domain variation of acceleration (top) and the cavity photon number (bottom). Note the simulation results are for an deeply unresolved sideband optomechanical system with $\tilde{\kappa} = 100$, $\widetilde{\Gamma_m} = 0.01$, $\widetilde{\Delta} = 20$, $\tilde{P} = 4e7$.

## 3.3 Optomechanical OPT generation for OTDR

It was shown in Figure 3.10 that a series of peaks in cavity photon number $|\tilde{a}|^2$ appear when the oscillation amplitude of OMO is large enough to produce the mushroom-like phase trajectory, these peaks can thus be potentially used for generating OPT for OTDR applications. Here, a comprehensive analysis of OMO-based OPT generation are conducted and clear applications for OTDR are shown.

### 3.3.1 OPT generation in different regimes

The cavity output field for different sideband regimes are studied by numerically solving the coupled equations Equation 3.11 and Equation 3.12 with the explicit Runge-Kutta method based on Dormand-Prince pair [112] and monitoring the cavity output field according to Equation 3.3.

As shown in Figure 3.11, the normalised output optical photon flux $|\widetilde{a_{out}}|^2 = \kappa_{ex}|\widetilde{a}|^2/2$ with time $\tilde{t}/2\pi$ are plotted under different values of $\tilde{\kappa}$, namely $\tilde{\kappa} = 0.1$, $\tilde{\kappa} = 0.5$, $\tilde{\kappa} = 2$, $\tilde{\kappa} = 10$, respectively. Other system dimensionless parameters are kept as constant: $\widetilde{\Gamma_m} = 1/1000$, $\tilde{\Delta} = 1$, $\tilde{P} = 100$. The integrating time is set to be long enough to reach the OMO steady-state. It can be found that the continuous wave input light is modulated to optical pulse and the output field are directly proportional to the intracavity field. This is because the two-sided coupling case as shown in Figure 3.1 is considered here where the non-input side is used as the output channel, such that the background continuous wave light is suppressed and the output field is related to the intracavity field.

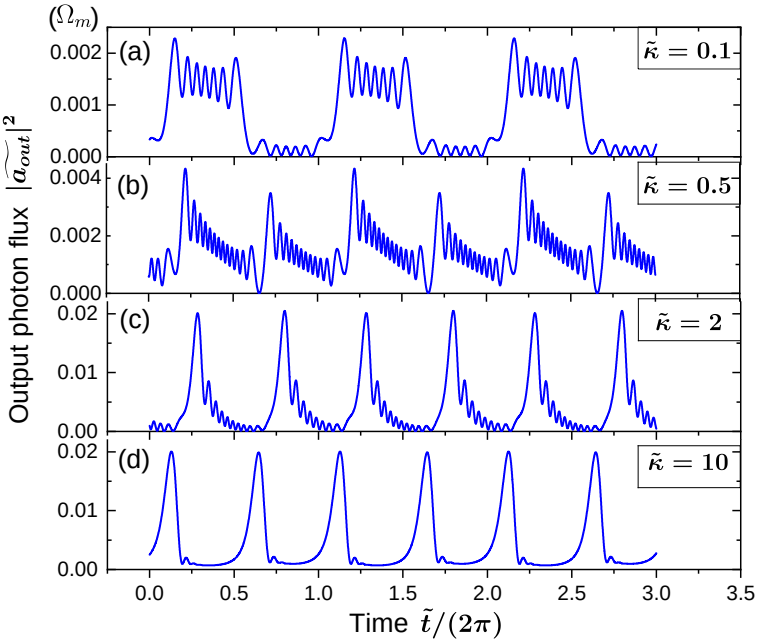


FIGURE 3.11: (a-d) OPT generation with normalised optical cavity decay rates $\tilde{\kappa} = 0.1,\ 0.5,\ 2,\ 10$, respectively. Other parameters are kept as constant: $\widetilde{\Gamma_m} = 1/1000$, $\tilde{\Delta} = 1$, $\tilde{P} = 100$.

It can be found that for all the cases, the mechanical frequency $\Omega_m$ determines the repetition rate of the OPT, with two optical pulses generated during one mechanical oscillation period. On the other hand, $\Omega_m$ also significantly affects the normalised input laser power $\tilde{P}$ as derived in Equation 3.13, which means an optomechanical system with a large mechanical frequency $\Omega_m$ requires a higher real input power $P_{in}$ to obtain the same optical pulse shape.

In terms of the pulse shape, the OPT generated in the RSR have many ripples (Figure 3.11 (a, b)), which is not desired for practical applications. This kind of shape has been experimentally observed in [119] and was attributed to being caused by the interference between the stationary pump light and the light emitted from the cavity upon discharging. Actually, in the RSR, the photon lifetime $\tau = 1/\kappa$ of the optical cavity is much longer than the mechanical oscillation period $1/\Omega_m$. Therefore, the optical cavity can not respond instantaneously to the fast mechanical oscillation, and there is always a delay between them. This leads to a complicated interference between the decaying cavity field and the input field and results in ripples in the output field.

With the increase of $\tilde{\kappa}$, the ripples gradually disappear (Figure 3.11 (c, d)), and short and smooth OPT can be obtained with the repetition rate at around $2\Omega_m$ in the deeply USR ($\tilde{\kappa} \gg 1$). The reason for the short and smooth shape has been given when explaining the mushroom-like phase trajectory for large-amplitude oscillation in the unsolved sideband regime in the last section. Even the optical cavity can build up, and decay very fast compared to the mechanical oscillation, there is still a decay cavity field that can interfere with the input field, which results in fast oscillation at the tail of each peak.

With the further increase of $\tilde{\kappa}$, this oscillation will become weaker and nearly invisible. By this means, the sharp optical pulses shape are generated, and the OMO continues. Therefore, the following analysis will be focused on the OPT analysis in the USR.

To evaluate the OMO-based OPT generator and provide guidance for the application design, the simulated extinction ratio (ER) and duty cycle (DC) of the generated OPT are plotted under different system parameters in Figure 3.12. Normalised input power $\tilde{P}$ with a value from $10^{-1}$ to $10^{4}$, normalised mechanical damping rate $\widetilde{\Gamma_m}$ from $10^{-6}$ to $10^{-2}$ are simulated for an optomechanical system with $\tilde{\kappa} = 10,\ 40,\ 100$ respectively. The laser detuning $\widetilde{\Delta}$ is set to an optimised value associated with a minimum threshold power (see Section 3.1.3.2). Figure 3.12 thus shows explicitly the characteristics of the generated OPT. Larger ER and smaller DC represent a sharper and shorter optical pulse shape.

It is clear that the ER increases linearly with input power $\tilde{P}$ in the logarithm plot scale, while the DC decreases with $\tilde{P}$. This means a higher input power is needed to produce a sharper and shorter optical pulse shape. When comparing the parallel lines with different colours representing different $\widetilde{\Gamma_m}$, it is clear that smaller $\widetilde{\Gamma_m}$ (larger mechanical Q-factor $Q_m$) leads to larger ER and smaller DC. Quantitatively, ER increases by 3dB when $\widetilde{\Gamma_m}$ decreases by one order of magnitude. The discrepancies for large value of $\tilde{P}$ are caused by the insufficient simulation time due to the limited computational resources when solving the differential equations. From the figures with varying $\tilde{\kappa}$, even though larger $\tilde{\kappa}$ leads to better pulse shape with suppressed ripples, it decreases ER when other parameters remain the same. This is because larger $\tilde{\kappa}$ represents lower optical Q-factor, lower cavity enhancement and weaker field amplitude, which will decrease the OMO amplitude and ER.

### 3.3.2 OMO-Based OPT generation for OTDR

Here, a design example is demonstrated to realise an OMO-based OPT generator for a DFOS application – OTDR. In the OTDR application, OPT is sent to the fibre and the backscattered optical signal is measured to sense the measurands along the fibre distributedly.

#### 3.3.2.1 Time-Frequency (T-F) localisation

As been introduced in Section 2, the measurand resolution and spatial resolution are correlated to each other, and there is a trade-off between them. The single optical pulse must be evaluated cooperatively in both the time (T)–domain and frequency (F)–domain.

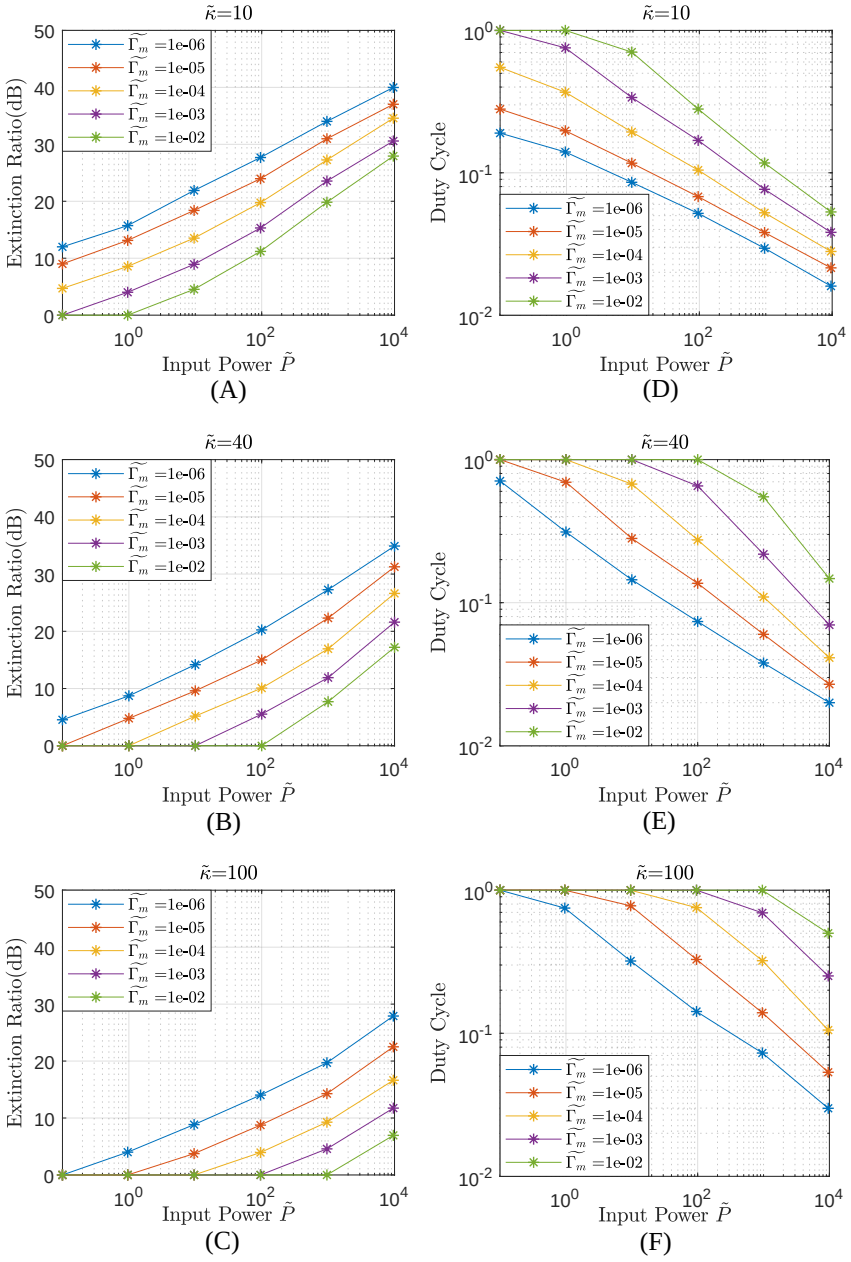


FIGURE 3.12: The characteristics of the generated OPT under different parameters. (A, B, C) The ER variation with $\tilde{P}$ and $\widetilde{\Gamma_m}$ when $\tilde{\kappa} = 10$, $\tilde{\kappa} = 40$, $\tilde{\kappa} = 100$, respectively. (D, E, F) The DC variation with $\tilde{P}$ and $\widetilde{\Gamma_m}$ when $\tilde{\kappa} = 10$, $\tilde{\kappa} = 40$, $\tilde{\kappa} = 100$, respectively. The laser detuning $\tilde{\Delta}$ is set to a constant at the optimal value associated with a minimum threshold power.

Here, the optical pulse generated in the OMO-based OPT generator is compared with Rectangular, Gaussian and Lorentzian pulse shape to evaluate their T-F localisation. The pulses all have 50 ns FWHM and 1 $\mu$s period, and the OMO-based optical pulse is generated with an optomechanical system with $\tilde{\kappa}$=100. The T–domain and F–domain of the pulses were plotted in Figure 3.13. The T–domain and F–domain variances obtained by Equation 2.28 and Equation 2.29 for the four pulse shapes and their product are given in Table 3.2.

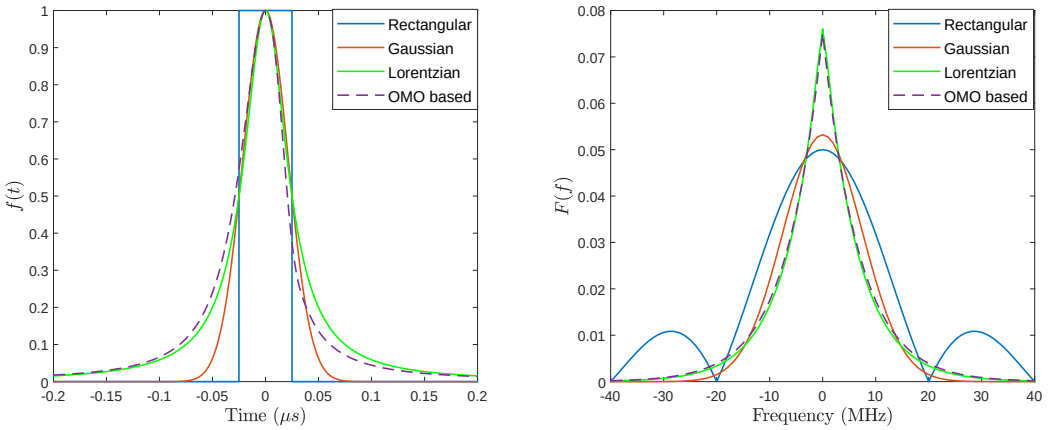


(A) (B)

FIGURE 3.13: Comparison between OMO based optical pulse and the traditional optical pulse (A) in time-domain. (B) in frequency-domain. The pulses all have 50 ns FWHM and 1$\mu$s period. The OMO based optical pulse is generated in an optomechanical system with $\tilde{\kappa} = 100$.

TABLE 3.2: Variance in the time-domain and frequency-domain with the product of the two variances for different optical pulse shapes

| | Rectangular | Gaussian | Lorentzian | OMO based |
|---|---|---|---|---|
| $\Delta T$ | 3.23e-12 | 2.91e-12 | 4.79e-12 | 4.86e-12 |
| $\Delta F$ | 8.38e+10 | 1.03e+9 | 8.92e+8 | 9.48e+8 |
| $\Delta T \times \Delta F$ | 0.2706 | 0.003 | 0.0043 | 0.0046 |

In terms of T-F localisation, the OMO based optical pulse is close to Lorentzian and Gaussian shapes, which are much better than the widely used Rectangular shape in DFOS. The OMO-based OPT generator is also much more straightforward than the traditional OPT generator used in DFOS, which usually requires function generators, EOM or AOM.

#### 3.3.2.2 OMO-based OPT generation examples for OTDR

As shown in Figure 3.14, an example of a real OMO-based OPT generator for the OTDR applications is here considered, including BOTDR, Phi-OTDR, POTDR.

The function generator and EOM which are used to generate the OPT in traditional OTDR can be replaced by the proposed OMO-based OPT generator. The OMO-based OPT generator example shown here is formed by suspending part of a racetrack-shaped optical microresonator, where the suspended beam serves as the mechanical resonator and is coupled to the optical cavity. The fundamental out-of-plane mechanical vibrating mode can alter the effective index of the suspended waveguide, and can thus change the optical cavity resonance frequency and realise optomechanical coupling. This kind of structure had been experimentally demonstrated to exhibit large-amplitude optomechanical oscillation [51]. It should be noted that only the out-of-plane vertical

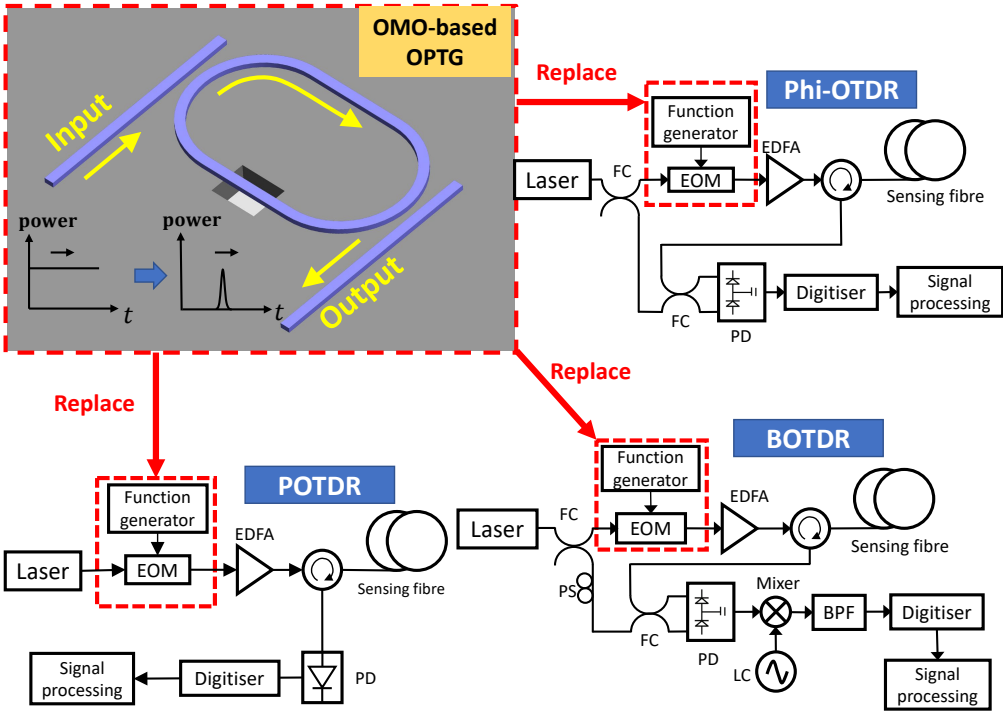


FIGURE 3.14: The upper-left box shows the schematic of an OMO-based OPT generator. It is formed by suspending part of a racetrack-shaped microresonator on an SOI substrate, where the mechanical resonator (suspended beam) is coupled to the optical cavity. The other three boxes show the classical OPT generators utilized in three types of DFOS (BOTDR, Phi-OTDR, and POTDR), which use a function generator and an EOM to generate OPT. These traditional OPT generators can be replaced by the OMO-based OPT generator. EOM: Electro-optic modulator, FC: Fibre coupler, PS: Polarisation scrambler, PD: Photodetector, LC: Local oscillator, BPF: Bandpass filter.

oscillation of the suspended beam are considered. This is mainly because the optical gradient force are generated between the beam and the substrate underneath, which drives the suspended beam vertically. In addition, the out-of-plane mechanical motion has the largest impact on the effective index of the suspended waveguide and can thus realise efficient optomechanical coupling. This kind of cavity optomechanical system in the form of racetrack-shaped optical microresonator is just one option of the various kinds cavity optomechanical system shown in Section 2.1.4.

As been analysed in Section 2, different optical pulse characteristics can get different OTDR measurement specifications. The repetition rate sets a limit on the maximum sensing distance, while ER and DC decide the measurand resolution and spatial resolution. For the OMO-based OPT generator, different optomechanical parameters can generate OPT with different repetition rate, ER and DC, and can fit the various OTDR system requirements. The OMO-based OPT generator based on SOI substrates with top silicon layer of four different thickness are considered, namely 110 $nm$, 220 $nm$, 500 $nm$, 1.5 $\mu m$, and their application in OTDR are explored. During the design of the cavity optomechanical system shown in Figure 3.14, the thickness of the beam $h$ and

the length of the beam $L$ are the two critical parameters. The value of $L/h$ was set to be 200 for all the four cases. The lengths of the beams are thus 22 $\mu m$, 44 $\mu m$, 100 $\mu m$ and 300 $\mu m$, respectively. To maintain the single-mode condition as will be introduced in Chapter 5, the width of the suspended beams are set to be 0.5 $\mu m$, 0.5 $\mu m$, 0.5 $\mu m$ and 1.1 $\mu m$, respectively. Note for the beam with thickness of 500 $nm$ and 1.5 $\mu m$, a rib-to-strip mode converter [120] is needed to realise the suspension and keep a low cavity loss.

TABLE 3.3: Four sets of optomechanical parameters of the OMO-based OPT generator for an OTDR application

| | Case 1 | Case 2 | Case 3 | Case 4 |
|---|---|---|---|---|
| Beam thickness ($\mu m$) | 0.11 | 0.22 | 0.5 | 1.5 |
| Beam length ($\mu m$) | 22 | 44 | 100 | 300 |
| Beam width ($\mu m$) | 0.5 | 0.5 | 0.5 | 1.1 |
| Mechanical frequency $\Omega_m$ ($Hz$) | 2.02e6 | 1.01e6 | 4.41e5 | 1.47e5 |
| Effective mass $m_{eff}$ ($pg$) | 1.2 | 4.4 | 23.0 | 457.2 |
| Mechanical Q-factor | 1000 | | | |
| Coupling coefficient $G$ ($Hz/nm$) | 1e8 | | | |
| Laser wavelength $\lambda_L$ ($nm$) | 1550 | | | |
| Optical cavity linewidth $\kappa$ ($Hz$) | 2.02e8 | 1.01e8 | 4.41e7 | 1.47e7 |
| Optical Q-factor | 9.58e5 | 1.92e6 | 4.39e6 | 1.32e7 |
| Input laser power $P_{in}$ ($W$) | 0.1 | | | |
| Normalised input laser power $\tilde{P}$ | 2.09e6 | 9.10e6 | 4.79e7 | 1.95e8 |

The four sets of optomechanical parameters are listed in Table 3.3. The fundamental out-of-plane mechanical resonant frequency $\Omega_m$ and effective mass $m_{eff}$ are obtained through the Finite Element Analysis (FEA) software COMSOL Multiphysic. The mechanical Q-factor was set to be 1000 for all the cases, corresponding to normalised mechanical damping rate $\widetilde{\Gamma_m} = 0.001$. The optomechanical coupling coefficient $G$ is set to be 0.1 $GHz/nm$, which can be easily achieved according to the results in [51] where $G = 1$ $GHz/nm$ was realised for the same structure. Input laser wavelength is set to be 1550 $nm$, which is most widely used in silicon photonics. The normalised optical damping rate $\tilde{\kappa} = 100$ is assumed for all the case, through which the optical cavity linewidth $\kappa$ and optical Q-factor can be obtained as shown in the table. This assumption also agrees with the truth that waveguide with larger cross-section has lower propagation loss, which will be shown in Chapter 5. The input laser power $P_{in}$ is assumed to be 100 $mW$ for all the case. According to Equation 3.13 which relates the normalised dimensionless input power $\tilde{P}$ to the real system parameters, the normalised dimensionless input power $\tilde{P}$ are thus found to be 2.09$e$6, 9.10$e$6, 4.79$e$7, 1.95$e$8, respectively.

By fitting these data to the Figure 3.12 (C, F), the DCs of the generated OPT are found to be 0.024, 0.013, 0.006, 0.003, respectively, and the ERs of the generated OPT are found to be 28.3 $dB$, 32.9 $dB$, 38.1 $dB$, 42.4 $dB$, respectively. The repetition rate and the pulse width can thus be obtained based on the mechanical resonant frequency and DC. The

corresponding sensing distance and spatial resolution can be obtained using the Equation 2.26 and Equation 2.27. The detail characteristics of the generated OPT and the OTDR measurement specification are listed in Table 3.4

TABLE 3.4: The characteristics of the generated OPT and corresponding OTDR measurement specifications for the four sets of optomechanical parameters

| | Case 1 | Case 2 | Case 3 | Case 4 |
|---|---|---|---|---|
| Duty cycle | 0.024 | 0.013 | 0.006 | 0.003 |
| Extinction ratio ($dB$) | 28.3 | 32.9 | 38.1 | 42.4 |
| Repetition rate ($Hz$) | 4.04e6 | 2.02e6 | 8.82e5 | 2.94e5 |
| Pulse period ($\mu s$) | 0.2475 | 0.4950 | 1.1338 | 3.4014 |
| Pulse width ($ns$) | 5.9 | 6.4 | 6.8 | 10.2 |
| Sensing distance ($m$) | 25.3 | 50.5 | 115.7 | 347.1 |
| Spatial resolution ($m$) | 0.60 | 0.65 | 0.69 | 1.05 |

From Table 3.3 and Table 3.4, the OTDR sensing distance can reach 347.1 $m$ in the 1.5 $\mu m$ SOI platform, and spatial resolution can reach 0.6 $m$ for the 110 $nm$ SOI platform. The ER can be as high as 42.4 $dB$. It can also be found that the thicker SOI platform is preferred for longer distance OTDR measurement, with 347.1 $m$ achieved in the 1.5 $\mu m$ SOI platform while only 25.3 $m$ can be achieved for 110 $nm$ SOI platform. The sensing distance can be further enhanced to several thousands of meters by decreasing the mechanical resonant frequency, which can be realised by using thicker SOI substrate or by increasing the beam length. The ER and DC can also be further enhanced by increasing the input laser power or the optomechanical coupling coefficient.

As a summary, here, I have demonstrated numerically that the OMO-based OPT generator can fulfil the pulse generation requirement of an OTDR. The OPT is analysed in both time and frequency domain, and it was found that the OMO-based OPT shape is close to Lorentzian and Gaussian shapes, which are much better than the widely used Rectangular shape in OTDR. Four cavity optomechanical examples of OMO-based OPT generator for OTDR were also demonstrated. The results shows that the OTDR measurement requirement can be fulfilled with reasonable and feasible optomechanical parameters. It was also found thicker SOI substrate is better for long-distance OTDR measurement.

## 3.4 Optomechanical SWOS generation for OFDR

The OMO process introduced above can modulate the optical cavity resonance frequency, which provides a mechanism for frequency modulation. In this section, I explore the potential of using the OMO process to generate a sweeping-wavelength optical signal (SWOS) for the OFDR application.

### 3.4.1 SWOS generation theory

The proposed scheme to get such a SWOS generator is shown in Figure 3.15. It can be based on the same cavity optomechanical device that has been introduced to realise OMO-based OPT generator in the last section. In this scheme, two laser sources, in which one is single-wavelength and another is broadband, are injected into the optomechanical system through the two ends. During the experiment, two optical isolators should be placed at the output of the two laser sources (port 1 and port 3) to isolate the laser transmitted back from the multimode interferometer (MMI).

It has been shown in the above analysis that a single-wavelength laser with a proper laser detuning and a larger-than-threshold optical power can lead to the OMO process, where the mechanical resonator is driven into oscillation. This optomechanical oscillation, in turn, changes the optical cavity resonant frequency and generate the OPT (port 4).

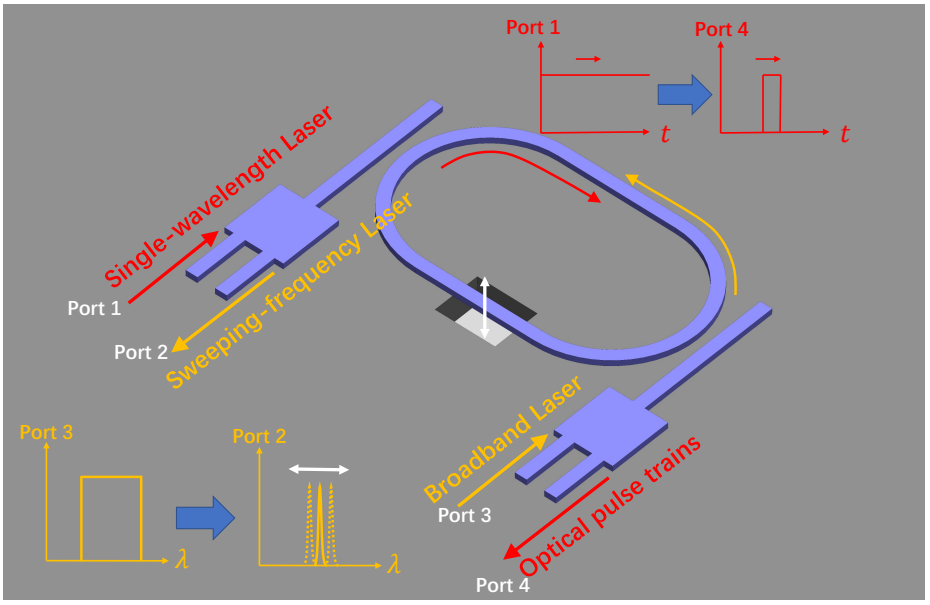


FIGURE 3.15: The schematic diagram of generating SWOS with the OMO process in a cavity optomechanical system. Two laser sources, with one being single-wavelength and another being broadband, are injected into the optomechanical system through the two ends. The single-wavelength laser with proper laser detuning and optical power can drive the mechanical resonator into oscillation. This oscillation, in turn, changes the optical cavity resonance frequency. Another broadband laser passing through the optical cavity is filtered into a single-wavelength laser source, whose frequency is modulated by the OMO process. The linewidth of the broadband laser source is chosen to be smaller than the FSR of the optical microcavity. During the experiment, two optical isolators should be put on the output of the two laser sources (port 1 and port 3) to isolate the laser transmitted back from the multimode interferometer (MMI).

The linewidth of the broadband laser source is chosen to be smaller than the FSR of the optical microcavity so that the broadband laser injected into the optomechanical

system passes through the optical cavity and is filtered into a single-wavelength laser (port 2) whose linewidth equals the decay rate $\kappa$ of the optical resonator. For instance, an easily available commercial broadband laser with 1 $nm$ linewidth can be chosen for an optical microresonator with 2 $nm$ FSR. Due to the optomechanical modulation on the optical resonant frequencies, the frequencies of the generated single-wavelength laser is modulated by the OMO process. Thus, a SWOS is realised. Note that the broadband laser is chosen to have a low power which does not affect the OMO process and the wavelength range is different from the wavelength of the single-wavelength laser to avoid interference between them.

The frequency of the generated optical source is chirped along with the mechanical oscillation. In the RSR ($\kappa < \Omega_m$), the optical cavity field can not respond fast enough to the mechanical motion, and the resulting interference between the input broadband light and the cavity field would result in a distorted-shape output field. In addition, with the increase of the oscillation amplitude, the OMO evolves into chaos and thus modulates the cavity resonance frequency randomly and arbitrarily, which is not desired. In the deeply USR ($\kappa \gg \Omega_m$), that the optical cavity responds fast enough to the mechanical motion, and the mechanical oscillation can be simultaneously imprinted into the frequency-chirping of the output field. Even though the OMO process develops from a harmonic motion into a mushroom-like phase trajectory (Figure 3.9) representing two oscillation amplitudes per period, this modulation is controllable and predictable. Therefore, the deeply USR should be used for OMO-based SWOS generation. In this regime, the generated optical pulse trains are also short and smooth.

### 3.4.2 OMO-based SWOS generation for OFDR

I now consider the OMO-based SWOS application in the OFDR, which is shown in Figure 3.16. The proposed OMO-based SWOS generator can replace the various traditional SWOS generator reviewed in Section 2.4.3. In the meantime, the simultaneously generated OPT can be used as a trigger signal to synchronise the sweeping system and signal processing system.

For the OFDR application, the main related parameters of the generated SWOS are the frequency-sweeping range $\Delta F$. The frequency-sweeping range $\Delta F = GA$ is linearly proportional to the dimensionless oscillation amplitude through the relation $\widetilde{A} = GA/\Omega_m$, where $G$ is the optomechanical coupling coefficient, $A$ is the real oscillation amplitude, $\Omega_m$ is the mechanical resonant frequency. Therefore, the frequency-sweeping range under different system parameters can be obtained by calculating $\Delta F = \Omega_m \widetilde{A}$. Note that for the mushroom-like OMO with two different amplitudes $A_1$ and $A_2$, the real amplitude is obtained by $A = (A_1 + A_2)/2$. The simulated normalised dimensionless oscillation amplitude $\tilde{A}$ variation with $\tilde{P}$ and $\widetilde{\Gamma_m}$ when $\tilde{\kappa} = 10,\ 40,\ 100,$

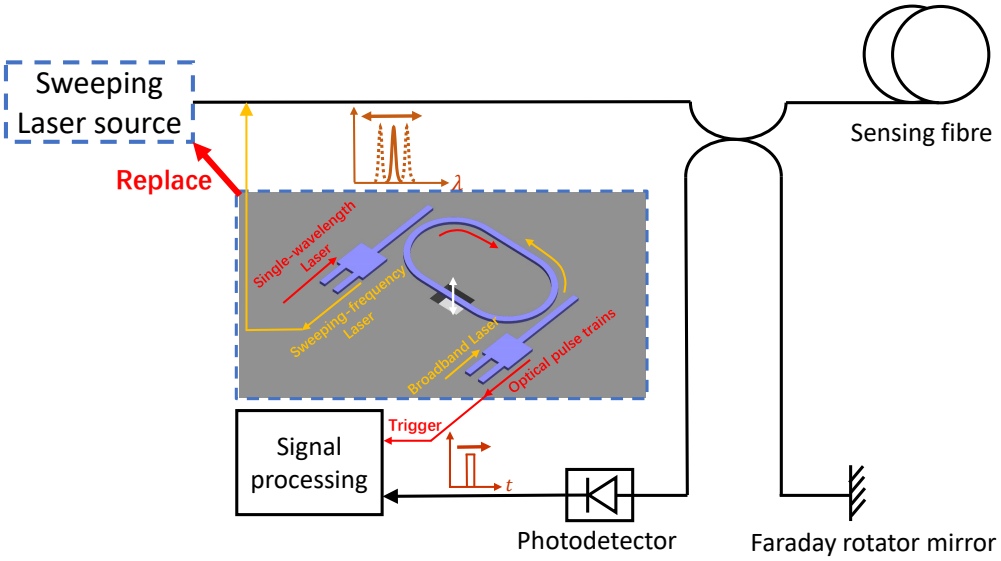


FIGURE 3.16: The schematic diagram of using the OMO-based SWOS in an OFDR application. The proposed OMO-based SWOS can replace the traditional sweeping-frequency sources, and the generated optical pulse trains can be used as a trigger signal to synchronise the sweeping system and signal processing system. Also, two optical isolators should be put on the output of the two laser sources to isolate the laser transmitted back from the multimode interferometer (MMI).

respectively, are shown in Figure 3.17. It is shown that the oscillation amplitude $\widetilde{A}$ increases linearly with the input power in the logarithmic scale plot, and one order of magnitude decreases in $\widetilde{\Gamma_m}$ leads to an $3dB$ increase of $\widetilde{A}$. A larger value of $\tilde{\kappa}$ leads to a fast response of the optical cavity, while at the same time it decreases the oscillation amplitude $\widetilde{A}$.

Here, the potential of generating OMO-based SWOS in an optomechanical system is explored with the same optomechanical parameters of the Case 4 shown in Table 3.3. As illustrated in Section 3.3, such an optomechanical system can generate OPT with pulse width at 10.2 $ns$, DC at 0.003, ER at 42.4 $dB$, which can be used for OTDR application with 347.1 $m$ sensing range and 1.05 $m$ spatial resolution. The main parameters are $\Omega_m/2\pi = 147\ kHz$, $\tilde{\kappa} = 100$, $\widetilde{\Gamma_m} = 1e-3$, $\tilde{P} = 1.95e8$. When looking at Figure 3.17 (C), it can be inferred that such a set of optomechanical parameters would lead to OMO with a normalised oscillation amplitude $\widetilde{A}$ being at high as around $2.68 \times 10^4$. The resulting optical cavity resonant frequency shift is $\Delta F = \widetilde{A}\Omega_m = 3.9\ GHz$. The theoretical spatial resolution can thus be obtained as,

$$\delta z = \frac{c}{2n_g \cdot \Delta F} = \frac{3e8}{2 \times 1.47 \times 3.9e9}\ m = 2.62 \times 10^{-2}\ m, \tag{3.41}$$

where the group index $n_g = 1.47$ of the SM-28 fibre at 1550 $nm$ has been used. The sensing distance is the same as in the OTDR application, which is 347.1 $m$. The laser linewidth $f_w$ equals the optical damping rate: $f_w = \kappa = 1.47e7\ Hz$. The coherent length

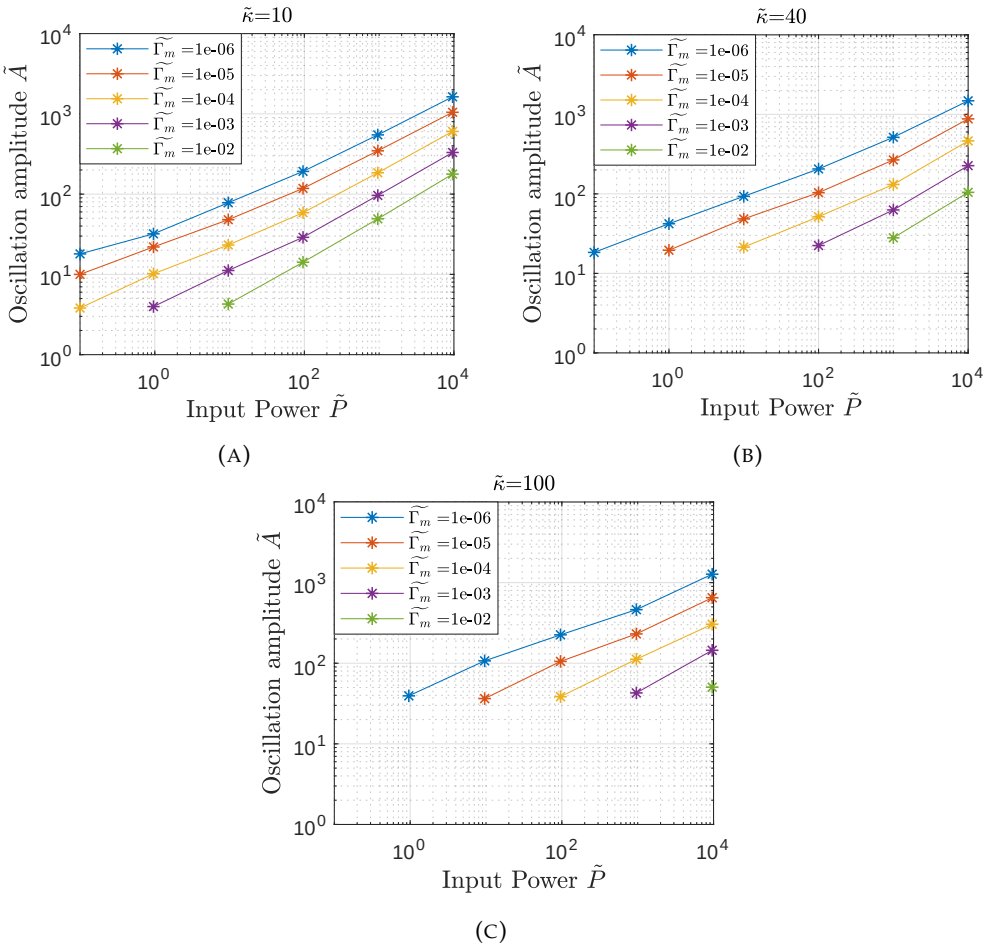


FIGURE 3.17: (A, B, C) The simulated mechanical oscillation amplitude $\widetilde{A}$ variation with $\tilde{P}$ and $\widetilde{\Gamma_m}$ when $\tilde{\kappa} = 10,\ 40,\ 100$, respectively. The laser detuning $\tilde{\Delta}$ is set to a constant at the optimal value associated with a minimum threshold power. The frequency-sweeping range depends on both the mechanical frequency and the mechanical resonant frequency, which can be expressed as $\Delta F = \widetilde{A}\Omega_m$.

of this laser source is thus given as,

$$L_c = \frac{c}{\pi f_w} = 6.5\ m, \tag{3.42}$$

Although this coherent length is quite limited, the long-distance of OFDR sensing beyond the coherence length has been investigated by using phase noise compensation [121, 88] or phase term analysis [122]. Also, it should be noted that the spatial resolution can be further enhanced by increasing the oscillation amplitude. For example, in [51], the authors demonstrated an oscillation amplitude greater than 300 $nm$ in an optomechanical system with $G = 1\ GHz/nm$, which corresponds to a sweeping range of 300 $GHz$ and spatial resolution of around 10 $\mu m$. The laser coherent length can be increased by a larger optical Q-factor. For instance, in [56], an optical Q-factor of 875 million can be obtained in a wedge-resonator, through which a laser coherent length of

431 $m$ can be obtained. However, in such a high-Q optical cavity, an extremely low mechanical resonance frequency is required to achieve the USR. The spatial resolution and laser coherent length of the OFDR measurement using the OMO-based SWOS with the optomechanical parameters in Case 4 in Table 3.3 and these two ideal cases are shown in Table 3.5.

TABLE 3.5: The spatial resolution and laser coherent length of the OFDR measurement using the OMO-based SWOS with the optomechanical parameters in Case 4 in Table 3.3 and other two ideal cases.

| | Case 4 | Ideal case |
|---|---|---|
| Spatial resolution (m) | 2.62e-2 | 1e-5 [51] |
| Laser coherent length (m) | 6.5 | 431 [56] |

In a traditional OFDR, the laser frequency is linearly chirped during the measurement so that the beat frequency is also linearly proportional to the position where the scattering takes place. In this proposed OMO-based SWOS generator, however, the laser frequency is swept by the OMO process, who develops from a harmonic motion into a mushroom-like phase trajectory representing two oscillation amplitudes per period with the increase of oscillation amplitude. The frequency-sweeping is not linear, therefore the position can not be mapped to the beat frequency linearly. To solve this issue, the generated OPT can be used as the synchronisation signal. The signal processing system can then add a window on the generated SWOS and use only a segment of that signal as having been implemented in [96]. Also, the nonlinear sweeping pattern can be processed by the signal processing algorithm to locate the precise position corresponding to the beating frequency [97].

As a summary, here, the OMO process is used to generate SWOS. A single-wavelength laser with proper detuning and enough power is used to drive the mechanical resonator to oscillation, and another broadband laser is filtered by the optical cavity whose resonance frequency is modulated by the OMO. The output of the broadband laser can thus be used as a SWOS. The unresolved-sideband regime should be used for the fast optical cavity response. An example of using this OMO-based SWOS for the OFDR application was demonstrated, and a theoretical spatial resolution $2.62 \times 10^{-2}$ $m$ and laser coherent length 6.5 $m$ can be obtained. Using the previously demonstrated examples where oscillation amplitude is large enough [51] or optical Q-factor is larger enough [56], spatial resolution as low as $1 \times 10^{-5}$ $m$ and laser coherent length as long as 431 $m$ could be obtained.

## 3.5 Conclusion and discussion

In this chapter, a novel solution of using the integrated optomechanical system to address the issues with the optical probe signal generation in the traditional DFOS system

has been explored. I first discussed the need for an integrated optical source in DFOS systems, followed by a comprehensive analysis of the cavity optomechanical coupling process regarding the OMO threshold and the OMO characteristic in different sideband regimes. The OMO displays harmonic motion when the oscillation amplitude is small. It then evolves into chaos in RSR and into a mushroom-like phase trajectory in USR. Lastly, it was shown that this OMO can be utilised to generate OPT that can be used for OTDR applications and SWOS that can be used for OFDR applications. Clear examples and the performance parameters are demonstrated.

During the design of the OMO-based OPT generator and SWOS generator, the trade-offs need to be considered. The first parameters that need to be decided is the mechanical resonant frequency $\Omega_m$, which determines the DFOS sensing distance. For the widely used SOI substrates with top silicon layer in several hundred manometers, fabricating mechanical resonators with $\Omega_m$ lower than $\sim MHz$ is challenging due to the large Young modulus and small effective mass [45]. These physical properties of traditional silicon photonics limit the period of the generated OPT and SWOS to be lower than $\mu s$, corresponding to a sensing distance of less than several hundred metres. Therefore, a thick SOI substrate is preferred. Thick SOI can also handle high optical power, which is necessary for increasing the mechanical oscillation amplitude, ER and frequency-sweeping range.

On the other hand, $\Omega_m$ also significantly affects the dimensionless normalised input laser power as derived in Equation 3.13, with a larger value of $\Omega_m$ leading to lower dimensionless $\tilde{P}$, which means a larger real input power $P_{in}$, optomechanical coupling coefficient $G$ or lower effective mass $m_{eff}$ is needed to obtain the same ER, DC or $\tilde{A}$. When the mechanical resonance frequency $\Omega_m$ is determined, a suitable optical cavity decay rate $\kappa$ should be chosen. A large value of $\kappa$ (approaching the USR) results in a sharper optical pulse and less delay between the mechanical motion and the optical cavity field; however, it leads to smaller ER, DC and oscillation amplitude $\tilde{A}$ under the same input power. This will cause low spatial resolution for both the OTDR and OFDR. In addition, a large $\kappa$ causes a broadened linewidth for the sweeping-frequency laser and thus a reduced coherent length, which also shortens the sensing distance.

Although the cavity optomechanical system parameters design are not independent of each other, and a lot of trade-offs and physical limitations as discussed above need to be considered, the proposed OMO-based OPT generator and OMO-Based SWOS generator will still potentially play an important role for short-distance DFOS applications. The proposed OMO-based OPT generator and OMO-Based SWOS generator do not rely on an external RF source, optical modulators for modulation and are fully integrated with silicon photonics platform; they thus provide unconventional and previously unattainable control of light to reshape the optical source generation in DFOS and result in an exceptional simplicity, size reduction that is hard to achieve in conventional solutions. In the long run, a fully on-chip optical probe signal generation can

be achieved by integrating the laser source on the chip using a heterogeneous integration method involving the III-V material, which will provide an important milestone on the path towards high-performance, affordable, and fully integrated dynamic DFOS system.

# Chapter 4

# Silicon optomechanics for on-chip optical trapping

On-chip optical trapping, which utilises the optical force to trap and manipulate objects on-chip, has potential applications in biological manipulation, Raman spectroscopy, and integrated quantum optomechanics. Among the various optical trapping schemes, on-chip dual-waveguide traps combine the benefits of stable trapping and mass production. Various dual-waveguide optical trappings have been reviewed in Chapter 2. Although many works have been conducted on the dual-waveguide trapping about the effect of particle size and gap distance on optical trapping capability, no systematic analysis have been done about the influence of the waveguide geometric size which obviously acts as an important parameters. There is thus a clear incentive to fill this gap by systematically investigating the effect of waveguide geometry on trapping capability, particularly the waveguide thickness under the single-mode condition. This is critical for maximising the optical trapping capability.

In this chapter, comprehensive studies on the SOI-based on-chip dual-waveguide trapping were conducted. The optical trapping capability of the SOI-based dual-waveguide structure was first demonstrated using the Lumerical FDTD Solution [123]. Then, the dual-waveguide optical trapping scheme is optimised, and scaling effects are shown. Lastly, the potential of using the OMO process as a method to separate and load micro/nano particles was explored.

## 4.1 Optical Trapping Force

The interaction between particles and the optical field generates an optical force that traps the particles, but the way this interaction can be described and analysed depends on the size of the particle and the wavelength of light.

When the size of a particle is much larger than the wavelength of the laser, the optical forces acting on the particle can be analyzed by ray optics treatment [124]. A qualitative analysis view of the ray optics method is intuitively shown below in Figure 4.1. It is mainly based on the fact that the momentum is transferred when the light is refracted and reflected while passing through a particle. Considering the two rays $a$ and $b$ in the figure, the rays refract as they enter and leave the surface of the dielectric particle, and the direction in which the rays exit changes with respect to the direction of incidence. Due to the conservation of momentum, the corresponding optical force $F_a$ and $F_b$ are generated. It can be found that the resultant force always pushes the particle to the focus of the beam. Thus a focused laser beam can form a stable 3D optical trap. In reality, the effect of surface reflection in the particles needs to be considered, which will push the particle forward along the direction of light. If this force is larger than the trapping force generated by refraction, the particle will be pushed out of the focus.

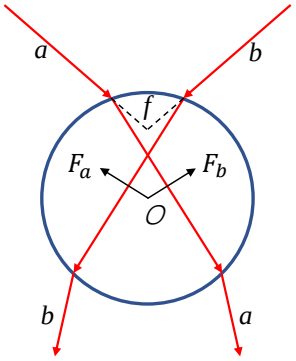


FIGURE 4.1: Qualitative analysis of optical force in Ray optics treatment

If the dimension of the particle is much smaller than the wavelength of the laser, then the light would fall into the regime of Rayleigh scattering [125]. The particle can be treated as a dipole in an inhomogeneous electromagnetic field, and the generated optical force on the dipole can be divided into two parts, gradient force and scattering force. The gradient force comes from the electrostatic interaction between the induced dipole and the electromagnetic field, and can be calculated as the sum of the Lorentz force acting on the particle, which is given by the combination of the electric and magnetic force on a point charge due to electromagnetic fields [126],

$$\mathbf{F} = \sum_i \mathbf{F}_i = \sum_i q_i(\mathbf{E}_i + \frac{d\mathbf{x}_i}{dt} \times \mathbf{B}), \tag{4.1}$$

where $\mathbf{F}$ is the Lorentz force, $q$ is the charge, $\mathbf{E}$ is the electric field intensity, $\mathbf{x}$ is the position vector of the particle, $\mathbf{B}$ is the magnetic flux density. Assume that the particle can be treated as a dipole separated by a distance $\mathbf{d} = \mathbf{x}_1 - \mathbf{x}_2$, then Lorentz force can

be written as,

$$\begin{aligned}\mathbf{F} &= q\left(\mathbf{E}_1 - \mathbf{E}_2 + \frac{d(\mathbf{x}_1 - \mathbf{x}_2)}{dt} \times \mathbf{B}\right) \\ &= q\left((\mathbf{d}\cdot\nabla)\mathbf{E} + \frac{d(\mathbf{d})}{dt} \times \mathbf{B}\right).\end{aligned} \tag{4.2}$$

The dipole momentum of the particle is given by $\mathbf{P} = q\mathbf{d} = \alpha\mathbf{E}$, where $\alpha$ is the polarizability of the particle. Substituting it into the above equation leads to the following expression,

$$\mathbf{F} = \alpha\left((\mathbf{E}\cdot\nabla)\mathbf{E} + \frac{d(\mathbf{E})}{dt} \times \mathbf{B}\right). \tag{4.3}$$

By using the following Maxwell Equation 4.4 and vector identity Equation 4.5,

$$\nabla \times \mathbf{E} = -\frac{d\mathbf{B}}{dt}, \tag{4.4}$$

$$(\mathbf{E}\cdot\nabla)\mathbf{E} = \nabla(\frac{\mathbf{E}^2}{2}) - \mathbf{E} \times (\nabla \times \mathbf{E}), \tag{4.5}$$

The results can be given by,

$$\begin{aligned}\mathbf{F} &= \alpha\left(\nabla\frac{\mathbf{E}^2}{2} - \mathbf{E} \times (\nabla \times \mathbf{E}) + \frac{d\mathbf{E}}{dt} \times \mathbf{B}\right) \\ &= \alpha\left(\nabla\frac{\mathbf{E}^2}{2} - \mathbf{E} \times (-\frac{d\mathbf{B}}{dt}) + \frac{d\mathbf{E}}{dt} \times \mathbf{B}\right) \\ &= \alpha\left(\nabla\frac{\mathbf{E}^2}{2} + \frac{d(\mathbf{E} \times \mathbf{B})}{dt}\right).\end{aligned} \tag{4.6}$$

It can be found that the second term of the above equation corresponds to the derivative of the Poynting vector, which will be zero for a stable continuous laser. Therefore, the optical force when the particle is much smaller than the laser wavelength is given by,

$$\mathbf{F}(\mathbf{r}) = \frac{\alpha}{2}\nabla|\mathbf{E}(\mathbf{r})|^2, \tag{4.7}$$

where $\mathbf{r} = (x, y, z)$ is the location of the centre of the particle, $\alpha$ is the polarisability of the induced dipole of a spherical dielectric particle given by [127],

$$\alpha = 4\pi\epsilon_2 a^3 \frac{\epsilon_1 - \epsilon_2}{\epsilon_1 + 2\epsilon_2}. \tag{4.8}$$

Here, $a$ is the radius of the spherical dielectric particle, $\epsilon_1$ and $\epsilon_2$ are the dielectric constant of the particle and the surrounding medium respectively. The relationship between electric field $\mathbf{E}$ and field intensity $I$ can be given by,

$$I(\mathbf{r}) = cn_2\epsilon_0\frac{|\mathbf{E}(\mathbf{r})|^2}{2}, \tag{4.9}$$

where $n_2$ is the refractive index of the surrounding medium, $\epsilon_0$ is the dielectric constant in the vacuum. For the dielectric material, $\epsilon_2 \approx \epsilon_0 n_2^2$. Combining the Equation 4.8 and

Equation 4.9 into the Equation 4.7 yeilds the following,

$$\mathbf{F}_{grad}(\mathbf{r}) = \frac{4\pi a^3 n_2}{c}\left(\frac{n_1^2 - n_2^2}{n_1^2 + 2n_2^2}\right)\nabla I(\mathbf{r}), \tag{4.10}$$

where $n_1$ is the refractive index of the dielectric spherical particle. From the equation above, it can be found that the gradient force on the particle is proportional to the gradient of the optical field intensity. This means that the gradient force acting on the particle always points toward the highest intensity part of the beam. If a focused laser beam is applied to a particle, then the particle will be trapped near the focus, and the gradient force acts as a restorative force that keeps the particle in the trap.

There is also a scattering radiation force acting on the particle in the propagation direction of the light beam. It originates from the radiation of secondary or scattered waves from the oscillating electric dipole in the electric field, which can be written as [125],

$$\mathbf{F}_{scat}(\mathbf{r}) = \mathbf{z}\frac{128\pi^5 a^6}{3c\lambda^4}\left(\frac{n_1^2 - n_2^2}{n_1^2 + 2n_2^2}\right)^2 n_2^5 I, \tag{4.11}$$

where $\lambda$ is the wavelength of the laser light, $\mathbf{z}$ represents the unit vector in the direction of propagation.

When looking at the optical gradient force Equation 4.10 and the optical scattering force Equation 4.11, it is interesting to note that the former scales with the particle size as $a^3$ while the latter scales faster as $a^6$. Therefore, for a certain value of particle size $a$, the scattering force will dominate. For the single beam optical trapping scheme where the scattering force is stronger than the gradient force, the particle will be pushed out of the trap. Therefore, this poses an upper limit on the particle size that a single beam optical trap can handle. For the standing wave trapping or dual-beam trapping, the scattering forces are balanced, and only the gradient forces work on the particle.

The third situation is when the particle size is comparable to the laser wavelength. In this case, neither ray optics nor Rayleigh scattering condition is met, and the generalized Lorenz-Mie theory should be used. It enables the calculation of optical forces with any laser source and particle shape, including the optical calculation in the Rayleigh regime. The theoretical derivation of the method is just too complex to be discussed here, a detailed description of this analytical method can be found in [128, 129].

## 4.2 Dual-waveguide optical trapping

In this section, the simulation setup in Lumerical FDTD solution for the dual-waveguide trapping will be introduced. Detailed introduction of FDTD method, simulation model,

field intensity distribution and the trapping capability of the dual-waveguide scheme will be given.

### 4.2.1 Finite-difference time-domain (FDTD) method

The finite-difference time-domain (FDTD) method [123] is used in this chapter to study the electromagnetic fields for the dual-waveguide optical trapping. FDTD is a method to solve Maxwell's equations in the time domain. The equations are solved numerically on a discrete grid in both space and time, and derivatives are handled with finite differences. Since it solves for all vector components of the electric and magnetic fields, it is a fully-vectorial simulation method. Due to the fact that it is a time-domain method, FDTD can usually calculate broadband frequency results with a single simulation. FDTD method has emerged as the primary and effective simulation method for electromagnetic wave interaction with material structures, especially in the wave optics regime where the feature size is on the order of the wavelength and diffraction, interference, coherence and other similar effects play a critical role.

This research aims at the simulation of the interaction of light emitted from the integrated waveguide and nano-size dielectric particles, which exactly falls into the scope of the FDTD method.

### 4.2.2 Dual-waveguide configuration

The dual-waveguide optical trapping model used for the simulation in Lumerical's FDTD solutions is shown below in Figure 4.2. Two identical rib waveguides with width $w$ and thickness $t$ made from an SOI substrate are separated by an intentionally designed gap with distance $L$. Compared to the TripleX and $Ti_2O_5$ platforms that have been used in previous dual-waveguide traps [74, 80], the SOI substrate shows more advantages because it is commercially available at low cost and is CMOS compatible. In addition, the state-of-the-art silicon photonics technologies facilitate the integration of electronics, optics, and mechanics on the same wafer, in the same fabrication facility.

In the simulation, two in-phase mode sources, with the same power of 50 $mW$ each, are placed at 0.5 $\mu m$ from the end facet of the waveguides with opposite injection directions. The fundamental transverse electric (TE) mode shown in Figure 4.3 is excited in each source. The material of the guided layer and bottom cladding layer are set to be Silicon and $SiO_2$, respectively. Before running the simulation, the refractive index is fitted according to the material library of the Lumerical software. The background index of the model is set to be 1, which corresponds to the air or vacuum environment. A rib geometry is chosen because it can maintain the single-mode condition even in thick waveguides. The etching ratio, defined as the ratio of the etched thickness to the overall

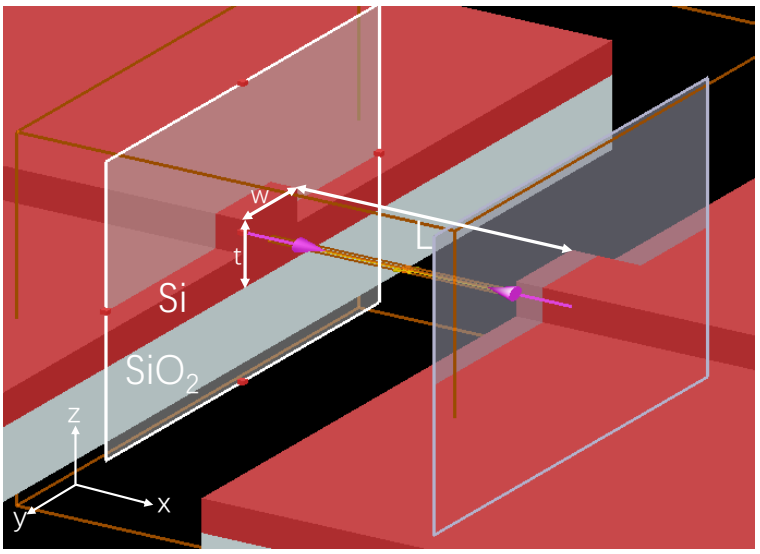


FIGURE 4.2: Schematic of the simulation model for the dual-waveguide optical trap. Two identical rib waveguides are separated by a gap distance L, and two in-phase mode sources with the same powers of 50 $mW$ are placed at 0.5 $\mu$m from the end facet of the waveguides with opposite injection directions. To maintain the single-mode condition, the waveguide width is set to be $w = 0.87\ t$, where $t$ is the thickness of the waveguide.

thickness of the silicon layer, is kept as a constant of 0.5, and the waveguide width is set to be $w = 0.87\ t$, which is the maximum value to maintain the single-mode condition [130]. The waveguide slab width is set to be 10 $\mu$m considering the higher-order mode leakage into the slab, and the thickness of $SiO_2$ is set to be 2 $\mu m$.

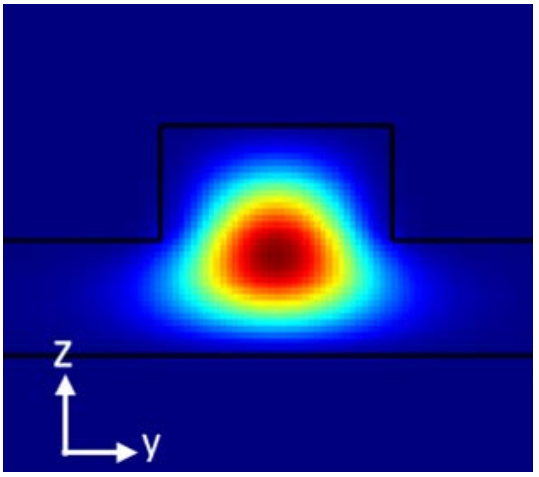


FIGURE 4.3: TE mode profile of the rib waveguide from the two in-phase mode sources.

The coordinate origin point is set to be at the centre of the gap in the x-direction, at the centre of the waveguide width in the y-direction and on the slab surface in the z-direction. The FDTD simulation domain is set to be 10 µm in both y- and z-direction. In the x-direction, the simulation domain is $L + 3\ \mu m$. A perfectly matched layer (PML) is used as the boundary condition. Three frequency-domain field and power monitors

are placed in three separate planes, namely the XY plane, XZ plane, and YZ plane, to measure the optical intensity distribution between the waveguides. When implementing the FDTD simulation, a 50 $nm$ mesh size is used, which is proven to be fine enough to resolve the fields through the FDTD mesh convergence test.

### 4.2.3 Intensity field profile

The dual-waveguide trap with waveguides thickness $t = 2\ \mu m$ and input wavelength $\lambda = 1550\ nm$ is first simulated to study the characteristics between the two waveguides. The simulated optical field profiles in the XY plane (Z=0) and XZ plane (Y=0), are shown in Figure 4.4 (A and B) for a gap distance $L = 1\ \mu m$, and in Figure 4.4(C and D) for a gap distance $L = 3\ \mu m$. In the intensity field profiles, the colours bar represent the intensity of the field. It can be found that both in the XY plane and XZ plane the light guided inside the waveguides diverges rapidly at the end facet and then interferes to generate several periodically distributed local maximum intensity points inside the gap area. There is one point for the gap distance $L = 1\ \mu m$ and three points for the gap distance $L = 3\ \mu m$. These hot points are the positions where particles can be trapped by the optical gradient force. The interference fringe can also be found in the waveguide, which is caused by the interference of propagating light and reflected light from the waveguide facet. Within the gap, the period deduced from the modulation patterns is in close agreement with the theoretical value of $\lambda/2 = 775\ nm$. When comparing the field profiles in XY plane and XZ plane, it is apparent that the beam leaving the waveguides in XZ plane is more divergent than in XY plane, since the confinement of the waveguide mode is tighter in the vertical direction than in the horizontal direction.

The periodic pattern within the gap is generated by interferometric modulations from two aspects. Firstly, it is the interference between the propagating light transmitted out of one waveguide facet and the reflected light from the facet of another waveguide. Secondly, it is the interference between the two counter-propagation beams which come from the two mode sources and are transmitted out of the end facets of the waveguides. Due to the much larger transmission over reflection at the air/silicon interface [44], the second type of interference dominates. Given the condition that the two mode sources are set in phase, there is a constructive interference effect at the centre due to the matched distances to the mode sources. Therefore, the intensity at the centre is always a local maximum while changing the gap. This constructive interference also happens at locations in the x-axis where $x = \pm\frac{k\lambda}{2}, k = 0, 1, 2...$, in which the gap distance $L$ must be greater than $\frac{(2k+1)\lambda}{2}$. These points are further called the trapping points.

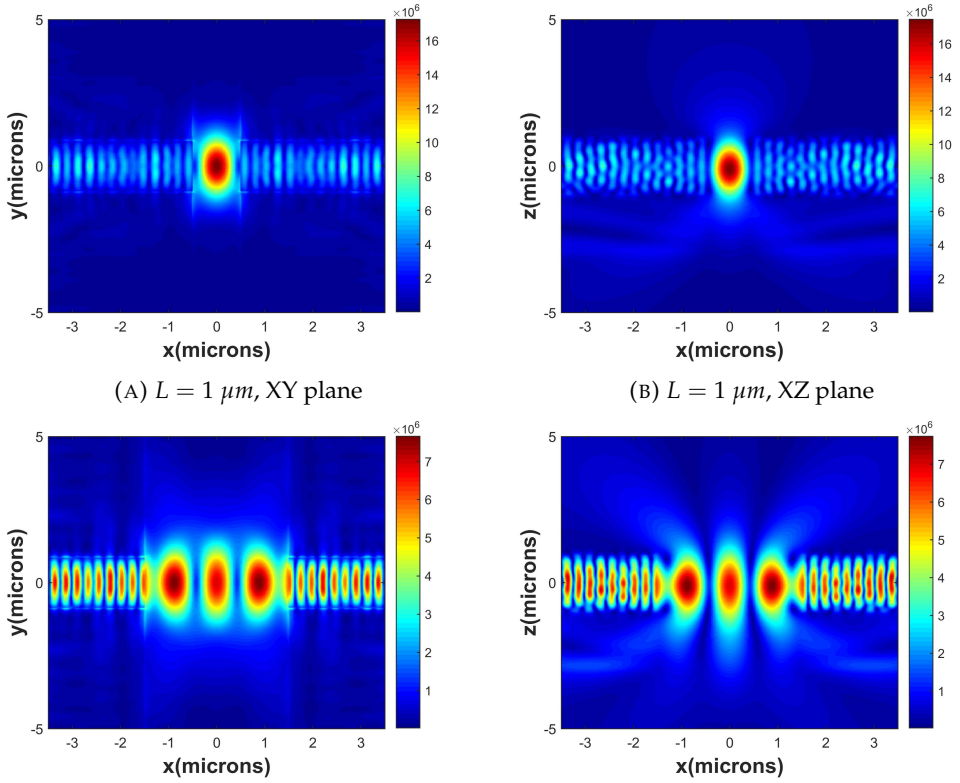


(A) $L = 1\ \mu m$, XY plane

(B) $L = 1\ \mu m$, XZ plane

(C) $L = 3\ \mu m$, XY plane

(D) $L = 3\ \mu m$, XZ plane

FIGURE 4.4: (A and B) Field intensity profile for a gap distance $L = 1\ \mu m$ in XY plane and XZ plane, respectively. (C and D) Field intensity profile for a gap distance $L = 3\ \mu m$ in XY plane and XZ plane, respectively.

### 4.2.4 Optical trapping force and trapping potential

Assuming a dielectric particle is placed within the gap, the particle will be trapped to one of the trapping points owning to the optical gradient force pointing to the region with the highest optical intensity. Due to the conservative nature of the optical gradient force, a unique value called trapping potential can be assigned to each location. The depth of the trapping potential well plays a crucial role in keeping the trapped particles within the optical trap and can be used to characterise the optical trapping capability. The deeper the potential well is, the more stable the optical trap becomes. According to Ashkin's stability criterion [64], the depth of the potential well has to be higher than $10k_BT$, where $k_B$ is the Boltzmann constant and $T$ is the ambient temperature, to make the optical trapping capability strong enough to offset the effect of Brownian thermal vibration of the particle so that the particle can be stably trapped.

In Lumerical's FDTD Solutions, the optical force acting on a particle can be calculated by calculating the volume integral of the time-averaged Lorentz force density for a cube enclosing the particle [131]. The force at each mesh point is given by,

$$\mathbf{F} = \epsilon_b \epsilon_0 (\nabla \cdot \mathbf{E})\mathbf{E} - iw\epsilon_0(\epsilon_r - \epsilon_b)\mathbf{E} \times \mathbf{B}, \tag{4.12}$$

where $\epsilon_0$ is the vacuum permittivity, $\epsilon_b$ and $\epsilon_r$ are the background relative permittivity of the medium and particle. After that, the trapping potential can be calculated by integrating the optical force over the space of the particle. Here, an SOI dual-waveguide optical trap with waveguide thickness $t = 3.5\ \mu m$ and gap distance $L = 4\ \mu m$ is demonstrated, in which a silica sphere with 200 $nm$ diameter is trapped at the centre. The input optical wavelength is 1550 $nm$ and the applied power is set to be 50 $mW$. The simulated optical force and trapping potential for the y-axis (Figure 4.5 (A)), z-axis (Figure 4.5 (B)) and x-axis (Figure 4.5 (C)) are plotted below respectively. In the figures, the resulting trapping potentials are normalized to $k_B T$ (T=300K).

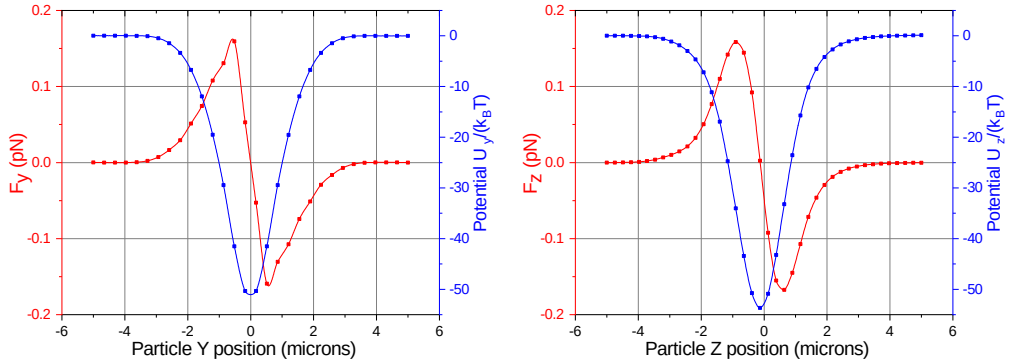


(A) The simulated optical force and trapping potential in the y-axis

(B) The simulated optical force and trapping potential in the z-axis

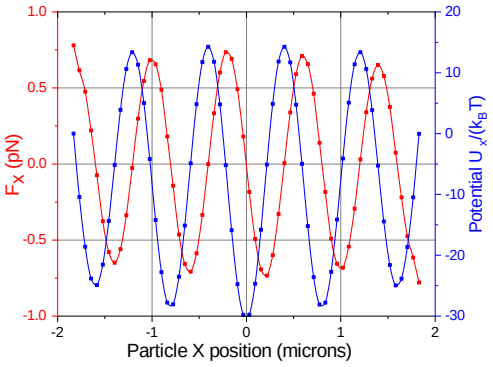


(C) The simulated optical force and trapping potential in the x-axis

FIGURE 4.5: (A, B and C) The simulated optical force and trapping potential for a silica sphere with 200 $nm$ diameter trapped at the centre of a dual-waveguide optical trap with waveguide thickness $t = 3.5\ \mu m$ and gap distance $L = 4\ \mu m$ in the y-axis, z-axis and x-axis respectively. Note that the applied optical power is 50 $mW$ each.

It can be found from Figure 4.5 (A and B) that a stable optical trap for 200 $nm$ particles can be formed along the y-direction and z-direction with a 50 $mW$ applied power. The optical force is linear around the centre and shows a restoring character attracting the particle to the centre. While in the X direction, multiple trapping points are generated along the x-axis, which agrees with the field intensity pattern analysis in Section 4.2.3. According to the criteria of stable trapping, the potentials in all three directions are deep enough to overcome the particle Brownian motion and thus form a stable optical trap.

### 4.2.5 Optical trapping capability for different particle size

The trapping capability, namely the optical force and trapping potential of the dual-waveguide optical trap is first studied for different particle sizes. The SOI dual-waveguide optical trap was set with waveguide thickness $t = 3.5\ \mu m$ and gap distance $L = 4\ \mu m$, in which a silica sphere with radius as 50 $nm$, 100$nm$, 150 $nm$ and 200 $nm$ is trapped at the centre. The input optical wavelength is 1550 $nm$, and the applied power is set to be 50 $mW$. The calculated optical forces and trapping potentials are shown below in Figure 4.6.

For optical force in z- and y-direction shown in Figure 4.6 (A, C), there is always a negative slope around the original point, and the force is linearly dependent on the displacement. This negative slope indicates that the force is a restoring force pushing the particle back to its origin. With the shifting distance increasing, the forces experience an extreme point, after which the force gradually falls back to zero. When increasing the particle size, the position of the extreme points move away from the origin, and a larger optical force is generated on the particle. From the optical trapping potential shown in Figure 4.6 (B, D), it can be seen that the depths of the potential wells are much higher than 10 which acts as the criteria for stable trapping. Crucially, it is clear that a larger particle leads to a deeper potential well.

For the optical force and trapping potential in the x-direction, it can be found from Figure 4.6 (E, F) that there are more than one points that can trap a particle; this originates from the optical interference within the gap. It can also be found that larger particle size leads to larger optical force and trapping potential. In the origin point, the optical force curve always has a negative slope that pushes the particles to an intensity local maximum point. However, it has been shown in [132] that with the further increase of the particle size, the optical force in a standing wave trap depends periodically on particle size and the trapping point changes between interference maxima and minima, which means the origin point is not always a trapping point.

The process of calculating optical force and trapping potential using the volume integration method shown above can only be implemented by parametrically sweeping the location of the particle to get the optical force acting on the particle at each position, which will require significant computational resources. The simulation time may even increase by orders of magnitude if the effect of gap distance and waveguide thickness also need to be analysed. Therefore, another figure of merit to quickly assess the optical trapping capability is desired.

It has been shown in section 4.1 that the particles interacting with light can be treated as point dipole charges in an electric field when the particle size falls into the Rayleigh scattering regime. The induced dipole moment can is $\mathbf{p} = \alpha\mathbf{E}$. The energy of the dipole

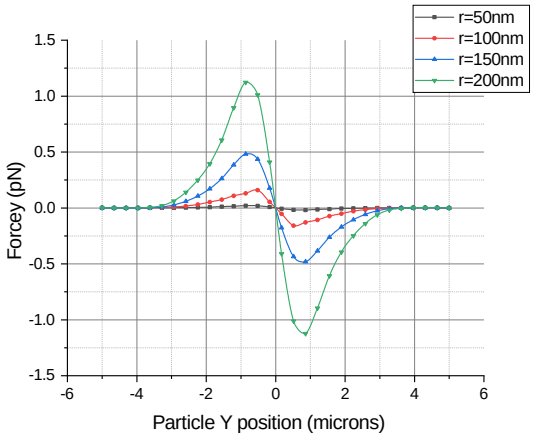


(A) Optical force in the y-axis

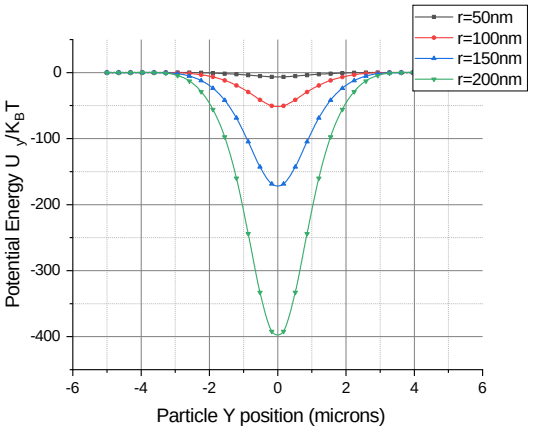


(B) Optical trapping potential in the y-axis

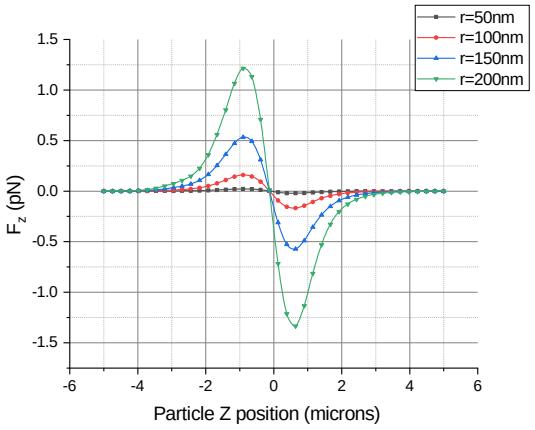


(C) Optical force in the z-axis

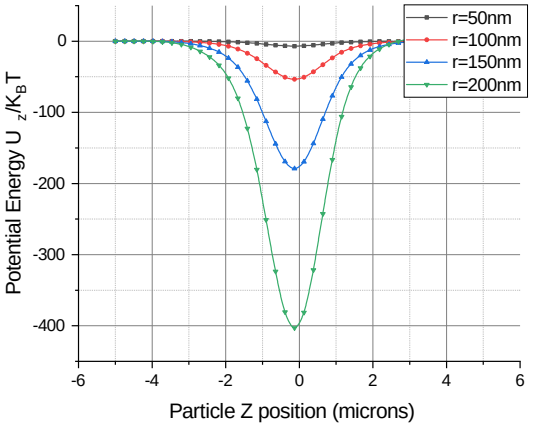


(D) Optical trapping potential in the z-axis

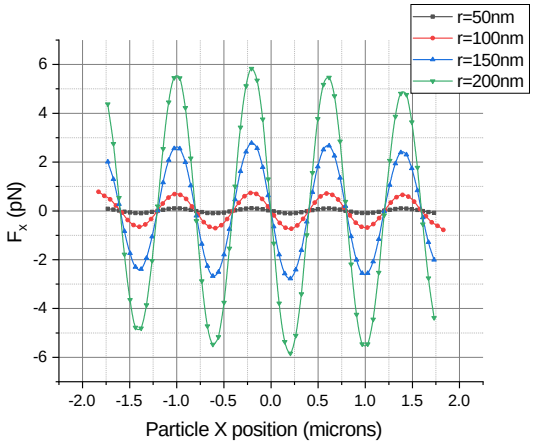


(E) Optical force in the x-axis

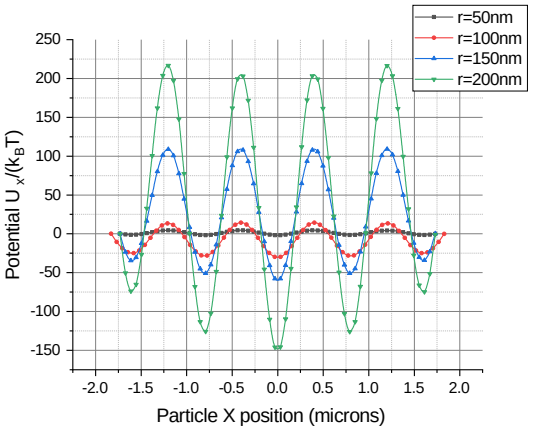


(F) Optical trapping potential in the x-axis

FIGURE 4.6: The simulated optical force and trapping potential for a silica sphere with radius of 50 $nm$, 100$nm$, 150 $nm$ and 200 $nm$ trapped at the centre of a dual-waveguide optical trap with waveguide thickness $t = 3.5\ \mu m$ and gap distance $L = 4\ \mu m$ in the y-axis, z-axis and x-axis respectively. Note that the applied optical power is 50 $mW$ each.

can be then written as [127],

$$U = -\mathbf{p} \cdot \mathbf{E} = -\alpha |\mathbf{E}|^2, \tag{4.13}$$

where $\alpha$ is the polarisability of the dielectric particle given by Equation 4.8. Therefore, the depth of the generated optical trapping potential well is given by,

$$U = -\frac{8\pi n_2 r^3 I(\mathbf{r})}{c}\left(\frac{n_1^2 - n_2^2}{n_1^2 + 2n_2^2}\right). \tag{4.14}$$

From Equation 4.14, the optical trapping potential is linearly proportional to the field intensity $I$, which means the optical trapping capability can be characterised by the optical intensity in the trapping point if the Rayleigh scattering condition is matched. Here, only the particles with dimensions from tens of nanometer to several hundred nanometers are studied, which match the Rayleigh particle condition for the simulation wavelength near 1550 $nm$. Therefore, a dual-waveguide optical trap configuration without a particle is used to simulate the trapping characteristics of the dual-waveguide optical trap. In the meantime, the optical intensity $I$ is also linearly proportional to the square of the electric field amplitude $|\mathbf{E}|^2$ from Equation 4.9. Thus, $|\mathbf{E}|^2$ is chosen to represent the optical intensity within the gap and to work as the figure of merit to assess the trapping capability under different waveguide thicknesses. It has to be understood that this depends on the prerequisite that the particle size falls into the Rayleigh scattering regime. For larger particles out of this regime, the optical potential is complicated and are not just related to the optical field intensity, which is beyond the scope of this research.

## 4.3 Dual-waveguide optical trapping optimisation and scaling effect

### 4.3.1 Intensity field distribution over different waveguide thickness

Following the discussion in section 4.2.5 that the field intensity can be used to characterise the trapping capability, the optical field distribution features within the gap of the optical traps are analysed under different waveguide thicknesses. When the wavelength $\lambda = 1550\ nm$, the simulated optical field intensity profiles in the x-axis for dual-waveguide traps with waveguide thicknesses from 0.5 $\mu m$ to 4 $\mu m$ are shown below in Figure 4.7 for gap distance $L = 0.775\ \mu m$, $L = 2.325\ \mu m$, $L = 3.875\ \mu m$, $L = 5.425\ \mu m$, respectively. Those four gap distance theoretically meet the standing wave condition when the wavelength is $\lambda = 1550\ nm$. It can be found the number of trapping points, namely the local intensity maximum points, increases with the gap distance $L$. In each of the trapping points along the x-axis, it is apparent that there is a waveguide thickness value in which the optical intensity reaches its local highest, meaning that there is an optimal waveguide thickness that maximises the optical intensity and trapping capability.

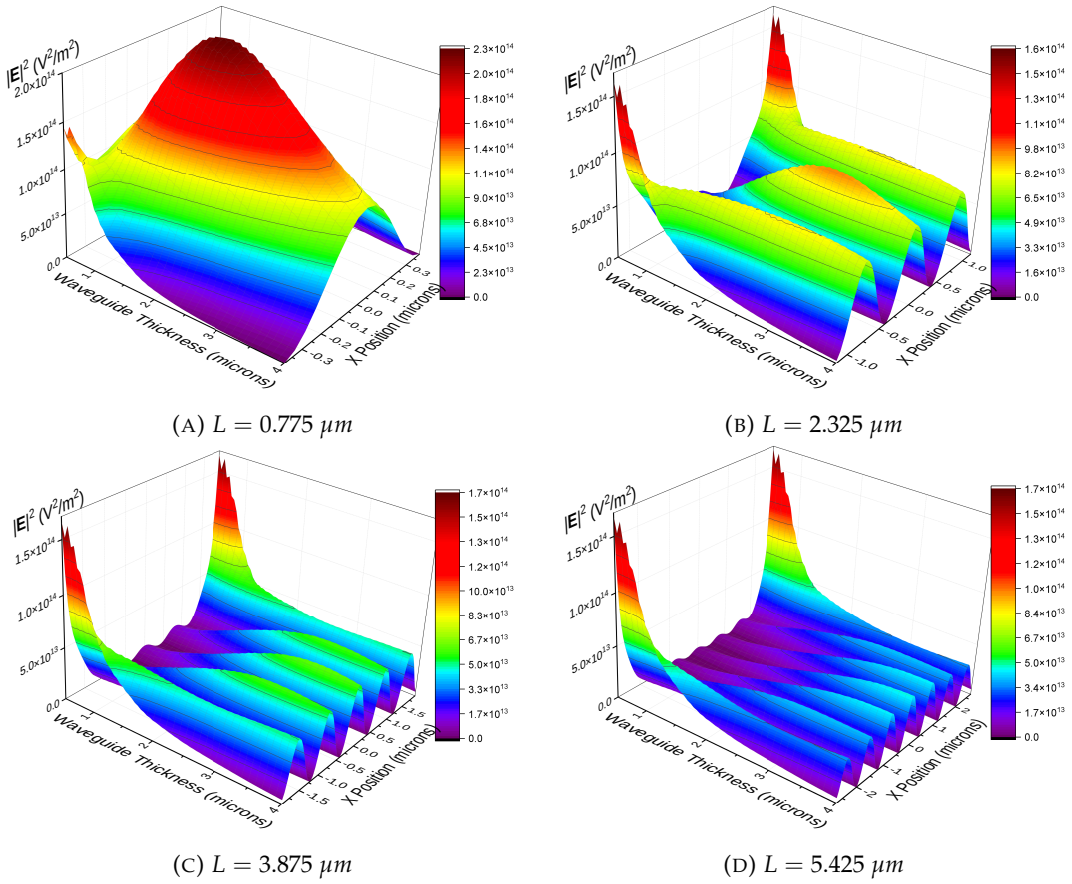


(A) $L = 0.775\ \mu m$ (B) $L = 2.325\ \mu m$

(C) $L = 3.875\ \mu m$ (D) $L = 5.425\ \mu m$

FIGURE 4.7: Field intensity profile in the x-axis for dual-waveguide trap with waveguide thickness from 0.5 $\mu m$ to 4 $\mu m$ when (A) the gap distance $L$=0.775 $\mu m$. (B) the gap distance $L$=2.325 $\mu m$. (C) the gap distance $L$=3.875 $\mu m$. (D) the gap distance $L$=5.425 $\mu m$. The grey line in the figures show the contour map of the optical intensity.

When looking at the field intensity near the edges of the gap in the four figures, it is interesting to note that the intensity curves at the edges almost align with each other for different gap distances and in the meantime, decreases with the waveguide thickness for each curve. This is because the input power of the two mode sources is set to be the same for different waveguide thicknesses, and thus the field intensity is reversely proportional to the waveguide cross-section area, which means the waveguide with smaller thickness has higher field intensity. Besides, across the air/silicon interface, i.e. the end of the waveguide, the field intensity distribution is continuous, and this makes the intensity at the two edges of the gap dependant only on the waveguide thickness and independent of the gap distances between two waveguides. Therefore, the values of the intensity at the edge of the gap are equal for configurations with the same waveguide thickness. On the other hand, the radiation loss within the gap increase with gap distance, so the overall intensity inside the gap decreases with the gap distance. This makes the peaks near the edge of a large distance gap more prominent than the counterpart in a small distance gap. Therefore, two high peaks on the two edges of the gap are observed clearly in the case of small waveguide thickness in Figure 4.7 (B,

C and D). As a comparison, the peaks in Figure 4.7 (A) is not that prominent due to the high-intensity hot spot inside the gap.

What deserves noting is the second-highest intensity area in Figure 4.7 (A) and the highest intensity areas in Figure 4.7 (B, C and D). They are at the edge of the gap area when the waveguide thickness is small. There are two theoretical trapping points close to the edge of the gap $x \approx \pm 0.775\ \mu m$ for Figure 4.7 (B), $x \approx \pm 1.55\ \mu m$ for Figure 4.7 (C), $x \approx \pm 2.325\ \mu m$ for Figure 4.7 (D), at the configuration with larger waveguide thickness, where the local maximum intensity points exist. Particles can be thus trapped here rather than attracted to the end facet. As for the case of small waveguide thickness, however, the intensity at the edge of the gap is too high that the theoretical trapping points disappear, and particles would be attracted to the end facet of the waveguides. This feature is very meaningful in overcoming the drawbacks in traditional dual-waveguide optical trapping, where particles can be easily attracted to the end of the waveguide, by properly designing the waveguide thickness and gap distance.

### 4.3.2 Optimal waveguide thickness for optical trapping

When the wavelength is $\lambda = 1550\ nm$, a parametric sweep of the gap distance $L$ and waveguide thickness $t$ in FDTD Solutions is conducted to study the effect of these two parameters on the field intensity at the trapping points, which represents the trapping capability there. The waveguide thickness $t$ is swept from 0.5 $\mu m$ to 4 $\mu m$, and the gap distance $L$ is swept from 0.5 $\mu m$ to 6.2 $\mu m$. During the simulation, the value of each input mode source electric amplitude for optical traps with different waveguides thicknesses are elaborately set to ensure that each input power of the two in-phase sources is kept as a constant at 50 $mW$. The input power is calculated by the built-in function "sourcepower" of the FDTD Solutions. By doing this, the effect of the input optical power on the trapping capability can be eliminated and the study can be focused on the impact of waveguide thickness $t$ and gap distance $L$.

As analysed above, there are multiple trapping points within the gap. For the trapping points located at $x = 0$, $x = \pm\lambda/2$, $x = \pm\lambda$, further called the centre, X1 and X2, Figure 4.8 (A ,B, C) show the relation of the field intensity as a function of the gap distance $L$ and the waveguide thickness $t$ respectively. The 'ridge' like intensity surfaces show that the field intensity generally decreases with the gap distance $L$ in all three of the graphs. This is intuitive because a larger gap distance means more radiation mode energy is diverged and lost to the outside medium environment, leading to a lower optical intensity within the gap. At the position of the ridges, however, periodically local maximum intensity points along the gap distance direction can be found, which are attributed to the constructive interference of light between the two waveguide facets when the gap distance $L$ matches the standing wave condition. It is also apparent that,

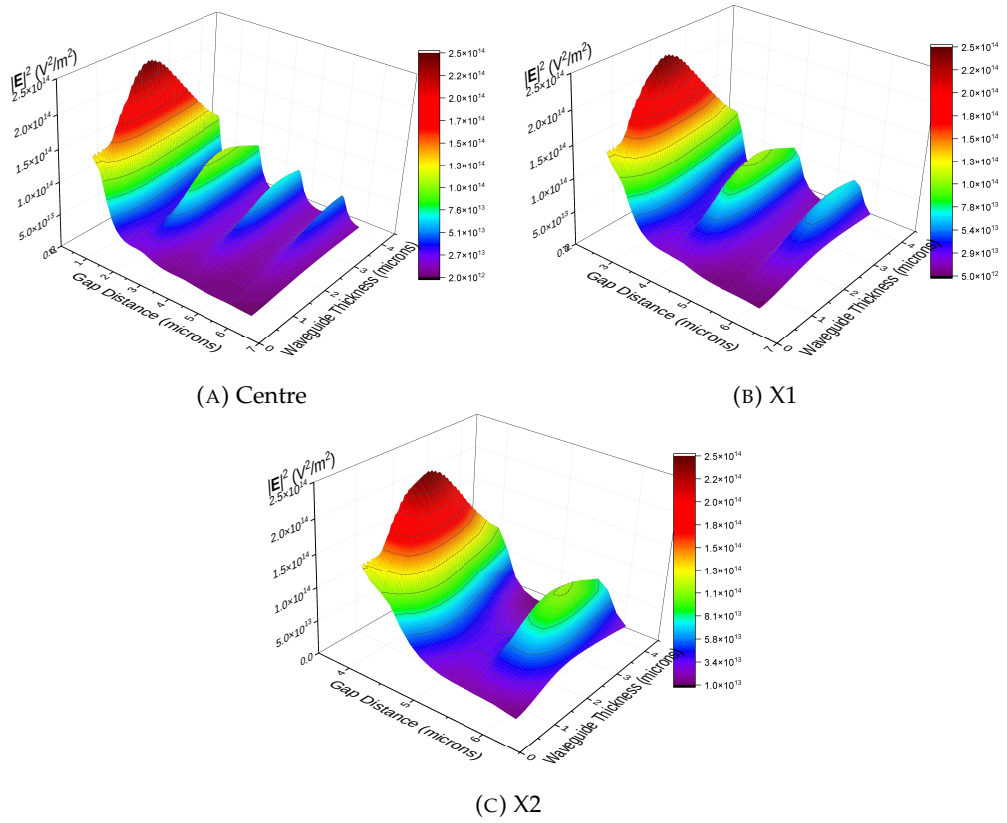


(A) Centre

(B) X1

(C) X2

FIGURE 4.8: (A,B, and C) The field intensity as a function of the gap distance $L$ and the waveguide thickness $t$ at the centre, X1, X2, respectively. The colour represents the optical intensity. The wavelength $\lambda = 1550\ nm$

for each gap distance $L$, there is a value of waveguide thickness $t$ that can maximise the optical intensity, which is called the optimal waveguide thickness $t_{op}$. These figures also show that $t_{op}$ is not a constant but rather dependent on the gap distance $L$. This can be understood by considering the dual-waveguide optical trap as a coupled-resonator model which has been introduced in [44]. In the coupled-resonator model, the maximum intensity within the resonator occurs when the critical coupling condition is matched, namely $\kappa_e = \kappa_i$, where $\kappa_e$ refers to the loss rate associated with the input coupling, and $\kappa_i$ refers to the remaining internal loss. In the dual-waveguide configuration described here, $\kappa_e$ and $\kappa_i$ are determined by waveguide thickness $t$ and gap distance $L$. Even though the accurate numerical relationship between them is still unclear and currently under exploration, what is certain is that there is an optimal combination of waveguide thickness $t$ and gap distance $L$ according to the coupled-resonator theory, thus there exists an optimal waveguide thickness $t_{op}$ for each gap distance $L$ to maximise the intensity.

Extracted from the field intensity profiles in Figure 4.8, Figure 4.9 shows the maximum optical intensity and the corresponding optimal waveguide thickness $t_{op}$ over the gap distance $L$ at the trapping points at the centre, X1, X2. From the red curves representing the maximum optical intensity, periodic peaks along with a descending trend are

observed. The periodic peaks come from intensity enhancement due to standing wave modulation, while the descending trend is caused by the increased optical energy loss to the environment with gap distance. It can also be found that the maximum intensity curves at the centre, X1, and X2 align with each other very well, meaning the maximum trapping capability for the centre, X1 and X2 are almost at the same level.

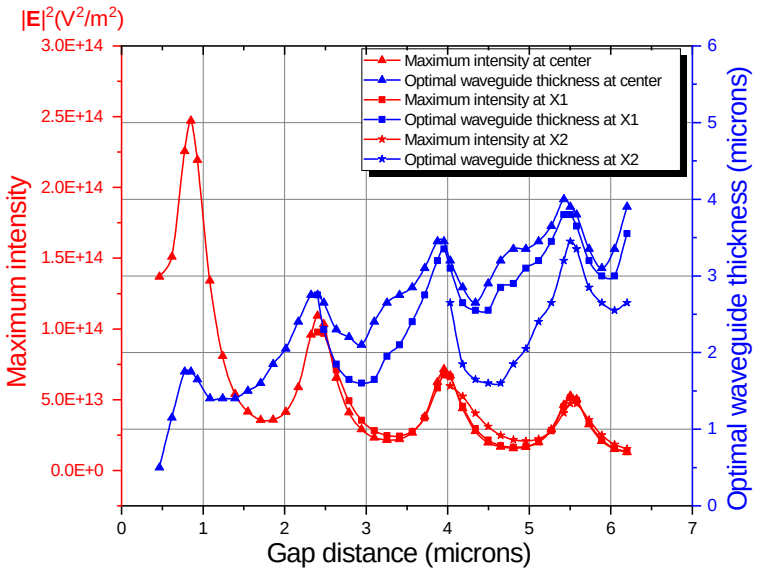


FIGURE 4.9: The extracted maximum optical intensity and optimal waveguide thickness $t_{op}$ as a function of the gap distance L at the centre, X1, X2. The blue curves represent the extracted data for the optical waveguide thickness $t_{op}$, while the red curves indicate the corresponding maximum optical intensity. The curves with triangular, rectangular, and star shape symbols represent the data for the trapping point at the centre, X1, and X2, respectively.

From the blue curves representing the optimal waveguide thickness $t_{op}$, it can be found that $t_{op}$ generally increases with the gap distance, which indicates a thicker waveguide is preferred to maximise the trapping capability with a larger gap distance. However, the trends do not monotonically increase but rather change with a periodic feature whose period matches perfectly with the red curves for maximum intensity.

Looking into the difference between the optical waveguide thickness curves for the three trapping points, it is found that the $t_{op}$ for the trapping point at the centre is larger than that for the trapping points at X1 and X2. Nevertheless, when the gap distance matches the standing wave condition, the $t_{op}$ is generally consistent with each other.

### 4.3.3 Scaling effect over the wavelength

In the above analyses, the wavelength $\lambda$ are set to be 1550 $nm$. However, other wavelengths can also be used in optical trapping applications, such as 785nm which has been used for Raman spectroscopy excitation in optical trapping demonstrated in [74].

In addition, the input optical wavelength can be easily tailored to maximise the trapping capability through a tunable laser, for which the role the input wavelength plays in the design of dual-waveguide optical traps must be explored. Therefore, in addition to the sweep of the waveguide thickness $t$ and the gap distance $L$, another parametric sweep of the wavelength $\lambda$ from 1100 $nm$ to 2000 $nm$ was conducted to study the effect of wavelength on the optimal waveguide thickness $t_{op}$. Again, waveguide thickness $t$ is swept from 0.5 $\mu m$ to 4 $\mu m$, and gap distance L is swept from 0.5 $\mu m$ to 6.2 $\mu m$. The input optical power is set to be the same at 50 $mW$ for each mode source to eliminate the effect of the input power.

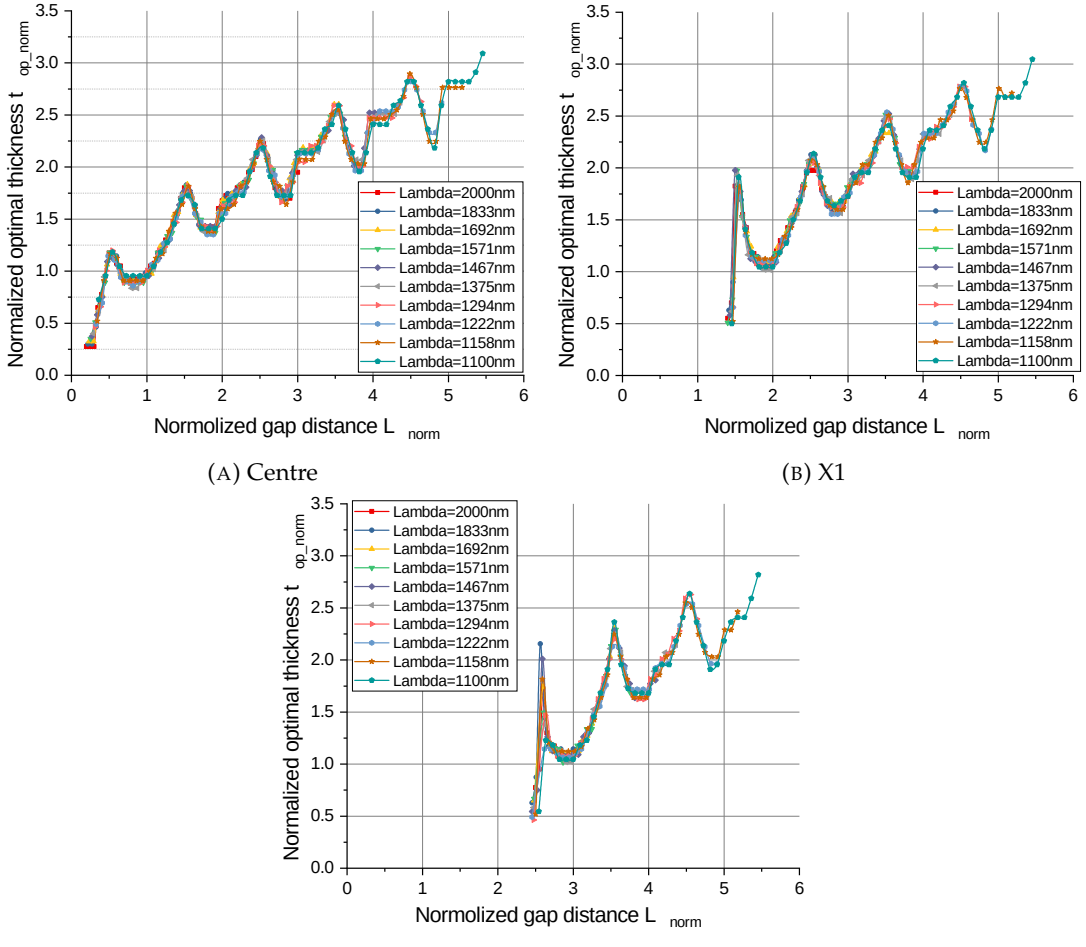


(A) Centre

(B) X1

(C) X2

FIGURE 4.10: (A,B, and C) Normalised optimal waveguide thickness $t_{op\_norm} = t_{op}/\lambda$ as a function of the normalised gap distance $L_{norm} = L/\lambda$ at the trapping point at the centre, X1, X2, respectively.

To take into account the effect of optical wavelength, the geometric value, namely the gap distance $L$ and the waveguide thickness $t$ are normalised to the input wavelength $\lambda$. Figure 4.10 show the normalised optimal waveguide thickness $t_{op\_norm} = t_{op}/\lambda$ as a function of the normalised gap distance $L_{norm} = L/\lambda$ at the trapping point at the centre, X1, X2, respectively. In each figure, the curves for different wavelengths are plotted with different colours and symbols. These three figures all demonstrate that,

for different input wavelengths $\lambda$, the $t_{op}/\lambda$ over $L/\lambda$ curves align with each other very well except for the discrepancy near the first peak in Figure 4.10 (C). This can be attributed to the dramatic intensity difference between the waveguide end facet and the X2 trapping point. These results clearly demonstrate the scaling effects of the optimal waveguide thickness and the gap distance over the optical wavelength. The scaling effect is intuitive because gap distance and waveguide thickness are both geometric parameters, so that the whole system for different wavelengths could be shrank or enlarged to make the systems equivalent to each other.

Analogous to the findings in Section.4.3.2 for a wavelength of 1550 $nm$, these curves also show that the normalised optimal waveguide thickness $t_{op\_norm}$ generally increases with the normalised gap distance $L_{norm}$, along with a periodic feature. The $t_{op\_norm}$ over $L_{norm}$ curves reach their peaks when the normalised gap distance is $L_{norm} = L/\lambda = n + 0.5, n = 0, 1, 2\ldots$, which matches the standing wave condition of the dual-waveguide configuration. In comparison to the curves at the trapping point at the centre shown in Figure 4.10 (A), the curves in Figure 4.10 (B, C) start from $L_{norm} \approx 1.5$ and $L_{norm} \approx 2.5$, because the trapping points X1 and X2 only exist when the $L_{norm} \geq 1.5$ and $L_{norm} \geq 1.5$, respectively.

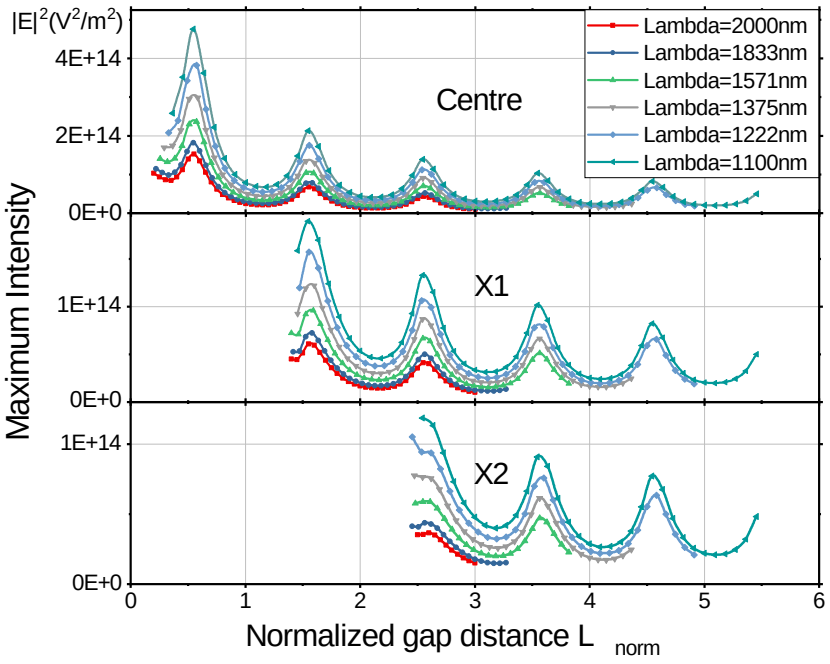


FIGURE 4.11: From top to bottom: Maximum intensity as a function of normalized gap distance $L_{norm} = L/\lambda$ at the trapping point at the centre, X1, X2, respectively. In each figure, the curves for different wavelengths are plotted with different colours and symbols.

Figure 4.11 show the corresponding maximum field intensity as a function of the normalised gap distance $L_{norm} = L/\lambda$ at the trapping point at the centre, X1, X2, respectively. These curves also show clear periodic standing wave features which result from the interference effect. It is interesting to note that the larger optical wavelength leads to

weaker trapping capability. This is obvious as larger optical wavelength $\lambda$ means larger gap distance $L$ in the case of the same normalized gap distance $L_{norm} = L/\lambda$, which gives rise to greater radiation loss within the gap. Therefore, a shorter input wavelength is generally preferred when a stronger trapping capability is desired. Communication band 1550 $nm$ wavelength laser is usually used in the SOI waveguide platform owing to its easy accessibility and low waveguide propagation loss, while wavelength below 1200 $nm$ can not be used in the SOI platform due to the high material absorption loss. Compared to the SOI platform, the previously used $Si_3N_4$ or $Ta_2O_5$ is transparent at visible wavelength 532 $nm$, which can be used to enhance the trapping capability as has been analysed above. However, the fabrication complexity may hinder their use.

From the point of application, the input power should always be made the best of to maximise the trapping capability within the gap. Further, the gap distance or wavelength can be adjusted to meet the standing wave condition when the optical intensity reaches a local maximum. Thus, here, the values of normalised waveguide thickness $t_{op\_norm}$ are roughly summarised for trapping points at the centre, X1, X2, when the standing wave condition is matched, namely the normalised gap distance $L_{norm} = L/\lambda = n + 0.5, n = 0, 1, 2\ldots$ Only a rough value of $t_{op\_norm}$ could be obtained because they are not always precisely located in the standing wave points due to the discrete and limited number of positions in the simulations. The results are shown below in Table 4.1. It can be seen from the table that when the gap distance matches the standing wave condition, the $t_{op}$ is generally consistent with each other for the trapping points at Center, X1, and X2. There is a subtle difference among them, showing that the $t_{op\_norm}$ is slightly smaller when trapping a particle at the side rather than that at the centre. Furthermore, it is evident that a larger waveguide thickness is desired with a larger gap distance, providing that the standing wave condition is fulfilled.

| Normalised gap distance | Normalised optimal waveguide thickness $t_{op\_norm}$ | | |
|---|---|---|---|
| | Centre | X1 | X2 |
| $L_{norm} = 0.5$ | 1.2 | – | – |
| $L_{norm} = 1.5$ | 1.8 | 1.8 | 0 |
| $L_{norm} = 2.5$ | 2.25 | 2.2 | 2.1 |
| $L_{norm} = 3.5$ | 2.6 | 2.5 | 2.4 |
| $L_{norm} = 4.5$ | 2.9 | 2.8 | 2.6 |
| ... | ... | ... | ... |

TABLE 4.1: The value of normalised optimal waveguide thickness $t_{op\_norm}$ when the Normalised gap distance $L_{norm}$ matches the standing wave condition for trapping point at Center, X1 and X2.

## 4.4 Optomechanical oscillation for separating micro/nano-particles

### 4.4.1 Micro/nano-article loading

A key technique to the application of optical trapping is the efficient and controllable particle loading process. For optical trapping in a liquid environment, the micro/nano particles can be suspended for a long time due to the buoyancy force, thus the particles near the optical trap can be easily captured. In the air or vacuum, however, the particles need to be detached from the storage surface and launched into air around the optical trap. This is not an easy process due to the large adhesion force between the particles and surface when compared to the gravitational force acting on the particle.

In previously demonstrated macroscopic optical trapping setup in optical trapping in air or vacuum, two methods are mainly utilized to launch the particles, ultrasonic nebuliser source and piezo vibration. Ultrasonic nebuliser breaks the diluted solution of the nanoparticles into small droplets and disperses the droplets containing nano particles into the optical trapping area. The solution must be highly volatile so that it can evaporate quickly, and then the particle can be trapped. Piezo vibration is used mainly for separating and loading micron-sized particles on the piezoelectric plate. High-frequency vibration of the plate can separate the particles from the surface of the plate due to the large acceleration acting on the particle.

For on-chip optical trapping in air or vacuum, the nebuliser cannot accurately spray the diluted solution to the designed trapping area but rather to the whole area of the chip, which causes huge contamination or even damage to the chip. The same issues also stand out for the external piezo vibration method, in which accurate loading seems impossible due to the large size of the piezoelectric plate. A plausible solution is to fabricate an on-chip piezoelectric vibrator to the optical trapping chip, but this requires heterogeneous integration of material with a high piezoelectric coefficient, which increases the complexity in terms of both designs and fabrication.

In the on-chip cavity optomechanical systems, it has been shown in Chapter 3 that the dynamic back-action effect can lead to on-chip self-sustained optomechanical oscillation (OMO), where the mechanical resonator is first heated and finally driven into oscillation by the optical cavity field. These self-sustained OMO devices can be fabricated on the SOI substrate with the fabrication process compatible with previously proposed on-chip dual-waveguide optical trapping. In addition, the oscillation can be excited and sustained purely by the optical field without the need of the introduction of external electrical input, which greatly eases the fabrication and application complexity.

Here, it is proposed that the on-chip cavity optomechanical oscillation process could be used to break the adherent force and load the particle to the optical trap.

### 4.4.2 Micro/Nano Particles separation threshold

When two particles in a vacuum or air are close to each other, attractive forces such as the Van der Waal's force arise between them. A pull-off force, which is the minimum force that breaks the connection, is thus necessary to separate the adhering particles. The interaction between two solid spheres is usually described by the model of Johnson, Kendall, and Roberts (JKR) [133] or the model of Derjaguin, Muller and Toporov (DMT) [134]. The JKR model is suitable for the analysis between large and soft particles, while DMT model is used for analysis for small and hard solid particles. For the on-chip optical trapping in vacuum considered in this part, micro/nano-size particles need to be trapped, and thus the DMT model is used for the analysis here. The DMT model predicts a pull-off force between two spherical particles as:

$$F = 4\pi R_e \gamma. \tag{4.15}$$

Here $\gamma$ is the effective solid surface energy and $R_e$ is the reduced radius of the two particle surfaces, $R_e = R_1 R_2/(R_1 + R_2)$, with $R_1$ and $R_2$ being the individual particle radii. For the case with two identical spherical particles, $R_e = R_1/2 = R_2/2$. For the case with a planar surface and a particle, the radius of the planer surface is $+\infty$, thus $R_e = R_1$, with $R_1$ being the radius of the particle. A large number of spherical particles are assumed to be on a planar surface, and the particles are not only adhered to each other but also to the surface. According to the analysis above, the pull-off force between particles is only half of that between the particle and the planar surface. When the surface is vibrated, and the acceleration is increased gradually, the particles will be set apart from each other before being pulled off from the surface. Therefore, the case of particles adhered to a planar surface is considered for the separation threshold analysis.

In [135], the authors conducted experiments based on the principles of atomic force microscopy (AFM) to directly measure the pull-off force between two silica spheres of radii between 0.5 and 2.5 $\mu m$. The results show a linear dependence of the pull-off force on the particle radius, and an effective solid surface energy $\gamma = 0.0186 J/m^2$ was obtained for the above DMT model. With this value of $\gamma$, the pull-off force between a 1 $\mu m$-diameter silica particle and a glass surface is calculated to be $88nN$. The gravitational force on the same particle is about 12 $fN$, which is seven orders of magnitude smaller than the pull-off force.

The separation threshold for silica microsphere particles stuck on a glass surface by the Van der Waal's force is then considered. The required acceleration to break the adhesive connection is thus given by,

$$a = \frac{F}{M} = \frac{4\pi R\gamma}{\frac{4}{3}\pi R^3 \rho} = \frac{3\gamma}{R^2 \rho}, \tag{4.16}$$

where $\rho = 2330\ kg/m^3$ is the density of the silica sphere. The calculated relationship between the required acceleration and the particle size is shown below in Figure 4.12. It can be found that a 1 $\mu m$ diameter silica microsphere particle needs at least an acceleration of about $1.2 \times 10^8 m/s^2$ to break the Van der Waal's force. The smaller the particle, the larger acceleration is required to break the connection.

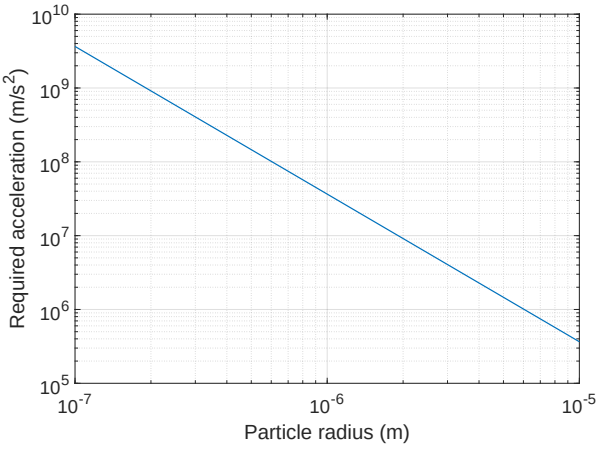


FIGURE 4.12: The required minimum acceleration needed to break the adherent force and separate a silica sphere from a flat surface.

### 4.4.3 Optomechanical oscillation for separating particles

In section 3.3, the application of OMO for optical pulse generation has been discussed, which analysed the optical field during the oscillation. Here, the mechanical motion during this oscillation will be discussed and the application for a sonicating source that can be used to separate micro/nano particles will be given.

For the purpose of separating particles using OMO, a large acceleration during the oscillation is required. For oscillation with a sinusoidal pattern, the acceleration is linearly proportional to the oscillation amplitude. It has been shown that this harmonic oscillation assumption breaks down in a large oscillation amplitude regime. From the OMO process in the chaos regime, the mechanical motion is random and quite sensitive to the initial condition. This poses challenges for the application for separating particles in on-chip levitated optomechanics because of the uncertainty when designing the on-chip cavity optomechanical device. Therefore, the chaos regime should be avoided for separating particles. For the OMO process with mushroomlike phase trajectory shown in Figure 3.9, it can be seen that the value of the normalised acceleration $d^2\tilde{x}/d\tilde{t}^2$ experiences an increase by nearly an order of magnitude to $6 \times 10^5$ when the optical cavity is in resonance, which is very beneficial for particle separation. Here, a real cavity optomechanical system is assumed with a reasonable set of parameters as: mechanical resonant frequency $\Omega_m/2\pi = 5\ MHz$, optomechanical coupling coefficient

$G = 2\pi \times 1\ GHz\ nm^{-1}$, effective mechanical mass $m_{eff} = 1\ pg$, input laser wavelength $\lambda_L = 1550\ nm$. According to the transformation relationships shown in Section 3.1.2, the maximum acceleration can be calculated as,

$$\frac{d^2x}{dt^2} = \frac{\Omega_m^3}{G}\frac{d^2\tilde{x}}{d\tilde{t}^2} \approx \frac{(2\pi \times 5 \times 10^6)^3}{2\pi \times 1 \times 10^{18}} \times 6 \times 10^5 \approx 2.96 \times 10^9\ m/s^2. \tag{4.17}$$

The required optical input power to realize this acceleration is,

$$P_{in} = \frac{\tilde{P} m_{eff} \Omega_m^4 \omega_L}{4G^2} \approx 300\ mW. \tag{4.18}$$

According to the results shown in Figure 4.12, this predicted acceleration acting on the particle can be realized by an input optical power with only 300mW, and in the meantime can theoretically separate a spherical silica particle with as small as radius 200 $nm$ from the surface of the optomechanical device.

## 4.5 Conclusion and discussion

In summary, the design, optimisation and scaling effect of dual-waveguide optical traps on the SOI platform are presented by comprehensive numerical simulations in Lumerical FDTD Solutions. In the simulations, two identical rib waveguides with two in-phase mode sources injected into opposite directions are designed to form a dual-waveguide optical trap. Within the gap, multiple interference maxima or hot spots can be formed, where the particles are trapped.

By studying the theoretical equations of optical force and trapping potential acting on a Rayleigh particle, it was found that the trapping capability can be characterised by the optical intensity at the trapping location. The simulations demonstrate that the waveguide thickness is a crucial parameter in the design of a dual-waveguide optical trap, and the optimal thickness depends on the gap distance between waveguides. The parametric sweep simulation found that the optimal waveguide thickness $t_{op}$ increase with the gap distance $L$ generally, and in the meantime is composited with periodic features whose period meets the resonance condition (standing wave in the gap). The wavelength from 1100 $nm$ to 2000 $nm$ was also swept and it was found that the optimal thickness shows a scaling effect over wavelength, meaning that the normalised optimal waveguide thickness $t_{op\_norm}$ shows the same features over normalised gap distance $L_{norm}$. The value of $t_{op\_norm}$ in various trapping points are summarised to provide explicit information on designing the optical trap. This optimization result and the scaling effects show the fundamental relationship of waveguide thickness, gap distance, input wavelength when designing an on-chip dual-waveguide optical trap, and provide comprehensive guidance to design such an optical trap. This will pave the

way for further applications of dual-waveguide optical traps in biological manipulation, Raman spectroscopy, on-chip levitated optomechanics, and integrated quantum photonics.

Lastly, it was proposed that the OMO process could be used to break the adherence force, which prevents the particle separating process. The adherent force between particles and surface are analytically derived, and the required acceleration to vibrate the particles from a surface is calculated for different particle size. Then, the acceleration variations during the OMO process were investigated, and it was found the mechanical resonator experiences an abrupt increase in acceleration when the OMO is in a mushroomlike phase trajectory. This increase is very beneficial for particle separation. A set of reasonable optomechanical parameters was assumed, and it was found an input power of 300 $mW$ can separate a spherical silica particle as small as 200 $nm$ from the surface of the optomechanical device. All of these works combined lay the foundation of a fully on-chip optical trapping system working on vacuum or air.

# Chapter 5

# Integrated optomechanical components based on thick SOI platform

The integration of silicon photonics circuits and mechanical structures increases both the design and fabrication complexity. In order to locate and solve the issues that may be encountered during the experimental demonstration of the two applications that has been discussed in Chapter 3 and Chapter 4, individual optomechanical components on silicon photonics platform need to be first tested.

In this section, I will present the on-chip integrated optomechanical components design, fabrication, and measurement based on a thick 1.5 $\mu m$ SOI platform. The components include single-mode rib waveguides, grating couplers, multimode interferometers (MMIs), waveguide Bragg gratings, high-Q micrometre-size optical resonators and mechanical resonators. The experimental results indicate that the components all function well, and these components pave the way for the full integration of on-chip silicon optomechanics, especially for two previously discussed applications.

## 5.1 The advantages of a thick SOI platform

As has been reviewed in Section 2, silicon photonics shows its strength in various aspects. In this project, therefore, SOI is used as the material platform for the integrated optomechanical system. SOI is an attractive platform for the integration of such devices, as it is easily commercial available with different specifications, and a lot of fabrication processes have been developed worldwide.

Currently, the majority of silicon photonics devices use SOI wafers with the top silicon layer of less than 300 $nm$, among which 220 $nm$ is most widely used. The motivations

to use the thin silicon layer come from various aspects [136]. Firstly, the thin silicon layer less than 300 $nm$ can surely maintain the single-mode condition in the vertical direction for both rib and strip waveguide. Secondly, the fabrication process of the SOI with a thin silicon layer is compatible with the CMOS foundry infrastructures. Thirdly, the SOI with a thin silicon layer is suitable for making pn-junction for modulator applications.

However, for the applications of integrated optomechanics applications discussed in the previous two chapters, SOI wafers with a thicker silicon layer are preferred. Thick SOI can also maintain the single-mode condition through a rib waveguide design. Even more, thick SOI is suitable for low-frequency application, can handle higher power, has low propagation loss and larger mode size, which are all important for cavity optomechanics for DFOS and optical trapping.

### 5.1.1 Low mechanical frequency

Thick SOI platform shows its special strengths for the applications of integrated optomechanics for long-distance DFOS measurement. As has been analysed in the Section 3.5, the mechanical resonance frequency $\Omega_m$ is usually larger than $\sim MHz$ in the thin SOI substrate, which limits the sensing distance to several hundred metres. The thick SOI platform, however, is suitable for fabricating a low-frequency mechanical resonator compared to the widely-used thin ($< 300\ nm$) SOI substrate. For example, the radial frequency of the fundamental vibration mode of a double-clamped beam is given by $\Omega_m = 6.4585\frac{h}{L^2}\sqrt{\frac{E}{\rho}}$ [137], where $h$ is the beam thickness, $L$ is the beam length, $E$ is the Young's modulus of the beam, $\rho$ is the material density of the beam. On the other hand, the length of the double-clamped beam can not be too long due to the residual compressive stress introduced by the SOI wafer bonding process. This compressive stress can cause buckling of the beam, which is not desired for a cavity optomechanical system. The beam buckles when the compressive stress is larger than $\pi^2 Eh^2/3L^2$ [137], where $E$ is the Young's modulus, $h$ is the thickness of the beam and $L$ is the length of the beam.

This relationship shows that the different beams with the same value of $L/h$ have the same capability to resist buckling. It can also be found that when scaling up the volume of the beam, the mechanical resonant frequency decreases with the same order of magnitude. Therefore, thick SOI platform can be used to fabricate a low-frequency mechanical resonator and thus provide a good solution for long-distance DFOS applications.

### 5.1.2 High power handling

The capability to handle high power in silicon waveguides is critical. Especially for the two applications that have been proposed in previous chapters, they both require high optical power. The OMO-based OPT and SWOS both needs high optical power to get a larger mechanical oscillation amplitude $A$, and thus a larger ER and larger frequency-sweeping range. The on-chip optical trapping also needs high optical power to increase the trapping potential to make the trapping more stable.

However, the two-photon absorption (TPA) effect in silicon is significant [138, 139]. The TPA is an instantaneous nonlinear absorption effect, and the absorption depends on the power per unit area in the waveguide. When a laser with high optical power per unit area is injected into the waveguide, the silicon waveguide will experience power saturation and self-heating, which will then generate free carriers and change the refractive index. This will be detrimental for the applications. Therefore, a larger waveguide cross-section can handle a high optical power.

According to [136], the power threshold for a 220 $nm$ thick waveguide (effective mode area 0.1 $\mu m^2$) is around 300 $mW$, while a thicker waveguide with an effective mode area 3.5 $\mu m^2$ can handle up to 10 $W$. Therefore, a thicker SOI platform is desired to increase the maximum handling power in a silicon waveguide.

### 5.1.3 Low waveguide propagation loss

A low waveguide propagation loss are critical when making high Q-factor optical cavities. Although it is shown in Section 3.3 that a lower optical Q-factor (unresolved sideband regime) is preferred for better optical pulse shape, a high-Q optical cavity is still needed to lower the required optical input power. In addition, a low waveguide propagation loss is also the key for large-scale silicon photonics circuits involving multiple components and functions, as many of them would introduce extra loss.

In silicon waveguides, the propagation losses originate from three sources: scattering, absorption and radiation [130]. For high optical power, the waveguide loss is mainly induced by the TPA effect. For low optical power, the absorption loss is mainly the band edge absorption and can be negligible for 1.5 $\mu m$ wavelength range. The radiation loss for a straight silicon waveguide can also be negligible. The main propagation losses come from the scattering caused by the waveguide surface roughness [62]. The waveguide mode in a thick waveguide and larger waveguide cross-section is tightly confined, and thus, the electromagnetic field has less interaction with the rough surface. However, the thin silicon layer can not confine the waveguide mode very well, leading to an increased overlap with the waveguide surface and a large waveguide propagation loss.

For instance, the rib waveguide in 220 $nm$ SOI platform fabricated in the CORNERSTONE Rapid Phototyping Platform has a waveguide loss of 3 $dB/cm$ [140], while the rib waveguide in 3 $um$ SOI platform developed by VTT shows a waveguide loss as low as 0.1 $dB/cm$ [141].

### 5.1.4 Large mode size

As shown in the dual-waveguide optical trapping optimisation in Chapter 4, the optical field experiences a sharp divergence and power loss at the end of the waveguide due to the small mode area. Also, the optimised waveguide thickness generally increases with the gap distance, which poses a limit on the size of the particle that can be trapped. In addition, considering the fact that silicon is an indirect band-gap semiconductor not applicable for making laser sources, integrating a mature and well-developed III-V semiconductor laser source in the silicon optomechanical chip is not straightforward and becomes a long-term goal.

Existing III-V lasers have a multi-micron mode size, which makes it difficult to integrate the lasers with the 220 $nm$ thick waveguides due to the large coupling loss induced by the mode area mismatch. For the thick SOI platform, however, the straightforward edge coupling can directly and efficiently guide the light from the III-V laser sources to the silicon chips. In [136], a coupling efficiency of 0.2 $dB$ has been achieved using a 3 $\mu m$ thick SOI. In addition, the simple V-groove structure can provide highly efficient coupling between single-mode optical fibre and the thick silicon waveguide in the multi-micron size scale [142].

## 5.2 Integrated photonic components design

### 5.2.1 1.5 $\mu m$ thick SOI platform

The advantages of the thick SOI platform have been discussed above. However, a larger bend radius is generally necessary to ensure low bend loss for thicker SOI waveguides. For single-mode strip waveguides in the thin ($< 300$ $nm$) SOI platform, the loss in the bend area mainly comes from the optical radiation loss, which can be reduced to sufficiently low with micrometre-scale bending radii. For the thick SOI platform, a rib waveguide must be used to enable the single-mode operation. However, rib waveguides have low lateral index contrast compared to strip waveguides, which results in extra loss due to the mode energy leaked into the slab. To solve this issue, large bend radii in the order of several hundred micrometres to millimetres must be used, and a larger waveguide thickness needs a larger bend radius [38] to avoid excessive optical loss. This leads to a larger footprint for the silicon photonics chip in a thick SOI

platform and is detrimental to the compactness of devices. Even though Euler-shape and multi-mode bends had been proposed and demonstrated good compatibility, with 10 $\mu m$ bend radius in a 4 $\mu m$ thick SOI showed loss below 0.02 $dB/90^{\circ}$, thicker waveguides still need a larger bend radius to enable low bend losses when compared to the bend in a thin SOI with the same design method [143].

Considering these trade-offs, an SOI wafer with 1.5 $\mu m$ thick silicon layer and 2 $\mu m$ thick buried oxide layer is used. Nevertheless, unlike the 220 $nm$ and 340 $nm$ SOI platforms where the photonic component designs are well-researched and easily available, the photonic components need to be specially designed for the 1.5 $\mu m$ SOI platform.

### 5.2.2 Optical waveguide

An optical waveguide is the most basic passive photonic component, which is used to guide light between different photonic components. In an optical waveguide, the optical energy is constrained in the dielectric structure by total internal reflection from the dielectric interfaces. The working principle of an optical waveguide can be demonstrated by the planar type waveguide as shown in Figure 5.1. The refractive index of the core layer, the lower substrate and the top cladding layer are $n_1$, $n_2$ and $n_3$ respectively. When $n_1 > n_2$, $n_1 > n_3$ and the incident angle is greater than the critical angle, and the total internal reflection can occur at the interface. Thus the light is confined to the core layer with a high refractive index $n_1$ and propagates to the right.

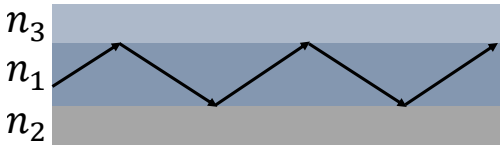


(A)

FIGURE 5.1: Total internal reflection, describing the working principle of a dielectric waveguide.

Rib and strip waveguides are the commonly used waveguides in silicon photonics. The cross-sections of these two types of the waveguide are shown in Figure 5.2 (A, B). For both of them, light is confined in the high refractive index core area, namely the silicon layer for an SOI wafer, with a $SiO_2$ substrate underneath. The cladding area can be either deposited $SiO_2$ or air. The electric field profiles of the fundamental TE modes of the two types of waveguide simulated by Lumerical Mode Solutions [144] are shown in Figure 5.2 (C, D). A waveguide mode is a time-harmonic solution to Maxwell's equations, which are determined by the cross-sectional refractive index profile of the waveguide. Each waveguide mode has an effective index $n_{eff}$, thus the propagation constant along the propagation direction of a waveguide is given by $k = n_{eff}\frac{2\pi}{\lambda}$, where $\lambda$ is the optical wavelength.

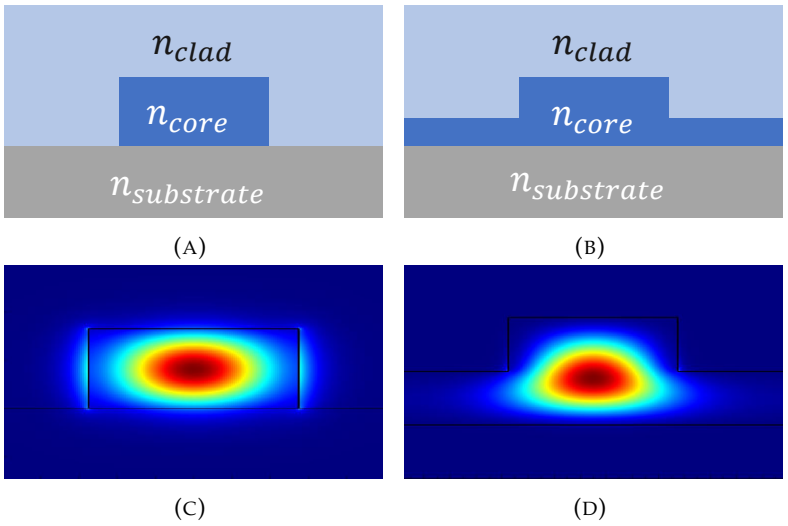


FIGURE 5.2: The cross-section and mode profile of rib and strip waveguide (A) Cross-section of a strip waveguide. (B) Cross-section of rib waveguide. (C) TE mode field profile of a strip waveguide. (D) TE mode profile of a rib waveguide.

Single-mode is usually preferred in silicon photonics to avoid unwanted coupling to higher order modes and the resulting detrimental mode beating and power radiation in the bend [143]. The single-mode strip waveguide usually has a dimension on the order of a few hundred nanometres in both width and height. The rib waveguide, however, can maintain the single-mode condition with micrometre-scale cross-section when correct waveguide dimensions are used, where higher optical modes leak into the slab regions [62]. To ensure the single-mode condition in 1.5 $\mu m$ SOI, the rib waveguide should be used instead of the strip waveguide. For a large cross-section rib waveguide with dimensional parameters shown above in Figure 5.3, the single-mode condition can be maintained by the condition [130]:

$$\frac{W}{H} \leq 0.3 + \frac{D/H}{\sqrt{1-(D/H)^2}}, \tag{5.1}$$

$$\frac{1}{2} \leq \frac{D}{H} \leq 1, \tag{5.2}$$

where $W$ is the width of the rib waveguide, $H$ is the thickness of the silicon layer and $D$ is the slab thickness. The waveguide that is used throughout this thesis has an $H = 1.5\ \mu m$, $D = 0.75\ \mu m$, and $W = 1.1\ \mu m$, which matches the single-mode condition mentioned above and ensure a large cross-section of the waveguide. The simulated effective index and group index of the fundamental TE model near 1550 $nm$ is $n_{eff} = 3.400$ and $n_g = 3.714$.

As can be seen from the mode field profile in Figure 5.2 (D), the confinement of mode in rib waveguide is tight and has less contact area with the etched sidewalls, so it has

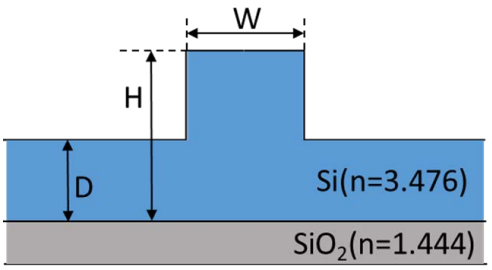


(A)

FIGURE 5.3: Cross-section of a silicon rib waveguide.

lower scattering losses which result in lower waveguide propagation losses. In addition to that, as the dimensions get larger, fabrication tolerances become easier to meet [145].

### 5.2.3 Grating coupler

Efficient light coupling between the external standard optical fibre and the silicon photonic chip is a key functionality for the integrated silicon optomechanical system. Various methods have been proposed, including edge couplers, microlenses couplers and grating couplers.

The edge coupler directly butt-couples a standard optical fibre to the facet of an optical waveguide with expanded waveguide mode, which can be realized by increasing the waveguide core size [146] or reducing the model confinement through the inverse taper [147]. The microlenses coupler [148] utilises a lens to focus the input laser beam to the end facet of an optical waveguide. For both these methods, all the inputs and outputs need to be routed to the edge of the chip for the coupling process, which greatly limits the test flexibility and increases the complexity of the design process of the chip. As for the grating coupler, light can be injected into or collected from the chip surface using the grating coupler, which can be designed to be anywhere on the chip. Grating couplers can thus be used for wafer-scale tests of the integrated photonic devices without the need to dice and polish individual devices. In addition, grating couplers provide relaxed alignment tolerances and comparatively high coupling efficiency. These benefits make grating couplers the most promising coupling method for integrated photonic devices [149].

The design of a complete 3-dimensional (3D) grating coupler is usually simplified to the 2-dimensional (2D) problem as the width of the grating is much larger ($> 10\ \mu m$) than the optical wavelength. The 2D schematic of a grating coupler made from SOI substrate is shown in Figure 5.4. The coupler consists of a silicon core layer, a top cladding layer, and a bottom buried $SiO_2$ layer. The silicon core layer is etched uniformly to form periodic structures. The cladding can be air or deposited $SiO_2$ to protect the functional

silicon top layer. $t_e$ is the etch depth of the grating, $\Lambda$ is the grating period, $w$ is the width of each grating teeth, and the duty cycle is defined as $DC = w/\Lambda$. The light beam incident in the waveguide from the left can be radiated to the free space with a specific angle $\theta$. It should be noted that an output grating coupler can also be used to couple a light beam into the chip with the same efficiency due to the reciprocity.

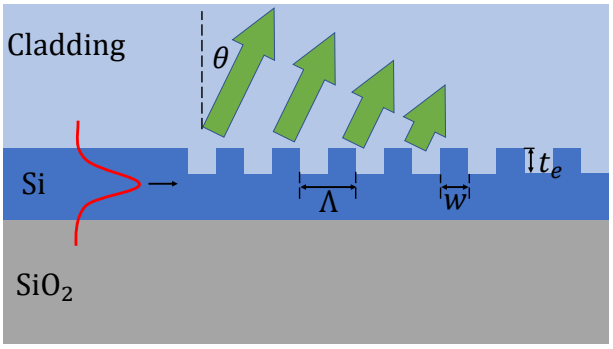


FIGURE 5.4: Schematic cross-section of a grating coupler.

The working principle of the grating coupler is the phase match condition, which requires that in the direction of propagation, the propagation constant in free space must be the same as that in the grating area. This phase match condition can be written as the well-known grating equation [150],

$$n_c sin\theta - n_{eff} = m \cdot \frac{\lambda_0}{\Lambda}, \tag{5.3}$$

where $n_c$ is the refractive index of the cladding, which in this design is 1 for air. $n_{eff}$ is the effective index in the grating region, which is decided by the effective index of the original non-etched waveguide, the etch depth $t_e$ and the duty cycle $DC$. $\lambda_0$ is the optical wavelength, $m = \pm 1, \pm 2, \pm 3...$ and corresponds to the different diffraction modes of the grating. Clearly only the diffraction modes with $m < 0$ can be radiated because the $n_{eff}$ much be larger than $n_c$ to confine the light in the waveguide. The condition under which the the $m$-th order diffraction order can be radiated out of the surface ($-90° < \theta < 90°$) is given by,

$$\frac{m\lambda_0}{-n_c - n_{eff}} < \Lambda < \frac{m\lambda_0}{n_c - n_{eff}}. \tag{5.4}$$

To achieve a high coupling efficiency, single-beam radiation is usually desired for grating coupler design.

Here, a grating coupler on the SOI substrate with 1.5 $\mu m$ thick top silicon layer and 2 $\mu m$ thick buried $SiO_2$ layer needs to be designed. The grating coupler is designed for the use of TE polarisation and 1550 $nm$ wavelength. Although the grating coupler has been widely used in SOI wafer with 220 $nm$ and 340 $nm$ thick silicon layer, their implementation on 1.5 $\mu m$ SOI platform is not straightforward. The main obstacle for

the design of a grating coupler in 1.5 $\mu m$ SOI is the multimode nature in the grating area due to the thick silicon layer. For the waveguide, a rib cross-section with width 1.1 $\mu m$ is used to maintain the single-mode condition. In the grating area, however, the waveguide is too wide to maintain the single-mode condition. Thus the waveguide is vertically multimode.

For the conventional grating coupler shown in Figure 5.5 (A), an adiabatic taper is used to expand the waveguide mode field from the waveguide to the grating. In this case, the mode field at the end of the taper is distributed within the full thickness, which would excite the unwanted higher-order modes in the grating region. Each mode has a different effective index $n_{eff}$ and thus multiple light beams are radiated separately with different angles, which will cause extra coupling loss.

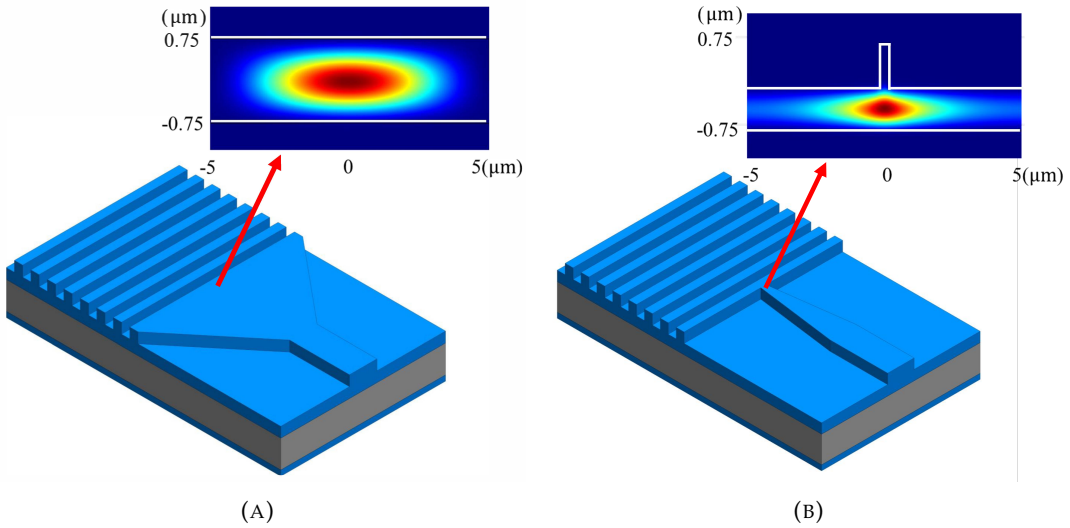


FIGURE 5.5: Schematic of a grating coupler. (A) Conventional design (B) Inverse taper design

To address the above issue, an inverse taper was introduced in the design of a grating coupler based on 1.5 $\mu m$ SOI to realize efficient coupling [151, 152]. As shown in Figure 5.5 (B), an inverse taper is utilized to transform the mode field distribution in both lateral and vertical directions, so the mode is actually pushed down to the bottom slab layer and expands in the lateral direction, which will limit the excitation field to the thinned slab region rather than the full thickness of the slab in the grating area. This inverse taper mechanism will suppress the excitation of higher-order modes and thus enhance the coupling efficiency.

By optimizing the dimension parameters of the inverse taper and grating coupler, the following optimal parameters were obtained: inverse taper end width $x_{end} = 0.33\ \mu m$, etching depth $t_e = 750\ nm$, grating period $\Lambda = 860\ nm$, grating duty cycle $DC = 0.5$. The width of the grating is set to $W_g = 15\ \mu m$ to increase the overlap between the optical fibre the gratings. Notably, this grating coupler design and waveguide design

in the last section can be etched in a single step due to the same height of waveguide and gratings, which is very beneficial for fabrication. Another feature of this design is that the grating coupler actually uses the second diffraction order ($m = -2$) with a negative diffraction angle $\theta = -13.4°$ from the vertical direction. This is quite different from most of the grating coupler designs, which use the first-order diffraction order ($m = -1$) and has a positive coupling angle.

Here, this novel design and the conventional design are simulated in Lumerical FDTD solutions [123]. A 2D grating coupler model is used to simulate the performance of the grating coupler. The grating coupler is simulated as a two-port device. As shown in Figure 5.6 (A,B), port 1 is set as the source at the end of the fibre to inject light from above the grating with a tilted angle, and port 2 lies in the waveguide area (the end of the taper) where the light goes out. The simulation boundary condition is set to be the perfect match layer (PML). For the simulation of the conventional grating coupler, the thickness of the output waveguide is defined as 1.5 $\mu m$, while the thickness of the output waveguide of the novel design is set to 0.75 $\mu m$.

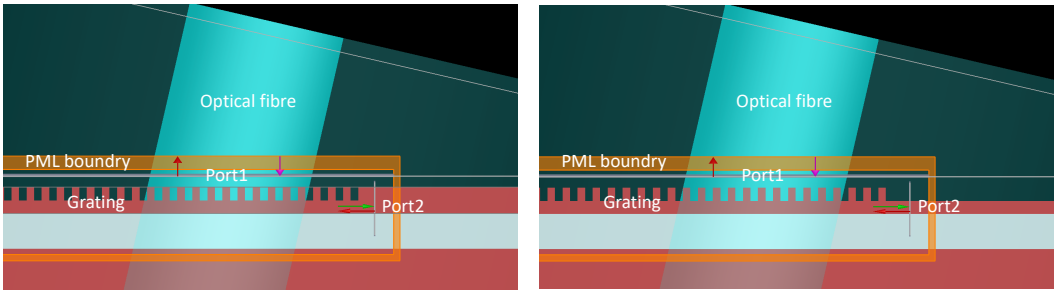


(A) (B)

FIGURE 5.6: The FDTD simulation model for (A) Conventional grating coupler (B) Grating coupler with reverse taper design

The performance of the grating coupler is characterized by the transmission through the grating coupler to the output waveguide. This transmission result can be obtained by viewing the "expansion for port monitor" result of port 2. The result is shown in Figure 5.7 by normalizing the transmission efficiency to $dB$, where the $T_{total}$ is the coupling efficiency of total power transmitted to the waveguide, while $T_{out}$ is just for the fundamental TE mode from the source port. It can be seen that almost all the power is propagating in the fundamental TE mode for inverse taper design, and a maximum coupling efficiency of $-2.4dB$ can be achieved at 1555 $nm$. In comparison, for the conventional grating coupler, the coupling efficiency in the fundamental TE mode can only reach $-6dB$ even though the overall transmission is around the same level in $-2.4dB$. This means more than half of the input power is in the higher mode and will be lost. Therefore, the grating coupler with inverse taper design will be used throughout the project.

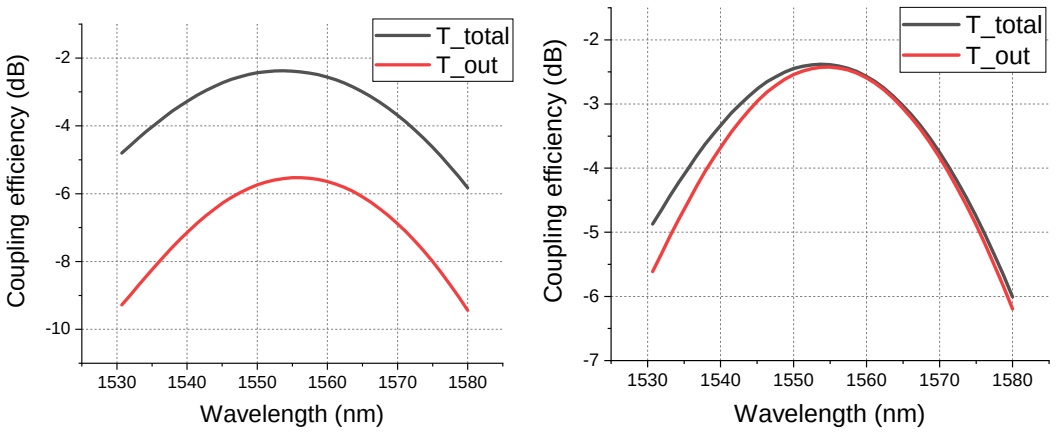


FIGURE 5.7: The FDTD simulation results for (A) Conventional grating coupler (B) Grating coupler with reverse taper design

### 5.2.4 Multimode interferometer (MMI)

An important function in silicon photonics is to split a guided light into two parts and combine them together. There are a few photonic components that can be used to fulfil this function, including Y-splitter, MMI, and directional coupler [62]. Y-splitter is the simplest structure. However, they typically have a higher loss and uneven splitting ratio due to the unavoidable fabrication error of the sharp tip between the two waveguides, which is very critical to the performance of the Y-splitter. For directional coupler, the two waveguides are brought in proximity to enable evanescent coupling between them. Light is coupled back and forth in the two waveguides along with the light propagation direction. An elaborate design of the coupling length and the separation distance between the waveguides can produce any splitting ratio of the coupler. However, the separation distance is normally in the order of several hundred nanometres and has less fabrication error tolerance.

In an MMI, higher modes are excited in the central multimode waveguide section. The interference of these modes can form the self-imaging of the input field at a certain distance [153]. Self-imaging occurs when all the modes in the multimode area arrive in phase at the same point. The output waveguides can be positioned at these self-imaging points where input light is split. Compared to Y-splitter and directional coupler, MMI does not require small gaps or fine tips, therefore have an easier fabrication process. In addition, it has low insertion losses, large optical bandwidth, low polarization dependence and low temperature sensitivity [38].

The typical $2 \times 2$ MMI and $1 \times 2$ MMI are shown in Figure 5.8. In this project, a $1 \times 2$ MMI is required to equally split and combine the light. $1 \times 2$ MMI based on 1.5 $\mu m$ thick silicon layer of SOI and rib waveguide structures has not been reported before, but an analogical $2 \times 2$ MMI was reported based on the same 1.5 $\mu m$ SOI platform.

More underlying theory and general design procedures can be found in [153]. The dedicatedly detailed design process for this $2 \times 2$ MMI on 1.5 $\mu m$ SOI can be found in [154, 155]. Eventually, they got optimal dimension parameters as following: MMI length $L_{MMI} = 256\ \mu m$, MMI width $W_{MMI} = 12.8\ \mu m$, waveguide width $W_w = 2.8\ \mu m$, waveguide separation distance $S = 2.15\ \mu m$, taper length $L_T = 100\ \mu m$.

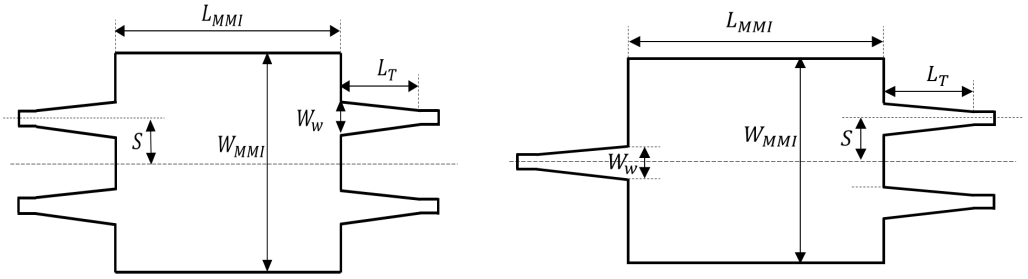


FIGURE 5.8: The schematic diagram of (A) $2 \times 2$ MMI and (B) $1 \times 2$ MMI

For the 1×2 MMI, the corresponding dimension parameters can be directly obtained according to the design characteristics table of MMI shown in Table1 in [153]. The MMI length $L_{MMI} = 256 \times 3/4 = 192\ \mu m$, MMI width $W_{MMI} = 12.8\ \mu m$, waveguide width $W_w = 2.8\ \mu m$, waveguide separation distance $S = 2.15 \times 3/2 = 3.225\ \mu m$, taper length $L_T = 100\ \mu m$.

The MMI with these dimension parameters is simulated using EME solver in Lumerical Mode Solutions [144]. The simulated field profile for the designed MMI is shown in Figure 5.9. The transmission of the fundamental mode can be acquired from the "user s-matrix" from the EME solver. The total transmission is around 98.7%. This simulation verified the functionality of this MMI, and this MMI will be used in this project.

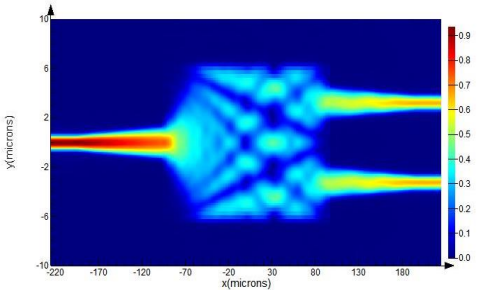


FIGURE 5.9: Simulated field profile of the designed $1 \times 2$ MMI

### 5.2.5 Waveguide Bragg grating

Optical filtering or wavelength selection is also an important function in silicon photonics, which can be usually realised by either ring resonators or waveguide Bragg

gratings. A schematic of waveguide Bragg grating is shown below in Figure 5.10. It is obvious that the waveguide Bragg gratings resembles the grating couplers because they are both structures with periodic features. These periodic features cause periodic modulation on the effective refractive index in the propagation direction of optical mode [156, 157]. For waveguide Bragg grating, this effective index modulated is usually achieved by varying the dimensions of the waveguide.

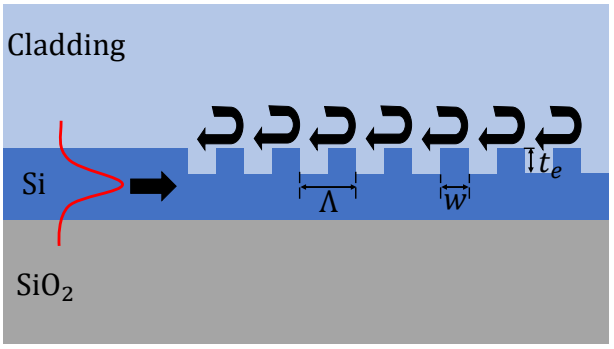


FIGURE 5.10: Schematic diagram of a Bragg grating

The difference between the grating couplers and the waveguide Bragg grating is the radiation angle of the input light. For grating couplers, the input light is radiated out of the chip surface with a tilted angle $\theta$. While for the waveguide Bragg gratings, the radiation angle $\theta = -90°$, which means the input light is reflected back. At each periodic transition of the effective index, part of the light will be reflected. The reflected light interferes constructively in a narrow band at a certain wavelength, resulting in a strong reflection back toward the source. This wavelength is called the Bragg wavelength $\lambda_B$. At other wavelengths, light can transmit through the Bragg grating structure. The Bragg wavelength $\lambda_B$ can be derived using Equation 5.3, in which the $\theta = -90°$, $m = -1$. The reflected light is guided in the same route back to the source, thus $n_c = n_{eff}$. The Bragg wavelength can therefore be readily written as,

$$\lambda_B = 2\Lambda n_{eff}, \tag{5.5}$$

where $\Lambda$ is the grating period, $n_{eff}$ is the averaged effective index of the grating area. One may argue that the $m = -2$ diffraction order can also be used for waveguide Bragg grating. If the $m = -2$ diffraction order is used, then the grating period is found to be $\Lambda = \lambda / n_{eff}$ by substituting $\theta_{m=-2} = -90°$. However, it can be found that the $m = -1$ diffraction mode can also be radiated with a vertical angle $\theta_{m=-1} = 0°$ with this grating period, leading to a huge loss of the Bragg grating. The same reason excludes the use of a higher diffracting mode for the waveguide Bragg grating application. This is also why the grating couplers have to be designed with a tilted radiation angle but not vertically radiating light out.

In this thesis, a rib waveguide based on a 1.5 $\mu m$ silicon layer of SOI is used. The rib waveguide has a height of 1.5 $\mu m$, a width of 1.3 $\mu m$ and an etching depth of 0.75 $\mu m$. Compared to strip waveguides, the overlap between the field profile and sidewalls is very low in the rib waveguide. This weak overlap leads to weaker effective index perturbations compared to strip waveguide gratings when using corrugations with the same size, thus allowing narrower bandwidth with larger periodic features [157].

To make Bragg gratings on the rib waveguide, there are several different configurations. The grating corrugations can be formed on the top [158, 159], on the sidewall [156], or on the slab [156]. In this single-etched waveguide containing only one 0.75 $\mu m$ etch step, etching corrugations on the sidewall is less complex and much more flexible. Therefore, the configuration shown in Figure 5.11 is used. The original width of the unperturbed waveguide is $W$. The corrugation on each sidewall has a width $\Delta W$ and consists of a recessed part and a protruding part ($\pm \Delta W/2$). The number of the gratings are N.

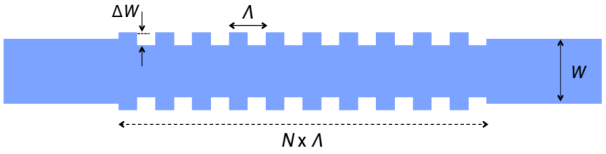


FIGURE 5.11: A top view schematic of a Bragg grating

The effective index of a rib waveguide with a height of 1.5 $\mu m$, width of 1.1 $\mu m$ and etching depth of 0.75 $\mu m$ has been simulated to be 3.400 for TE mode. Due to the weak perturbation on the effective index in a rib waveguide, this value will be used as the averaged effective index in the Bragg grating area. Then, the Bragg wavelength was chosen to be 1550 $nm$, and the corresponding grating period can be now easily derived by using Equation 5.5. The period can be obtained as $\Lambda = \lambda_B/(2n_{eff}) \approx 228\ nm$. Another undecided parameter is the corrugation width $\Delta W$ shown in Figure 5.11. It has been advised that larger corrugation and a higher period number can lead to stronger reflection and wider bandwidth [157]. The influence of these parameters will be analyzed by simulation. An analysis with different grating periods was also carried out to study its influence.

Again, the EME solver in Lumerical Mode Solutions is used for the simulation. During the simulation, only one period of the grating structure needs to be simulated, and the period number can be easily set when editing EME. Two ports are set at each end of the solver to calculate the transmission and reflection. The result can be viewed using the wavelength sweep feature in the EME Analysis window.

All the results are shown in Figure 5.12. It can be found that the simulation results of the Bragg grating agree well with the theory. In Figure 5.12 (A), a pronounced reflection peak appears near the 1550 $nm$ and has a bandwidth of around 3 $nm$ in the first design

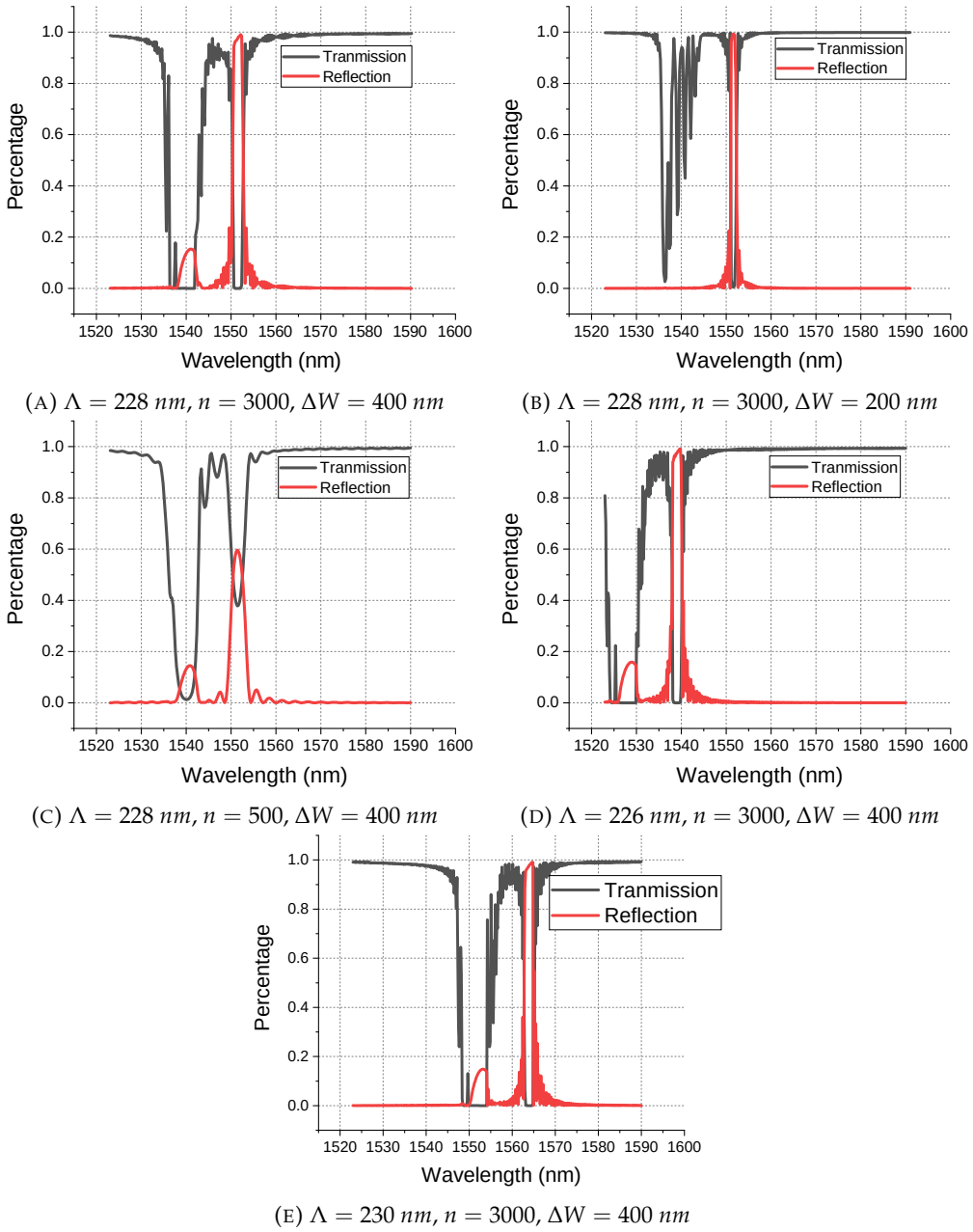


(A) $\Lambda = 228\ nm$, $n = 3000$, $\Delta W = 400\ nm$

(B) $\Lambda = 228\ nm$, $n = 3000$, $\Delta W = 200\ nm$

(C) $\Lambda = 228\ nm$, $n = 500$, $\Delta W = 400\ nm$

(D) $\Lambda = 226\ nm$, $n = 3000$, $\Delta W = 400\ nm$

(E) $\Lambda = 230\ nm$, $n = 3000$, $\Delta W = 400\ nm$

FIGURE 5.12: Simulated transmission and reflection spectrum of the Bragg grating with the dimension parameters.

with $\Lambda = 228\ nm$, $n = 3000$ and $\Delta W = 400\ nm$. In Figure 5.12 (B), the corrugation width $\Delta W$ was reduced to 200 $nm$, and it was found that shorter corrugation width $\Delta W$ leads to a narrower bandwidth. From the result of Figure 5.12 (C), in which the number of the period $n$ was reduced to 500, it was found the extinction ratio decreases. This is due to weaker reflection with less grating periods. When comparing Figure 5.12 (A, D, E), it was found that the Bragg wavelength is very sensitive to the grating period $\Lambda$. When decreasing the period $\Lambda$ to 226 $nm$ by only 2 $nm$, the Bragg wavelength was reduced by around 12 $nm$, and vice versa. The Bragg wavelength increases to around 1563 $nm$ when the period increases to 230 $nm$. It can also be noted that at a shorter wavelength, a

broad drop in the transmission spectrum is present. This is caused by the higher leaky modes [158, 159], which cannot be guided in a single-mode rib waveguide. Therefore, they are not reflected and leak out of the waveguide.

In this project, various waveguide Bragg gratings will be fabricated and tested to verify the simulation results.

## 5.3 Device fabrication

In this section, the fabrication process to create the aforementioned photonic components, optical microresonators and mechanical resonators on a 1.5 $\mu m$ SOI wafer is discussed. The related fabrication imperfections during the fabrication process are also discussed. All the fabrication processes are completed in Southampton Nanofabrication Centre.

### 5.3.1 Fabrication flow

Figure 5.13 shows the outline of the fabrication process flow. The fabrication process starts with a $30mm \times 40mm$ SOI chip with 1.5 $\mu m$ thick silicon layer and 2 $\mu m$ BOX layer (Figure 5.13 (A)). The chip is kept in 210°C oven for 2 hours before 550 nm of ZEP-520A electron beam resist is spun onto the top surface of the chip (Figure 5.13 (B)). The chip is then prebaked with 180°C for 3 minutes and spun with Espacer. A thin film of Espacer is highly conductive, therefore it solves problems related to positional errors during electron-beam (Ebeam) lithography processes (JEOL JBX 9300FS).

The next step is the first Ebeam lithography (Figure 5.13 (C)). All of the photonic components will be defined by this step. The electron beam resists ZEP-520A experiences a physical change when exposed to high energy electrons. After the pattern written process, the chip is first rinsed with DI water to remove the Espacer and then blow-dried. It is then developed in ZED-N50 developer for 135 seconds by heavily shaking the chip, followed by rinsing in Isopropyl alcohol (IPA) for 45 seconds two more times. The developer will dissolve the regions that were exposed to the high energy electron beam. The chip is then blow-dried and ready for the next step process.

The fourth step is the shallow etching of 750 $nm$. The region where the resist was dissolved and removed will be etched and other regions were protected from being etched by the resist. This transfers the patterned resist into the silicon layer of the SOI chip (Figure 5.13 (D)). This is accomplished by inductively coupled plasma (ICP) tool with Oxford Instruments Plasmalab 100 System. The chip is placed on a carrier wafer with Santovac vacuum oil between them, before loading them to the lock-in chamber. Vacuum oil is used for two reasons. Firstly, it works as an adhesive connector that

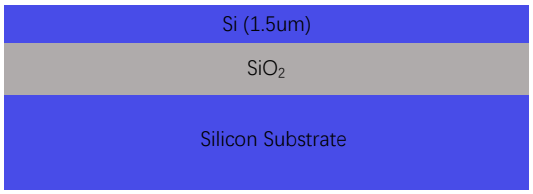


(A) Start Material: 1.5 $\mu m$ SOI with 2 $\mu m$ BOX

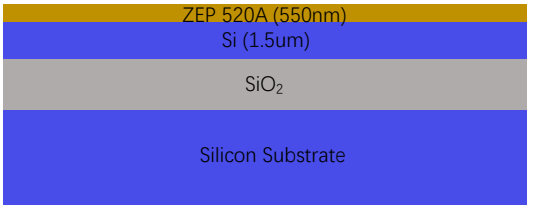


(B) Ebeam resist (ZEP 520A) spin # 1 (550 nm)

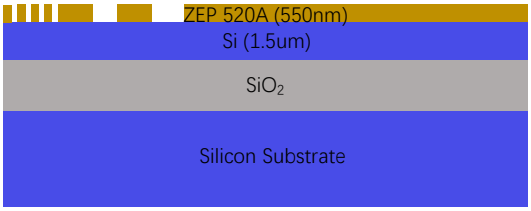


(C) Ebeam Lithography and development

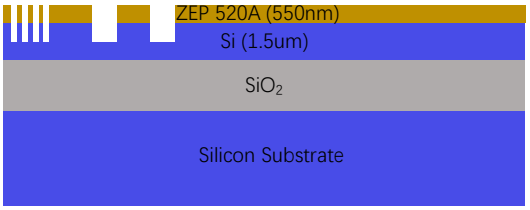


(D) 750 nm shallow ICP etching

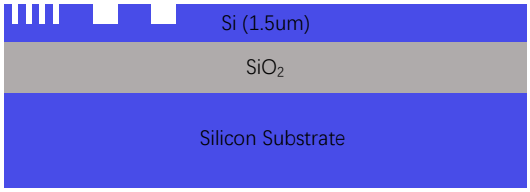


(E) Resist strip (Oxygen Plasma Ash)

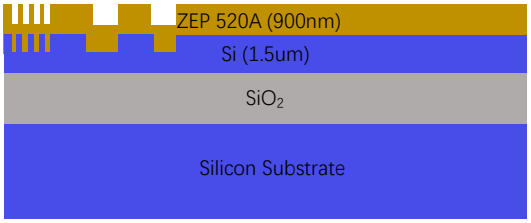


(F) Ebeam resist (ZEP 520A) spin # 2 (900 nm)

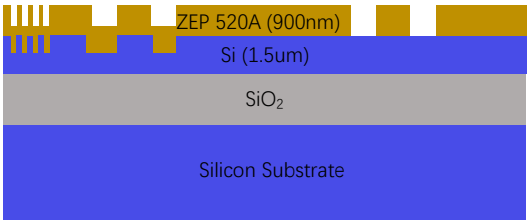


(G) Ebeam Lithography and development

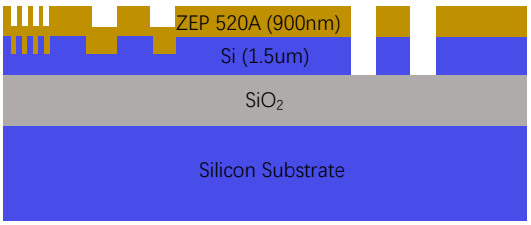


(H) 1.5 $\mu m$ deep ICP etching

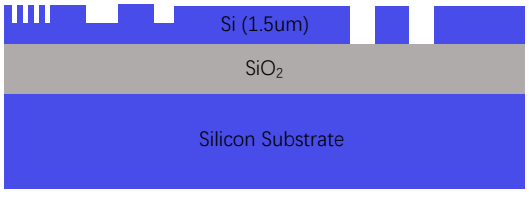


(I) Resist strip (Oxygen Plasma Ash )

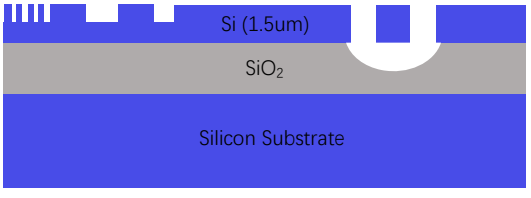


(J) HF vapour etch

FIGURE 5.13: The schematic diagram of the fabrication process. There are two Ebeam lithography steps and two ICP etches. The steps from (A) to (E) are processed for the waveguide, grating coupler and alignment marks; The steps from (F) to (I) is the processing of micro-gap and beam; The last HF vapour etch step suspends the beam and form the mechanical resonator.

can keep the small chip steady during the movement. Secondly, it is a good thermal conductor and can thus keep the temperature of the chip the same at the base plate, which is critical for the ICP etching. The 750 $nm$ etch process is finished with 3-4 steps. After each step, the chip needs to be characterized by Ellipsometer to measure the etch depth and calculate the etch rate. After the etching, the back of the chip needs to be cleaned to remove the vacuum oil. The remaining resist is then stripped by Oxygen Plasma Asher (Figure 5.13 (E)).

A series of the same steps are repeated to spin a resist of 900nm (Figure 5.13 (F)), expose the chip to electron beam (Figure 5.13 (G)) and etch the chip by 1.5 $\mu m$ to BOX layer (Figure 5.13 (H)). A thicker resist is needed because of the deeper etch. The resist is then stripped by plasma Asher (Figure 5.13 (I)). This step is used to define the geometry of the mechanical structure, which in this project is a cantilever beam.

The last step is to suspend the mechanical structure (Figure 5.13 (J)) by Hydrofluoric (HF) acid etching. HF can etch out the $SiO_2$ while keeping the silicon structure remained. The most widespread method of HF etch is wet chemical etching using a solution of HF and water. However, as the solutions dry, the free-moving microstructures can be fulled to stick to each other after the release process due to the air-liquid interface surface tension, which can damage the microstructures. To avoid this problem, HF vapour etching is used, where the $SiO_2$ etching is accomplished by HF etchant in the gas phase. HF vapour etching is thus suitable for releasing fragile microstructure such as the suspended waveguide and cantilever.

### 5.3.2 Fabrication imperfection analysis

The real fabricated device is unlikely to be the same as designed, and the fabrication imperfections always exist due to various sources. The usually discussed fabrication imperfections are surface roughness and misalignment. Here, I will discuss a fabrication imperfection during the deep etching process, which in some sense may serve as a novel fabrication method.

Figure 5.14 show the waveguide cross-section view taken by scanned electron microscope (SEM) after the deep 1.5 $\mu m$ silicon ICP etch, namely after the step (I) in Figure 5.13. This deep etch into the $SiO_2$ layer is used to form the mechanical structure and the shown rib waveguide should have been protected by the thick resist ZEP-520A during the etch. However, it was found that the rib waveguide is etched and two "very-thin walls" are formed on both sides of the waveguide, with width on the order of several nanometres.

This phenomenon can be explained by looking at Figure 5.15, where the schematic diagrams of the waveguide cross-section before and after the deep ICP etch are shown. During this fabrication process, 600 $nm$ thick resist was spun on the chip. This value is

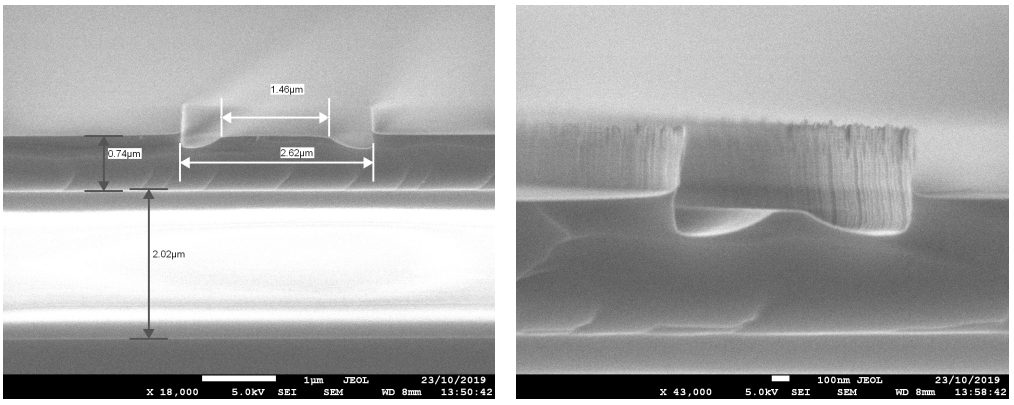


(A) (B)

FIGURE 5.14: Thin wall caused by thin resist

based on the ICP etching selectivity ratio of around 3:1 between silicon and ZEP520A from previous experiences. For an ICP etch with 1.5 $\mu m$, 600 $nm$ thick resists thus should have been thick enough to protect the waveguide from being etched.

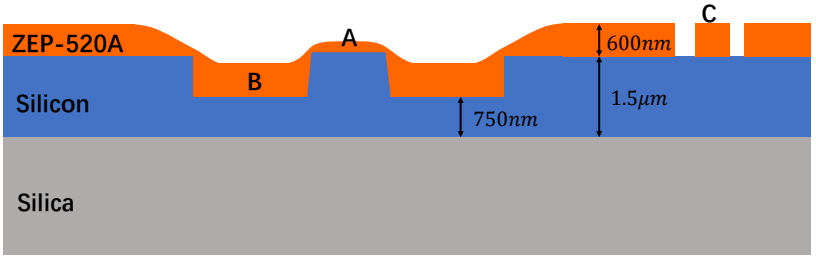


(A) Waveguide cross-section before deep ICP etch

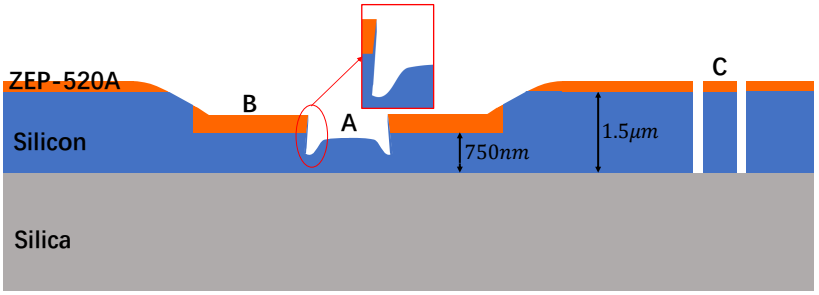


(B) Waveguide cross-section after deep ICP etch

FIGURE 5.15: The schematic diagram of the waveguide cross-section view after the second resist spin

Nevertheless, from the Figure 5.15 (A) showing the waveguide cross-section before the deep etch, it can be found that the resist coating near the stair is quite different from that in a flat surface. On top of the stair (area A), the thickness of the resist is less than the designed 600 $nm$, while in the bottom of the stair (area B), a resist with thickness larger than 600 $nm$ can be obtained. The designed 600 $nm$ resist can only be made at the flat area (area C). Therefore, the resist on top of the waveguide is not thick enough to protect the underneath waveguide. On the other hand, during the

first ICP etch, the sidewall of the formed rib waveguide is not perfectly vertical. The resist covering this tilted sidewall can thus protect the silicon from being etched. The Figure 5.15 (B) shows the cross-section diagram after the 1.5 $\mu m$ deep etch. It can be found the waveguide is etched and two "very-thin walls" are formed on either side of the waveguide. The vertical angle of the waveguide sidewall and the thickness of the resist decide the thickness of the "very-thin wall".

This fabrication imperfection was finally resolved when increasing the resist thickness to 900 $nm$, but this fabrication imperfection provides a potential solution for fabricating vertical thin-wall structures on an SOI chip.

## 5.4 Integrated photonic components measurement

This section will show the observed images, experimental setup and measurement results of the designed silicon photonic components, including grating couplers, MMIs and waveguide Bragg gratings.

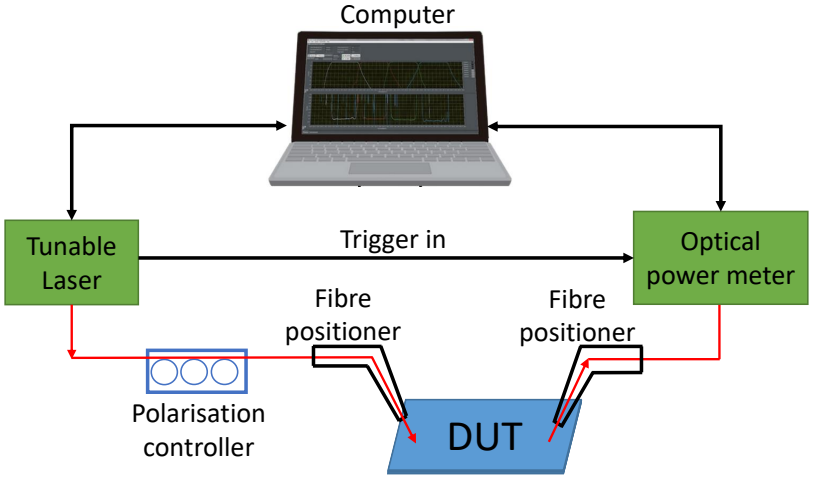


(A)

FIGURE 5.16: The schematic diagram of the experimental setup used to measure the on-chip photonic devices.

### 5.4.1 Measurement setup

The diagram of the experimental setup for silicon photonic components characterisation is shown in Figure 5.16. A continuous-wave (CW) tunable laser in C&L band (Keysight 81940A) is utilised as the laser source. The light coming from the tunable laser is guided to a polarisation maintaining (PM) fibre and then passes through the polarisation controller, where the polarisation of the light can be controlled. Then, the

fibre is fixed to a positioner, through which the fibre can be moved in x, y and z direction and the angle of the fibre can be changed. At the end of the fibre, the fibre cladding is stripped and cleaved to expose the fibre core. After that, the light is coupled into the Device Under Test (DUT) via grating couplers, and coupled out of the DUT into another fibre using the same method. Lastly, the light in this fibre is fed into the optical power meter (Keysight 81634B). The tunable laser and the power meter are connected and synchronised with the lightwave measurement mainframe (Keysight 8163B), so that the real-time wavelength transmission spectrum can be measured. To achieve a complete alignment between the fibre and the grating coupler, the transnational motion on X-Y-Z stage, the angle of the fibre arm and the polarisation of the input light need to be finely adjusted to make the optical power transmitted out from the DUT as large as possible. A microscope over the chip is used to aid the alignment process. A micrometre is used to adjust the angle of the fibre arm. After the fibre has been fully aligned, the laser wavelength is then swept and the power transmission in the optical power meter is recorded, through which the transmission spectrum of the DUT is obtained.

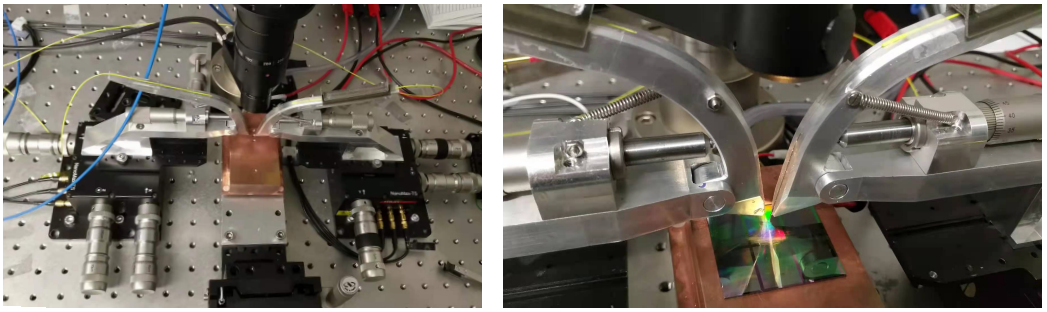

(A) (B)

FIGURE 5.17: The fibre coupling platform

The fibre coupling platform as shown in Figure 5.17 consists of two piezoelectric controlled stages adjusting the fibre position, one manual stage for adjusting the sample under test, another manual stage for adjusting the microscope. Other components not shown here include piezoelectric controller, microscope illumination, thermal controller, microscope display monitor and pumping system for fixing the sample.

### 5.4.2 Grating coupler

The SEM images of the fabricated grating coupler with inverse taper design are shown in Figure 5.18. The inverse taper is clearly shown and connects to the uniform gratings. The measured grating period is $\Lambda = 857\ nm$, and teeth width is $w = 427\ nm$, which are close to the designed parameters 860 $nm$ and 430 $nm$ respectively shown in the last section.

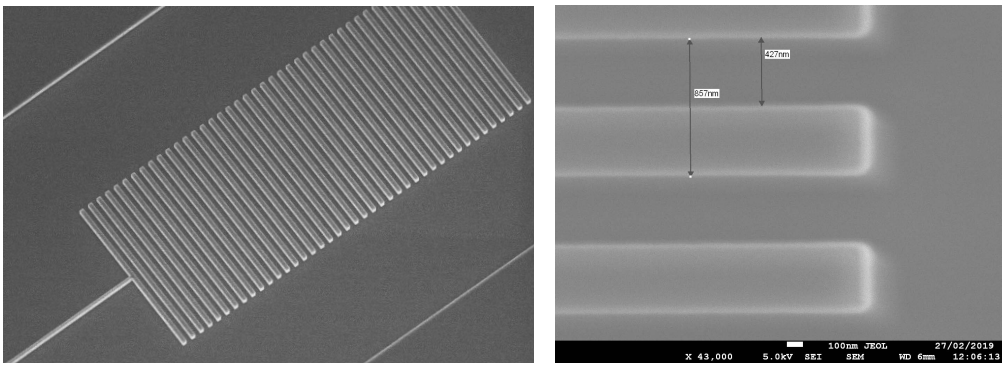


(A) (B)

FIGURE 5.18: The SEM images of the fabricated grating coupler. (A) shows the inverse taper connected to uniformly etched gratings. (B) shows the measured dimensional size of the grating period, with grating period $\Lambda = 857\ nm$ and teeth width $w = 427\ nm$, which are close to the designed parameters 860 $nm$ and 430 $nm$ respectively shown in the last section.

The coupling efficiency of the designed grating coupler is tested. The coupling angle is set to $-13.4°$. The fibre stage and polarization controller are first adjusted to maximise the transmission. Figure 5.19 (A) shows the measured coupling efficiency and simulation coupling efficiency. The measured coupling efficiency is obtained from the measured data divided by a factor of 2 because there are two grating couplers. It can be seen from the results that the peak transmission wavelengths in both the measurement and simulation are around 1555 $nm$, showing a good agreement. However, the measured maximum coupling efficiency is around 5.5 $dB$ while the simulation value is around 3 $dB$. The extra losses could be attributed to the setup intrinsic losses and 5.5 $dB$ loss per grating coupler is an acceptable result when compared to other measurement results from the fabricated grating couplers based on 220 $nm$ or 340 $nm$ SOI in CORNERSTONE MPW foundry [160, 140], where they can get around 5dB loss per grating coupler. The result also shows a 3 $dB$ bandwidth of 40 $nm$.

The coupling angle influence on the performance of the grating coupler is then studied. As shown in Figure 5.19, the measured coupling efficiency of the grating coupler with coupling angle from $-11°$ to $-15°$ are plotted. It can be found that the coupling angle influences the central wavelength of the grating coupler, with a larger angle leading to a decrease central frequency. The tuning coefficient, defined as $\delta\lambda/\delta\theta$, is calculated to be around 5 $nm$ per degree. This relationship between the coupling angle $\theta$ and the central frequency can also be verified via Equation 5.3. It was also found that the best coupling efficiency occurs for the coupling angle with around 13°, which validates the optimisation results of the grating coupler. Another point to notice is the periodic ripples on the transmission spectrum, which is inevitably caused by the Fabry-Perot cavity form by the two grating couplers and the waveguide.

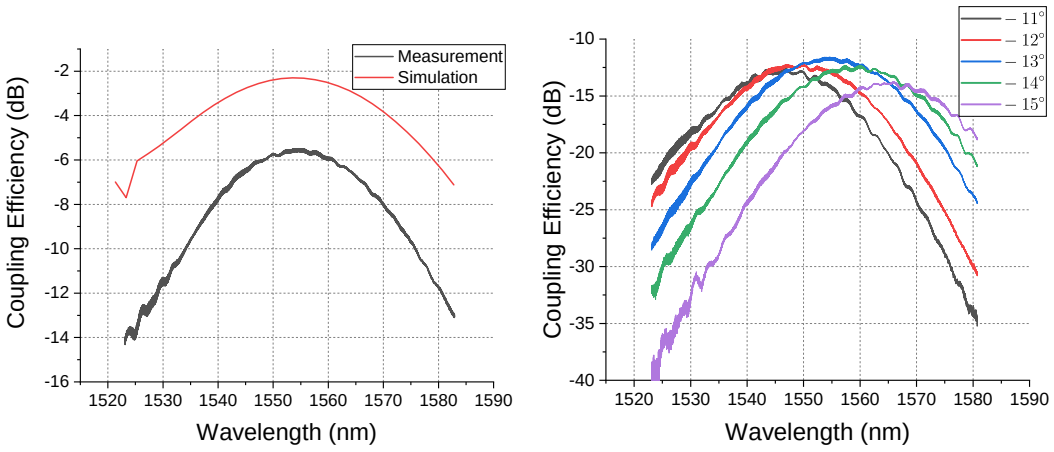


(A) (B)

FIGURE 5.19: (A) The measurement and simulation result of a single grating coupler with inverse taper design, the coupling angle is set to be $-13.4°$. The data is obtained from the measured coupling efficiency divided by a factor of 2 because there are two grating couplers. (B) The measurement results of the grating coupler with coupling angle varying from $-11°$ to $-15°$.

### 5.4.3 MMI

The fabricated MMI is shown in Figure 5.20, which shows a good geometry. The main figure of merit of a $1 \times 2$ MMI is the inertial loss and the power splitting ratio between the two output waveguides. For an ideal $1 \times 2$ MMI, the power transmitted out from any output waveguide should be 50% of the input power, which corresponds to a $-3dB$ coupling loss. The fabricated MMI is tested using a cascaded MMIs structure fabricated in the same chip. The cascaded structure is shown below in Figure 5.21. A number of MMIs are connected through one of the two outputs and the input, and another output of each MMI is connected to a power meter to measure the insertion loss and split ratio of MMI.

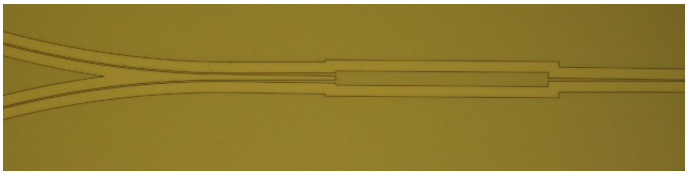

FIGURE 5.20: The image of the fabricated $1 \times 2$ MMI.

In this measurement, 8 MMIs are cascaded and measured with a 1550 $nm$ wavelength laser using grating couplers. The measured result is shown in Figure 5.22. It can be seen that the transmission shows a perfect linear relationship with the unit number. The measured data is linearly fitted, and an average split ratio of 2.96 $dB/unit$ is derived. This value is very close to the ideal value of 3dB and proves that the design of the MMI is perfect.

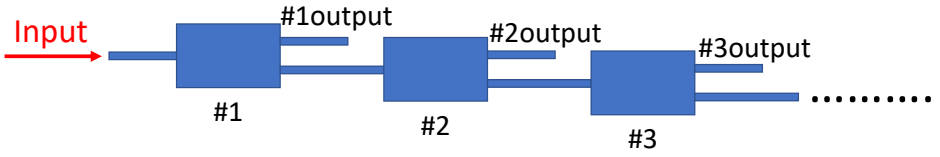


FIGURE 5.21: Schematic of the cascaded MMIs test structure, with the input of an MMI connected to one of the outputs of another MMI.

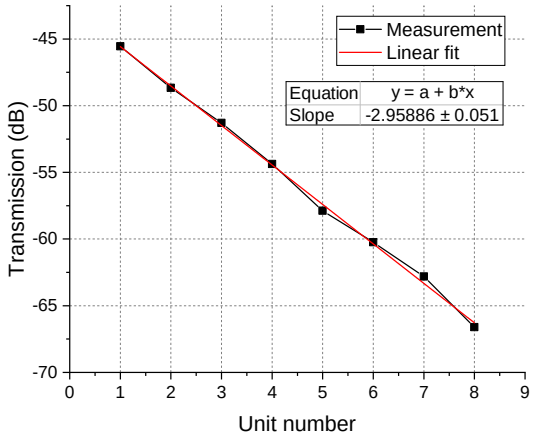


FIGURE 5.22: The measurement result of the cascaded MMIs. The lines with black dots are the experimental measurement results, and the red line shows the linear fitted data. An average power spitting ratio of 2.96 $dB$ is inferred from the results, which shows the functionality of the fabricated MMI.

### 5.4.4 Waveguide Bragg grating

The SEM images of the fabricated waveguide Bragg gratings are shown in Figure 5.23.

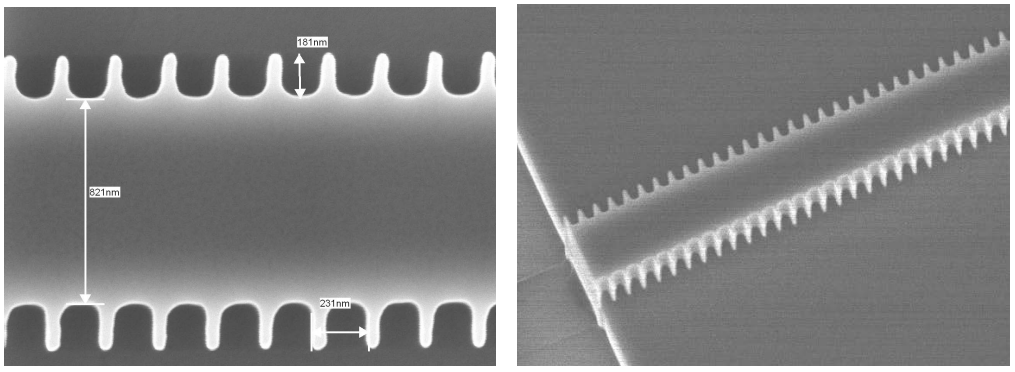


(A) (B)

FIGURE 5.23: Waveguide Bragg grating

The measured corrugation width is $\Delta W = 181\ nm$, grating period $\Lambda = 231\ nm$, which are close to the designed parameter 200 $nm$ and 228 $nm$ respectively. However, the designed square corrugations on each sidewall of the waveguide Bragg grating are fabricated to be in round shapes. This can be attributed to the unavoidable fabrication

errors. The image taken from a tilted angle shows that the etching of the sidewalls of the waveguide Bragg grating is vertical and form a good geometry.

Bragg gratings are tested under two different conditions, namely with a gap or without a gap.

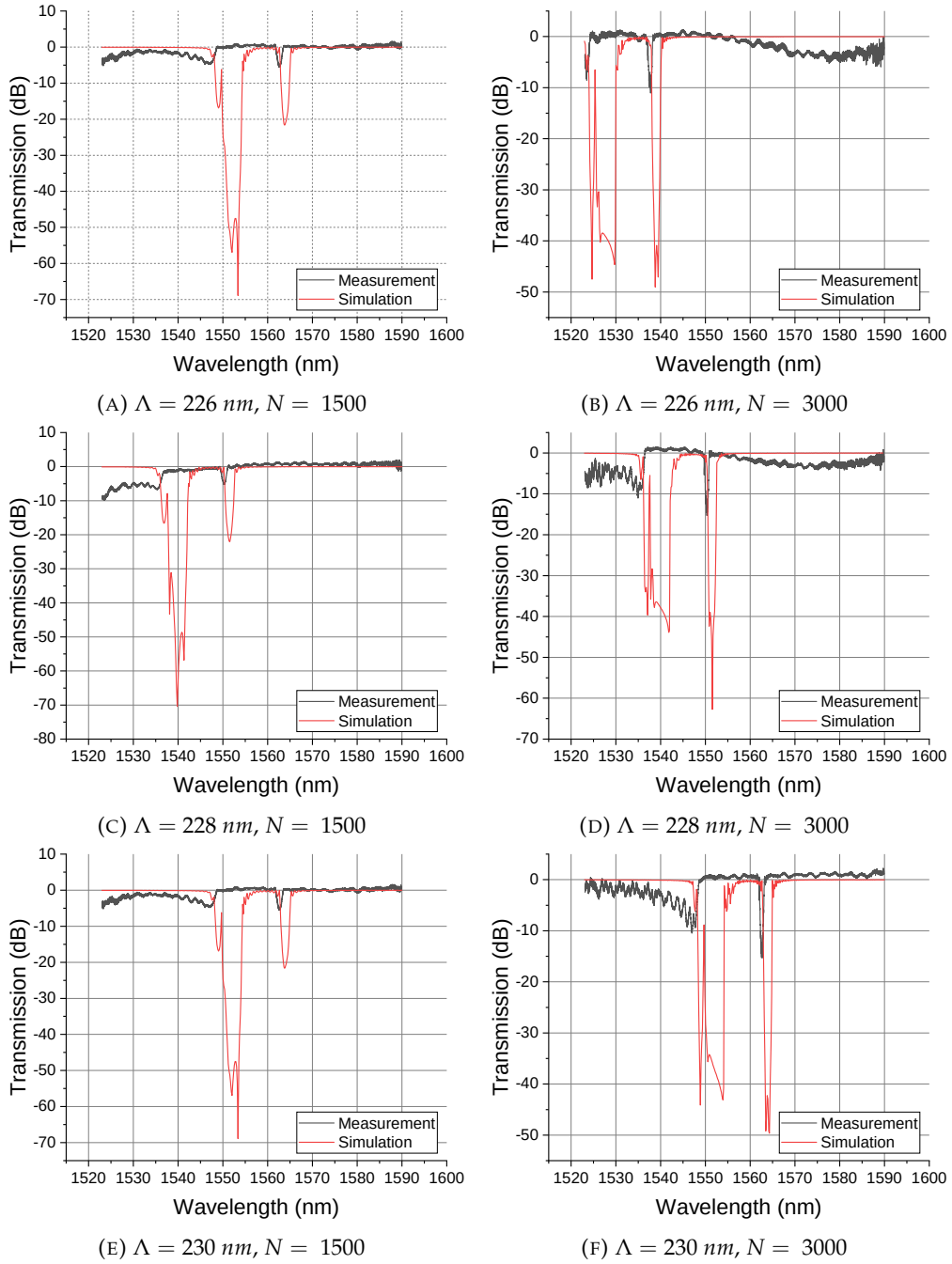


(A) $\Lambda = 226\ nm$, $N = 1500$ (B) $\Lambda = 226\ nm$, $N = 3000$

(C) $\Lambda = 228\ nm$, $N = 1500$ (D) $\Lambda = 228\ nm$, $N = 3000$

(E) $\Lambda = 230\ nm$, $N = 1500$ (F) $\Lambda = 230\ nm$, $N = 3000$

FIGURE 5.24: Measurement results for the waveguide Bragg gratings without gap, the parameters are (A) $\Lambda = 226\ nm$, $N = 1500$. (B) $\Lambda = 226\ nm$, $N = 3000$. (C) $\Lambda = 228\ nm$, $N = 1500$. (D) $\Lambda = 228\ nm$, $N = 3000$. (E) $\Lambda = 230\ nm$, $N = 1500$. (F) $\Lambda = 230\ nm$, $N = 3000$;

| Device number | Period / (nm) | Number of gratings | Bragg wavelength/(nm) | | Extinction ratio/(dB) | |
|---|---|---|---|---|---|---|
| | | | Test | Simulation | Test | Simulation |
| 1 | 226 | 1500 | 1537.6 | 1539.1 | 5.5 | 21.9 |
| 2 | | 3000 | 1537.6 | 1539.1 | 11.1 | 49 |
| 3 | 228 | 1500 | 1550.3 | 1550.5 | 4.5 | 22.1 |
| 4 | | 3000 | 1550.3 | 1550.5 | 14.6 | 62.7 |
| 5 | 230 | 1500 | 1562.6 | 1563.8 | 5.8 | 21.6 |
| 6 | | 3000 | 1562.6 | 1563.8 | 16 | 49.1 |

TABLE 5.1: The measurement and simulation results of Bragg grating without a gap.

When the waveguide Bragg gratings are tested without a gap, its two sides are connected with the waveguide without any gap between them. Figure 5.24 show the measured results and the corresponding simulated results of the Bragg gratings with different grating periods and number of gratings. The corrugation width is set to be $\Delta W = 200\ nm$. Note the measured results have been normalized by subtracting the grating coupler loss from the transmission.

It can be seen from the results that the simulated and measured Bragg wavelengths have slight mismatches of around 2nm for all the devices with different periods. This mismatch can be attributed to the unavoidable fabrication imperfection such as over-etching. However, for the Bragg gratings with the same period but a different number of periods, the Bragg wavelengths match well and these results show fabrication uniformity. In terms of the extinction ratio, it is apparent that a larger number of periods leads to a higher extinction ratio. This is due to stronger reflection with more grating periods. Nevertheless, the extinction ratios for measurement is obviously much smaller than the simulation. This may be caused by the round shape corrugations rather than the ideal square corrugations, which cause weaker reflections. The simulated broad drops in transmission spectrum in shorter wavelength can also be seen from the measurement results for all the devices, this is due to the higher leaky mode in the rib waveguide. However, the broad drop wavelength ranges in simulation and measurement do not agree well and show clear deviations. This may be caused by the fact that an ideal rib waveguide cannot be simulated by the EME solver in Lumerical, and only a finite slab region can be used to represent the large slab in a real rib waveguide. This may cause deviation when calculating waveguide higher mode profiles which leak into the slab. The key parameters of the Bragg grating test without a gap can be summarized in Table 5.1.

When the waveguide Bragg gratings are tested with a gap, there is a gap between one side of the grating and the input waveguide, and another side is connected with the output waveguide directly. The gap is introduced here to analyse the effect of gaps in silicon photonics, and to make preparations for the future experimental implementation of dual-waveguide optical trapping. Figure 5.25 show the measured results with

different grating periods and gap distances. Note the measured results is not normalised.

Three different grating periods and four different gap distances are tested. The number of period of all the devices is 3000. The corrugation widths are set to be $\Delta W = 200\ nm$. For each of the plots from top to bottom, the gap distances of the spectrum are 1 $\mu m$, 3 $\mu m$, 6 $\mu m$, 8 $\mu m$. It can be found that the gap between the grating and the waveguide causes a large loss when comparing results to the grating coupler test results with no gap. A 1 $\mu m$ gap results in around 10 $dB$ optical loss. From the results of devices with different gap distances, it can found that increased gap distance results in an increased loss. The loss increases dramatically with the gap distance when the gap is small. When the distance increased to 6 $\mu m$, the change in loss is no longer explicit. It can also be seen from the results that the Bragg wavelength is quite accurate and stable for each period of the device even though a gap is introduced.

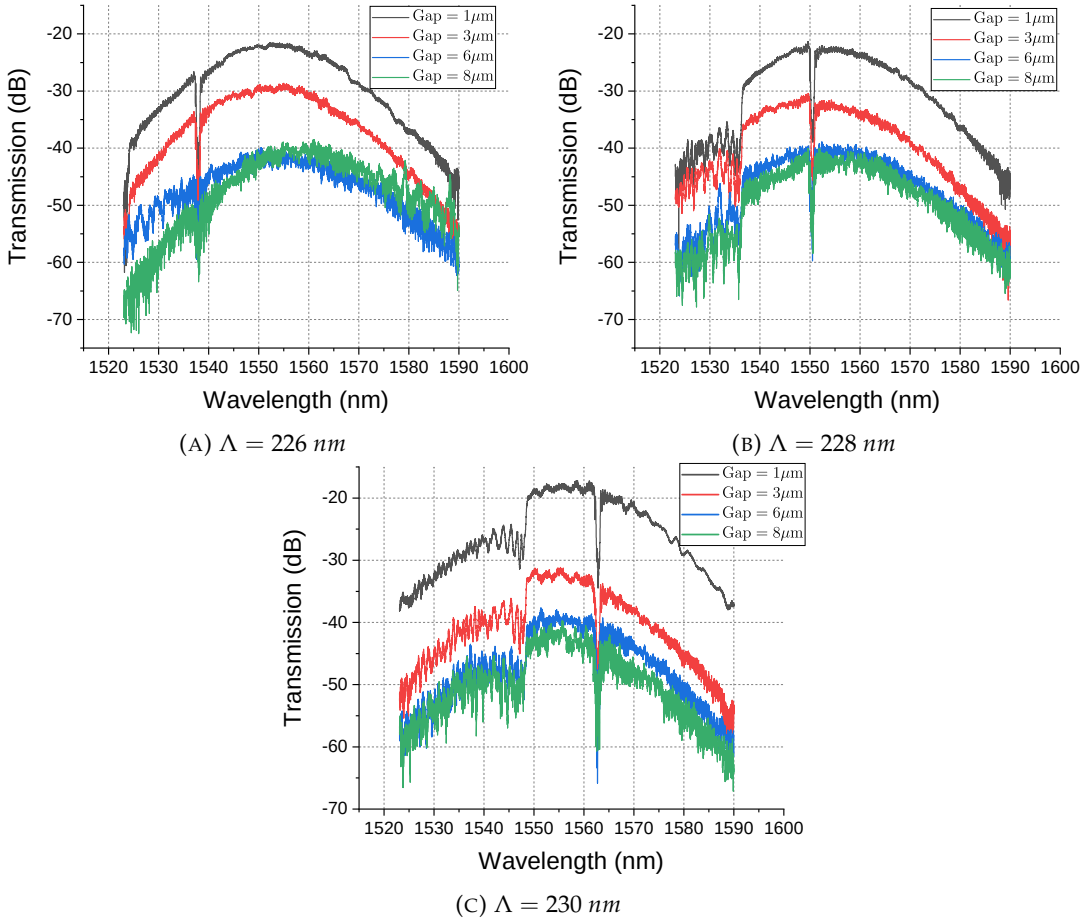


(A) $\Lambda = 226\ nm$

(B) $\Lambda = 228\ nm$

(C) $\Lambda = 230\ nm$

FIGURE 5.25: The test results of Bragg grating with gaps for different periods. (a) Period $\Lambda = 226\ nm$. (b) Period $\Lambda = 228\ nm$. (c) Period $\Lambda = 230\ nm$

From the measurement of Bragg grating with a gap or without a gap, it can be found that the Bragg grating shows a uniform performance in terms of Bragg wavelength.

This is very beneficial when it is used as an optical filter. Also, when gaps are introduced in the device, the Bragg grating still functions well.

## 5.5 Measurement and parameter extraction of optical microresonators

The optical resonator is an important component of an integrated optomechanical system. Here, a series of racetrack-shape microresonators are fabricated on the 1.5 $\mu m$ SOI platform. The microresonators were measured and the coupling parameters were extracted.

The fabricated racetrack-shape microresonators are shown below. Figure 5.26 (A) shows that the microresonator in a racetrack-shape is coupled to a bus waveguide, and the coupling happens at the straight section where two straight waveguides are in close proximity to each other. Figure 5.26 (B) shows the enlarged view of the coupling area. The designed waveguide width and gap distance are 1.1 $\mu m$ and 250 $nm$ respectively, while they are measured to be 1.06 $\mu m$ and 290 $nm$. This is caused by the inevitable over-etching effect during the fabrication process. The racetrack consists of two semicircles with a radius 400 $\mu m$ and two straight waveguides with a length 20 $\mu m$, such the perimeter of the cavity is $L = 2553.3$ $\mu m$.

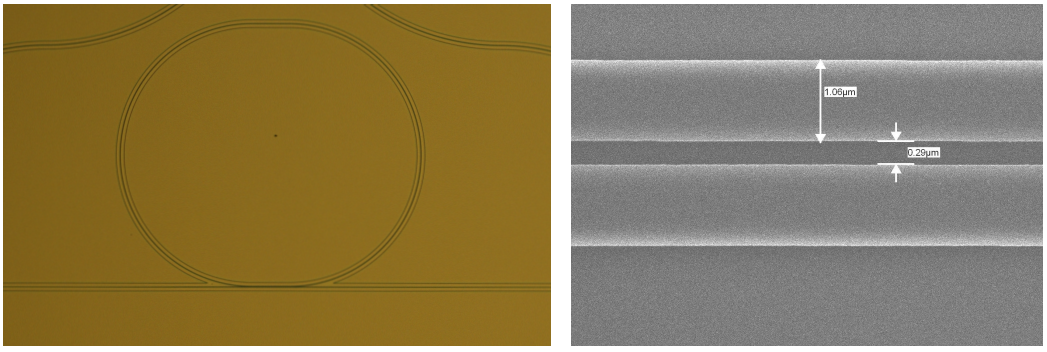


(A) (B)

FIGURE 5.26: The images of the fabricated racetrack-shape optical microresonator

In order to study the coupling behaviour of the resonators, the coupling gap is varied from 250 $nm$ to 750 $nm$. The measured transmission spectrums of the microresonators are shown in Figure 5.27. The transmission measurement of the resonators at around 1543.5 $nm$ shows optical resonances with a FSR of 250 $pm$. The theoretical FSR can be calculated as $FSR = \lambda^2/(Ln_g)$, where the group index $n_g$ in this frequency was simulated to be 3.724. This leads to a theoretical FSR of 250.5 $pm$, which is very close to the measured value 250 $pm$.

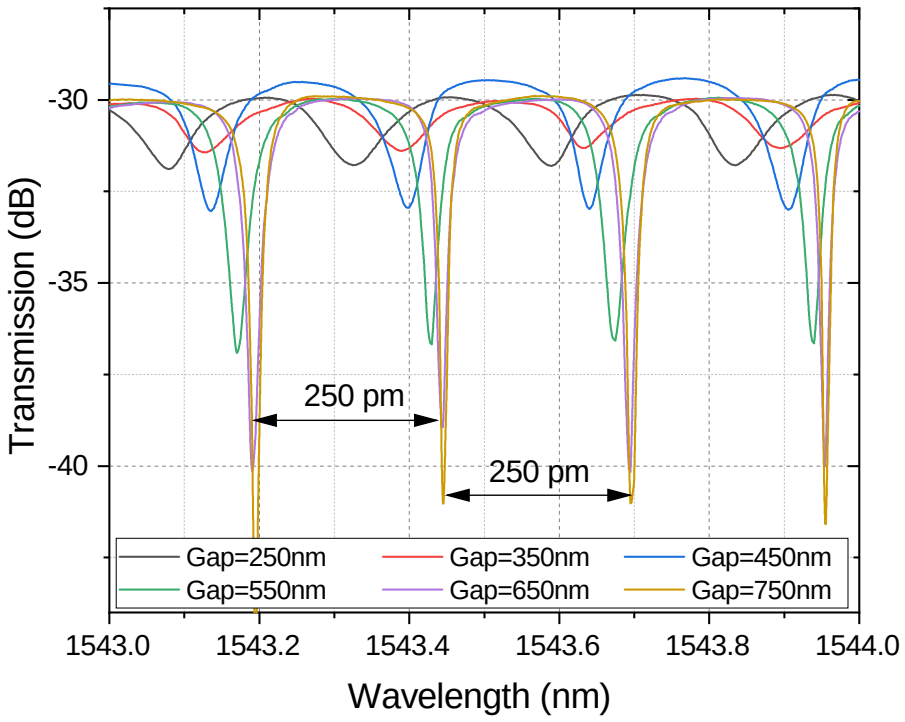


FIGURE 5.27: The measured transmission spectrums of the racetrack-shape microresonator for six different coupling distances, 250 $nm$, 350 $nm$, 450 $nm$, 550 $nm$, 650 $nm$, 750 $nm$

When increasing the gap distance, the strength of the external coupling rate $\kappa_e$ decreases. It can be found from the results that a larger gap distance leads to a larger ER. For the microresonator with a gap distance 750 $nm$, the ER can be up to 12dB. This value is far away from the critical coupling regime, therefore all the measurements are in the over-coupling regime.

The spectrum is then fitted with a Lorentz shape using the curve fitting tool in Origin 2021 software [161]. The fitting Lorentz function is given by,

$$y = y_0 + \frac{2A}{\pi}\frac{w}{4(x - x_c)^2 + w^2}. \tag{5.6}$$

The parameters $y_0$, $W$, $A$, $x_c$ in this fitting function can thus be extracted using the curve fitting tool for the transmission spectrum with different gap distances. This fitting Lorentz function can be compared to Equation 2.14 which describes the transmission of a WGM microresonator coupled to a bus waveguide, and the relationship between them can be written as,

$$\kappa = \kappa_i + \kappa_e = w, \tag{5.7}$$

$$4\kappa_e\kappa_i \cdot y_0 = \frac{-2Aw}{\pi}. \tag{5.8}$$

Note here the parameter $y_0$ comes from the coupling loss of the system, which for this

optical microresonator measurement is around 30 $dB$. The parameter $\kappa_e$ and $\kappa_i$ which represent the damping rate of the optical microresonators can then be extracted. The extracted values of $\kappa_e$, $\kappa_i$, and $\kappa = \kappa_i + \kappa_e$ are plotted in Figure 5.28 (A), it can be found the external damping rate $\kappa_e$ decreases monotonously with the increase of gap distance. For the intrinsic damping rate $\kappa_i$, a lower-than-expected value can be seen when the gap distance is 350 $nm$. This could be attributed to a measurement error. It can also be verified from this plot that the microresonators were in the over-coupling regime, as $\kappa_e$ is always larger than $\kappa_i$.

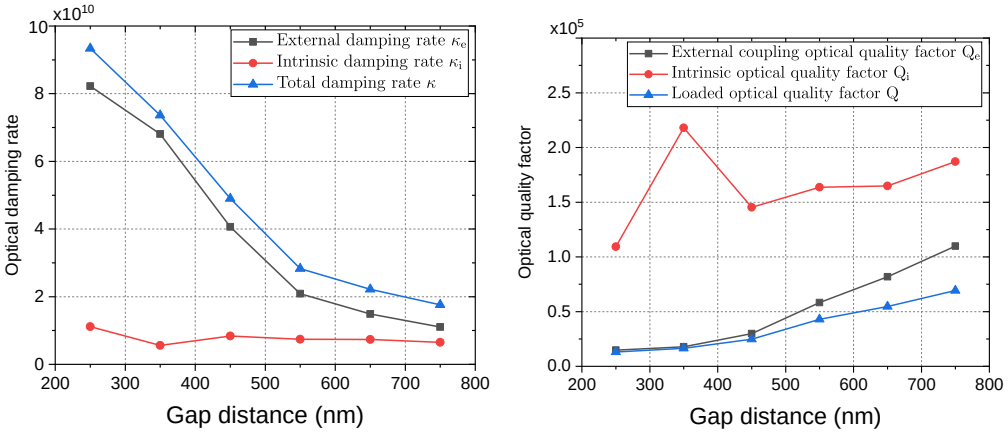


(A) (B)

FIGURE 5.28: (A) The extracted values of optical damping rate $\kappa_e$, $\kappa_i$, and $\kappa = \kappa_i + \kappa_e$ for different gap distances. (B) The extracted values of optical Q-factor $Q_e$, $Q_i$, and $1/Q = 1/Q_e + 1/Q_i$ for different gap distances.

The corresponding optical Q-factors were also calculated and shown in Figure 5.28 (B), where the external coupling optical Q-factor $Q_e$, intrinsic optical Q-factor $Q_i$ and the directly measured loaded optical factor $Q$ are shown. The loaded optical Q-factor $Q$ increases with the gap distances, and a maximum value of Q=69227 was experimentally obtained when the gap distance is 750 $nm$. The fitted intrinsic optical Q-factor $Q_i$ generally increases with the gap distance except for an error point when the gap distance is 350 $nm$. This relationship could be caused by a better etching quality in the gap area when the gap distance increases. The maximum $Q_i$ can be as large as around $1.87 \times 10^5$.

Another important parameter is the waveguide loss $\alpha$, which is usually with a unit $dB/cm$. This value can be derived from the intrinsic optical damping rate $\kappa_i$. When there is no external coupling to an optical microresonator, the photon energy in the cavity decays at the intrinsic damping rate $\kappa_i$, which can be expressed as [26],

$$\frac{dW}{dt} = -\frac{\kappa_i}{2\pi} W, \tag{5.9}$$

Where $W$ is the cavity photon energy. Assuming the initial energy is $W_0$, the cavity photon energy can thus be given by,

$$W = W_0 e^{-\frac{\kappa_i}{2\pi}t}. \tag{5.10}$$

The energy loss in $dB$ when the photons travel around the cavity for a full circle is thus expressed as $10 \cdot \log 10(e^{-\frac{\kappa_i T_{rt}}{2\pi}})$, where $T_{rt} = Ln_{eff}/c$ is the round trip time of the cavity, $L$ is the cavity path length and $c$ is the light speed. The waveguide loss in the unit $dB/cm$ can thus be written as,

$$\alpha = \frac{10 \cdot \log 10(e^{-\frac{\kappa_i T_{rt}}{2\pi}})}{100 \cdot L} = \frac{\log 10(e^{-\frac{\kappa_i L n_{eff}}{2\pi c}})}{10 \cdot L}. \tag{5.11}$$

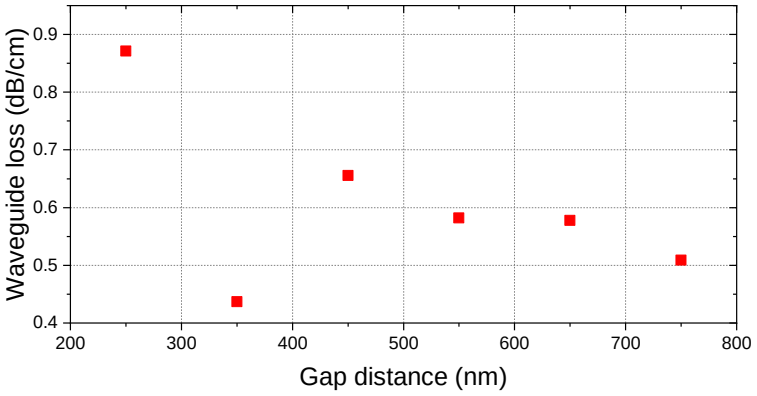


FIGURE 5.29: The calculated waveguide loss

This equation can thus be used to get the waveguide loss. The calculated waveguide losses for different gap distances are shown in Figure 5.29. It can be seen that an averaged waveguide loss of around $0.6dB/cm$ can be obtained for the rib waveguide based on 1.5 $\mu m$ SOI platform. Compared to other waveguide losses that have been achieved in the SOI platform [162, 163], this value is quite competitive and represents a high level of waveguide quality, especially when considering the fact that the no pre- or post- processes for decreasing surface roughness have been carried out.

## 5.6 Brownian motion measurement of mechanical resonators

Micro/nano mechanical resonator is the basic component of an integrated optomechanical system. Here, mechanical resonators in the form of a cantilever beam on the 1.5 $\mu m$ SOI platform were fabricated. The cantilever beams are formed on the top silicon layer of the SOI wafer by ICP etching the surrounding silicon, and subsequently suspended by etching away the $SiO_2$ layer underneath using the vapour HF.

Suspended cantilever beams with designed width at 300 $nm$ and different lengths were fabricated, and the one with 8 $\mu m$ length is shown in Figure 5.30 (A). The cantilever is formed within a gap area. Figure 5.30 (B) shows the beam width measurement of a 12 $\mu m$ length beam. The measured beam width is 193.7 $nm$. This width shrink is caused by the over-etching effect. Actually, some cantilevers with 100 $nm$ beam width were also designed, but they just "disappeared" after the etching process, which can also be explained by the over-etching. The thickness of the beam is thinned to 750 $nm$ during the first 750 $nm$ etch step except for the end area, where it is formed by etching away half the rib waveguide and therefore the thickness here is 1.5 $\mu m$.

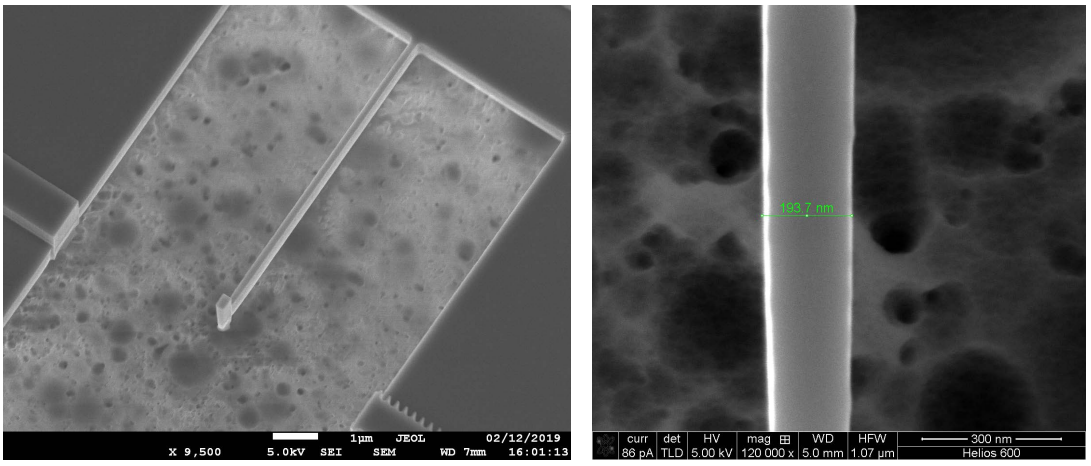


(A) (B)

FIGURE 5.30: Suspended cantilever mechanical resonator

To prove that the cantilever was indeed suspended, the thermomechanical ('Brownian') motion of the suspended cantilever beam needs to be characterised. As shown in Section 2, the displacement PSD would show a Lorentzian peak near the mechanical resonance. The setup as shown in Figure 5.32 [164, 165] was used to do this measurement.

The setup is based on an existing scanned electron microscope (SEM). SEM is typically used to get a static image of an object by scanning a focused beam of free electrons over the object and detecting secondary electron emission current $I(\mathbf{r})$ ($\mathbf{r}$ is the coordinate). The secondary electron current $I$ is sensitive to the position of the object, and is modulated proportionally by the mechanical motion of nanostructure. The recording of a real-time change of the time-dependent secondary electron current $I(t)$ thus includes the motion information of the nanostructures. Therefore, a spectral analysis of the time-domain recording $I(t)$ can reveal the natural resonant frequencies and the displacement amplitude of the nanostructure.

During the experiment, the chamber was pumped to $7.5 \times 10^{-6}$ $mbar$, and focused the beam of free electrons at the end of the suspended cantilever, where the vibration amplitude is maximum. The secondary electron current $I(t)$ was recorded by a Lock-in

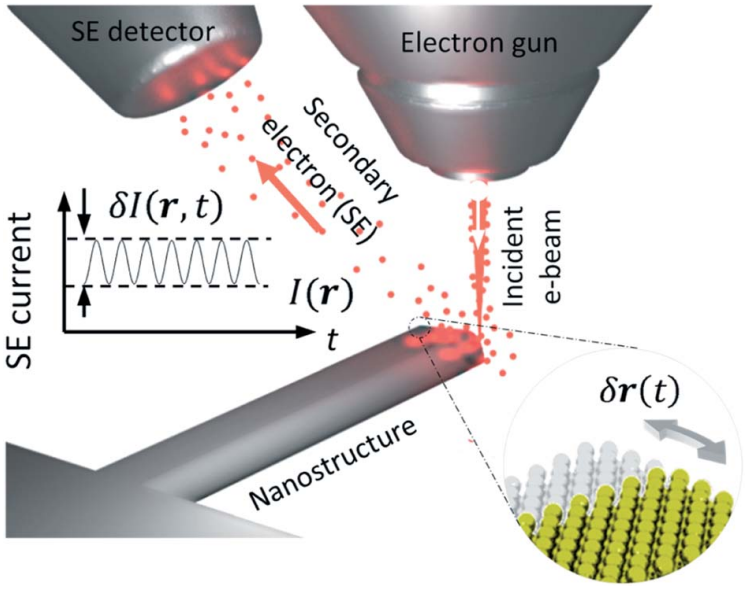


FIGURE 5.31: Detection scheme of the cantilever motion [164]. When a focused beam of electrons hits the surface of an oscillating nanostructure, the secondary electron current $I$ is modulated by the mechanical motion of nanostructure. Spectral analysis of the SE current thus provides the motion information of the nanostructure.

| Beam length | Resonant frequency (MHz) | |
|---|---|---|
| | Simulation | Experiment |
| 12 $\mu m$ | 1.702 | 1.639 |
| 8 $\mu m$ | 3.707 | 2.931 |
| 6 $\mu m$ | 6.399 | 5.201 |

TABLE 5.2: The fundamental in-plane resonant mode frequency of the suspended cantilever obtained from finite element simulation and experiment, respectively.

amplifier and then analysed with the build-in frequency spectrum analyser. The measured electrical voltage noise PSDs $S_v(\Omega)$ (unit: $V^2/Hz$) of the suspended cantilevers with different lengths are shown in Figure 5.32, where Figure 5.32 (A, B, C) is the result for beam length 12 $\mu m$, 8 $\mu m$ and 6 $\mu m$ respectively. A pronounced resonance peak can be found in each graph, with the enlarged view shown in the inset. The peaks are fitted with a Lorentz function with a constant baseline. The inferred mechanical resonance frequencies and Q-factors are shown in the inset. The measured resonance frequencies were compared to the simulated fundamental in-plane resonance frequencies obtained from COMSOL finite elements analysis in Table 5.2. Note that the measured beam width 193.7 $nm$ is used for the simulation. Good agreements can be found between the experiments and simulations. The measured mechanical Q-factor is on the order of thousand, which can be further increased by pumping to a higher vacuum level and elastic phononic engineering [59]. Because no external force was applied to the cantilever, the pronounced Lorentz peaks thus correspond to the fundamental in-plane mechanical resonant mode. The higher-order in-plane modes were not observed due to the limited bandwidth of the secondary electron detector.

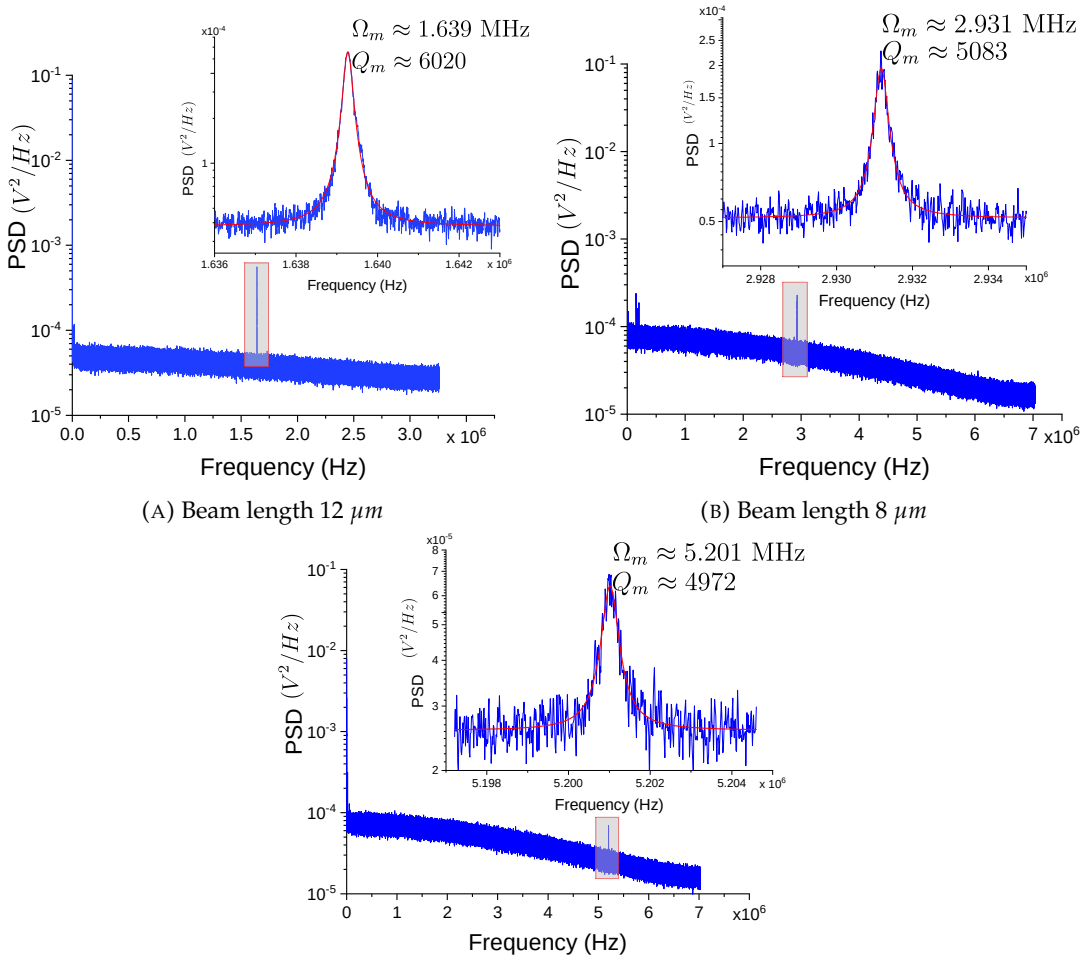


(A) Beam length 12 $\mu m$

(B) Beam length 8 $\mu m$

(C) Beam length 6 $\mu m$

FIGURE 5.32: The measured thermal noise spectrum originated from the Brownian motion of the suspended cantilever beam with a length of (A) 12 $\mu m$. (B) 8 $\mu m$. (C) 6 $\mu m$. The insets show the enlarged view of the thermomechanical spectrum (blue) and the Lorentz fitting (red) near the peak.

It should be noted that the measured signal is the electrical voltage PSD. The displacement PSD can be calibrated by using Equation 2.24. The amplitude of the Lorentz peak in the electrical voltage PSD corresponds to the thermomechanical noise spectrum density at resonance: $S_{xx}^{th}(\Omega_m) = 4k_BT/m_{eff}\Gamma_m\Omega_m^2$ (unit: $m^2/Hz$). Using standard beam theory and the finite element simulations, the effective mass can be obtained for each beam. The transduction gain of the measurement system can thus be acquired and defined as: $T_g = \sqrt{S_{xx}^{th}(\Omega_m)/S_v(\Omega_m)}$ (unit: m/V).

To conclude, this project has successfully fabricated an on-chip mechanical resonator in the form of a suspended cantilever. The full suspension is verified by the measured thermomechanical spectrum of the cantilever using a house-in setup for nanomotion observation. This novel method for mechanical thermal Brownian motion measurement is also an important supplementary means to optomechanical measurement.

## 5.7 Conclusion and discussion

In this chapter, the individual integrated silicon optomechanical components are designed, fabricated, and measured based on a 1.5 $\mu m$ thick SOI platform. Thicker SOI wafers can fabricate low-frequency mechanical resonators, handle higher optical power, has lower propagation loss and larger mode size, which are beneficial for biedan two applications, cavity OPT or SWOS generator for DFOS and dual-waveguide optical trapping. The cavity optomechanical OPT or SWOS generator for DFOS need a high optical input power for sharper pulses generation or wider frequency sweeping range, and a lower mechanical frequency is suitable for long-distance DFOS application. The dual-waveguide optical trapping application needs a high optical power and low waveguide propagating loss. However, a thicker SOI would also need a larger bend radius and result in a large footprint. Considering the trade-offs, 1.5 $\mu m$ thick SOI platform is selected.

The individual components include single-mode rib waveguides, grating couplers, MMIs, waveguide Bragg gratings, optical microresonators and mechanical resonators. These components are not only the basic components for the two previously discussed applications in Chapter 3 and Chapter 4, but also are important build blocks for a wide range of integrated silicon optomechanical applications. The fabrication processes are introduced, and the imperfection has been analysed. The measurement results prove that all the individual photonics components function well. Especially, the optical microresonator and mechanical resonator both have comparatively high Q-factor, and the waveguide has a low propagation loss. All of these works combined lay a solid foundation for the full integration of a silicon optomechanical system in the future, particularly for the cavity optomechanical OPT or SWOS generator for DFOS and dual-waveguide optical trapping.

# Chapter 6

# Conclusion

## 6.1 Summary

To summarise my work, this thesis discussed the integration of optomechanics and silicon photonics—integrated silicon optomechanics, and explored its applications in DFOS and optical trapping. This thesis also demonstrated a novel 1.5 $\mu m$ SOI platform for integrated optomechanics.

1). Firstly, a novel application of using the integrated optomechanical system to address the issues with the traditional optical probe signal generation in the DFOS system was proposed, and explicit examples were demonstrated. The proposed application was based on the OMO process induced by optomechanical dynamic back-action.

A comprehensive analysis of the cavity optomechanical coupling process was conducted by non-dimensionalizing the theoretical coupling equations describing the coupling process, through which only four system parameters are needed and the analysis complexity is greatly eased. The OMO threshold was then analytically derived. A dead-zone that forbade the onset of OMO was found and the optimal detuning value and the associated minimum threshold power were derived. The OMO characteristic in different sideband regimes was studied, and the OMO displays harmonic motion when the oscillation amplitude is small. It then evolves into chaos in RSR and into a mushroomlike phase trajectory in USR.

The OMO process in deeply USR can modulate the optical cavity field instantaneously, through which a single-wavelength continuous-wave laser can be intensity-modulated to OPT for OTDR application, and a broadband laser can be frequency-modulated to SWOS for OFDR application. The ER and DC of the OPT and the frequency-sweeping

range of the SWOS were systematically simulated under different optomechanical system parameters. Based on this design guidance, four sets of optomechanical parameters were designed with different SOI thicknesses. Using these OPT and SWOS generated by these designed optomechanical systems, the OTDR and OFDR measurement performance were theoretically calculated. The results show the capability of these optomechanical systems for the DFOS applications. It was also found that the SOI substrate with a thicker silicon layer is preferred for longer-distance DFOS applications.

2). Secondly, the design, optimisation and scaling effect of dual-waveguide optical traps on the SOI platform were presented by comprehensive numerical simulations in Lumerical FDTD Solutions. By studying the theoretical equations of optical force and trapping potential acting on a Rayleigh particle, it was found that the trapping capability can be characterised by the optical intensity at the trapping. The simulations demonstrate that the waveguide thickness is a crucial parameter in the design of a dual-waveguide optical trap, and the optimal thickness depends on the gap distance between waveguides. The parametric sweep simulation found that the optimal waveguide thickness increase with the gap distance generally, and in the meantime, is composited with periodic features whose period meets the resonance condition (standing wave in the gap). The wavelength was also swept and it was found that the optimal thickness shows a scaling effect over wavelength. The value of optimal thickness in various trapping points is summarised in Table 5.1 to provide explicit information on designing the dual-waveguide optical trap.

In addition to the dual-waveguide optical trapping, it was also proposed that the OMO process could be used to break the adherence force, which prevents the particle separating process and load particles. The adherent force and the required acceleration to separate the particles from a surface are analytically derived for different particle sizes. The acceleration variations during the OMO process were then investigated, and it was found the mechanical resonator experiences an abrupt increase in acceleration when the OMO is in a mushroom-like phase trajectory. This increase is very beneficial for particle separation. A set of reasonable optomechanical parameters was assumed, and it was found an input power of 300 $mW$ can separate a spherical silica particle as small as 200 $nm$ from the surface of the optomechanical device. All of these works combined lay the foundation of a fully on-chip optical trapping system working on vacuum or air.

3). Lastly, the individual integrated silicon optomechanical components are designed, fabricated, and measured based on a novel 1.5 $\mu m$ thick SOI platform, including single-mode rib waveguides, grating couplers, MMIs, waveguide Bragg gratings, optical microresonators and mechanical resonators. The 1.5 $\mu m$ thick SOI platform, rather than the widely-used thin ($< 300\ nm$) SOI platform, is chosen for its higher optical power handling capability, lower propagation loss, larger waveguide mode size, and comparatively small bend radius. In addition, this thick SOI platform is suitable for fabricating

low- frequency mechanical structures compared to the thin SOI platform. The fabrication processes containing two etch steps are introduced, and the imperfection has been analysed. The measurement results prove that all the individual photonics components function well. All of these works combined lay a solid foundation for the full integration of a silicon optomechanical system in the future.

## 6.2 Outlook

The contribution of this thesis mainly contains two theoretical applications of integrated silicon optomechanics and an experimental demonstration of a novel 1.5 $\mu m$ silicon optomechanical platform. Therefore, the future work of this project will be the experimental demonstrations of the proposed applications.

1). Experimental demonstration of OMO-based OPT generator and OMO-based SWOS generator for DFOS application based on 1.5 $\mu m$ SOI platform. The four sets of optomechanical parameters with different SOI thicknesses show that thick SOI is preferred for long-distance DFOS application. In the next stage, the implementation in 1.5$\mu m$ platform should be explored, in which low resonance frequency mechanical resonator can be made and long-distance sensing is thus possible. To further reduce the mechanical resonance frequency, a long suspended cantilever beam can be used, which can be coupled to a WGM optical cavity via the near-field. To improve the optical Q-factor further, the resist-reflow process [166] can be used to get a smoother sidewall. Also, the Ebeam lithography and ICP etching recipe both need to be optimised to reduce the roughness on the sidewall to reduce waveguide propagation loss.

2). The applications of on-chip dual-waveguide trapping. The first and most explicit application is biological particle trapping. The dual-waveguide optical trapping chip can be used for biological particle trapping, including blood cells and bacteria, and particle identification through the use of lasers with different power and wavelength to trap different particles. This dual-waveguide optical trapping is also promising for widespread applications in areas such as water-quality monitoring and medical diagnostics, for example, detection of human cells indicative of a disease and harmful bacteria.

The dual-waveguide trapping can also be exploited to be used for sensing applications like the traditional macroscopic levitated optomechanics. To enable the sensing application, the experiment must be conducted in a vacuum environment. Actually, a vacuum setup for integrated silicon optomechanics testing has been built and tested. It is based on a cube vacuum chamber and self-designed fibre coupling stage compatible with the chamber. Optical signals and electrical signals are introduced into the chamber through feedthrough. Once a particle is trapped and the vacuum is on, its properties including mass, radius, oscillation frequency, oscillation amplitude, and damping factor

could be obtained by measuring its displacement PSD. The parametric feedback cooling [67] can then be used to cool the thermal motion of the trapped particle and realise stable trapping. Ultrasensitive sensing can be explored following the parametric feedback cooling, including force sensing, displacement sensing, and acceleration sensing. The high-Q factor of the levitated particle holds great promise for ultrasensitive sensing. It has also been found that the precession motion exists in levitated optomechanics and the precession period can be precisely measured [167]. This precession motion can be linked to the gyroscope motion under the effect of gravity and may serve as a novel mechanism for measuring gravity.

3). Full integration of all the components into the same chip. The fascinating long-term perspective is the possibility of integrating all the components to a single chip with vacuum packaging, including laser source, an optical detector, optical modulator, particle source and ASIC for signal processing. Although laser sources and detectors in silicon photonics have not been reported with sufficient efficiency and reliability, yet it is currently a very hot research area for many groups in the world. Once been fully integrated, the integrated silicon optomechanics chip will open up new avenues with respect to high-sensitivity sensing application and fundamental quantum physics research with a compact chip-scale device.

# References


[1] Johannes Kepler. De cometis. *Libelli tres. Mylius: Augustae Vindelicorum*, 1619, 1619.

[2] James Clerk Maxwell. Xxvi. on a method of making a direct comparison of electrostatic with electromagnetic force; with a note on the electromagnetic theory of light. *Philosophical transactions of the Royal Society of London*, (158):643–657, 1868.

[3] Peter Lebedew. Untersuchungen über die druckkräfte des lichtes. *Annalen der Physik*, 311(11):433–458, 1901.

[4] Ernest Fox Nichols and Gordon Ferrie Hull. The pressure due to radiation.(second paper.). *Physical Review (Series I)*, 17(1):26, 1903.

[5] Albert Einstein. On the development of our views concerning the nature and constitution of radiation. *Phys. Z*, 10(22):817–825, 1909.

[6] Arthur Ashkin. History of optical trapping and manipulation of small-neutral particle, atoms, and molecules. *IEEE Journal of Selected Topics in Quantum Electronics*, 6(6):841–856, 2000.

[7] TH MAIMAN. Stimulated optical radiation in ruby. *Nature*, 187(4736):493–494, 1960.

[8] Tobias J Kippenberg and Kerry J Vahala. Cavity optomechanics: back-action at the mesoscale. *Science*, 321(5893):1172–1176, 2008.

[9] Markus Aspelmeyer, Pierre Meystre, and Keith Schwab. Quantum optomechanics. *Physics Today*, 65(7):29–35, 2012.

[10] VB Braginski and AB Manukin. Ponderomotive effects of electromagnetic radiation. *Sov. Phys. JETP*, 25(4):653–655, 1967.

[11] VB Braginskiĭ, Anatoli B Manukin, and M Yu Tikhonov. Investigation of dissipative ponderomotive effects of electromagnetic radiation. *Soviet Journal of Experimental and Theoretical Physics*, 31:829, 1970.

[12] B Abbott, S Jawahar, N Lockerbie, and K Tokmakov. Ligo scientific collaboration and virgo collaboration (2016) gw150914: first results from the search for binary black hole coalescence with advanced ligo. physical review d 93 (12). issn 1550-2368. *PHYSICAL REVIEW D Phys Rev D*, 93:122003, 2016.

[13] Vladimir Borisovich Braginskii and Borisovich Manukin, Anatoliĭ. *Measurement of weak forces in physics experiments*. University of Chicago Press, 1977.

[14] VB Braginsky and F Ya Khalili. *Quantum Measurement*. Cambridge University Press, 1992.

[15] Arthur Ashkin. Acceleration and trapping of particles by radiation pressure. *Physical review letters*, 24(4):156, 1970.

[16] Arthur Ashkin. Applications of laser radiation pressure. *Science*, 210(4474):1081–1088, 1980.

[17] M Bhattacharya, AN Vamivakas, and P Barker. Levitated optomechanics: introduction. *JOSA B*, 34(6):LO1–LO2, 2017.

[18] James Millen, Tania S Monteiro, Robert Pettit, and A Nick Vamivakas. Optomechanics with levitated particles. *Reports on Progress in Physics*, 83(2):026401, 2020.

[19] David Hempston, Jamie Vovrosh, Marko Toroš, George Winstone, Muddassar Rashid, and Hendrik Ulbricht. Force sensing with an optically levitated charged nanoparticle. *Applied Physics Letters*, 111(13):133111, 2017.

[20] Fernando Monteiro, Sumita Ghosh, Adam Getzels Fine, and David C Moore. Optical levitation of 10-ng spheres with nano-g acceleration sensitivity. *Physical Review A*, 96(6):063841, 2017.

[21] Lei-Ming Zhou, Ke-Wen Xiao, Zhang-Qi Yin, Jun Chen, and Nan Zhao. Sensitivity of displacement detection for a particle levitated in the doughnut beam. *Optics letters*, 43(19):4582–4585, 2018.

[22] Uroš Delić, Manuel Reisenbauer, Kahan Dare, David Grass, Vladan Vuletić, Nikolai Kiesel, and Markus Aspelmeyer. Cooling of a levitated nanoparticle to the motional quantum ground state. *Science*, 367(6480):892–895, 2020.

[23] Vijay Jain, Jan Gieseler, Clemens Moritz, Christoph Dellago, Romain Quidant, and Lukas Novotny. Direct measurement of photon recoil from a levitated nanoparticle. *Physical review letters*, 116(24):243601, 2016.

[24] Steven Chu. Nobel lecture: The manipulation of neutral particles. *Reviews of Modern Physics*, 70(3):685, 1998.

[25] Harold J Metcalf and Peter van der Straten. Laser cooling and trapping of atoms. *JOSA B*, 20(5):887–908, 2003.

[26] Markus Aspelmeyer, Tobias J Kippenberg, and Florian Marquardt. Cavity optomechanics. *Reviews of Modern Physics*, 86(4):1391, 2014.

[27] Benjamin S Sheard, Malcolm B Gray, Conor M Mow-Lowry, David E McClelland, and Stanley E Whitcomb. Observation and characterization of an optical spring. *Physical Review A*, 69(5):051801, 2004.

[28] A Dorsel, John D McCullen, Pierre Meystre, E Vignes, and H Walther. Optical bistability and mirror confinement induced by radiation pressure. *Physical Review Letters*, 51(17):1550, 1983.

[29] Simon Gröblacher, Klemens Hammerer, Michael R Vanner, and Markus Aspelmeyer. Observation of strong coupling between a micromechanical resonator and an optical cavity field. *Nature*, 460(7256):724–727, 2009.

[30] Stefan Weis, Rémi Rivière, Samuel Deléglise, Emanuel Gavartin, Olivier Arcizet, Albert Schliesser, and Tobias J Kippenberg. Optomechanically induced transparency. *Science*, 330(6010):1520–1523, 2010.

[31] Albert Schliesser, Olivier Arcizet, Rémi Rivière, Georg Anetsberger, and Tobias J Kippenberg. Resolved-sideband cooling and position measurement of a micromechanical oscillator close to the heisenberg uncertainty limit. *Nature Physics*, 5(7):509–514, 2009.

[32] Hossein Rokhsari, Tobias J Kippenberg, Tal Carmon, and Kerry J Vahala. Radiation-pressure-driven micro-mechanical oscillator. *Optics Express*, 13(14): 5293–5301, 2005.

[33] Arthur H Hartog. *An introduction to distributed optical fibre sensors*. CRC Press, Taylor & Francis Group, 2017.

[34] David Erickson, Xavier Serey, Yih-Fan Chen, and Sudeep Mandal. Nanomanipulation using near field photonics. *Lab on a Chip*, 11(6):995–1009, 2011.

[35] Olav Gaute Hellesø, Pål Løvhaugen, Ananth Z Subramanian, James S Wilkinson, and Balpreet Singh Ahluwalia. Surface transport and stable trapping of particles and cells by an optical waveguide loop. *Lab on a Chip*, 12(18):3436–3440, 2012.

[36] Gyllion Brian Loozen and Jacob Caro. On-chip optical trapping of extracellular vesicles using box-shaped composite sio 2-si 3 n 4 waveguides. *Optics express*, 26 (21):26985–27000, 2018.

[37] Shaoliang Yu, Jinsheng Lu, Vincent Ginis, Simon Kheifets, Soon Wei Daniel Lim, Min Qiu, Tian Gu, Juejun Hu, and Federico Capasso. On-chip optical tweezers based on freeform optics. *Optica*, 8(3):409–414, 2021.

[38] David J. Thomson, Callum G. Littlejohns, Stevan Stanković, Milos Nedeljkovic, and Scott A. Reynolds. *Silicon Photonics*, pages 1–22. American Cancer Society, 2015. ISBN 9780471346081. . URL https://onlinelibrary.wiley.com/doi/abs/10.1002/047134608X.W8287.

[39] Markku Tilli, Mervi Paulasto-Kröckel, Matthias Petzold, Horst Theuss, Teruaki Motooka, and Veikko Lindroos. *Handbook of silicon based MEMS materials and technologies*. Elsevier, 2020.

[40] GC Righini, Yannick Dumeige, Patrice Féron, Maurizio Ferrari, G Nunzi Conti, Davor Ristic, and Silvia Soria. Whispering gallery mode microresonators: fundamentals and applications. *La Rivista del Nuovo Cimento*, 34(7):435–488, 2011.

[41] DK Armani, TJ Kippenberg, SM Spillane, and KJ Vahala. Ultra-high-q toroid microcavity on a chip. *Nature*, 421(6926):925–928, 2003.

[42] Wei C Jiang and Qiang Lin. Chip-scale cavity optomechanics in lithium niobate. *Scientific reports*, 6(1):1–7, 2016.

[43] Matt Eichenfield, Ryan Camacho, Jasper Chan, Kerry J Vahala, and Oskar Painter. A picogram-and nanometre-scale photonic-crystal optomechanical cavity. *nature*, 459(7246):550–555, 2009.

[44] Hermann Haus. *Waves and fields in optoelectronics*. Prentice-Hall, 1984.

[45] Andrew N Cleland. *Foundations of nanomechanics: from solid-state theory to device applications*. Springer Science & Business Media, 2013.

[46] Michel Pinard, Y Hadjar, and Antoine Heidmann. Effective mass in quantum effects of radiation pressure. *The European Physical Journal D-Atomic, Molecular, Optical and Plasma Physics*, 7(1):107–116, 1999.

[47] Herbert B Callen and Theodore A Welton. Irreversibility and generalized noise. *Physical Review*, 83(1):34, 1951.

[48] Peter R Saulson. Thermal noise in mechanical experiments. *Physical Review D*, 42 (8):2437, 1990.

[49] Ewold Verhagen, Samuel Deléglise, Stefan Weis, Albert Schliesser, and Tobias J Kippenberg. Quantum-coherent coupling of a mechanical oscillator to an optical cavity mode. *Nature*, 482(7383):63–67, 2012.

[50] Xiankai Sun, Xufeng Zhang, and Hong X Tang. High-q silicon optomechanical microdisk resonators at gigahertz frequencies. *Applied Physics Letters*, 100(17): 173116, 2012.

[51] Mahmood Bagheri, Menno Poot, Mo Li, Wolfram PH Pernice, and Hong X Tang. Dynamic manipulation of nanomechanical resonators in the high-amplitude regime and non-volatile mechanical memory operation. *Nature nanotechnology*, 6(11):726–732, 2011.

[52] Emanuel Gavartin, Pierre Verlot, and Tobias J Kippenberg. A hybrid on-chip optomechanical transducer for ultrasensitive force measurements. *Nature nanotechnology*, 7(8):509–514, 2012.

[53] Gustavo S Wiederhecker, Long Chen, Alexander Gondarenko, and Michal Lipson. Controlling photonic structures using optical forces. *nature*, 462(7273):633–636, 2009.

[54] Jasper Chan, TP Mayer Alegre, Amir H Safavi-Naeini, Jeff T Hill, Alex Krause, Simon Gröblacher, Markus Aspelmeyer, and Oskar Painter. Laser cooling of a nanomechanical oscillator into its quantum ground state. *Nature*, 478(7367):89–92, 2011.

[55] Emanuel Gavartin, Remy Braive, Isabelle Sagnes, Olivier Arcizet, Alexios Beveratos, Tobias J Kippenberg, and Isabelle Robert-Philip. Optomechanical coupling in a two-dimensional photonic crystal defect cavity. *Physical review letters*, 106 (20):203902, 2011.

[56] H Lee, T Chen, J Li, K Y Yang, S Jeon, O Painter, and K J Vahala. Chemically etched ultrahigh-Q wedge-resonator on a silicon chip. *Nature Photonics*, 6(6):369–373, 2012. ISSN 1749-4885. . URL https://www.nature.com/articles/nphoton.2012.109.pdf.

[57] Martin HP Pfeiffer, Junqiu Liu, Arslan S Raja, Tiago Morais, Bahareh Ghadiani, and Tobias J Kippenberg. Ultra-smooth silicon nitride waveguides based on the damascene reflow process: fabrication and loss origins. *Optica*, 5(7):884–892, 2018.

[58] Yeghishe Tsaturyan, Andreas Barg, Anders Simonsen, Luis Guillermo Villanueva, Silvan Schmid, Albert Schliesser, and Eugene S Polzik. Demonstration of suppressed phonon tunneling losses in phononic bandgap shielded membrane resonators for high-q optomechanics. *Optics express*, 22(6):6810–6821, 2014.

[59] Amir H Ghadimi, Sergey A Fedorov, Nils J Engelsen, Mohammad J Bereyhi, Ryan Schilling, Dalziel J Wilson, and Tobias J Kippenberg. Elastic strain engineering for ultralow mechanical dissipation. *Science*, 360(6390):764–768, 2018.

[60] RA Soref and JP Lorenzo. Single-crystal silicon: a new material for 1.3 and 1.6 $\mu$m integrated-optical components. *Electronics Letters*, 21(21):953–954, 1985.

[61] Graham T Reed, G Mashanovich, F Yand Gardes, and DJ Thomson. Silicon optical modulators. *Nature photonics*, 4(8):518–526, 2010.

[62] David Thomson, Aaron Zilkie, John E Bowers, Tin Komljenovic, Graham T Reed, Laurent Vivien, Delphine Marris-Morini, Eric Cassan, Léopold Virot, Jean-Marc Fédéli, et al. Roadmap on silicon photonics. *Journal of Optics*, 18(7):073003, 2016.

[63] Arthur Ashkin and JM Dziedzic. Optical levitation in high vacuum. *Applied Physics Letters*, 28(6):333–335, 1976.

[64] Arthur Ashkin, James M Dziedzic, John E Bjorkholm, and Steven Chu. Observation of a single-beam gradient force optical trap for dielectric particles. *Optics letters*, 11(5):288–290, 1986.

[65] Arthur Ashkin and JM Dziedzic. Optical levitation by radiation pressure. *Applied Physics Letters*, 19(8):283–285, 1971.

[66] Debabrata Goswami. Nobel prize in physics–2018. *Resonance*, 23(12):1333–1341, 2018.

[67] Jamie Vovrosh, Muddassar Rashid, David Hempston, James Bateman, Mauro Paternostro, and Hendrik Ulbricht. Parametric feedback cooling of levitated optomechanics in a parabolic mirror trap. *JOSA B*, 34(7):1421–1428, 2017.

[68] PRT Jess, V Garcés-Chávez, Daniel Smith, M Mazilu, Lynn Paterson, A Riches, CS Herrington, W Sibbett, and K Dholakia. Dual beam fibre trap for raman microspectroscopy of single cells. *Optics express*, 14(12):5779–5791, 2006.

[69] Gambhir Ranjit, David P Atherton, Jordan H Stutz, Mark Cunningham, and Andrew A Geraci. Attonewton force detection using microspheres in a dual-beam optical trap in high vacuum. *Physical Review A*, 91(5):051805, 2015.

[70] Satoshi Kawata and T Tani. Optically driven mie particles in an evanescent field along a channeled waveguide. *Optics letters*, 21(21):1768–1770, 1996.

[71] Shiyun Lin, Ethan Schonbrun, and Kenneth Crozier. Optical manipulation with planar silicon microring resonators. *Nano letters*, 10(7):2408–2411, 2010.

[72] Thijs van Leest and Jaap Caro. Evanescent field trapping of bacterial spores using photonic crystal cavities. In *Frontiers in Biological Detection: From Nanosensors to Systems V*, volume 8570, page 857006. International Society for Optics and Photonics, 2013.

[73] MM Van Leest, F Bernal Arango, and J Caro. Optical forces and trapping potentials of a dual-waveguide trap based on multimode solid-core waveguides. *Journal of the European Optical Society-Rapid publications*, 6, 2011.

[74] Martijn Boerkamp, Thijs van Leest, Jeroen Heldens, Arne Leinse, Marcel Hoekman, Rene Heideman, and Jacob Caro. On-chip optical trapping and raman spectroscopy using a triplex dual-waveguide trap. *Optics express*, 22(25):30528–30537, 2014.

[75] Arne Leinse, RG Heideman, EJ Klein, R Dekker, CGH Roeloffzen, and DAI Marpaung. Triplex™ platform technology for photonic integration: Applications from uv through nir to ir. In *2011 ICO International Conference on Information Photonics*, pages 1–2. IEEE, 2011.

[76] Gyllion B Loozen, Arnica Karuna, Mohammad MR Fanood, Erik Schreuder, and Jacob Caro. Integrated photonics multi-waveguide devices for optical trapping and raman spectroscopy: design, fabrication and performance demonstration. *Beilstein journal of nanotechnology*, 11(1):829–842, 2020.

[77] Balpreet Singh Ahluwalia and Olav Gaute Hellesø. Optical waveguide loop for planar trapping of blood cells and microspheres. In *Optical Trapping and Optical Micromanipulation X*, volume 8810, page 88100T. International Society for Optics and Photonics, 2013.

[78] Pål Løvhaugen, Balpreet Singh Ahluwalia, Thomas R Huser, and Olav Gaute Hellesø. Serial raman spectroscopy of particles trapped on a waveguide. *Optics express*, 21(3):2964–2970, 2013.

[79] Øystein Ivar Helle, Balpreet Singh Ahluwalia, and Olav Gaute Hellesø. Optical transport, lifting and trapping of micro-particles by planar waveguides. *Optics express*, 23(5):6601–6612, 2015.

[80] Balpreet Singh Ahluwalia, Øystein Ivar Helle, and Olav Gaute Hellesø. Rib waveguides for trapping and transport of particles. *Optics express*, 24(5):4477–4487, 2016.

[81] MK Barnoski and SM Jensen. Fiber waveguides: a novel technique for investigating attenuation characteristics. *Applied optics*, 15(9):2112–2115, 1976.

[82] Qing Bai, Qinglin Wang, Dong Wang, Yu Wang, Yan Gao, Hongjuan Zhang, Mingjiang Zhang, and Baoquan Jin. Recent advances in brillouin optical time domain reflectometry. *Sensors*, 19(8):1862, 2019.

[83] Yixin Zhang, Xuelin Wu, Zhoufeng Ying, and Xuping Zhang. Performance improvement for long-range botdr sensing system based on high extinction ratio modulator. *Electronics letters*, 50(14):1014–1016, 2014.

[84] Linqing Luo, Bo Li, Yifei Yu, Xiaomin Xu, Kenichi Soga, and Jize Yan. Time and frequency localized pulse shape for resolution enhancement in stft-botdr. *Journal of Sensors*, 2016, 2016.

[85] Ulrich Glombitza and Ernst Brinkmeyer. Coherent frequency-domain reflectometry for characterization of single-mode integrated-optical waveguides. *Journal of Lightwave technology*, 11(8):1377–1384, 1993.

[86] Dan Zhao, Dzmitry Pustakhod, Kevin Williams, and Xaveer Leijtens. High resolution optical frequency domain reflectometry for analyzing intra-chip reflections. *IEEE Photonics Technology Letters*, 29(16):1379–1382, 2017.

[87] Jihong Geng, Christine Spiegelberg, and Shibin Jiang. Narrow linewidth fiber laser for 100-km optical frequency domain reflectometry. *IEEE Photonics Technology Letters*, 17(9):1827–1829, 2005.

[88] Fumihiko Ito, Xinyu Fan, and Yusuke Koshikiya. Long-range coherent ofdr with light source phase noise compensation. *Journal of Lightwave Technology*, 30(8): 1015–1024, 2011.

[89] Huolei Wang, Liang Kong, Adam Forrest, David Bajek, Stephanie E Haggett, Xiaoling Wang, Bifeng Cui, Jiaoqing Pan, Ying Ding, and Maria Ana Cataluna. Ultrashort pulse generation by semiconductor mode-locked lasers at 760 nm. *Optics express*, 22(21):25940–25946, 2014.

[90] Ewoud Vissers, Stijn Poelman, Camiel Op de Beeck, Kasper Van Gasse, and Bart Kuyken. Hybrid integrated mode-locked laser diodes with a silicon nitride extended cavity. *Optics Express*, 29(10):15013–15022, 2021.

[91] Kasturi Saha, Yoshitomo Okawachi, Bonggu Shim, Jacob S Levy, Reza Salem, Adrea R Johnson, Mark A Foster, Michael RE Lamont, Michal Lipson, and Alexander L Gaeta. Modelocking and femtosecond pulse generation in chip-based frequency combs. *Optics express*, 21(1):1335–1343, 2013.

[92] Junqiu Liu, Erwan Lucas, Arslan S Raja, Jijun He, Johann Riemensberger, Rui Ning Wang, Maxim Karpov, Hairun Guo, Romain Bouchand, and Tobias J Kippenberg. Photonic microwave generation in the x-and k-band using integrated soliton microcombs. *Nature Photonics*, 14(8):486–491, 2020.

[93] Mian Zhang, Brandon Buscaino, Cheng Wang, Amirhassan Shams-Ansari, Christian Reimer, Rongrong Zhu, Joseph M Kahn, and Marko Lončar. Broadband electro-optic frequency comb generation in a lithium niobate microring resonator. *Nature*, 568(7752):373–377, 2019.

[94] Siqi Liu, Kan Wu, Linjie Zhou, Liangjun Lu, Bingjian Zhang, Gangqiang Zhou, and Jianping Chen. Optical frequency comb and nyquist pulse generation with integrated silicon modulators. *IEEE Journal of Selected Topics in Quantum Electronics*, 26(2):1–8, 2019.

[95] JP Von Der Weid, Rogiero Passy, G Mussi, and Nicolas Gisin. On the characterization of optical fiber network components with optical frequency domain reflectometry. *Journal of Lightwave Technology*, 15(7):1131–1141, 1997.

[96] Qingwen Liu, Xinyu Fan, and Zuyuan He. Time-gated digital optical frequency domain reflectometry with 1.6-m spatial resolution over entire 110-km range. *Optics Express*, 23(20):25988–25995, 2015.

[97] Zhen Guo, Gaoce Han, Jize Yan, David Greenwood, James Marco, and Yifei Yu. Ultimate spatial resolution realisation in optical frequency domain reflectometry with equal frequency resampling. *Sensors*, 21(14):4632, 2021.

[98] Optical Reflection and Transmission | Luna, 2021. URL https://lunainc.com/capability/optical-transmission-and-reflection.

[99] Tunable Lasers | SANTEC CORPORATION - The Photonics Pioneer, 2021. URL https://www.santec.com/en/products/instruments/tunablelaser/?dm=1703_en_OFC.

[100] Tunable Laser Source Instruments | Keysight, 2021. URL https://www.keysight.com/gb/en/products/photonic-products/optical-component-test-products/optical-laser-source-products/tunable-laser-source-modules.html.

[101] Zhiping Zhou, Bing Yin, and Jurgen Michel. On-chip light sources for silicon photonics. *Light: Science & Applications*, 4(11):e358–e358, 2015.

[102] Tobias J Kippenberg and Kerry J Vahala. Cavity opto-mechanics. *Optics express*, 15(25):17172–17205, 2007.

[103] Albert Schliesser, Pascal Del'Haye, Nima Nooshi, KJ Vahala, and Tobias J Kippenberg. Radiation pressure cooling of a micromechanical oscillator using dynamical backaction. *Physical Review Letters*, 97(24):243905, 2006.

[104] Mohammad-Ali Miri, Giuseppe D'Aguanno, and Andrea Alù. Optomechanical frequency combs. *New Journal of Physics*, 20(4):043013, 2018.

[105] P Djorwe, JY Effa, and SG Nana Engo. Multistability, staircases, and optical high-order sideband combs in optomechanics. *JOSA B*, 37(11):A36–A44, 2020.

[106] Florian Marquardt, JGE Harris, and Steven M Girvin. Dynamical multistability induced by radiation pressure in high-finesse micromechanical optical cavities. *Physical review letters*, 96(10):103901, 2006.

[107] M. Poot, K. Y. Fong, M. Bagheri, Whp Pernice, and H. X. Tang. Backaction limits on self-sustained optomechanical oscillations. *Physical Review A*, 86(5):1844–1853, 2012.

[108] Thales Figueiredo Roque, Florian Marquardt, and Oleg M Yevtushenko. Nonlinear dynamics of weakly dissipative optomechanical systems. *New Journal of Physics*, 22(1):013049, 2020.

[109] Max Ludwig, Björn Kubala, and Florian Marquardt. The optomechanical instability in the quantum regime. *New Journal of Physics*, 10(9):095013, 2008.

[110] Frank M Buters, Hedwig J Eerkens, Kier Heeck, Matthew J Weaver, Brian Pepper, Sven de Man, and Dirk Bouwmeester. Experimental exploration of the optomechanical attractor diagram and its dynamics. *Physical Review A*, 92(1):013811, 2015.

[111] Constanze Metzger, Max Ludwig, Clemens Neuenhahn, Alexander Ortlieb, Ivan Favero, Khaled Karrai, and Florian Marquardt. Self-induced oscillations in an optomechanical system driven by bolometric backaction. *Physical review letters*, 101(13):133903, 2008.

[112] Lawrence F Shampine and Mark W Reichelt. The matlab ode suite. *SIAM journal on scientific computing*, 18(1):1–22, 1997.

[113] Tal Carmon, MC Cross, and Kerry J Vahala. Chaotic quivering of micron-scaled on-chip resonators excited by centrifugal optical pressure. *Physical review letters*, 98(16):167203, 2007.

[114] L Bakemeier, A Alvermann, and H Fehske. Route to chaos in optomechanics. *Physical review letters*, 114(1):013601, 2015.

[115] Alan Wolf, Jack B Swift, Harry L Swinney, and John A Vastano. Determining lyapunov exponents from a time series. *Physica D: nonlinear phenomena*, 16(3): 285–317, 1985.

[116] Calculation lyapunov exponents for ode, 2021. URL https://www.mathworks.com/matlabcentral/fileexchange/4628-calculation-lyapunov-exponents-for-ode.

[117] Ferdinand Brennecke, Stephan Ritter, Tobias Donner, and Tilman Esslinger. Cavity optomechanics with a bose-einstein condensate. *Science*, 322(5899):235–238, 2008.

[118] Ming Gao, Fu-Chuan Lei, Chun-Guang Du, and Gui-Lu Long. Self-sustained oscillation and dynamical multistability of optomechanical systems in the extremely-large-amplitude regime. *Physical Review A*, 91(1):013833, 2015.

[119] Tal Carmon, Hossein Rokhsari, Lan Yang, Tobias J Kippenberg, and Kerry J Vahala. Temporal behavior of radiation-pressure-induced vibrations of an optical microcavity phonon mode. *Physical review letters*, 94(22):223902, 2005.

[120] Timo Aalto, Kimmo Solehmainen, Mikko Harjanne, Markku Kapulainen, and Päivi Heimala. Low-loss converters between optical silicon waveguides of different sizes and types. *IEEE photonics technology letters*, 18(5):709–711, 2006.

[121] Xinyu Fan, Yusuke Koshikiya, and Fumihiko Ito. Phase-noise-compensated optical frequency-domain reflectometry. *IEEE Journal of Quantum Electronics*, 45(6): 594–602, 2009.

[122] Zhenyang Ding, X Steve Yao, Tiegen Liu, Yang Du, Kun Liu, Qun Han, Zhuo Meng, Junfeng Jiang, and Hongxin Chen. Long measurement range ofdr beyond laser coherence length. *IEEE Photonics Technology Letters*, 25(2):202–205, 2012.

[123] Nanophotonic FDTD Simulation Software - Lumerical FDTD, 2021. URL https://www.lumerical.com/products/fdtd/.

[124] Arthur Ashkin. Forces of a single-beam gradient laser trap on a dielectric sphere in the ray optics regime. *Biophysical journal*, 61(2):569–582, 1992.

[125] Yasuhiro Harada and Toshimitsu Asakura. Radiation forces on a dielectric sphere in the rayleigh scattering regime. *Optics communications*, 124(5-6):529–541, 1996.

[126] James P Gordon. Radiation forces and momenta in dielectric media. *Physical Review A*, 8(1):14, 1973.

[127] Julls Adams Stratton. Electromagnetic theory, mcgrow-hill book company. *Inc., New York, and London*, pages 205–207, 1941.

[128] Gérard Gouesbet, Gérard Gréhan, and Bruno Maheu. Scattering of a gaussian beam by a mie scatter center using a bromwich formalism. *Journal of optics*, 16(2): 83, 1985.

[129] Gérard Gouesbet, Bruno Maheu, and Gérard Gréhan. Light scattering from a sphere arbitrarily located in a gaussian beam, using a bromwich formulation. *JOSA A*, 5(9):1427–1443, 1988.

[130] Graham T Reed and Andrew P Knights. *Silicon photonics: an introduction*. John Wiley & Sons, 2004.

[131] Optical force on a particle – Lumerical, 2021. URL https://support.lumerical.com/hc/en-us/articles/360042214494-Optical-force-on-a-particle-2D-.

[132] Pavel Zemánek, Alexandr Jonáš, and Miroslav Liška. Simplified description of optical forces acting on a nanoparticle in the Gaussian standing wave. *Journal of the Optical Society of America A*, 19(5):1025–1025, 2002. ISSN 0740-3232. . URL https://www.osapublishing.org/abstract.cfm?URI=josaa-19-5-1025.

[133] Kenneth Langstreth Johnson, Kevin Kendall, and aAD Roberts. Surface energy and the contact of elastic solids. *Proceedings of the royal society of London. A. mathematical and physical sciences*, 324(1558):301–313, 1971.

[134] Boris V Derjaguin, Vladimir M Muller, and Yu P Toporov. Effect of contact deformations on the adhesion of particles. *Journal of Colloid and interface science*, 53(2): 314–326, 1975.

[135] Lars-Oliver Heim, Jürgen Blum, Markus Preuss, and Hans-Jürgen Butt. Adhesion and friction forces between spherical micrometer-sized particles. *Physical Review Letters*, 83(16):3328, 1999.

[136] Aaron J Zilkie, Pradeep Srinivasan, Andrea Trita, Thomas Schrans, Guomin Yu, Jerry Byrd, David A Nelson, Karl Muth, Damiana Lerose, Mazin Alalusi, et al. Multi-micron silicon photonics platform for highly manufacturable and versatile photonic integrated circuits. *IEEE Journal of Selected Topics in Quantum Electronics*, 25(5):1–13, 2019.

[137] Minhang Bao. *Analysis and design principles of MEMS devices*. Elsevier, 2005.

[138] Xinzhu Sang, En-Kuang Tien, and Ozdal Boyraz. Applications of two photon absorption in silicon. *Journal of optoelectronics and advanced materials*, 11(1):15, 2009.

[139] Hon Ki Tsang, Chak Sham Wong, Tak Keung Liang, IE Day, SW Roberts, Arnold Harpin, John Drake, and Mehdi Asghari. Optical dispersion, two-photon absorption and self-phase modulation in silicon waveguides at 1.5 $\mu$ m wavelength. *Applied Physics Letters*, 80(3):416–418, 2002.

[140] Callum G Littlejohns, David J Rowe, Han Du, Ke Li, Weiwei Zhang, Wei Cao, Thalia Dominguez Bucio, Xingzhao Yan, Mehdi Banakar, Dehn Tran, et al. Cornerstone's silicon photonics rapid prototyping platforms: Current status and future outlook. *Applied Sciences*, 10(22):8201, 2020.

[141] Abdul Rahim, Jeroen Goyvaerts, Bertrand Szelag, Jean-Marc Fedeli, Philippe Absil, Timo Aalto, Mikko Harjanne, Callum Littlejohns, Graham Reed, Georg Winzer, et al. Open-access silicon photonics platforms in europe. *IEEE Journal of Selected Topics in Quantum Electronics*, 25(5):1–18, 2019.

[142] Andrew Rickman. The commercialization of silicon photonics. *Nature Photonics*, 8(8):579–582, 2014.

[143] Matteo Cherchi, Sami Ylinen, Mikko Harjanne, Markku Kapulainen, and Timo Aalto. Dramatic size reduction of waveguide bends on a micron-scale silicon photonic platform. *Optics express*, 21(15):17814–17823, 2013.

[144] Optical Waveguide Design Software - Lumerical MODE, 2021. URL `https://www.lumerical.com/products/mode/`.

[145] Isa Kiyat, Atilla Aydinli, and Nadir Dagli. High-q silicon-on-insulator optical rib waveguide racetrack resonators. *Optics express*, 13(6):1900–1905, 2005.

[146] Na Fang, Zhifeng Yang, Aimin Wu, Jing Chen, Miao Zhang, Shichang Zou, and Xi Wang. Three-dimensional tapered spot-size converter based on (111) silicon-on-insulator. *IEEE Photonics Technology Letters*, 21(12):820–822, 2009.

[147] R Takei, M Suzuki, E Omoda, S Manako, T Kamei, M Mori, and Y Sakakibara. Silicon knife-edge taper waveguide for ultralow-loss spot-size converter fabricated by photolithography. *Applied Physics Letters*, 102(10):101108, 2013.

[148] A Delâge, S Janz, B Lamontagne, A Bogdanov, D Dalacu, D-X Xu, and KP Yap. Monolithically integrated asymmetric graded and step-index couplers for microphotonic waveguides. *Optics Express*, 14(1):148–161, 2006.

[149] Dirk Taillaert, Peter Bienstman, and Roel Baets. Compact efficient broadband grating coupler for silicon-on-insulator waveguides. *Optics letters*, 29(23):2749–2751, 2004.

[150] Theodor Tamir and Song-Tsuen Peng. Analysis and design of grating couplers. *Applied physics*, 14(3):235–254, 1977.

[151] C Alonso-Ramos, Alejandro Ortega-Moñux, I Molina-Fernández, P Cheben, L Zavargo-Peche, and R Halir. Efficient fiber-to-chip grating coupler for micrometric soi rib waveguides. *Optics Express*, 18(14):15189–15200, 2010.

[152] C Alonso-Ramos, A Ortega-Moñux, L Zavargo-Peche, R Halir, J de Oliva-Rubio, I Molina-Fernández, P Cheben, D-X Xu, S Janz, N Kim, et al. Single-etch grating coupler for micrometric silicon rib waveguides. *Optics letters*, 36(14):2647–2649, 2011.

[153] Lucas B Soldano and Erik CM Pennings. Optical multi-mode interference devices based on self-imaging: principles and applications. *Journal of lightwave technology*, 13(4):615–627, 1995.

[154] Robert Halir, I Molina-Fernández, A Ortega-Monux, JG Wanguemert-Perez, Dan-Xia Xu, Pavel Cheben, and Siegfried Janz. A design procedure for high-performance, rib-waveguide-based multimode interference couplers in silicon-on-insulator. *Journal of Lightwave Technology*, 26(16):2928–2936, 2008.

[155] Robert Halir, A Ortega-Moñux, I Molina-Fernadez, JG Wanguemert-Perez, Pavel Cheben, Dan-Xia Xu, Boris Lamontagne, and Siegfried Janz. Compact high-performance multimode interference couplers in silicon-on-insulator. *IEEE Photonics Technology Letters*, 21(21):1600–1602, 2009.

[156] Xu Wang, Wei Shi, Han Yun, Samantha Grist, Nicolas AF Jaeger, and Lukas Chrostowski. Narrow-band waveguide bragg gratings on soi wafers with cmos-compatible fabrication process. *Optics express*, 20(14):15547–15558, 2012.

[157] Xu Wang. *Silicon photonic waveguide Bragg gratings*. PhD thesis, University of British Columbia, 2013.

[158] Thomas Edward Murphy, Jeffrey Todd Hastings, and Henry I Smith. Fabrication and characterization of narrow-band bragg-reflection filters in silicon-on-insulator ridge waveguides. *Journal of lightwave technology*, 19(12):1938, 2001.

[159] Ivano Giuntoni, Andrzej Gajda, Michael Krause, Ralf Steingrüber, Jürgen Bruns, and Klaus Petermann. Tunable bragg reflectors on silicon-on-insulator rib waveguides. *Optics express*, 17(21):18518–18524, 2009.

[160] Cornerstone-silicon photonics rapid prototyping foundry. https://www.cornerstone.sotonfab.co.uk/, 2021.

[161] OriginLab - Origin and OriginPro - Data Analysis and Graphing Software, 2021. URL https://www.originlab.com/.

[162] Aleksandr Biberman, Michael J Shaw, Erman Timurdogan, Jeremy B Wright, and Michael R Watts. Ultralow-loss silicon ring resonators. *Optics letters*, 37(20):4236–4238, 2012.

[163] Long Zhang, Lanlan Jie, Ming Zhang, Yi Wang, Yiwei Xie, Yaocheng Shi, and Daoxin Dai. Ultrahigh-q silicon racetrack resonators. *Photonics Research*, 8(5): 684–689, 2020.

[164] Tongjun Liu, Jun-Yu Ou, Kevin F MacDonald, and Nikolay I Zheludev. Detection of sub-atomic movement in nanostructures. *Nanoscale Advances*, 3(8):2213–2216, 2021.

[165] Tongjun Liu, Jun-Yu Ou, Eric Plum, Kevin F. MacDonald, and Nikolay I. Zheludev. Visualization of subatomic movements in nanostructures. *Nano Letters*, 0(0):null, 0. . URL https://doi.org/10.1021/acs.nanolett.1c02644. PMID: 34469159.

[166] Jingnan Cai, Peng Huei Lim, Yasuhiko Ishikawa, and Kazumi Wada. Silicon waveguide sidewall smoothing by resist reflowing. *Journal of Nonlinear Optical Physics & Materials*, 19(04):801–809, 2010.

[167] Muddassar Rashid, Marko Toroš, Ashley Setter, and Hendrik Ulbricht. Precession motion in levitated optomechanics. *Physical review letters*, 121(25):253601, 2018.

# Publication List

[1] Xiangming Xu, David J Thomson, and Jize Yan. "Optimisation and scaling effect of dual-waveguide optical trapping in the SOI platform." Optics Express 28, no. 22 (2020): 33285-33297.

[2] Xiangming Xu, Hailong Pi, Wangke Yu, and Jize Yan. "On-chip optical pulse train generation through the optomechanical oscillation." Optics Express 29, no. 23 (2021): 38781-38795.

[3] Xiangming Xu, Hendrik Ulbricht, David J Thomson, Goran Mashanovich, and Jize Yan. "Scaling effect and optimization of SOI dual-waveguide optical trapping." In 2020 IEEE Photonics Conference (IPC), pp. 1-2. IEEE, 2020.